Wide band TX Leakage Cancellation for FDD Transceivers

by

Han Su

A thesis submitted in fulfillment

of the requirements for the degree of

DOCTOR OF PHILOSOPHY

in

Department of Electronic Engineering

National University of Ireland, Maynooth

7$^{\text{th}}$ June 2017

Head of Department

Prof. Ronan J. Farrell

Supervisor

Prof. Ronan J. Farrell

Contents

Abstract

Frequency division duplex (FDD) is the most widely used full duplex technique for modern wireless communication systems. A device called a duplexer is needed in order to separate the transmitter (TX) and the receiver (RX) signals. To avoid RX being saturated and desensitized, the isolation between the TX and RX ports of the duplexer needs to be as large as possible. However, such a duplexer is less desirable for a base station due to its bulky size, high cost and design challenges. Relaxing the isolation performance requirement of the duplexer allows TX signal to appear in the RX path. Such a signal is known as TX leakage and consists of in-band and out-of-band portions. Due to the fact that the in-band leakage can't be filtered out with conventional filtering techniques, an active cancellation system is required.

This thesis will present a novel wide band TX leakage cancellation approach along with two new modelling techniques. The cancellation system is based on the analog finite impulse response (FIR) filter structure and consists of several cancellation paths (also known as taps). In each of the taps, there is an attenuator, phase shifter and delay line. These components are utilized to recondition the reference signal which is the replica of the output signal of the high power amplifier (PA) in the TX path. The output of the cancellation system (the cancellation signal) in theory should have the same amplitudes, but 180° phase offsets from the leakage signal within the band of interest. By combining the cancellation signal and the leakage, the latter can thus be suppressed. The two novel modelling techniques, named as the modified adaptive delay filter using direct cross-correlation (MADF-DC) and the modified compressed sampling matching pursuit (MCoSaMP) are proposed in this thesis. The two algorithms are developed from the classic adaptive delay filter (C-ADF) and the classic compressed sampling matching pursuit (C-CoSaMP), respectively. These modelling techniques can provide the optimization of not only the amplitudes and phase, but the delays. They are designed for the cancellation system in order to achieve wide band cancellation with the minimum hardware resources.

The evaluation of the cancellation system was carried out utilizing a test bench, which represented a typical base station. Experimental results show that greater than 15 dB of cancellation has been achieved for 35 MHz bandwidth at the carrier frequency of 897.5 MHz using four taps. In contrast, such result is about 7 dB less than the simulated cancellation performance. The reasons of such performance degradation have been analysed and will be presented in this thesis.

Acknowledgments

I couldn't have gone so far on this project without the help from other people. Hence, I would like to take this opportunity to express my gratitude to the people who have supported and helped me during these years.

Firstly, I would like to thank my supervisor, Dr. Ronan Farrell for giving me a chance to work on this project and continuously supporting me along the way. I would also like to express my thanks to everyone in the department since I started as an undergraduate.

I would like to thank my family for providing the shoulders when I need them. Thank you, mum, for everything that you have provided for me. You told me to be strong, so I am. Thank you, parents-in-laws, for all your supports so that I can focus on the PhD studies. Thank you, my little angel. My world has become more colourful since you were born.

I would like to thank all other people who have helped me.

Ying, thank you for supporting me, for believing in me, for cheering me up, for motivating me, for loving me, for your encouragement, for your criticism, for your hard work, for the wonderful daughter that you brought to me... This list can go on forever. It was you who made this happen.

List of Published and Accepted Contributions

Published Contributions

- H. Su, Z. Wang, S. Ibrahim and R. Farrell, "A Digitally Assisted Analog Cancellation System at RF Frequencies for Improving the Isolation Performance of a Ceramic Duplexer," 46th European Microwave Conference (EuMC), 2016, London

- S. Ibrahim, H. Su, Z. Wang, and R. Farrell, "A New RF Interference Cancellation using A Novel 3-Pole Bandstop Resonator designed using Tapped CRLH T-Line Model," 46th European Microwave Conference (EuMC), 2016, London

- Z. Wang, S. Ibrahim, H. Su, and R. Farrell, "Generalised Digital Predistortion of RF Power Amplifiers with Low-rate Feedback Signal," 46th European Microwave Conference (EuMC), 2016, London

- H. Su, Z. Wang and R. Farrell, "Compressed-sampling-based behavioural modelling technique for wideband RF transmitter leakage cancellation system," 13th International Conference on Synthesis, Modeling, Analysis and Simulation Methods and Applications to Circuit Design (SMACD), Lisbon, Portugal, 2016, pp. 1-4.

- H. Su, G. Szczepkowski and R. Farrell, "Wideband Tx leakage cancellation using adaptive delay filter at RF frequencies," 25th IET Irish Signals & Systems Conference 2014 and 2014 China-Ireland International Conference on Information and Communications Technologies (ISSC 2014/CIICT 2014), Limerick, 2014, pp. 396-401.

- H. Su, G. Szczepkowski and R. Farrell, "TX Leakage Cancellation with Adaptive Delay Filter", 17th Research Colloquium on Communications and Radio Science into the 21st Century, 30th April - 1st May 2014, Royal Irish Academy, Academy House, 19 Dawson Street, Dublin 2.

List of Figures

List of Tables

List of Abbreviations

3GPP	3rd generation partnership project
ADC	analog-to-digital converter
ADS	Advance Design System
BAW	bulk acoustic wave
BAW-SMR	solidly-mounted resonator bulk acoustic wave
CW	continuous wave
DAC	digital-to-analog converter
DL	down-link
DMS	dual mode surface acoustic wave
DPD	digital pre-distortion
EVM	error vector magnitude
FBAR	film bulk acoustic resonator
FFT	fast fourier transform
FPC	four-port canceller
IDT	interdigital transducer
IIP2	second order input intercept point
IM2	second order intermodulation distortion
IM3	third order intermodulation distortion
LC	inductor and capacitor
LMS	least-mean-square
LNA	low noise amplifier

LS	least squares
LTE	long term evolution
MADF-DC	Modified adaptive delay filter using direct cross-correlation
MCoSaMP	Modified Compressive Sampling Matching Pursuit
MIMO	multi-input-multi-output
NMSE	normalised mean square error
PCB	printed circuit board
PH	Parallel Hammerstein
Q-factor	quality factor
RF-MEMS	RF microelectromechanical systems
RRH	remote radio head
SAW	surface acoustic wave
SC-FD	same channel full duplex
SMU	model number of the vector signal generator that is manufactured by Rohde & Schwarz
SNR	signal to noise ratio
TDD	nuclear magnetic resonance
UE	user equipment
UL	up-link
VGA	variable gain amplifier
VNA	vector network analyser
WCDMA	wideband code division multiple access
WGN	white Gaussian noise

List of Symbols

A	power level of the noise floor of PA in chpater 2 or power level of the leakage after the LNA in chapter 3
$A_{S_c}(f)$	magnitude response of the cancellation signal
$A_{S_l}(f)$	magnitude response of the leakage
B	power level of the in-band leakage before the LNA
$B(m)$	magnitude of the weighting vector
C	saturation point of the LNA in chpater 2 or power level of the RX signal after the LNA in chapter 3
D	power of RX signal before LNA
E	power of signal within TX band after LNA and conventional filtering
G	LNA gain
I component	in-phase component
ISO_{des}	required additional isolation performance of the duplexer
M	the order of the cancellation system
N	number of samples at the baseband
N_{path}	number of local oscillating signal for n-path technque
PL_f	free space path loss in dB
P_{NTX}	power of the noise at the output of the PA
P_{Sen}	sensitivity of the receiver at the antenna port of a medium range base station
P_{TX}	power of the transmitted signal for 5 MHz carrier bandwidth

Q component	quadrature component
$S_c(f)$	frequency response of the cancellation signal
$S_l(f)$	frequency response of the leakage
$Z(f)$	frequency response of the resulting signal after the cancellation
$\hat{e}(n)$	resulting modelling error
$\hat{h}(n)$	the approximated impulse response of the duplexer at the baseband
$\hat{h}_I(m)$	the real part of the approximated impulse response of the duplexer
$\hat{h}_Q(m)$	the imaginary part of the approximated impulse response of the duplexer
$\hat{out}(n)$	the estimated output of the duplexer model
$\hat{x}(n)$	baseband reference signal
$\hat{x}_I(n)$	the real part of the baseband reference signal
$\hat{x}_Q(n)$	the imaginary part of the baseband reference signal
$\hat{y}(n)$	baseband desired/leakage signal
$\hat{y}_I(n)$	the real part of the baseband desired signal
$\hat{y}_Q(n)$	the imaginary part of the baseband desired signal
$\mathbb{C}(f)$	cancellation performance with respect to frequency
$\overline{ref}(t)$	reference signal of the cancellation architecture
$\phi(m)$	phase of the weighting vector
$\theta_{S_c}(f)$	phase response of the cancellation signal
$\theta_{S_l}(f)$	phase response of the leakage signal
$\triangle A(f)$	amplitude mismatch in log scale between the cancellation and leakage signals
$\triangle\theta(f)$	phase mismatch between the cancellation and the leakage signals
$\widetilde{out}(t)$	analog output of the approximated duplexer model at the baseband

$d(m)$	the desired delay of the mth cancellation block
d_{km}	distance in kilometres
$des(n)$	desired signal at the baseband
f_{MHz}	frequency in MHz
f_c	centre frequency
f_s	sampling frequency
$h(n)$	actual impulse response of the duplexer at the baseband
$in(t)$	input signal of the RF cancellation block
k	number of paths in simultaneous TX RX system design technique
$l(t)$	leakage signal at RF
lo	local oscillation signal
$lo(t)$	local oscillation signal with respect to time t
m	index for the cancellation paths
n	baseband sample index at the critical sampling rate
$out(n)$	actual output of the ideal duplexer model
$rec(t)$	the cancellation signal of the cancellation block
$ref(t)$	a small portion of the reference signal in the cancellation architecture.
$rx(t)$	received signal
$tx(t)$	TX signal
$y(t)$	RF signal at the receiver
α	power gain between the through and coupling ports of the coupler in chapter 3 or the sum of squares of $\hat{\mathbf{x}}(n)$ in chapter 4
$\bar{N}$	total number of samples of the simulated RF signal
$\bar{n}$	sample index for the simulated RF signal
β	the sum of squares of $\hat{\mathbf{x}}_w(n_{up})$
γ	the multiplication results of β and the scaling factor

$\hat{\mathbf{ep}}_{up}(n_{up})$	the error signal of the previous step using MADF-DC at high sampling frequency
$\hat{\mathbf{e}}_{m+1}(n)$	resutling error for the next iteration using MADF-DC technique.
$\hat{\mathbf{h}}$	different notation of $\hat{\mathbf{h}}(n)$
$\hat{\mathbf{leak}}(n)$	resulting leakge signal after applying the whitening filter
$\hat{\mathbf{ref}}(n)$	resulting reference signal after applying the whitening filter
$\hat{\mathbf{x}}(n)$	input vector of the unknown system consisting the elements of $\hat{x}(n)$, $\hat{x}(n-1)$, ... as elements
$\hat{\mathbf{x}}_w(n_{up})$	white signal vector at the high sampling frequency
$\hat{\mathbf{y}}(n)$	output vector of the unknown system consisting the elements of $\hat{y}(n)$, $\hat{y}(n-1)$, ... as elements
$\hat{\mathbf{y}}_w(n_{up})$	output signal vector of the unknown system using the white input signal at the high sampling frequency
$\hat{d}(m)$	estimated delay of the mth tap
$\hat{X}$	sparse input matrix
$\hat{X}_{CS}$	the new matrix that is formed by the vectors in the down-sampled matrix of $\hat{X}_{up}$ at $\mathbf{l}_m$ locations
$\mathbb{C}$	cancellation performance in simulation
$\delta(n)$	dirac delta function of n
$\mathbf{d}_{max}$	maximum delay range vector consisting of $d_{max}(1)$,$d_{max}(2)$, ... as elements
$\mathbf{d}_{min}$	minimum delay range vector consisting of $d_{min}(1)$, $d_{min}(2)$, ... as elements
$\mathbf{g}$	impulse response of the filtering effect of the PA
$\mathbf{g}_{LPF}(n_{up})$	ideal impulse response of the lowpass filter at the high sampling frequency
$\mathbf{h}$	difference notation for $\mathbf{h}(n)$
$\mathbf{h}(n)$	the impulse response vector of the unknown system consisting of $h(n)$, $h(n-1)$, ... as elements

$\mathbf{h}_{up}(n_{up})$	the actual impulse response of the unknown system at the high sampling frequency
$\mathbf{K}$	upsampling vector consisting of $K(1)$, $K(2)$, ... as elements
$\mathbf{leak}(n)$	baseband leakage signal with the filtering effect of the PA
$\mathbf{l}_m$	the locations of the most significant coefficients that are determined by the C-CoSaMP kernel.
$\mathbf{ref}(n)$	baseband reference signal with the filtering effect of the PA
$\mathbf{R}_{\hat{\mathbf{x}},\hat{\mathbf{y}}}$	Cross-correlation between $\hat{\mathbf{x}}$ and $\hat{\mathbf{y}}$.
$\mathbf{R}_{\hat{\mathbf{x}}_{up},\hat{\mathbf{ep}}_{up}}(q)$	cross-correlation vector between $\hat{\mathbf{x}}_{up}$ and $\hat{\mathbf{ep}}_{up}$
$\mathbf{R}_{\hat{\mathbf{x}}_{up},\hat{\mathbf{y}}_{up}}$	cross-correlation between $\hat{\mathbf{x}}_{up}(n_{up})$ and $\hat{\mathbf{y}}_{up}(n_{up})$
$\mathbf{R}_{\hat{\mathbf{x}}_w}$	auto-correlationof $\hat{\mathbf{x}}_{up}(n_{up})$
$\mathbf{R}_{\hat{\mathbf{x}}}$	auto-correlation of $\hat{\mathbf{x}}$.
$\mathbf{U}$	downsampling factor
$\mathbf{w}_w$	tap weight vector of the whitening filter
$\bar{d}_{max}$	maximum delay value for unconstrained MADF-DC
$\bar{d}_{min}$	minimum delay value for unconstrained MADF-DC
$\mathbf{k}$	vector of the system order for simulation
$\mathbf{w}$	tap weighting vector consisting of $w(1), w(2), \dots, w(m)$ as elements
$\overline{\mathbf{ref}}(n)$	ideal reference signal at the baseband with white property
Φ	the phase between the two impulses in the example of chapter 4
$\tau(m)$	time delay of the mth
τ_0	resolution of the delay estimation using critical sampling frequency
$\Theta(m)$	phase component vector at RF
$\tilde{\mathbf{h}}(n)$	resulting impulse response at the critical sampling frequency
$\triangle\hat{\mathbf{h}}(n)$	resulting impulse response after the cancellation

$\triangle IL_{CPL}^{RX}$	the insertion loss difference of the directional coupler at RX between the coupling and through ports.
$\triangle IL_{CPL}^{TX}$	the insertion loss difference of the directional coupler at the output of the PA between the coupling and through ports.
$\widetilde{x}(t)$	analog output of the baseband reference signal
a, b	some constants
$A(m)$	attenuation vector for RF attenuators
BW	bandwidth of the cancellation
BW_{LPF}	bandwidth of the lowpass filter
$d(\tilde{m})$	resulting fractional delay, is equal to $\frac{\hat{d}(\tilde{m})}{K}$ where $\tilde{m} = 1, 2, \ldots, m$ represents all the taps that have already been estimated and K respresents the up-sampling ratio
D_{max}	the maximum delay constraint in samples
$d_{max}(i))$	maximum delay limit elements with respect to $j = 1, 2,..., J$
D_{min}	the minimum delay constraint in samples
$d_{min}(i))$	minimum delay limit elements with respect to $i = 1, 2,..., I$
f_{sc}	critical sampling frequency at the baseband for simulation
f_s^{RF}	sampling frequency at RF for simulation
I	Number of elements of minimum delay limit vector $\mathbf{d}_{min}$
IL_{Att}^m	attenuation of the variable attenuator in the mth tap
IL_{CMB}^m	insertion loss of the combiner from the combining port to the mth input port.
IL_{del}^m	the insertion loss of the delay block of the mth tap
IL_{Fix}^m	the insertion loss of the fixture of the mth tap
IL_{min}^m	required minimum attenuation level for the mth tap in order to implement the cancellation system using only passive components
IL_{misc}^m	insertion loss of other RF components including cabling and connectors, etc..

IL_{PH}^m	insertion loss of the phase shifter in the mth tap
IL_{SPL}^m	insertion loss of the splitter from the mth splitting port to the input port.
J	Number of elements of maximum delay limit vector $\mathbf{d}_{max}$
$K(p)$	upsampling ratio elements with respect to $p = 1, 2,..., P$
LO	local oscillating signal for the simulation
N_{up}	Total number of samples of the upsampled signals
n_{up}	sampling index for upsampled signals
P	Total number of elements of the upsampling ratio vector $\mathbf{K}$
$P - P.Can.$	peak-to-peak cancellation performance
Q	the length of the measured output or the maximum iteration, depending on the context.
R_1, R_2, R_3	Resistors in the pi-network for designing the fixed attenuators
Z_0	characteristic impedance
Z_{in}	Input impedance
Z_{out}	Output impedance

1 Introduction

1.1 Motivation

It can be foreseen that the demand of higher data speed will continue beyond the current wireless technologies. To support such demand, the transmission and reception bandwidths and the quality requirement of the received signal are increasing. In the spectrum that is already heavily congested, the frequency separation between transmitter (TX) and receiver (RX) bands will thus be reduced. Therefore, for a frequency division duplex (FDD) base station with single antenna configuration (shown in Figure. 1.1), a duplexer is needed to separate the TX and RX. FDD is the most widely deployed full duplex mode in the current wireless mobile communications systems and devices including the current 4G Long Term Evolution (LTE) systems. Due to the limited isolation performance of the duplexer, a portion of TX signal appears at the receiver. This portion of TX signal is known as TX leakage and it consists of the in-band and out-of-band portions with respect to the RX frequency band. Since the in-band leakage falls within the same frequency band as RX signal, it is more problematic. The power of the in-band leakage is inversely proportional to the isolation performance of the duplexer. Therefore, a high performance duplexer is usually used in a base station to prevent the in-band leakage from desensitizing the receiver. However, such a component is unfavourable due to large form factor and high cost. Additionally, the reduced frequency separation between TX and RX makes the design of such high isolation duplexer more difficult.

Relaxing the performance requirement of the duplexer could potentially reduce the cost and the form factor of such a component. More importantly, the design challenge of the high performance duplexer could be reduced. Therefore, the overall cost and size of the base station could be reduced. However, relaxing the performance requirement of the duplexer could the increase of the leakage, especially the in-band
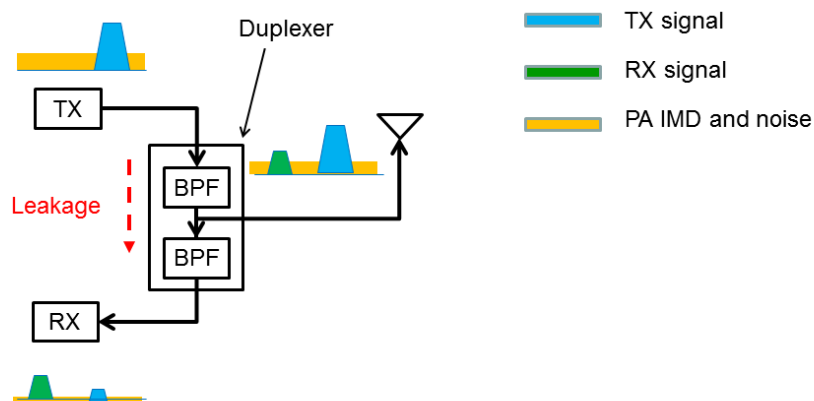
Figure 1.1: Transmitter, receiver and the leakage

portion which is formed by the noise and intermodulation of the power amplifier (PA). Therefore, desensitization of the receiver could occur. The in-band leakage can't be filtered out using conventional filtering techniques.

The motivation of this dissertation is to develop a technique that can reduce the requirement of the high isolation performance duplexer by suppressing the in-band leakage at RF frequencies. This thesis will discuss the motivation in more detail in later chapters. The dissertation will present a novel cancellation system for suppressing the in-band TX leakage at the RF frequency. It is a wideband solution and is designed for a duplexing device with more complex characteristics. Along with the cancellation architecture, two novel modelling algorithms are proposed in this thesis for characterizing the duplexer more accurately. Due to the imperfection of RF components, a novel implementation technique is also presented in this thesis.

1.2 Structure of the Thesis

The dissertation is outlined as follows:

- Chapter 2 introduces the state-of-the-art leakage cancellation techniques, including the passive and active solutions. The passive solutions involve using the duplexing devices that are commonly deployed in an FDD/SC-FD transceiver. Whereas, for active solutions, digital and analog cancellation techniques have been reviewed.

- Chapter 3 presents the proposed cancellation architecture. The cancellation architecture consists of the modelling and the cancellation blocks. Details of such an architecture including the operation and the purposes of each block in the cancellation system have been discussed. The linkage between the baseband modelling and the RF realization is also established. At the end of this chapter, the purpose of a new modelling algorithm is discussed.

- Chapter 4 describes one of the two modelling algorithms in order to more accurately characterize the duplexer. This novel algorithm is named as modified adaptive delay filter using direct cross-correlation (MADF-DC). In addition to the details of this novel modelling technique, simulations have been performed on three duplexing devices, i.e. two duplexers and one circulator. This is to demonstrate that the algorithm is suitable for a duplexing device with any characteristics. At the end of this chapter, simulations have been re-performed for the three duplexing devices in order to present the possibility of implementing such system using only passive components.

- Chapter 5 explains the theory of the other modelling algorithm that is proposed in this thesis, i.e. modified compressed sampling matching pursuit (MCoSaMP). Similar simulations have been performed using MCoSaMP and the results are compared with the ones that are obtained by using MADF-DC.

- Chapter 6 shows the validation of the proposed cancellation architecture. A test bench has been constructed. Modelling results using both modelling algorithms are illustrated. The RF cancellation block is implemented based on the parameters that are obtained by MADF-DC and the measured cancellation performance is displayed. An implementation technique using low performance RF components is also described. Performance comparison between the modelling and measured results is presented. The reasons that cause such performance difference are discussed. Finally, the achieved results using the proposed cancellation system are compared with the state-of-the-art solutions.

- Chapter 7 concludes the dissertation and discusses the possible future work.

2 Background

2.1 Introduction

As a fourth generation (4G) mobile communication standard, long term evolution (LTE) has made a significant improvement on the data speed compared to third generation standards. It can be foreseen that the data speed will continue to increase in the future. In order to achieve such data speed, it requires not only the deployment of more advanced techniques at the digital baseband, but also wider bandwidths for transmission and reception. The later one could be very challenging since the spectrum is already very congested. The design of RF components becomes more difficult and thus many issues arise. The transmitter (TX) leakage is one of these problems and will be discussed in detail in this section.

Since this thesis focuses on the leakage problem for certain types of base stations, first of all, the variety of base stations is discussed.

2.2 Size and Power Rating of Base Stations

Depending on the coverage and output power, base stations for wireless mobile communications can be distinguished into four types (shown in Figure. 2.1): femtocell, picocell, microcell and macrocell [1]. Femtocell, picocell and microcell are usually grouped as small cells. In long term evolution (LTE) specification which is defined by the 3rd generation partnership project (3GPP), these cell terms are not used to identify the classes of base stations. Instead of using macrocell, microcell, picocell and femtocell, the corresponding terminologies are: wide area base station, medium range base station, local area base station and home base station [15], respectively. In this thesis, all these terms are used when describing the base station classes.
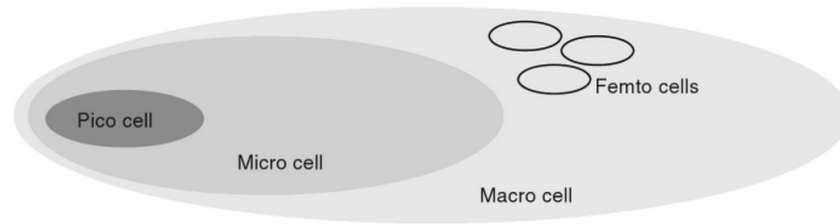
Figure 2.1: Size comparison of common cell units [1]

A macrocell is usually deployed in order to provide coverage over a larger area. It can cover the area with radius up to tens of kilometres. In LTE specification, the maximum output power of a macrocell is not limited. The typical output power of a macrocell is tens of Watts. This type of base station usually requires a tower so that the antennas can be mounted on. Traditionally, the baseband unit along with the rest of the RF components is located at the bottom of the tower. Long RF cables are required in order to connect the antennas with the RF unit. This causes significant power loss due to the cabling insertion loss. Hence, the efficiency of the high power amplifier (PA) is reduced and the running cost of the base station is increased. The remote radio head (RRH) technology enables the mounting of the entire RF unit on the top of the tower. As the radio unit is close to the antenna, the power loss is significantly reduced. The RF unit with RRH technology consists of the full RF transceiver including the digital-to-analog converters (DACs) and analog-to-digital converters (ADCs). This unit is connected to the baseband unit at the bottom of the tower with fibre optic cables. Since digital signals are more immune to noise and losses that are caused by the cables, high power amplifiers are not needed at this section (baseband) of the base station. Therefore, the running cost of the base station can be reduced.

Compared to macrocells which are designed for providing signal coverage, smaller cells are focused on increasing user capacity. In a smaller area where the traffic density is high, such as a large shopping centre, a microcell is usually deployed in order to fill the demand of capacity and coverage. A microcell can cover up to 2 km radius in a rural area [16]. The total output power of a typical microcell base station can be up to 10 W [1]. The baseband and RF elements of a microcell are usually integrated into one unit. However, this unit typically doesn't include the antenna and the AC power adaption pack. An example of such microcell base station [17] is MB4300 all-in-one LTE base station system.

A picocell is used for increasing user capacity of indoor and outdoor environment in a high data traffic area, e.g., an office building or a small shopping centre. The coverage area for a picocell is typically tens of meters which is much smaller than the one for the microcell. The output power range of a picocell base station is usually between 1 and 5 Watts [1].

A femtocell is the smallest indoor cell unit that is used to provide services for a small number of users. It is designed for home use where coverage may be poor. The output power of a femtocell is typically 1 to 20 mW. This small cell can cover 10 to 20 square meters of area. Femtocells were not widely developed in 2G systems. However, these cells are more attractive for 4G LTE networks. Though in 2013, the market of those femtocells was not as strong as expected, it was suggested that the demand is increasing due to technological advancements and falling device costs. A market value of over three billion dollars is expected by 2020 [18].

There are also two more terms in describing the types of base stations: umbrella cell and metrocell. An umbrella cell describes a cell that consists of larger cells and a few smaller cells, for instance, a macrocell and a number of microcells or picocells. A metrocell is a base station that is similar to a larger picocell or smaller microcell [16]. All elements of this type of base station have been embedded into one unit including antennas. Due to the compact size, metrocells are more widely deployed. A typical metrocell base station is shown in Figure. 2.2.

This dissertation focuses on the macrocells and the high power metrocells since both of the types require high performance duplexers which are expensive, large and difficult to design. More details on different types of the duplexers will be discussed in Sec. 2.5. The proposed methodology could also be utilized in other types of base stations. However, due to the low cost and small form factors of the duplexers used in these smaller base stations, the need of active cancellation techniques at RF frequencies in these base stations need to be justified.

2.3 Full Duplex Modes of Transceivers

In order to provide high speed data rate, transceivers in wireless communication base stations operate in full duplex mode which allows transmission and reception
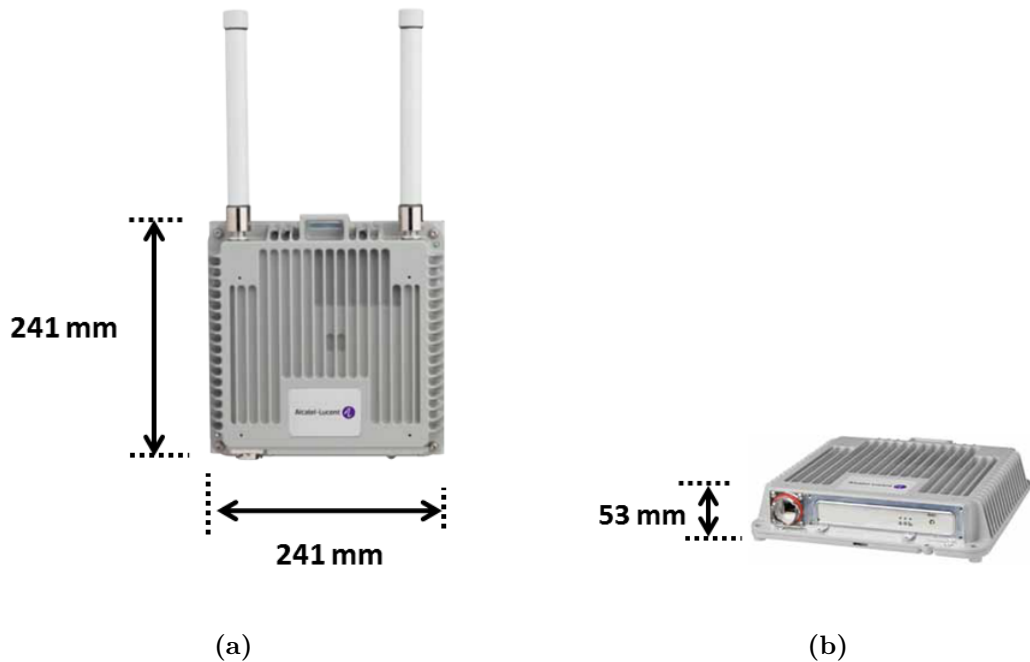
Figure 2.2: A typical metrocell base station [2]. (a) Front view. (b) Bottom view with bracket removed.

to operate simultaneously. Traditionally, there are two commonly used full duplex modes: Time Division Duplex (TDD) and Frequency Division Duplex (FDD). These two modes are widely deployed in modern wireless communication systems. Recently, a new full duplex mode has brought the attention of many researchers, known as Same Channel Full Duplex (SC-FD). Each of these are described briefly below.

2.3.1 Time-Division Duplexing

The operation of a TDD transceiver is shown in Figure 2.3(a). The transmission and reception use the same frequency bands, but at different time slots. Theoretically, each time slot can be placed close to each other. However, due to the non-ideal rising and falling edges of the switching activities, there must be a time gap between two adjacent time slots. Strictly speaking, a TDD transceiver is not a full-duplex system due to its asynchronous transmission and reception at the radio frequency (RF). Due to the reason that the sampling time at the baseband is significantly less than the switching time at RF between transmission and reception, TDD successfully

emulates full-duplex through half-duplex links.
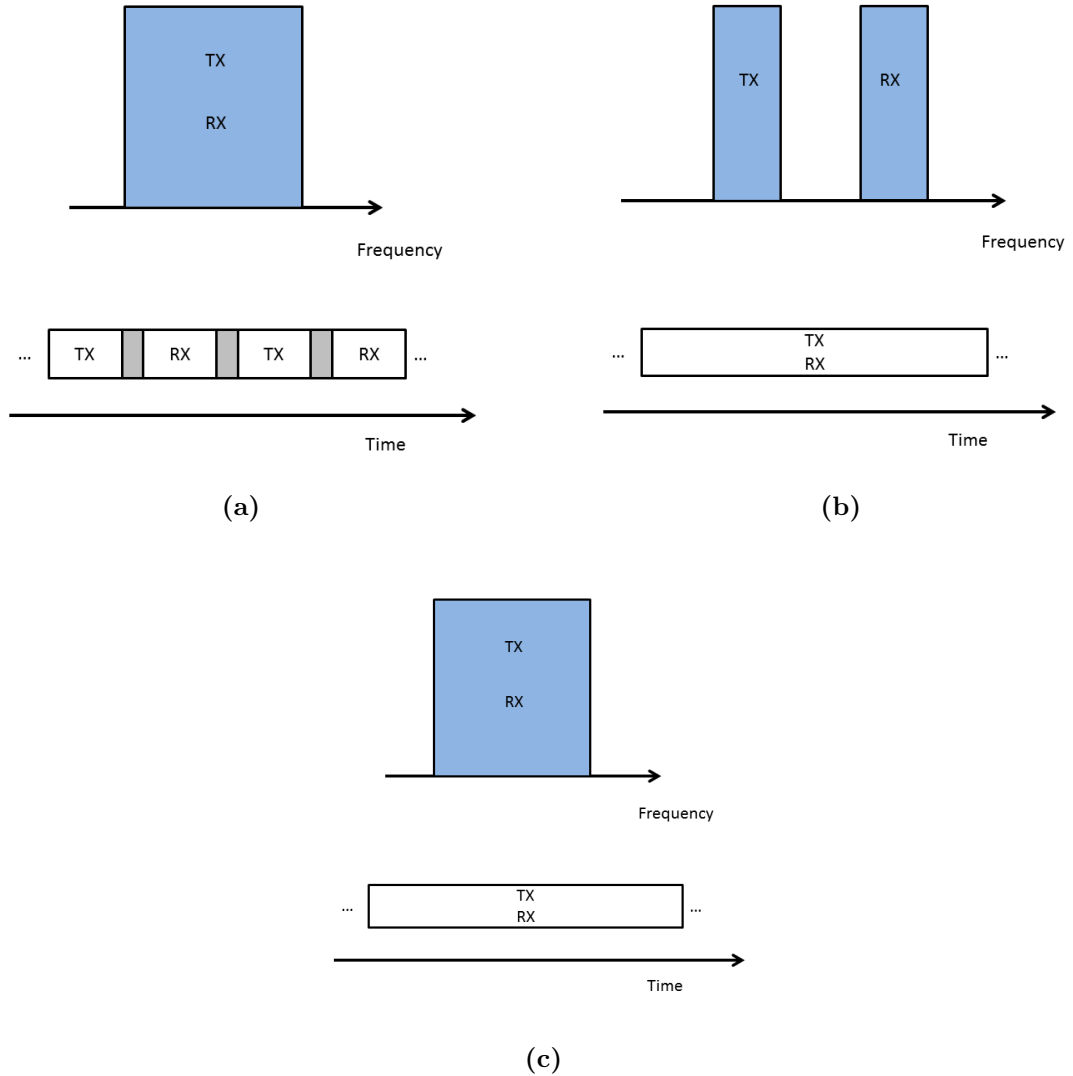
Figure 2.3: Full duplex modes. (a) TDD. (b) FDD. (c) SC-FD.

2.3.2 Frequency-Division Duplexing

The operation of an FDD transceiver is shown in Figure 2.3(b). It transmits and receives the signals simultaneously, but at different frequency bands. There is a frequency gap between the edges of the TX and RX bands, named as the guard band. Its purpose is to separate the TX and RX band far enough so that the high power TX signal can be attenuated by filters.

According to the research from GSA (Global Mobile Suppliers Association) in 2016 [19], FDD transceivers are more widely used in comparison with TDD transceivers. This type of full duplex mode is also suitable for long range communications, in contrast to TDD mode. However, in FDD transceivers, filters are needed in order to separate TX and RX signals. This adds in additional cost of hardware. Due to its nature of operation, spectrum is not used as efficiently as the TDD mode.

Compared to FDD, TDD systems require less frequency spectrum for allocating the transmitter (TX) and receiver (RX) signals. The up- and down-link capacity can also be easily changed into balanced or imbalanced configuration according to the demand [20]. These are advantages since frequency spectrum is getting more and more crowded. The drawback is that a TDD system is rather more complex compared to an FDD system. Additionally, time latency could also be introduced, especially for long distance communications.

2.3.3 Same Channel Full Duplex

Differentiating between FDD and TDD systems, recent publications show that transmitting and receiving signals at the same time and same frequency band can double the throughput [21]. Systems with such functionality are sometimes denoted as full duplex systems [21] [22] which introduce conflict with the other two full duplex modes, i.e. the FDD and TDD. In [23], those systems are named as SC-FD. In this thesis, SC-FD will be used to represent those systems. The operation concept of SC-FD is shown in Figure 2.3(c).

SC-FD has attracted a lot of attention from researchers in the wireless communication field. The advantage of SC-FD is not only that the data rate can be dramatically increased, but also the expensive spectrum resources can be utilized more efficiently. Despite the advantages, SC-FD is under development and is far from being practically deployed. Researchers are trying to solve some key problems such as large self-interference and in-band blockers that are caused by its own and the nearby transmitters, respectively. These will be discussed in more detail later in this thesis.

In this thesis, we focus on the problems that relate to the FDD and SC-FD transceivers. These problems will be explained in detail later in this chapter.

2.4 Antenna Configurations of Transceivers

An FDD or SC-FD transceiver may be constructed using either a single antenna or multi-antenna configuration. In this section, these two configurations are explained.

2.4.1 Single Antenna Configuration

The block diagram of the single antenna configuration is shown in Figure 2.4(a). A transceiver with single antenna configuration is that the TX and RX share a common antenna. Since an FDD/SC-FD transceiver allows the transmission and reception simultaneously, a duplexing component is needed to separate the TX and RX signals. In an FDD transceiver, such duplexing component is a duplexer whereas in an SC-FD transceiver, it is usually a circulator.

The advantage of this configuration is that the space which is occupied by the antenna is significantly less than the multi-antenna configuration which will be described next. This is a very important advantage, especially for base stations using remote radio head (RRH) technology or smaller cells such as picocell or femtocells. Additionally, for a conventional macro cell, the cost of the additional antenna can be significant.

On the other hand, using single antenna configuration, the isolation between TX and RX solely depends on the performance of the duplexer. High performance duplexer is usually required. This requirement can increase the overall cost and form factor of the transceiver, significantly. Additionally, from GSM to LTE, the bandwidths of the transmission and reception have increased significantly from 20 KHz to 20 MHz. It can be foreseen that the bandwidths will continue to grow. As a result, the spectrum will become more crowded. The frequency band between TX and RX is thus reducing. For future communications, designing those high performance duplexers becomes more challenging.

2.4.2 Multi-antenna Configuration

The block diagram of the transceiver using the multi-antenna configuration is shown in Figure 2.4(b). In contrast with the single antenna configuration, this structure

uses two or more separate antennas for TX and RX. In both TX and RX, there is a bandpass filter. The bandpass filter in TX is to reduce the unnecessary transmission outside the TX frequency band. It also helps to prevent the reflected signal from damaging the TX front-end. The filter in the receiver is to filter out the out-of-band interferences including the TX signal. So far, the purpose of the two filters in the multi-antenna configuration is the same as the duplexing device in the single antenna configuration.

Due to the physical separation of the TX and RX antennas, additional isolation between TX and RX is achieved. This is the advantage of using the separate antennas for TX and RX. In order to provide the additional isolation, the TX and RX antennas need to be separated by some physical distance. The distance depends on the desired level of isolation and the frequency of the TX signals. The free space path loss formula in [24] gives

$$PL_f = 32.4 + 20log_{10}d_{km} + 20log_{10}f_{MHz} \tag{2.1}$$

where PL_f is the free space path loss in dB, d_{km} is the distance in kilometres and f_{MHz} is the frequency in MHz. According to (2.1), for a TX signal at 900 MHz and 20 dB isolation, TX and RX antennas must be separated by about 26 cm. Imagine in a base station with multi-input-multi-output (MIMO) compatibility, the space that is needed for allocating the antennas is vast. For this reason, the configuration is less commonly used compared to the single antenna one. This thesis focuses on the single antenna configuration. To complete the argument, the methodology proposed in this thesis could also be deployed in multi-antenna configuration as the characteristics of the antenna separation is less complex compared to the duplexers. Therefore, the details of the multi-antenna configuration are not included in the discussion.

2.5 Duplexer in an FDD Transceiver

A duplexer in an FDD transceiver (shown in Figure 2.4(a)) usually consists of two bandpass filters which are connected via an impedance transformation circuit to a common antenna port. One of the bandpass filters is centred at TX band and the other is centred at RX band. The duplexer not only provides the isolation between
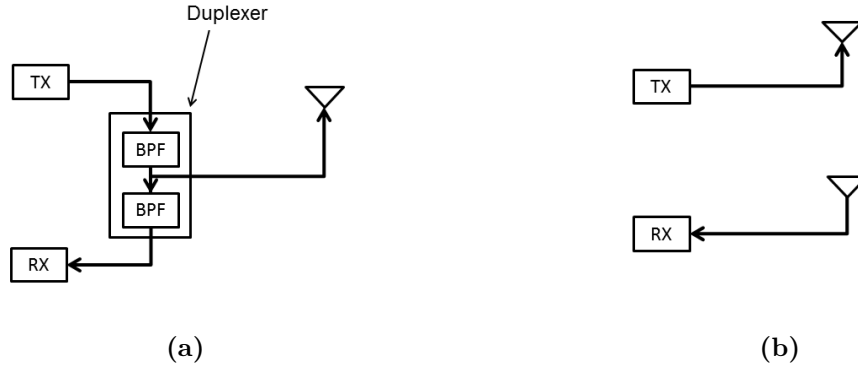
Figure 2.4: Antenna configurations of transceivers (a) Single antenna configuration. (b) Multi-antenna configuration

the TX and RX paths, but also protects RX performance being degraded from high power out of band blockers.

The band-pass filter centred at TX band is to shape the TX signal so that the transmitted signal at the antenna satisfies the specification requirements. On the other hand, the band-pass filter centred at the RX band thus attenuates the TX signal in order to protect the RX front-end being interfered by the high power TX signal. The RX side of the duplexer also plays an important role in reducing the out-of-band blockers that is received at the antenna.

Ideally, the filters of the duplexer have infinite attenuation on the out-of-band signals. However, in reality, the attenuation is limited and depends on the material, the order and the structure of the duplexer.

A duplexer is usually one of the following types, lumped elements, cavity, ceramic, surface acoustic wave (SAW), bulk acoustic wave (BAW) and film bulk acoustic resonator (FBAR) etc. Some hybrid duplexers are also available [25]. They are designed in order to replace SAW and BAW duplexers. Since lumped elements and hybrid duplexers are not commercially used in all applications, these two types of duplexers are not included in the discussion in this thesis.

This section also includes the circulator which is often seen in an SC-FD transceiver in the discussion in order to compare with duplexers. Firstly, the cavity duplexer is described as below.

2.5.1 Cavity Duplexer

A resonator in a cavity duplexer is called a cavity, which has the electrical length of a quarter of a wavelength and is utilized to determine the centre frequency of the filter [26]. Coaxial, waveguide and helical resonators are widely used to implement the cavity filters. The input and output of the cavity filter are often connected with four configurations (shown in Figure. 2.5), which are direct tap, loop, capacitive and transformer configurations [27]. The structure can be chosen depending on the desired coupling power [27]. For connecting a number of cavities, capacitive or transformer coupling configuration is often used. For connecting with the input and output ports of the filter, direct tap or loop coupling is preferable.
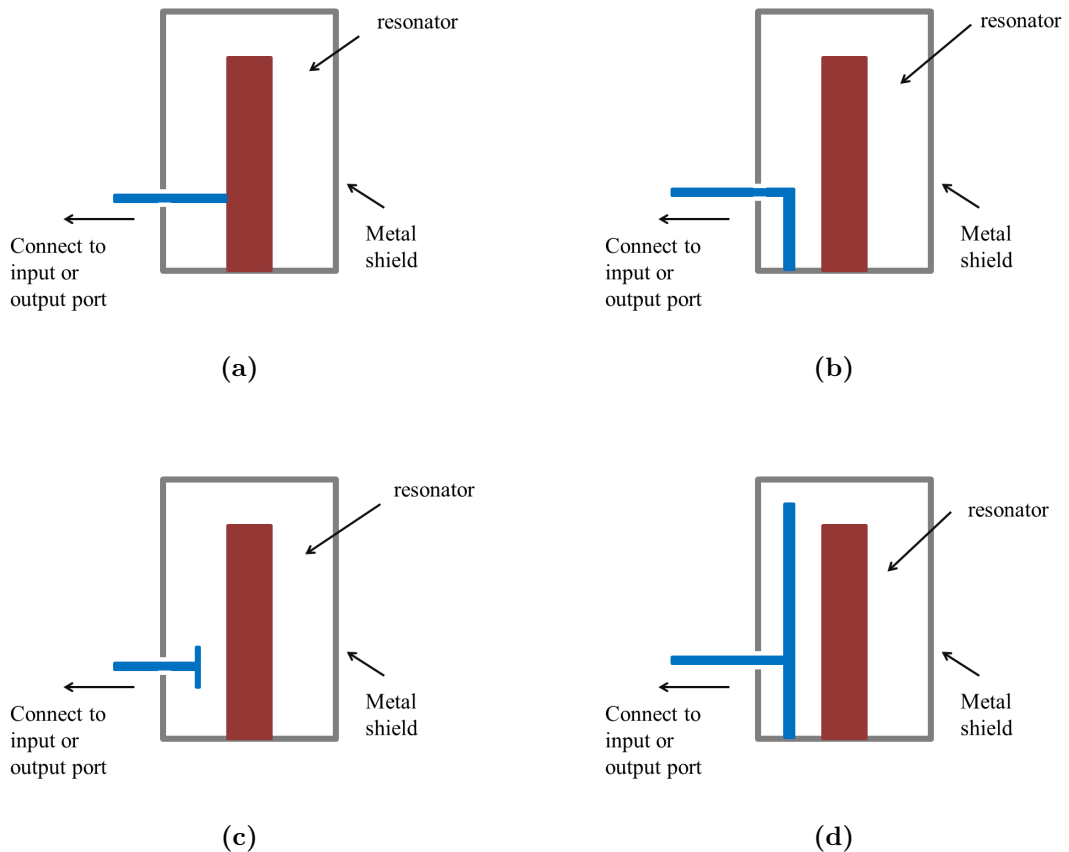
Figure 2.5: Cavity resonator with different input-output configurations. (a) Direct tap. (b) Loop. (c) Capacitive. (d) Transformer

The high quality factor (Q-factor) property of the cavity filters makes them very good candidates for separating TX and RX signals. Due to the high quality factor

of this technology, high isolation between TX and RX can be easily achieved by increasing the number of cavities without significantly affecting the insertion loss. For illustration purpose, a high isolation duplexer for wideband code division multiple access (WCDMA) band V is shown in Figure. 2.6. This cavity duplexer can provide about 97 dB of isolation with insertion loss of less than 1 dB for frequency separation of 20 MHz (approximately 2% of the carrier frequency) between TX and RX bands [3]. Additionally, this design can handle 100 W of the continuous wave (CW) signal power and up to 4000 W of peak power.

(a)

(b)
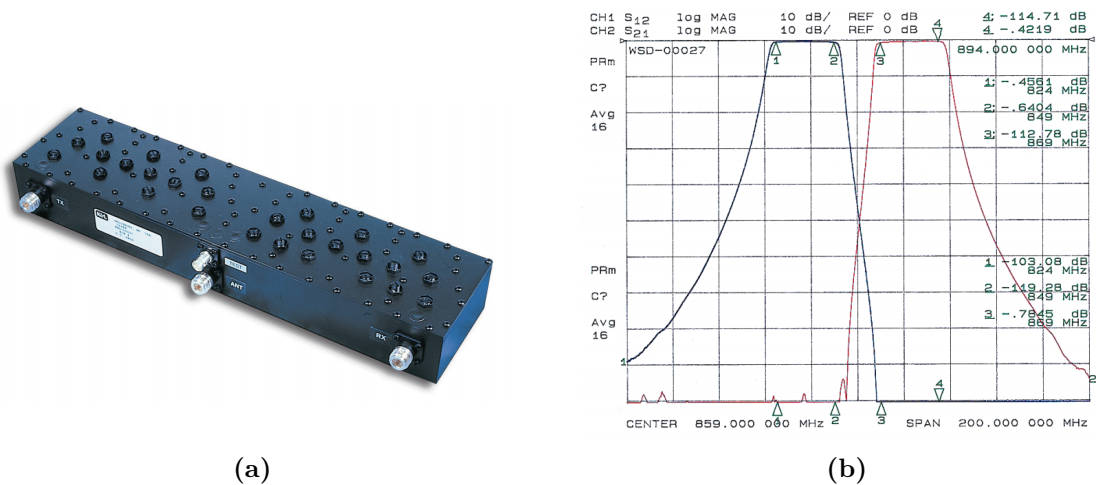
Figure 2.6: A base station duplexer for WCDMA band V [3]. (a) WSD-00027 duplexer. (b) Frequency response

Very often, off-the-shelf cavity duplexers need to be tuned in order to satisfy the specification. For cavity filters, this can be achieved by changing the characteristics of the resonators or loops. The cross-section of typical band-pass and band-reject cavities [4] are shown in Figure. 2.7. Firstly, by tuning the adjusting knob, the length of the adjustable element section within the cavity is changed, which results the change of the resonating frequency. The adjustable coupling loop can also be used to tune the location of the notch. This is achieved by changing the coupling between the connection ports and the resonator.

The automatic tuning methodologies including mechanical [28] [29], magnetic [30] and electrical [31] [32] tunings are available. Mechanical tuning is the best in terms of quality factor, power-handling capability and linearity comparing to the other two methods [33]. The latest publication suggests that an air cavity filter can be tuned via piezomotors along with RF microelectromechanical systems (RF-MEMS)

capacitor banks. However, it is far from being commercially available. To-date, the most widely used tuning methodologies is manual tuning. This involves one or more RF technicians or engineers turning the screws on top of the cavity duplexers in order to obtain the desired frequency response. Tuning a cavity duplexer is an important procedure. This is because duplexers are designed and manufactured so that they can provide the best rejection of the TX signal across the whole RX frequency band. However, each service provider only occupies a fraction of that particular frequency band. Therefore, duplexers need to be tuned so that the highest isolation can be achieved within the frequency band that is owned by the service provider. The tuning of a cavity filter is a long and tedious process. This is much worse as the order of the filter increases. The labour cost is high which increases the overall cost of the base station.
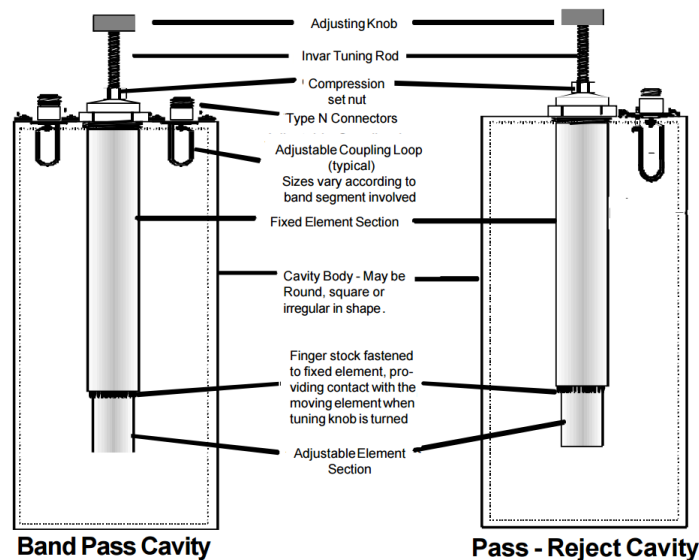
Figure 2.7: Cross-section of a typical band-pass and band-reject cavities [4]

Cavity duplexers are widely used in macrocell and microcell base stations due to their high power handling and low insertion loss properties [5]. Sometimes, they can also be seen in some of the high power picocell base stations [34]. Usually, the body of a cavity duplexer is lathed from a block of metal (usually aluminium) in order to minimize passive intermodulation. Sometimes, the resonator is plated with a thin film of copper. As a result, a cavity duplexer is expensive. According to the research [35], the cost of the duplexer is about one sixth of the total price of the whole base station. What's more, the form factor of a cavity duplexer is also large. A typical metrocell base station is shown in Figure. 2.8 with the back case removed.

The component with a large number of screws at the bottom of the base station is the cavity duplexer. It can be seen that nearly one third of the volume of the base station is occupied by the duplexer. The cost and the form factor of the cavity duplexer directly relate to the orders of the filters. Reducing the order will certainly reduce the size of the duplexer, so that the base station can be designed in a more compact form. However, the rejection of the duplexer is also reduced. A balance is needed between the rejection and size when designing a cavity duplexer for a base station.

Figure 2.8: A typical metrocell base station with back case removed [5].

2.5.2 Ceramic Duplexer

A ceramic filter is a type of dielectric filter where resonators are constructed with ceramic material. The resonators of these type of filters are formed by metallized holes inside a plated monoblock of high-permittivity ceramic [6]. The electrical length of the resonator is the same as cavity duplexer which is also a quarter of a wavelength long.

There are two types of ceramic filters, ceramic puck and ceramic coaxial filters. A ceramic puck filter is constructed with ceramic puck resonators enclosed with a metal cavity. This type of ceramic filter is shown in Figure. 2.9 and is widely used in satellites during 1980s [6].
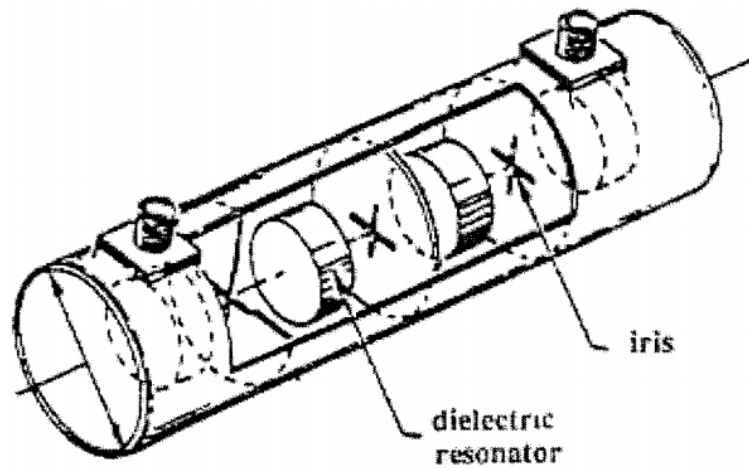
Figure 2.9: A ceramic puck filter [6]

Most of the ceramic duplexers are constructed with the coaxial resonator structure and are widely available for wireless communication systems. A ceramic coaxial resonator is shown in Figure. 2.10 [7]. The outer body of the ceramic resonator is silver-plated with one end connected with the inner conductor [7]. The Q-factor of this type of filter can have a value between 150 to 500 [7].
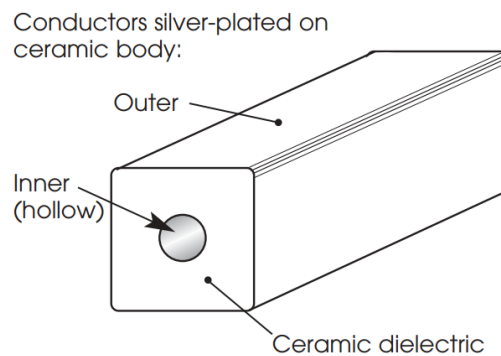
Figure 2.10: A ceramic coaxial resonator [7]

A typical ceramic duplexer can allow approximately 5 W of continuous wave (CW) signal entering any of its ports. This type of duplexer is usually deployed in a smaller cell such as a picocell [36] or a femtocell [37], where output power of the base station is small. There are high power ceramic duplexers available which have maximum

power up to 20 W [38]. However, the insertion loss can be as large as 2.2 dB which is a lot greater than the one of the cavity duplexer. The maximum isolation that those ceramic duplexers can provide is also limited to about 70 dB.

2.5.3 Surface Acoustic Wave Duplexer

Surface acoustic wave (SAW) is a mechanical wave propagating along the surface of a piezoelectric substrate and was discovered by Lord Rayleigh in 1885 [39]. In a SAW device, two interdigital transducers (IDTs) are used on a piezoelectric substrate in order to convert an electrical signal to an acoustic wave and then back to an electrical signal. Common piezoelectric materials are crystals of quartz, lithium niobate and lithium tantalate. Since the wavelengths of SAWs are much shorter than electromagnetic signals at the same frequency, filters with SAW technologies can be realised in very compact forms.
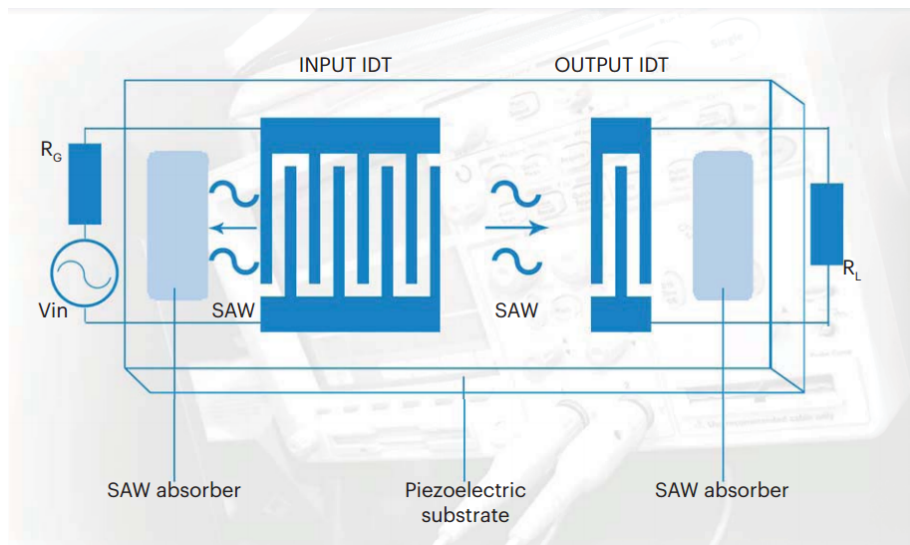
Figure 2.11: Top view of a basic SAW device [8]

A SAW duplexer can normally be adopted using either dual mode SAW (DMS) or ladder style structures. Both of the structures can provide high Q-factor which makes them good candidates for wireless communication devices. The insertion losses of these duplexers are about 3 dB, which means higher losses comparing to the cavity duplexers. The two structures are shown in Figure. 2.12. Maximum power durability of 1.2 Watt [40], small form factor, high Q-factor and cheap in cost make SAW duplexers be widely used in femtocells and user equipments (UEs). Due to the

large challenge of lithography and patterning of the IDTs, SAW filters are mainly suitable for the frequencies below 2 GHz [10].
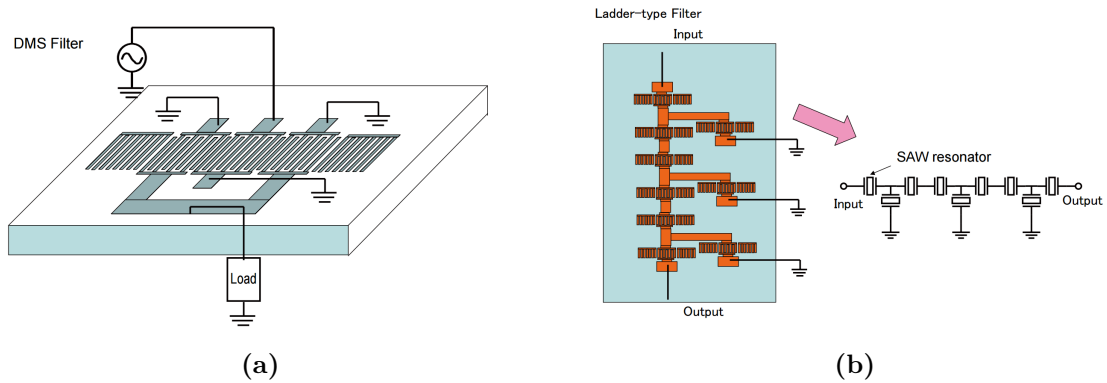
Figure 2.12: Two common structures of SAW filters [9]. (a) DMS filter structure. (b) Ladder style structure

2.5.4 Bulk Acoustic Wave Duplexer

The first commercial bulk acoustic wave (BAW) filters were introduced in 2001 [10]. It was a new technology that was designed to compete with SAW in the market of filtering for the wireless mobile communications. Unlike SAW, BAW propagate vertically in a thin film of piezoelectric (usually quartz crystal) material and bounced between the top and bottom metal electrode surfaces to form a standing acoustic wave [10]. The basic structure of BAW filter is shown in Figure. 2.13.

In order to avoid the acoustic waves escaping into the substrate, an acoustic Bragg reflector is created. The reflector consists of a number of stacked thin layers. The number of layers directly relates to the required reflection coefficient and the mechanical impedance ratio between the successive layers [41]. The device fabricated by using this approach is called solidly-mounted resonator BAW or BAW-SMR device, which is shown in Figure. 2.14.

On the other hand, instead of using the reflector, substrate underneath of the active area of the piezolayer can be etched away. The resonator that is fabricated by this process is named as filter bulk acoustic wave resonator (FBAR). The cross-section view of FBAR including the fabrication process is shown in Figure. 2.15.
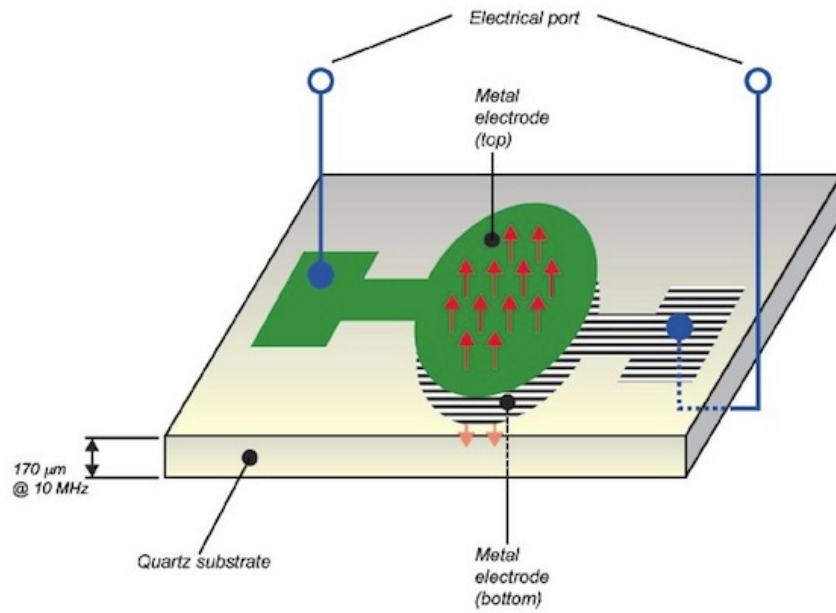
Figure 2.13: Basic structure of a BAW filter [10]
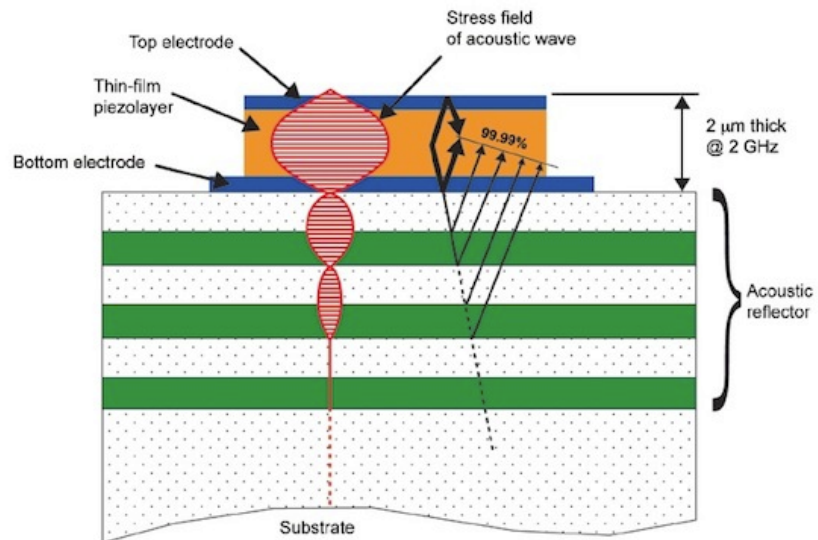
Figure 2.14: The cross-section view of a BAW-SMR device [11]
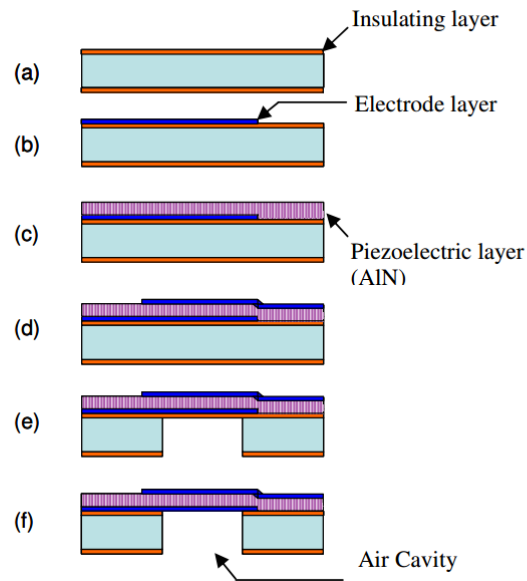
Figure 2.15: Cross-section of FBAR [12]

As with SAW filters, BAW filters can only handle signal power up to approximately 1 W and are suitable for smaller cells or mobile devices. At higher frequencies (typically, greater than 2 GHz), duplexers using BAW technology are more attractive than SAW ones, even though the price is about 4 times higher [10]. The size of a BAW device is similar to the SAW ones which is much smaller than the ceramic and cavity ones. The size comparison is shown in Figure. 2.16. Comparing to air cavity duplexers, BAW devices are much smaller in size and lower in cost, but with larger insertion loss and poorer power handling capability.

2.5.5 Circulator in an SC-FD Transceiver

A circulator is used in a single antenna SC-FD system [21] [42] [43] and acts as a duplexing device which is shown in Figure 2.17(b). A circulator is normally a three-port ferrite device that only allows the signal to flow in one direction. The operation concept of a circulator is that the magnetic field is generated by the ferrite material circles around the centre of the circulator. The signal applied to one port of the circulator is forced to follow the circular motion of the magnetic field and absorbed by the impedance of the output port next to the input one [14]. Due to the strong magnetic field, it is unlikely that the input signal flows in the opposite
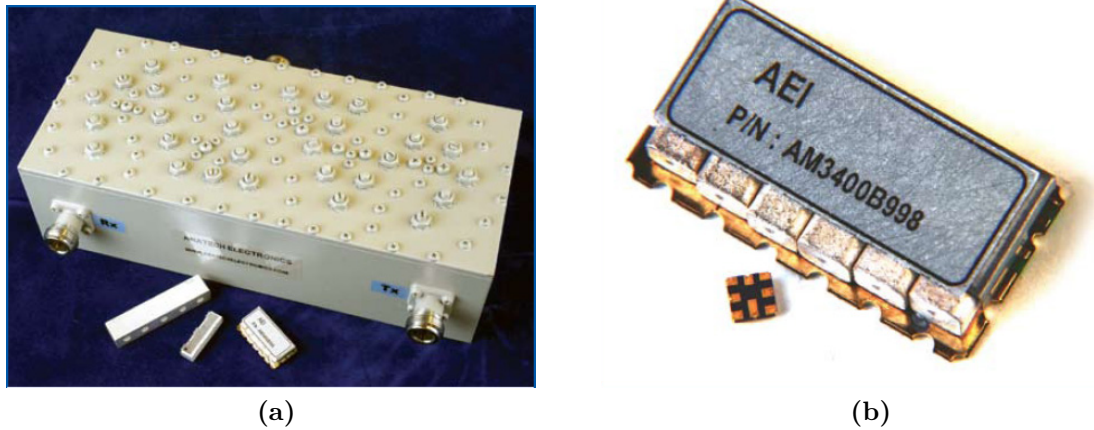
Figure 2.16: Size comparison of duplexers using different technologies [13].. (a) A cavity duplexer VS ceramic ones. (b) A ceramic duplexer VS a SAW one

to the magnetic field. In the case that the circulator is used while the third port is terminated with a matched impedance, it is normally called an isolator. The circulator and isolator examples are shown in Figure 2.17(a). The insertion loss of a circulator is usually very low along the signal flowing direction.
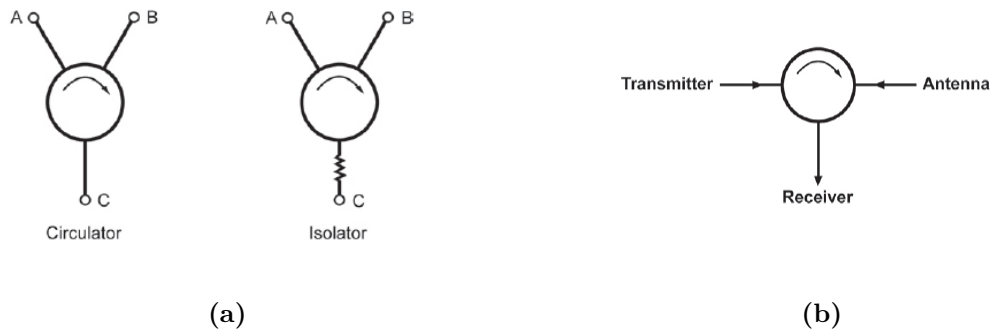
Figure 2.17: A circulator and its applications [14]. (a) A circulator and an isolator. (b) A circulator that is used as a duplexing device

In theory, there is no energy flowing opposite the signal flowing direction so that the isolation between TX and RX is ideally infinite. In reality, there is still a small portion passing through. The isolation performance of the circulator between adjacent ports opposite the magnetic field flowing direction is typically 20 dB. Comparing to off-the-shelf duplexers, this value is rather small. Hence, this configuration is not widely used in modern transceivers, unless additional filtering/cancellation methodologies are applied. The magnitude response of a circulator within the bandwidth

is relatively flat and its phase response is very linear compared to the off-the-shelf duplexers. Most commonly, a circulator is used as an isolator so that any reflections from the load, due to impedance mismatch are absorbed by the termination of the isolator and not by the signal source.

A circulator can be made in the form of microstrip lines, strip lines, coaxial and waveguide, etc. Circulators were successfully implemented at the frequencies from 100 MHz up to 140 GHz. The maximum power rating can be at approximately 2 kW of average power [44].

2.5.6 Summary of the duplexing devices

The most commonly used duplexing devices have been summarised in (Table. 2.1). Overall, duplexers can provide limited isolation between TX and RX in a single antenna FDD transceiver. The isolation performance depends on the implementation technology of the duplexer. On the other hand, a circulator can only provide basic isolation. In order to compare the isolation performance, a ceramic, a cavity and a circulator have been measured using the vector network analyser (VNA, model number is ZVB-20 by Rohde & Schwarz). The measured results are shown in Figure. 2.18.

The circulator is SKYFR-000788 by Skyworks Solutions, Inc.. The recommended operating frequency range is 2490 MHz to 2710 MHz. It has been mounted on a customised printed circuit board (PCB) with SMA connectors. The cavity duplexer is IT-102C009 by Innertron, Inc.. The ceramic duplexer (SCD900AE4) is manufactured by Samnova. Both the duplexers are designed for WCDMA band VIII, of which the up-link (UL) band is between 880 MHz and 915 MHz and down-link (DL) between 925 MHz and 960 MHz. These duplexing components will be used in the simulations and/or the hardware verifications of this thesis.

Although the frequency range of the circulator is different from the two duplexers, one can still observe that the differences of the characteristics between the circulator and two duplexers. Comparing the magnitude responses, the isolation performance of the off-the-shelf duplexers is much greater than the one of the circulator. Additionally, the magnitude response of the circulator is much flatter than the ones of the other two duplexers. The phase responses of the two duplexers are less linear

and the delay response are much more complex than the ones of the circulator. Between the ceramic and the cavity duplexer, the characteristics of the latter are more complex than the other one. How the characteristics of the different duplexing devices relate to the design difficulty of the cancellation system will be discussed in more details in the later chapters.

Table 2.1: Summary of duplexers

Type of the Duplexing Device	Isolation	Power Han-dling	Charact. of the Iso. Path	Form Factor	Cost	Application
Cavity	Highest	Highest	Most complex	Largest	Highest	Macrocell, Microcell, High power picocell
Ceramic	High	Mid	Complex	Mid	High	Picocell, Femtocell
SAW/BAW	High	Lowest	Complex	Smallest	Cheapest	Mobile device, Femtocell
Circulator	Lowest	High	Simple	Mid to Large	Mid	SC-FD transceiver, Isolator

Apart from the isolation requirement, a duplexer must be able to filter the out-of-band interference/blocker, which a circulator is not capable of. As a result, circulators are not suitable for FDD base stations, though they inherently can handle high input power.

SAW/BAW/FBAR duplexers are significantly cheaper and smaller compared to the alternatives, such as cavity or ceramic duplexers. However, due to the high power property of the TX signals and the requirement of low insertion loss of both TX and RX chains, SAW duplexers are not possible to be deployed in medium or wide area base stations such as microcells and macrocells. They are widely used in smaller cells, e.g., femtocells or mobile devices.

In comparison with the cavity duplexers, ceramic duplexers are smaller and more cost friendly, which are ideal for base stations that are sensitive to the size and cost
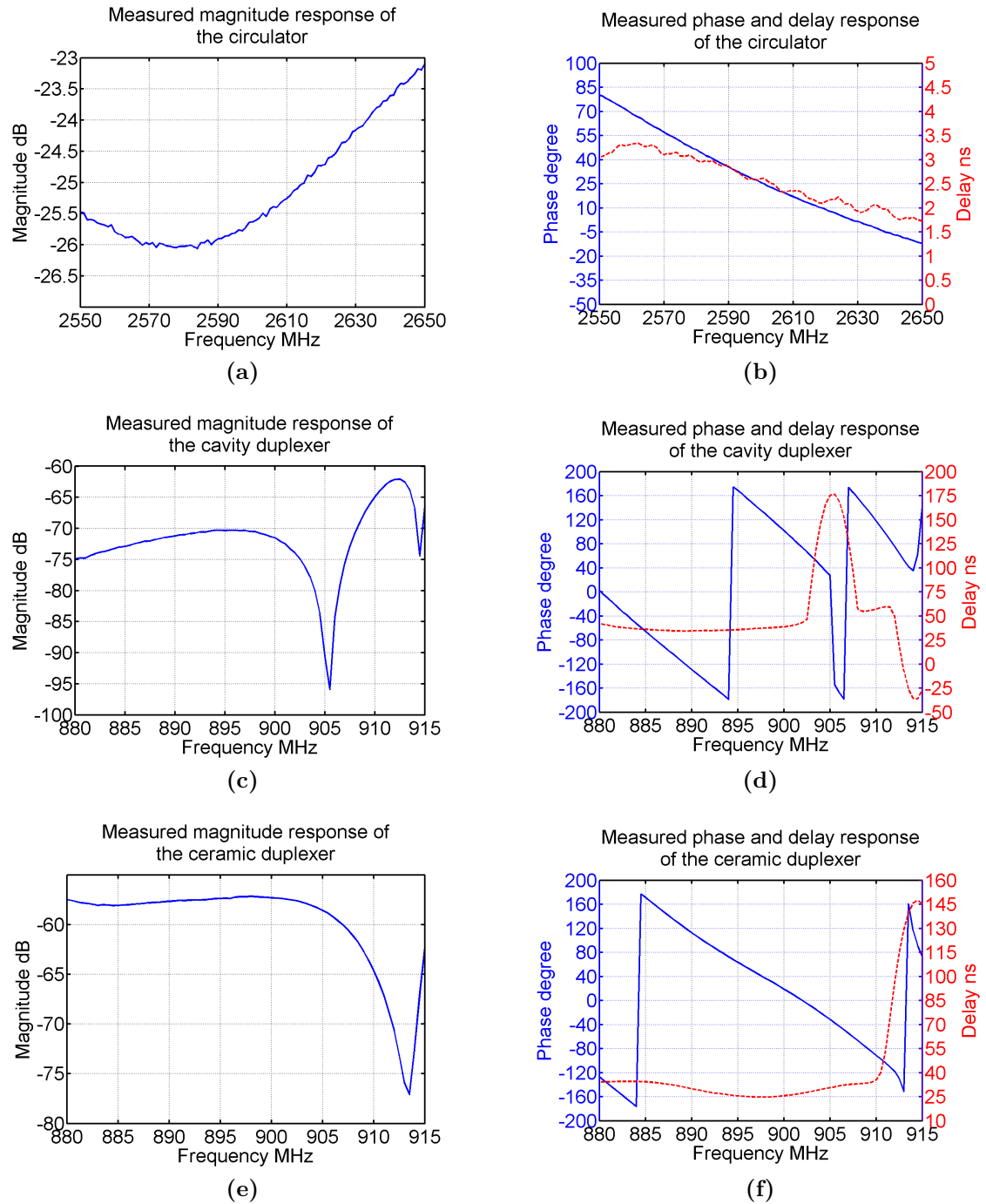
Figure 2.18: Measured characteristics of the circulator (SKYFR-000788 by Sky-
works Solutions, Inc.), cavity (IT-102C009 by Innertron, Inc.) and ceramic
(SCD900AE4 by Samnova) duplexers (a) Magnitude response of the circulator.
(b) Phase and delay response of the circulator. (c) Magnitude response of the cav-
ity duplexer. (d) Phase and delay response of the cavity duplexer. (e) Magnitude
response of the ceramic duplexer. (f) Phase and delay response of the ceramic
duplexer.

of duplexers. However, the higher insertion loss and lower isolation performance are less favourable when compared to the cavity duplexers.

There are many desirable properties with cavity duplexers, such as high power handling, low insertion loss, high out-of-band rejection and high isolation between TX and RX, etc. As discussed before, the downside of such performance is that the cost is high and the size of the duplexer is large. For macrocells with RRH technologies, microcells and some high power picocells, these downsides are unfavourable for the high level of integration.

What's more, since higher data speed is demanded, larger bandwidths of transmission and reception are required. For instance, the bandwidth of a GSM channel is approximately 200 KHz [45], whereas for LTE, each channel can be as large as 20 MHz [46]. It can be foreseen that the increase of channel bandwidth will continue beyond LTE. On the other hand, the valuable frequency spectrum is already highly congested especially at UHF frequencies. Therefore, for the future FDD transceivers, frequency separation between TX and RX frequency bands will thus be reduced. This will increase the challenge of designing such high performance cavity duplexer.

Since the cost, form factor and the design challenges of the cavity duplexers directly relate to the desired performance, they can thus be reduced if the performance requirements are relaxed. Then cheaper and smaller cavity or ceramic duplexers could be used in base stations instead of the high performance cavity one.

2.6 Challenges of TX Leakage using Passive Components

As discussed previously, the isolation between TX and RX of an FDD transceiver depends on the performance of the duplexer. In reality, there may still be some signals from the TX path appearing in RX. The output of the high power amplifier (PA) contains the wanted TX signal, as well as the unwanted out-of-band emissions of TX, especially of the PA itself. According to the state-of-the-art publications on digital pre-distortion (DPD) amplifier, the power level of the out-of-band emission can still be as large as -50 dBc [47] [48] [49] [50]. Due to the limited isolation of

the duplexers between TX and RX, a portion of the high power TX signal and the out-of-band emissions of the PA appear in the RX chain. This signal is known as TX leakage. In fact, in the case that cables that carry TX and RX signals are close to each other, then the signal at the output of the PA could also appear in RX by coupling. This is another source of the TX leakage. However, since the power of this form is insignificant compared to the prior one, in this thesis, the term TX leakage only refers to the one that is caused by the limited isolation of the duplexer. Relaxing the isolation performance requirement of the duplexer causes the increase of TX leakage. This needs to be suppressed in order to replace the high performance duplexer with a lower one.

The TX leakage consists of two parts, i.e. the in-band and the out-of-band portions with respect to the RX frequency band. The out-of-band leakage is mainly the remaining portion of the actual TX signal after being filtered by the duplexer. Due to the high power nature of the TX signal, the power of the out-of-band leakage can be significantly higher than the received signal. The existence of this out-of-band leakage can potentially saturate the RF front-ends and thus cause desensitization of RX. In the worst-case scenario, RF front-end modules of RX could be damaged if the power of the leakage is excessive. This is illustrated in (Figure. 2.19), where the peak power of the TX leakage is greater than the saturation point (point C). However, since the out-of-band leakage can possibly be reduced with additional filtering, it is less problematic than the in-band portion. By using an additional bandpass filter, the out-of-band leakage is then reduced to power level E and the in-band portion remains the same at the power level B.

Using an additional filter does not contradict with the motivation of this thesis. This is because this filter is added only in the RX path where the power of the signals is low. As a result, a low power rating filter with high rejection performance, such as a SAW or BAW filter can be used. Using this filter wouldn't increase the cost and the form factor of the base station significantly.

On the other hand, the in-band TX leakage is more problematic since it is completely within the RX band and cannot be filtered with conventional filtering techniques. The existence of such in-band TX leakage can thus desensitize RX, directly. It can be seen in (Figure. 2.19) that the remaining in-band leakage (in red line) is significantly higher than the RX signal (in blue line), thus causing the desensitization of the receiver.
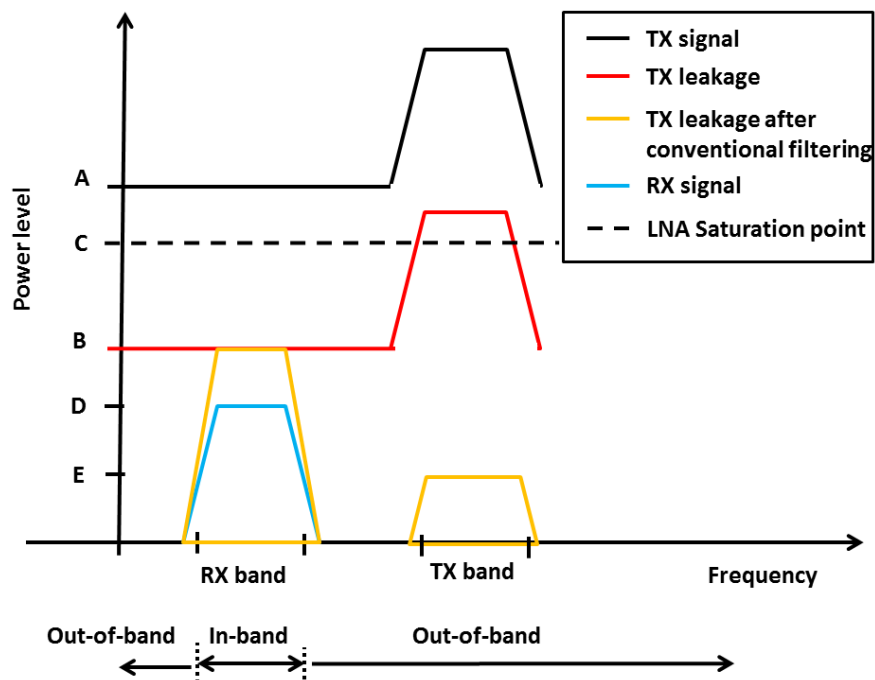
Figure 2.19: In-band and out-of-band leakage

In order to further show how the in-band TX leakage causes desensitization problems, a brief calculation is performed. Consider an LTE medium area base station which is operating in band VIII (UL: 880 - 915 MHz and DL: 925 - 960 MHz). According to 3GPP specification [46], the maximum output power of a medium area base station is less than 38 dBm per carrier. We can assume there is one 5 MHz carrier, i.e. $P_{TX} = 38\,dBm/5\,MHz$.

A typical noise level of a high power amplifier in a base station is approximately -50 dBc. The power of the noise at the output of the PA is thus:

$$
\begin{aligned}
P_{NTX} &= P_{Tx} - 50 \\
&= -12\,dBm/5\,MHz
\end{aligned}
\tag{2.2}
$$

The sensitivity of the receiver at the antenna port of a medium range base station is given in [46] as $P_{Sen} = -93.5\,dBm/5\,MHz$. Therefore, the difference between P_{NTX}

and P_{Sen} is the required additional isolation performance of the duplexer which is

$$
\begin{aligned}
ISO_{des} &= P_{NTX} - P_{Sen} \\
&= 81.5\,dB
\end{aligned}
\tag{2.3}
$$

Therefore, additional 21.5 dB of isolation must be obtained by other techniques if such a high performance duplexer is replaced with a lower one which has minimum isolation of 60 dB.

2.7 State-Of-the-Art Active Solutions

There are many active cancellation architectures available in order to provide extra isolation in addition to the passive solutions. Some active techniques are designed for the out-of-band TX leakage suppression, e.g. the feed-forward cancellation in [51] and the feed-back cancellation in [52]. Some of the techniques are for replacing the off-the-shelf duplexer with adaptive/hybrid components, for instance, the dual path antenna and hybrid duplexer in [43], the RF front-end design in [53], the tunable hybrid duplexer in [54] and the multi-band RF duplexer design in [55], etc.. These solutions are either for narrow band applications or with small out-of-band blocker rejection. Therefore, in this thesis, these designs will not be discussed in more detail. More of the active solutions are focused on in-band leakage cancellation and these are the ones to be discussed in this dissertation.

In many active cancellation architectures, the leakage signal is reproduced by using the TX signal. The reproduced leakage signal should have the same magnitude and 180 degree phase offset from the actual leakage at any frequency within the band of interest. Adding the original and the reconstructed leakage signals performs the cancellation. Since the reconstructed leakage signal has no components from the RX signal, theoretically, after cancellation, the RX signal remains unchanged.

Active solutions consist of digital and analog cancellations. These active cancellation techniques will be introduced in the following sections.

2.7.1 Digital Baseband Cancellation

Digital baseband cancellation systems suppress the leakage in the digital domain. These systems require little additional hardware, which is a significant advantage over analog cancellation techniques. Digital cancellation systems can be separated into two categories, the baseband to baseband and the RF to baseband cancellations, depending on what the reference signal is.

2.7.1.1 Baseband to Baseband

Leakage cancellation using a baseband to baseband structure is shown in Figure. 2.20. It uses the baseband TX and RX digital signals as the reference and desired signals, respectively. Both linear and non-linear systems can be implemented with this approach. Cancellation systems using digital baseband approach are deployed in both FDD and SC-FD system with single or separate antennas. In the transceiver with single antenna configuration, a duplex device such as an off-the-shelf duplexer or circulator is used.
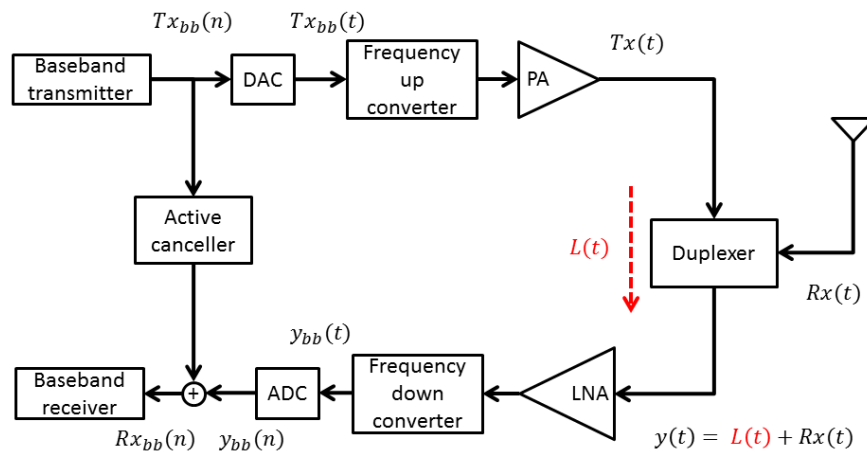
Figure 2.20: Baseband to baseband digital cancellation structure

2.7.1.1.1 With Linear Model The digital cancellation system can be implemented using first order FIR filters in the case that the system to be identified is linear. Coefficients can be determined using classic adaptive filter algorithms such as the least-mean-square (LMS) for recursive adaptation [56]. Such approach is widely used in noise cancellation for audio devices, due to its simplicity of implementation.

The least-squares (LS) for non-recursive adaptation technique has been reported in [57] for zero-IF receivers. More practical parameters are considered in this approach including channel mismatching between the transmitter and receiver and non-ideality of the receivers.

The digital cancellation using classic linear model can only achieve limited cancellation due to the IQ image of the TX leakage which is caused by the non-ideal property of the analog RF circuit [58]. Despite the original TX baseband signal, its conjugate can also be used in order to suppress the IQ image of the leakage. This technique is named by the author of [58] as "widely linear cancellation". It is designed in order to suppress the self-interference of an SC-FD system.

2.7.1.1.2 With Non-linear Model Linear FIR structures that are similar to the previous techniques are suitable for linear systems only. As the reference signal for the cancellation system is the transmitter baseband signal, there is no information about the non-linearity of the devices in the transmitter and receiver. Such non-linear devices include the high power amplifier (PA) in the transmitter, low noise amplifier (LNA) in the receiver, ADC/DAC and mixers of the transceiver, etc.. The baseband reference signal in the structure shown in Figure. 2.20 does not have information on these non-linearities. Therefore, the satisfied cancellation results will not be achieved by using the linear FIR structure. Since for base stations, the power amplifier of the transmitter suffers from non-linearity, aspects of non-linearities should be considered in order to suppress the in-band leakage successfully with the digital cancellation structure that is shown in Figure. 2.20. There are techniques that focus on reducing the third order (IM3) and the second order intermodulation distortions (IM2).

In [59], IM3 which is caused by the LNA is suppressed by firstly obtaining IM2 products of the LNA with an alternative RX path. Then the cancellation signal for the IM3 can be regenerated by mixing the obtained IM2 products with the

baseband TX signal. The adjustments of the amplitude and phase are needed so that the cancellation signal has the same amplitude and 180 degree out-of-phase with the IM3 distortion signal. By combining the two, the IM3 signal of the LNA is thus cancelled.

In [60], it tries to reduce IM2 that is caused by the mixer. Since the second order input intercept point (IIP2) of the mixer in the receiver is finite, the existence of the high power TX leakage can cause IM2 products which fall within the RX frequency band. As a result, the receiver sensitivity is reduced. IM2 products can be suppressed using a parallel augmented Volterra model. This technique creates a behavioural model by using the TX baseband signal and IM2 signal in the receiver. The coefficients of the Volterra model are calculated with LS algorithm.

Instead of reducing IM2 and IM3 components caused by the high power TX leakage, the whole transceiver path from the baseband transmitter to the baseband receiver can also be modelled in [61] with a non-linear modelling technique. Parallel Hammerstein (PH) model, a special case of the generalised Volterra series, has been used in order to suppress the leakage including all the non-linear components in the transceiver path. This approach shares the same idea as the widely deployed DPD systems for PAs.

2.7.1.2 RF to Baseband

An alternative approach to baseband-to-baseband structure is to use the reference signal which is obtained by down-converting the TX signal from RF to baseband. Since a power amplifier is a non-linear device, the output of the PA not only contains the TX signal, but also the intermodulation products due to the non-linearity of the PA. Additionally, apart from the additional thermal noise introduced by the PA, the high gain also raises the noise floor. Pure baseband-to-baseband approach has no information about the extra thermal noise. As a result, the cancellation performance at the baseband is limited. In order to obtain better cancellation, the output of the PA can be duplicated by using a directional coupler. The replica of the PA output is frequency down-converted and digitized by an auxiliary receiver. The digitized signal is used as the reference signal for the baseband cancellation system. The structure of this type of cancellation system is shown in Figure. 2.21.
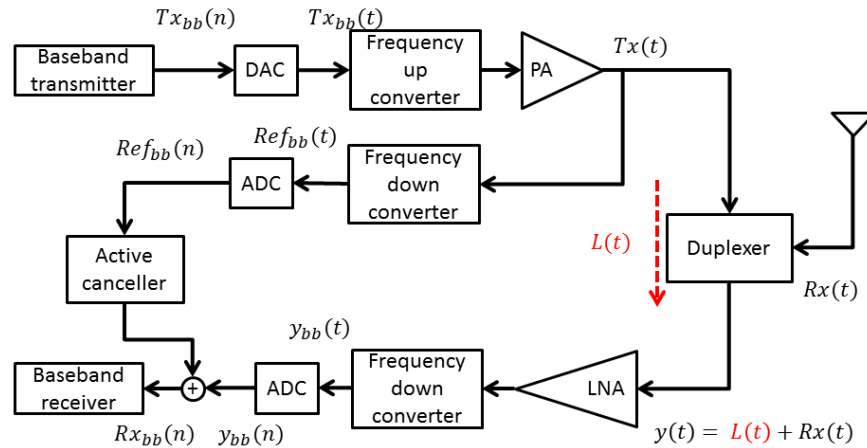
Figure 2.21: RF to baseband digital cancellation structure

A technique called sub-band adaptation has been reported in [62] in order to reduce the TX leakage digitally and efficiently. This approach aims at reducing the TX leakage in the full RX band for an existing FDD transceiver using an off-the-shelf duplexer. Adaptation for the full RX band requires a large computation load. As a result, the sub-band adaptation was deployed in [62]. The tested transceiver operates in WCDMA band I of which the RX bandwidth is 60 MHz. This technique treats the full RX band as a combination of a number of smaller channels. For each channel, the leakage is cancelled individually. Therefore, the system achieves on par or better cancellation results than the full band adaptation techniques. This method achieved about 15 dB of cancellation for the bandwidth of interest.

2.7.1.3 Summary of Baseband Cancellation

The performance of the digital baseband cancellation solutions is summarized in Table. 2.2. One of the greatest advantages of the digital baseband cancellation techniques is that there is little hardware required for achieving good cancellation. This certainly adds no additional cost to the base station. It seems like the digital baseband cancellation techniques are the solutions to the TX leakage problems. However, the reality is not as simple as it looks. In the case that the leakage with excessive power reaches the RF front-end of the receiver, noise floor increases due to saturation and blocking. The latter is a more serious issue and can cause improper gain adjustment on the desired RX signal at the input of the ADC. The valuable

ADC resolution is thus wasted and results in large quantization error. Therefore, the increase of the noise due to blocking is mainly from the quantization noise. The reference signal in any digital cancellation technique discussed in this section has no information on the quantization error. As a result, desensitization of the receiver occurs irrespective of the digital cancellation performance. This will be discussed in more detail in the next chapter.

Table 2.2: Summarised baseband digital cancellation techniques

Reference	Duplexer type	Type	Technique	Evaluation method	BW (MHz)	Can. perf. (dB)
Frotzscher et al. [57]	Simulated duplexer[1]	FDD	Classic LS	Sim.	N/A	25
Kamizuma et al. [59]	Power combiner	FDD	IM3 canceller	Meas.	20	12
Li et al. [56]	Antenna separation	SC-FD	Classic LMS	Sim.	10	20
Kiayani et al. [60]	Filter[2]	FDD	IM2 canceller	Sim.	10	40
Anttila et al. [61]	Antenna separation	SC-FD	PH model	Sim.	12.5	10
Korpi et al. [58]	Antenna separation	SC-FD	Widely linear	Sim.	N/A	70
Pratt et al. [62]	off-the-shelf duplexer	FDD	Sub-band	Meas.	100[3]	35

2.7.2 Analog Cancellation

There are a large number of analog cancellation structures being reported to-date for both FDD and SC-FD transceivers. They can be grouped into two categories, baseband-to-RF and RF-to-RF cancellation systems.

2.7.2.1 Baseband-to-RF

Baseband-to-RF cancellation techniques (shown in Figure. 2.22) take advantage of the flexibility of the digital cancellation system. On the other hand, it achieves the cancellation at the radio frequencies. This structure models the leakage path by using the TX and leakage signals at the digital baseband. The model is then used to generate a baseband cancellation signal which is up-converted to RF by an auxiliary transmitter. Combining with the cancellation signal, the RF leakage is thus suppressed.
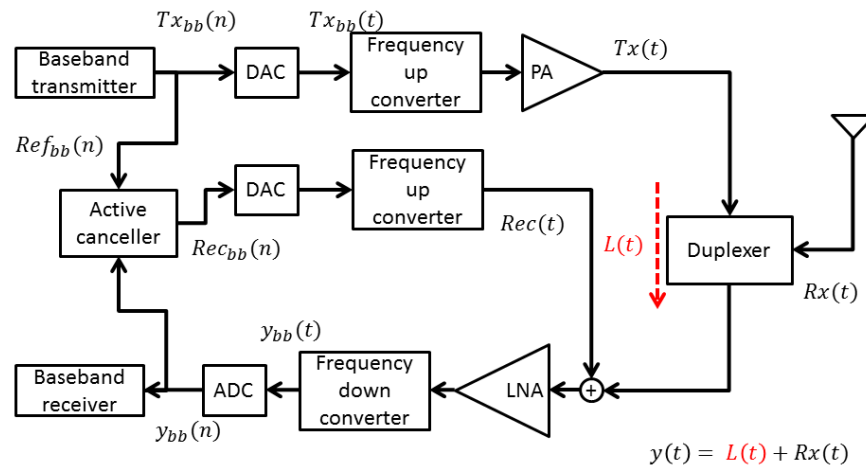
Figure 2.22: Baseband to RF cancellation structure

The channel modelling of this structure requires estimating both the leakage and the cancellation paths at RF. This is done by sending two orthogonal pilot signals via the two paths and calculating the magnitude and phase response of the channels. Dot-division is then performed in order to obtain the characteristic differences of frequency response between the two paths. This is applied to the baseband transmitted signal in frequency domain at the baseband in order to obtain the cancellation signal. An inverse fourier transform and frequency up-conversion are needed to bring the baseband signal to RF [63].

In this technique, only a few RF components are required including the auxiliary

transmitter, a RF attenuator and a power combiner. However, this cancellation structure is suitable for low power rating transceivers in which the power amplifiers are operating within the linear region. This is similar to the digital techniques using the baseband TX signal as the reference. There is no information about the in-band noise and distortions which are introduced by the main TX path, particularly from the high power amplifier. In the worst-case scenario, for an LTE base station, the error vector magnitude (EVM) can be as high as 17.5% [64] which means that the in-band distortion is only 15 dB lower than the power of the TX signal. As a result, this technique can only achieve up to 15 dB of cancellation when being deployed in a base station.

2.7.2.2 RF-to-RF

Another approach for suppressing the leakage at RF is by using the RF-to-RF structure. The basic concept of RF-to-RF solutions is reproducing the response of leakage path with an active cancellation block at RF. With the same input signal as the duplexer, the output of the cancellation block ideally is the same as the leakage, but 180° out of phase across the frequency band of interest. Therefore, accurate modelling of the leakage path is critical. The majority of RF-to-RF solutions use tap-based structures. In the tap-based structure, there are a number of auxiliary paths (or taps) in the cancellation block. In each of the path, there can be a delay, a variable attenuator and a variable phase shifter.

Depending on the techniques of modelling, RF-to-RF analog cancellation solutions can be grouped into two categories: without digital assistance and with digital assistance.

2.7.2.2.1 Without Digital Assistance An analog cancellation system without digital assistance usually consists of an active cancellation block at RF only, with no additional modelling blocks. The system level block diagram is shown in Figure. 2.23. One of the representatives of these cancellation techniques has been presented in [65]. This technique takes a fraction of the TX signal at the output of the PA and splits the in-phase (I) and quadrature (Q) components by using a quadrature phase power splitter. Each of the components mixes with the error signal. Initially, such error would be the leakage signal. Each of the resulting signals of the mixing is then

filtered by a lowpass filter in order to eliminate the image signals from the mixing. The bandwidth of the lowpass filter needs to be greater than the bandwidth of the cancellation system, but smaller than the lowest frequency of the image. The *I* and *Q* components at RF are then mixed again with the output of the lowpass filter. The re-conditioned *I* and *Q* signals are added together in order to form the cancellation signal. Finally, the error signal is obtained by subtracting the resulting cancellation signal from the leakage. The block diagram of this technique is shown in Figure. 2.24.
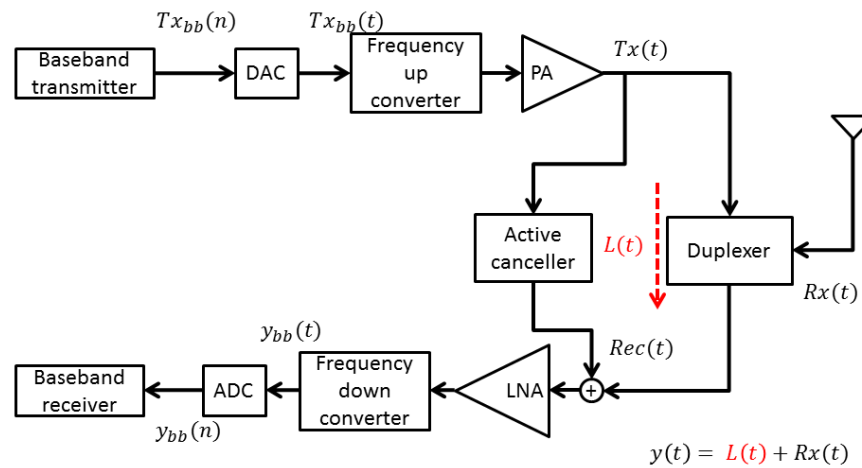
Figure 2.23: RF to RF cancellation structure without digital assistance

This technique is actually the RF adaptation of the classic LMS adaptive noise canceller [66] and it has been simplified so that only one tap is deployed. Therefore, it is theoretically suitable for the purpose of narrow band leakage cancellation or wide band cancellation if the duplexer has simple characteristics, e.g., a circulator. In the case that the leakage path of the duplexer has perfectly flat magnitude and linear phase responses, wide band cancellation could still be achieved. This is only true when the delay of the main cancellation path is identical to the one in the leakage path. Since four mixers have been deployed in this structure, the rising of the noise floor is expected. In order to avoid significantly reducing the signal to noise ratio (SNR) of the receiver, the cancellation can only occur at the output of the LNA. Thus, this does not assist with any saturation effects in the LNA.
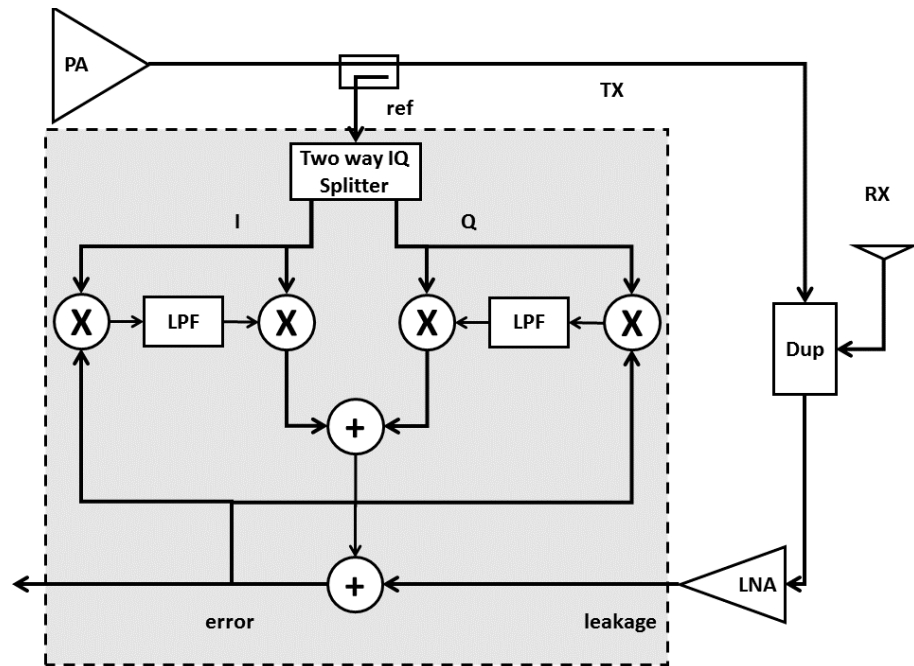
Figure 2.24: LMS adaptive filter of TX leakage
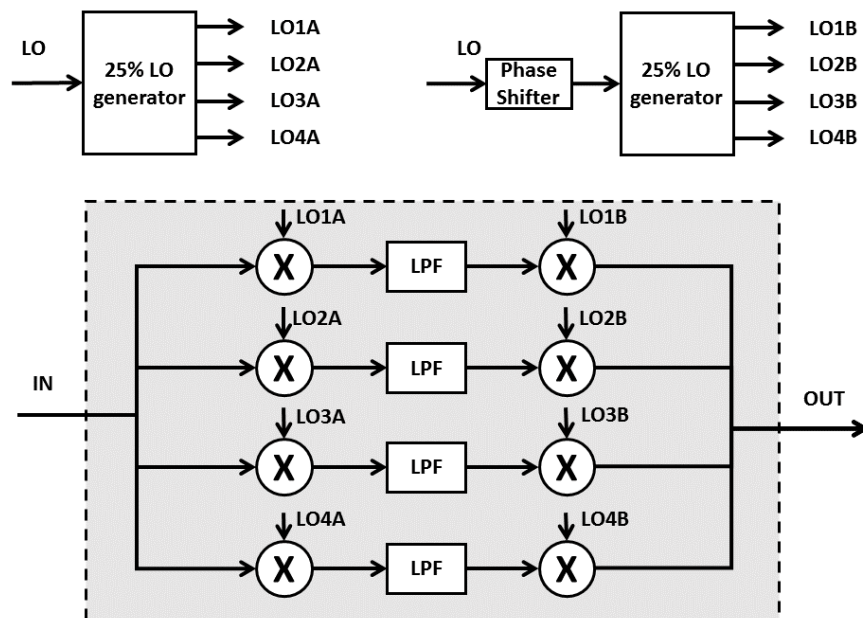
Figure 2.25: N-path filter based active canceller

A wideband cancellation system is presented in [23], which also creates the cancellation signal using down- and up-conversions. First, the TX reference signal from the output of the PA is down-converted to baseband. The baseband analog signal is then filtered by an analog adaptive filter. The resulting signal is the baseband cancellation signal. It is then up-converted to RF by the second mixer and combined with the leakage in order to realize the cancellation. In this system, a digital method called an N-path filter [23] is deployed in analog. Instead of mixing with one oscillation signal, a number of local oscillation signals, *lo* are generated so that the phase between two adjacent *lo* signals are $\frac{\pi}{N_{path}}$ radians, where N_{path} is the number of *lo* signals. The system structure is shown in Figure. 2.25. The author claimed that this technique is designed for both single antenna transceivers with any duplexing devices and the multi-antenna transceivers. The system can also be implemented in an IC which is a big advantage. Although it was claimed that this technique is suitable for improving the isolation performance of all major duplexing devices, the duplexer used for demonstrating the results only has simple characteristics. The duplexer used for the measurements is a custom device using inductors and capacitors (LC). In this paper, it also includes the results that are obtained by using antenna separation technique. Nevertheless, for both the LC duplexer and the antenna separation, the transfer functions are linearly changing in magnitude response within the band of interest. There is no experimental/theoretical evidence showing that this technique can work as claimed when a ceramic or cavity duplexer is used. Furthermore, since active components (mixers) have been used in this technique, unpleasant noise/distortion injection can be expected in the receiver.

In [42], the cancellation system is based on the tap-based structure. There are a number (k paths in total in Figure. 2.26) of main cancellation paths with a dedicated delay block in each of them. The delay blocks are equally spread along all the cancellation paths. This means that the delay difference between any two adjacent pairs of the main cancellation paths is the same. They are dependent on the bandwidth of the cancellation system, regardless of the carrier frequency. The author decides to use pre-calculated phase shifters rather than the more flexible variable phase shifters. Due to imperfections in the fixed phase shifters, the actual phase values differ from the calculated ones, which results in cancellation degradation. It is proved by the author that the effect that the phase imperfection has on the cancellation performance is reduced by splitting the phase with a number of phase shifters. As a result, a few sub-paths are implemented within each main cancellation
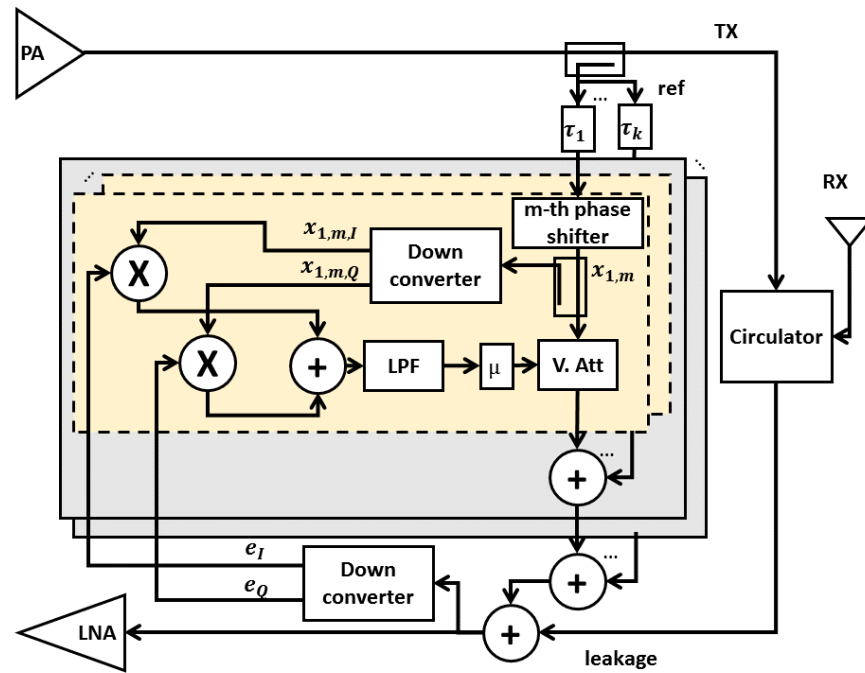
Figure 2.26: Block diagram of the simultaneous TX and RX system design

path.

A fixed phase shifter and a variable attenuator are placed in each sub-path. In order to avoid cancellation performance being affected by the imperfect phase rotation of the variable attenuators, a directional coupler is placed between the phase shifter and the variable attenuator in each sub-path. The signal in each sub-path is captured by down-converting the signals at the coupling port of the directional coupler. With the down-converted RX signal, the attenuation level of each variable attenuator can be adapted in a closed loop manner, using steepest-descent method.

In the simulation that the author presented, there are three tap delays and three phase shifters in each main cancellation path. This means that there are totally nine paths in this system. Therefore, two nine-way power splitters are needed, as well as one two-way splitter for cancelling the leakage. Additionally, there is one directional coupler in each of the sub-path giving the total number of couplers to be nine. As a result, there are nine down-converters, baseband adaptation blocks and variable attenuators needed in order to realise the system. The large complexity and poor reliability of the system make it difficult to be realized in practice.

2.7.2.2.2 With Digital Assistance RF cancellation systems can also be constructed with the assistance of digital baseband controllers. The baseband controller makes decisions depending on either only the error signal (more commonly, the power strength of the error signal) or both the baseband reference and the error signals. The general block diagram for this type of analog cancellation is shown in Figure. 2.27. Depending on the need, the cancellation could occur before or after the LNA. If the reference signal is required, usually it is the down-converted TX signal from the output of the PA [67]. The active canceller at RF can be constructed using the tap-based structure as in [68], named as double loop cancellation system (shown in Figure. 2.28). Basically, the system consists of two cancellation paths. In each path, there is a vector modulator and a delay line. The delays are pre-calculated with the centre frequency of the cancellation given. Generally, the delays in the two paths are greater and smaller, respectively, than the group delay of the duplexer which in this case is a circulator. The vector modulators are the tuning components for controlling the attenuation levels and the phase in the cancellation paths. Taking the advantages of relatively simple characteristics of the circulator, the I and Q components of the vector modulators are tuned individually and repeatedly in small steps until the error signal is minimized.

Using the circulator as the duplexing device is the key for this technique to achieve large cancellation bandwidth and good performance. This is because the magnitude response and delay of the circulator is relatively constant across the band of interest. Therefore, it is much easier to match the characteristics of the leakage path and the cancellation over a wide bandwidth. Though this technique has presented the relationship between the delays in the cancellation paths and the group delay, it is only suitable for a circulator. This is because the whole algorithm is based on the assumption that the magnitude and delay of the duplexer is constant.

The tuning algorithm for the attenuation and phase values in the previous system may require a long time in order to reach the optimal point. Global searching algorithms such as Modified Dithered Linear Search have been implemented in [69]. In terms of structure, it is very similar to the double loop cancellation. The vector modulators are replaced with phase shifters and variable attenuators. There is also one delay in each of the four paths in the system. The searching algorithm adds small random values to the weighting vector and observes the change of the strength of the error signal. The weighting vector should be altered in the opposite direction of the change in the power of the error signal. The basic isolation in the test system is
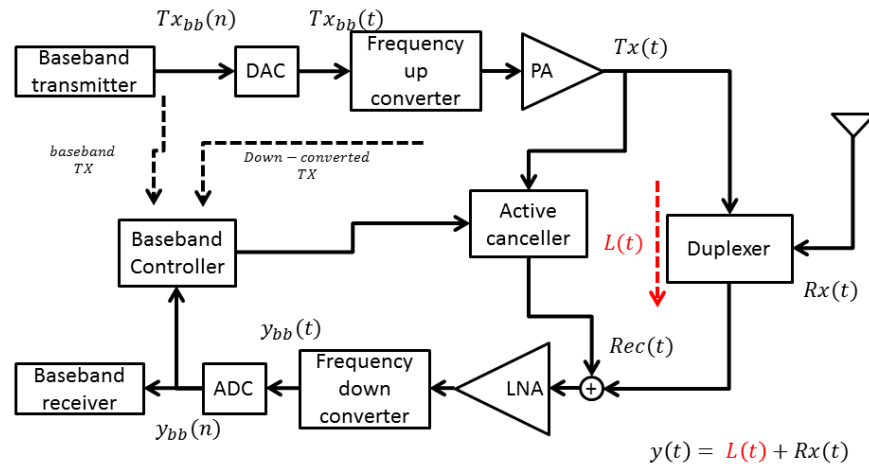
Figure 2.27: RF to RF cancellation structure with digital assistance
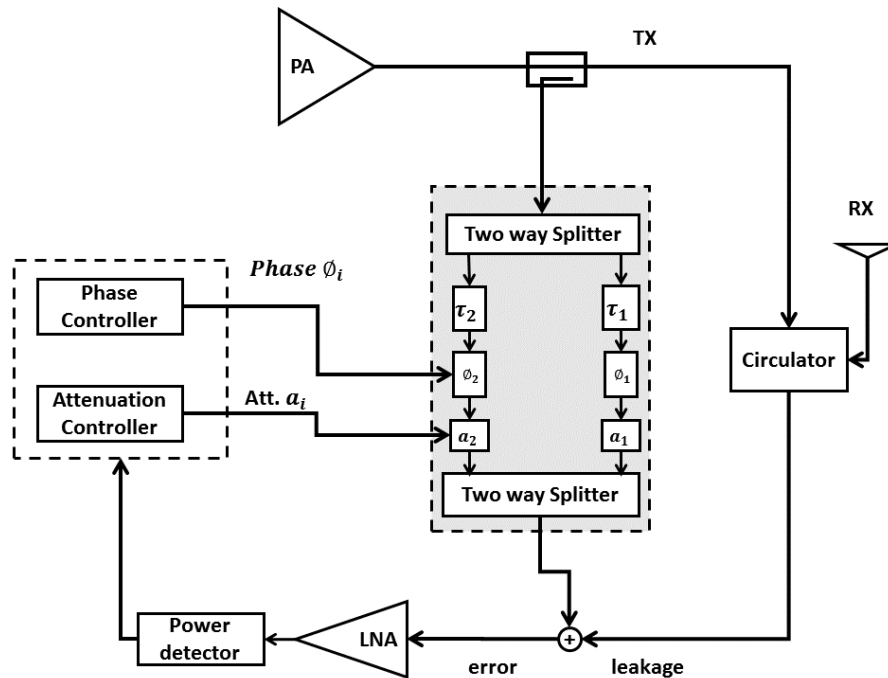
Figure 2.28: Double loop cancellation

achieved by using antenna separation. Over 20 dB of cancellation for the bandwidth of 100 MHz has been achieved.

In this paper, there is still little information on how to calculate the delays and the duplexing technique of this system is antenna separation, which is less complex than an off-the-shelf duplexer. More detailed information has been given in [70] with the same structure. The information about how to choose the delay is not given in this paper. Therefore, it is unknow if the proposed technique in [70] can successfully suppress the leakage when a duplexer is used.

A similar tap-based cancellation technique has been discussed in [71] which uses a SAW duplexer to separate the TX and RX signals (shown in Figure. 2.29). Within each cancellation tap, there is an LNA, phase shifter and a variable attenuator. In order to avoid TX signal being injected into RX chain, a notch filter which is centred at the TX frequency is placed in the cancellation system. Apart from the notch filter, this technique is similar to the double loop cancellation technique. The author of this technique explained that this is a narrow band solution due to delay mismatch.
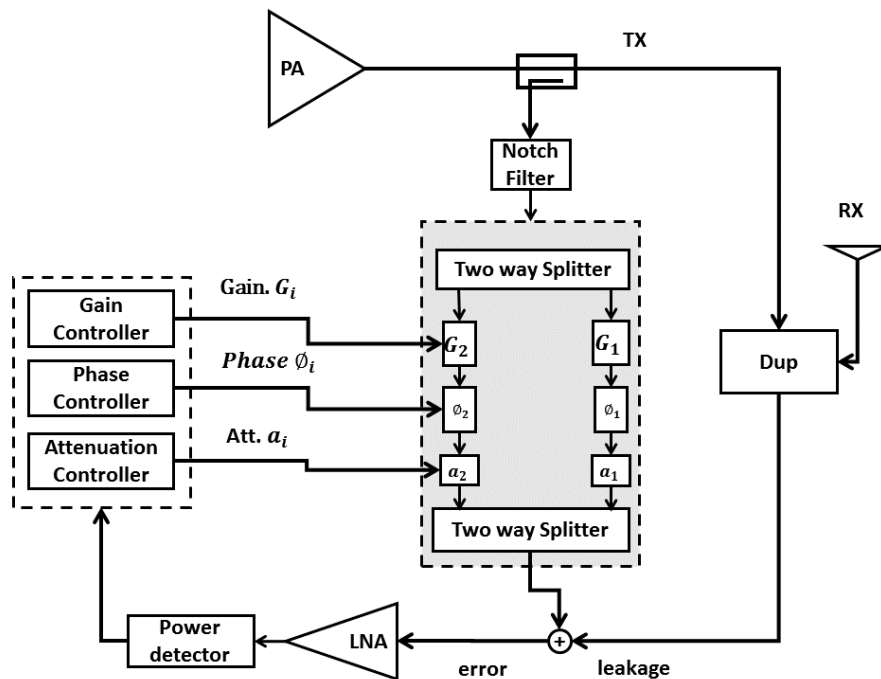
Figure 2.29: Dual path feed-forward cancellation system

A single tap cancellation system for a balanced receiver [72] is shown in Figure. 2.30. The cancellation block consists of a number of capacitors, two out of which are

tunable. These two tunable capacitors effectively produce phase and attenuation for the cancellation block. The realisation of the cancellation is done by the so-called four-port canceller (FPC) in which, there is also a tunable capacitor connected at the port-4. The transceiver uses a SAW duplexer in order to separate the TX and RX signals. It can be seen from the measured cancellation performance that this is also a narrow band solution.
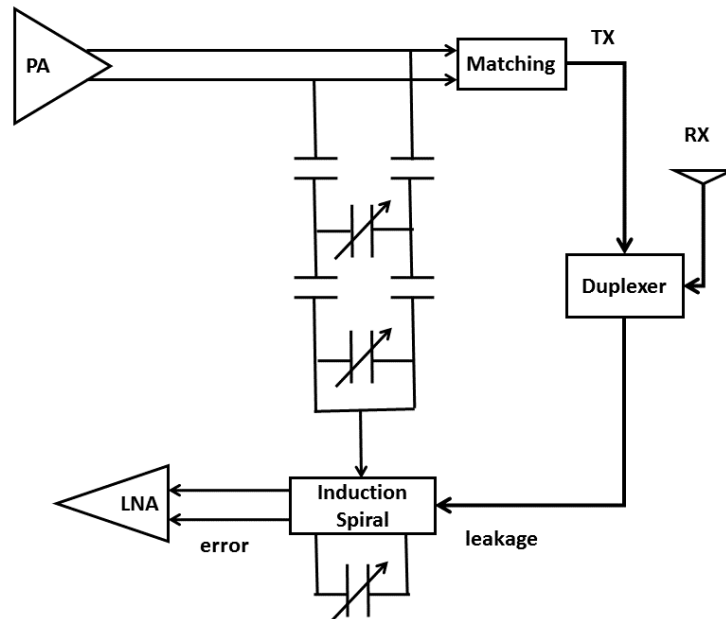
Figure 2.30: Integrated hybrid passive cancellation system

In the SC-FD cancellation design of [21], the author believes that the leakage cancellation at RF is similar to the sinc interpolation in digital domain. Therefore, it can be constructed by placing attenuators with certain delays (shown in Figure. 2.31). By tuning the attenuation, theoretically, the leakage can be cancelled completely. The publication also states that in order to reduce the number of taps in the cancellation system and provide high cancellation performance, the taps should only be placed at the delays which matter the most. Therefore, the taps which have the delays close to the group delay of the circulator are the most important ones. Therefore, half of the taps were placed before the group delay of the circulator and the other half were placed after. The attenuations are firstly pre-tuned based on the measured frequency response of the circulator by using preamble of the TX signal (WIFI). Then gradient algorithm is used to achieve the desired cancellation performance.
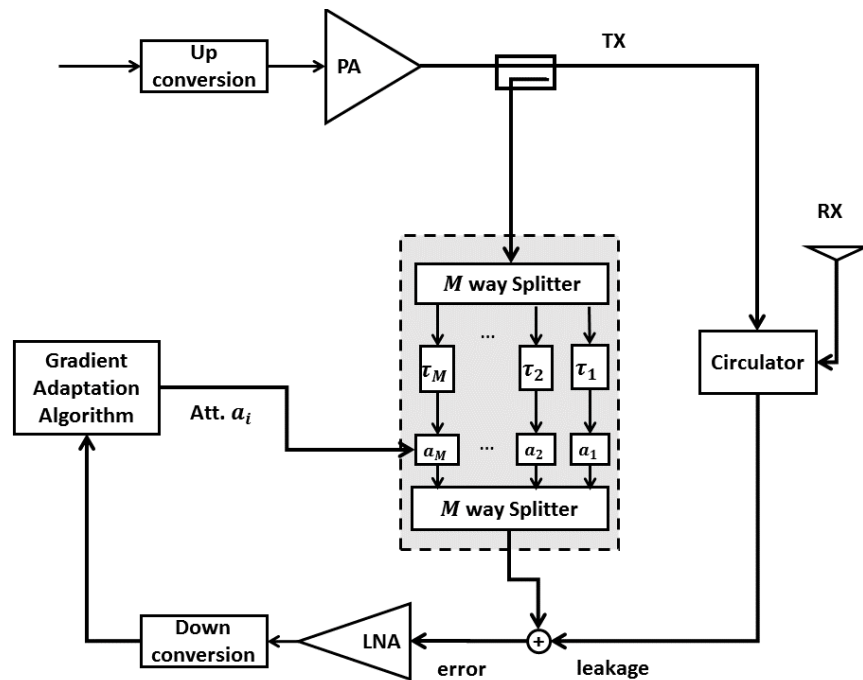
Figure 2.31: Cancellation system structure diagram for full duplex radios

The knowledge given in this publication about the choice of delays is not enough for implementing such system for an off-the-shelf duplexer. As mentioned before, the characteristics of a circulator are much simpler compared to an off-the-shelf duplexer. The technique didn't specify how to implement the system when the group delay of the isolation path of the duplexer is not a constant value across the frequency band. It is not sufficient by only knowing that the delays need to be placed before and after the group delay of the duplexer. Additionally, there are no phase controls in the cancellation system. As a result, more taps are needed (up to sixteen taps) in order to compensate the lack of phase control.

Systems with similar tap-based structures in this sub-category can also be found in [73] and [74]. The problems mentioned above remain unsolved.

2.7.2.3 Summary of RF Cancellation

Analog cancellation techniques are summarised in Table. 2.3. Some of the techniques have achieved promising performance in simulations [60] [61]. However, due to the ideal properties of those simulations, when implementing these techniques in practice, the performance cannot be guaranteed. The measured results are reported

with large cancellation (over 20 dB) over wide bandwidth (greater than 20 MHz) [23] [42] [73] [74] [21]. Six of the literatures mentioned above are designed for FDD systems. But none of them used an off-the-shelf duplexer. In order to solve the TX leakage problem for an FDD base station, a cancellation system that can provide high cancellation with large bandwidth is desired. Such a system is not yet available, as can be seen from the comparison tables.

Table 2.3: Summarised RF cancellation techniques

Publications	Year	Dup. type	Type	Tech.	Eva. method	BW (MHz)	Can. perf. (dB)
Duarte et al. [63]	2012	Ant. sep.	SC-FD	BB to RF	Meas.	0.625	25
Zhou et al. [23]	2015	LC	FDD	Analog N-path	Meas.	24	25
Aparin et al. [65]	2006	SAW	FDD	Cont. LMS	Meas.	1.23	16
Bharadia et al. [21]	2013	Circ.	SC-FD	Tap based	Meas.	80	62
Yang-Seok et al. [42]	2013	Circ.	SC-FD	Tap based	Sim.	10	100
Kannangara et al. [61]	2007	Circ.	FDD	Tap based	Sim.	5	40
Kolodziej et al. [69]	2014	Ant. sep.	SC-FD	Tap based	Meas.	30	31
O'Sullivan et al. [71]	2005	SAW	FDD	Tap based	Meas.	4.5	20
Tong et al. [72]	2015	FBAR	FDD	Tap based	Meas.	5	23
Hong et al. [73]	2012	Circ.	SC-FD	Tap based	Meas.	40	32
Kim et al. [74]	2013	SAW dup.	FDD	Tap based	Meas.	60	25

2.7.3 Digital and Analog Combined Cancellation

Analog and digital cancellation can also be combined for better cancellation performance. In fact, this has already been implemented in [63] and [21] etc. Over 90 dB of cancellation in total has been reported in [21] and about 73 dB is reported in [63]. Though the overall cancellation performance is outstanding, in order to relax the isolation performance requirement of the duplexer, the RF cancellation is the effective one. In the case that wideband RF cancellation for a transceiver using a duplexer is not achievable, the performance of the receiver would be degraded regardless the performance of the digital cancellation. This will be discussed in more detail in the following chapter.

2.8 Summary

This chapter has started with an introduction to base stations. It explained the duplexing devices that are used in the single antenna FDD and SC-FD transceivers. In a single antenna FDD transceiver, the duplexing device is usually a duplexer of the following technologies: cavity, ceramic, SAW and BAW duplexers. In SC-FD transceivers with common antenna configuration, circulators are usually deployed. Depending on the technologies that are used, properties of the duplexers such as the electrical performance and the physical characteristics are vastly different, particularly in the context of insertion loss, isolation performance and power handling. Current FDD transceivers in medium and large area base stations widely use high performance cavity duplexers to separate TX and RX signals. The high cost of the high performance cavity duplexers is undesired. Moreover, due to the demand of higher data rate, the bandwidth of the transceiver is increasing. As a result, the required bandwidth of the duplexer also increases. The transient bands of the duplexer are getting narrower. Such a design requirement is getting more and more difficult to be achieved due to the practical limitation of passive filter technologies, i.e. Q-factor. Therefore, other solutions are needed in order to assist the existing passive solutions to achieve the desired isolation performance and/or reduce the stringent requirement of the passive filter design. For these purposes, many active cancellation techniques have been published not only for FDD, but also for SC-FD systems. This chapter has discussed the state-of-the-art active solutions, including the digital and RF cancellation techniques.

Digital cancellation systems are flexible and require no or little additional hardware. Cancellation performance achieved by using digital cancellation techniques are shown in the summarised performance table of the digital cancellation system. However, RX will be desensitized with the existence of in-band leakage at RF, independent of the digital cancellation performance. This will be explained in more detail in the next chapter.

After the discussion of the digital cancellation techniques, RF techniques have also been compared in this chapter. The RF solutions involve reproduction and cancellation. The reproduction is that the RF leakage signal is reconstructed in order to obtain the cancellation signal. Then the cancellation is achieved by adding (or subtracting) the cancellation and leakage signals. The cancellation steps of all existing RF solutions are similar. The difference is at the reproduction step. The details of those RF solutions have been explained in this chapter. Though, many of those RF solutions showed excellent cancellation performance, no techniques have proved that wide band cancellation can be achieved when using an off-the-shelf duplexer. The author of this thesis suggests that the important aspect of implementing a wide band RF cancellation system is to correctly estimate the delays, as well as the phase and attenuations. Unfortunately, the information on how to determine the delays, irrespective to the type of duplexers, is missing from the state-of-the-art literatures.

In the next chapter, a novel cancellation system architecture will be introduced. It will show that the proposed cancellation system is a wideband active solution for suppressing the in-band leakage at RF frequency.

2.9 Contributions of this Chapter

1. Comparison of the state-of-the-art cancellation techniques including both digital and analog. The strengths and weaknesses of those techniques have been discussed.

3 The Proposed Cancellation System

3.1 Introduction

In the previous chapter, we have discussed the purpose of the in-band TX leakage cancellation system and reviewed the state-of-the-art solutions. The existing techniques failed to provide sufficient performance for wideband cancellation for an FDD transceiver using a duplexer at RF frequency. Attempting to solve the in-band TX leakage problem, a new cancellation system is proposed in this chapter.

3.2 The Proposed Cancellation Architecture

A cancellation system architecture is proposed in this section in order to solve the leakage problem in an FDD transceiver. The block diagram of the proposed system is shown in Figure. 3.1. The concept of the proposed system is developed from the FIR filter structure and the system is implemented at RF. It is capable of in-band leakage cancellation. The proposed cancellation system is designed for a duplexer with more complex characteristics, for instance, a cavity duplexer. As mentioned in Sec. 2.5.1, tuning the cavity duplexer requires a human to physically adjust the screws on top of the component. The time for the tuning process is proportional to the complexity of the duplexer. Therefore, using the proposed cancellation system could reduce or omit the labour cost of the tuning process. As a result, the overall cost of the base station can be reduced. In addition, the proposed cancellation system reduces the isolation performance requirement of the duplexer. Therefore, the cavity duplexer could be replaced with a high power ceramic duplexer. In this case, not only the cost, but also the occupied size is reduced. The proposed cancellation system can also reduce the design challenges of the duplexer for future communications due to the relaxation of the isolation requirement.
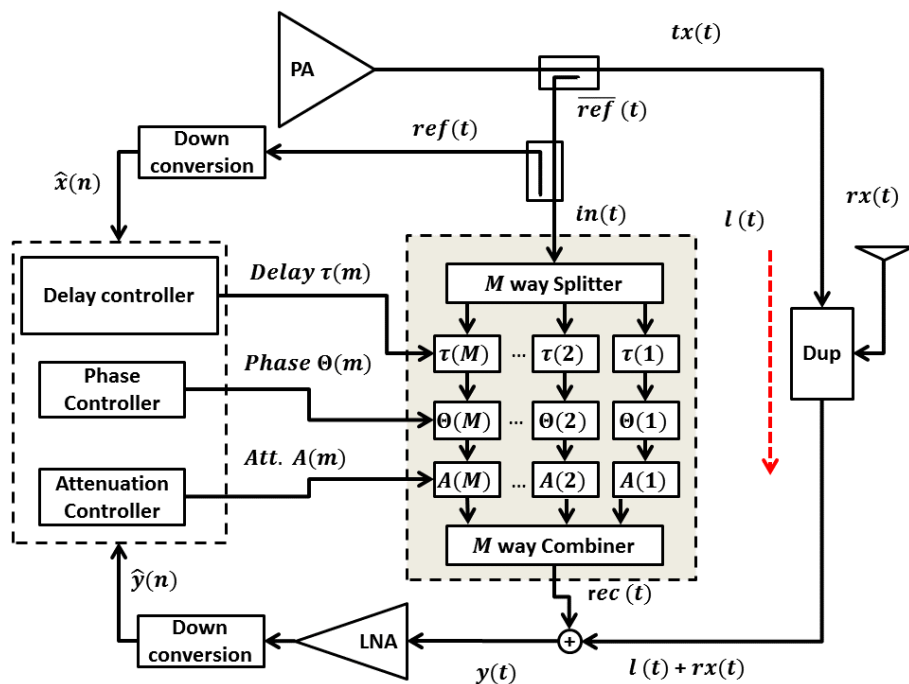
Figure 3.1: The proposed cancellation system

The proposed cancellation system consists of an RF cancellation block and a baseband modelling block. There are two RX paths, one of which is the main receiver and the other one is the auxiliary RX. The auxiliary receiver is for capturing the output signal of the PA as the reference. The two receivers must be synchronized in order to more accurately model the duplexer. The RF cancellation block is the analog implementation of an FIR filter structure. It consists of a number of cancellation paths, or taps. The number of taps represents the order of the cancellation system. In each cancellation tap, there is a delay block, an attenuator and a phase shifter. The values of these RF components are given by the outputs of the baseband modelling block.

The modelling block uses the frequency down-converted reference and leakage signals to approximate the leakage path at the baseband. The tap weights and delays are optimized so that the error between the baseband leakage and the approximated signals is minimized. During or upon the completion of the modelling, the delay blocks, attenuators and phase shifters in the cancellation block are set according to the output of the modelling block, i.e., tap weights and delays. The relation between the modelling outputs and the values of the RF components will be discussed later in this chapter. The details of the algorithms for the modelling block will be discussed

in later chapters. In order to achieve a wideband cancellation, the optimization of the delays enables the third degree of freedom in addition to the optimization of the amplitudes and phase. The importance of the delay optimization will be shown in later sections of this chapter. The details of the modelling techniques will be discussed in later chapters of this thesis.

3.2.1 The Purposes of the RF Cancellation

It is important that the in-band leakage is suppressed at RF frequencies before reaching the LNA. Digital cancellation at baseband is unacceptable mainly due to two reasons: the increase of the quantization noise and the saturation of the LNA.

The increase of the quantization noise In a typical FDD receiver, there is a device named as variable gain amplifier (VGA) placed after the mixer and just before the ADC. The purpose of the VGA is to amplify the weak RX signal to a level so that the ADC can digitize such signal more effectively and accurately [75]. The gain of the VGA is automatically adjusted depending on the power of the signal at its input. In the ideal case, i.e. no in-band leakage or interferences exist at the receiver, the signal at the input of the VGA is thus the RX signal.

In the case that the in-band TX leakage exists in the receiver, the desired RX signal as well as the leakage are frequency down-converted to baseband and arrive at the input port of the VGA. The gain of the VGA is adjusted based on the in-band leakage power since it is significantly higher than the power of the RX signal. As a result, a much smaller gain is obtained and by which the RX signal is amplified. The resulting in-band leakage after the VGA reaches approximately full scale of the ADC whereas the RX signal is still very little. For this reason, most of the ADC's resolution is ineffective on the desired RX signal which causes the increase of the quantization noise. Hence, the SNR is reduced and thus the receiver performance is degraded. The digital cancellation techniques can significantly suppress the leakage at the baseband, but is ineffective on the quantization noise. Therefore, with the existence of the leakage at the input of the ADC, the desensitization of RX occurs irrespective of the digital cancellation performance. For this reason, the in-band TX leakage has to be suppressed before the VGA. In fact, the cancellation should occur before the LNA to avoid the saturation. This will be discussed next.

Saturation of the LNA   In the proposed cancellation architecture, the location of the cancellation is at the input of the LNA. The question arises if the leakage can be cancelled at the output of the LNA instead of at the input. This can be seen from the following example that is shown in Figure. 3.2. This example shows the possible consequences when the cancellation is somewhere after the LNA.

As discussed in the previous chapter, relaxing the performance requirement of a duplexer can cause the power of the in-band leakage significantly higher than the receiver sensitivity. In Figure. 3.2, it is assumed that the power of the RX signal before the LNA is at the sensitivity level of the receiver. The power level of the leakage before the LNA is at the level B, which is much greater than the RX signal. Let the gain of the LNA be G. Both the RX signal and the leakage could be amplified by this gain. This could result that the power level of the leakage and the RX signal increases towards to point A and C, respectively. We now have two possible cases:
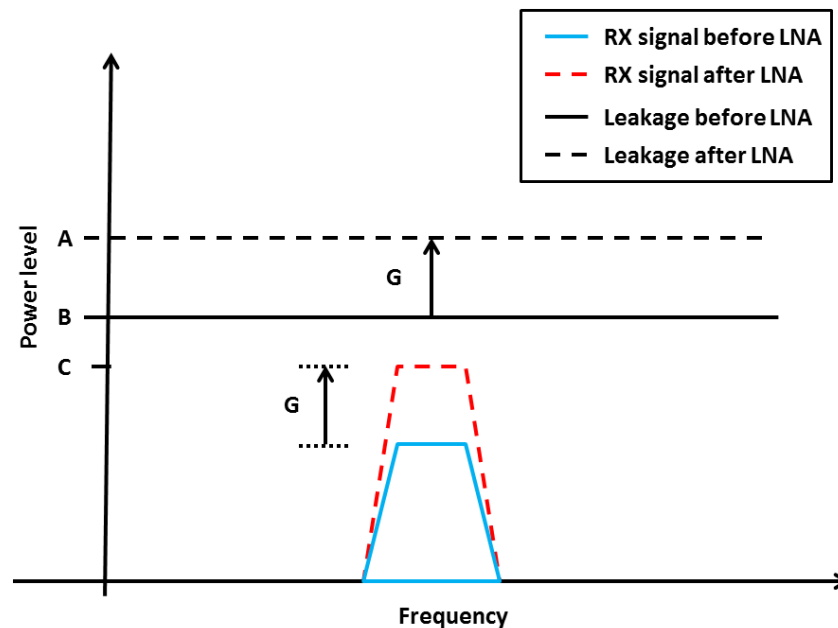
Figure 3.2: Signals at the input and output of the LNA

LNA with a smaller saturation level   If the saturation level of the LNA is less than A, then the saturation of the LNA occurs and the leakage level can only reach a level as high as the saturation point. Due to the saturation of the LNA, the noise floor will be increased. In addition, the RX signal after the LNA would be

amplified by a gain that is smaller than G. The resulting RX power level would be at a level that is less than C. With the increase of the noise floor and the decrease of the RX signal power level, the SNR decreases irrespective of the cancellation performance when the cancellation location is after the LNA. Therefore, in the case that the saturation level of the LNA is less than A, the in-band leakage needs to be suppressed before reaching the LNA. The threshold level of the saturation level A is approximately equal to the sum of the power of the in-band leakage and the gain in logarithm scale.

LNA with a larger saturation level   In the case that the saturation level of the LNA is greater than A, no saturation occurs. However, it is still not acceptable to cancel the leakage after the LNA. This is due to the reason that the system to be characterized in this case becomes the combination of the duplexer and the LNA. Comparing this system with one that only consists of the duplexer alone, additional gain has been provided by the LNA. This gain must also be applied in the cancellation block. Thus, it will result in the need for an amplifier in the cancellation block. This active component could potentially increase the noise figure of the receiver and therefore, should be avoided. As a result, in this thesis, the input of the LNA is chosen as the cancellation location.

3.2.2 The Operation of the Cancellation System

In Figure. 3.1, the transmitter signal $tx(t)$ at the output of the high power amplifier (PA) is coupled with a directional coupler in order to obtain the reference signal $\overline{ref}(t)$. A small portion of the reference signal ($ref(t)$) at RF is coupled off from $\overline{ref}(t)$ (by another directional coupler). Then it is frequency down-converted to baseband and digitized. This signal $\hat{x}(n)$ ideally carries all the information about the transmitted signal. It, along with the signal $\hat{y}(n)$ at the baseband of the receiver, will then be used for modelling the duplexer. The signal $\overline{ref}(t)$ passes through the coupler with little insertion loss. This becomes the input signal of the cancellation block and denoted as $in(t)$. It is then split by the M-way power splitter, where M is the number taps of the cancellation system. In each tap, there is a variable delay line, a phase shifter and a variable attenuator connected together. The variable delay line could be replaced with a pre-calculated fixed delay line. In this case, the

tuning process will need to be replaced with the calculation of the delay values. The detail of the calculation process will be discussed in Chapt. 6. Each split signal of $in(t)$ is delayed, phase-shifted and attenuated in each tap before being combined by an M-way power combiner in order to produce the cancellation/reconstructed signal $rec(t)$.

There are two phases of operation, namely: modelling and cancellation. In the modelling phase, the transceiver operates in off-line mode, i.e. no signals are transmitted/received at the antenna. Hence, there is no desired signal $rx(t)$ and the signal in the receiver before the cancellation is only the leakage. TX transmits the training signal within the RX band. Typically, the training signal is white Gaussian noise (WGN). The bandwidth of the WGN is the same as that of the cancellation system. This is to ensure the power of $ref(t)$ is high enough so that it can be digitized by ADC to obtain $\hat{x}(n)$. The filtering effect of the PA can be ignored as this will be compensated at the baseband using whitening filter. Additionally, the RF cancellation block is turned off by setting all the attenuators to maximum attenuation. Therefore, the received signal before the Low Noise Amplifier (LNA) is the leakage signal, i.e., $y(t) = l(t)$. This signal is frequency down-converted to baseband. The delay, phase and amplitude for the corresponding components in the RF cancellation block are then calculated by the baseband processor using $\hat{x}(n)$ and $\hat{y}(n)$, where $\hat{y}(n)$ is the baseband signal of $y(t)$. The details of the algorithms will be discussed in Chapt. 4 and Chapt. 5. Since the cancellation block is designed to match the transfer function of the duplexer, it is independent of the signal types once the modelling is completed.

Once the essential parameters are successfully calculated, the cancellation system is then changed into the cancellation phase. The delay, phase shifter and attenuator of each tap are set to the values that are calculated by the baseband controller. The transmitter is set to transmit in TX frequency band. The reconstructed signal ideally has the same amplitude but 180° offset from the leakage signal. After summing $rec(t)$ and $l(t)$, the leakage is then cancelled. Some adjustments of the attenuators and phase shifters can further be carried out to fine tune the RF cancellation block. Once the satisfaction condition is reached or the power of the error signal within the band of interest is minimized, the transceiver can then be turned back online. Ideally, the leakage signal $l(t)$ is eliminated and only desired signal $rx(t)$ arrives at the input of LNA.

3.2.3 Unique Properties of the Proposed System

The proposed cancellation architecture shares some aspects with the existing solutions. The proposed solution utilizes the output of the PA and approximates the transfer function of the leakage path. These are similar to the techniques that are shown in [65] [66] and [23] etc.. The cancellation block of the proposed solution consists of a number of cancellation paths. In each path, there is a delay, a variable attenuator and a phase shifter. Similar structure can be seen in [42] [67] and [69] etc.. However, there are many novelties that differentiate the proposed solution from the existing ones.

3.2.3.1 Higher level of complexity

As discussed earlier in this chapter, in order to prevent the receiver performance from being degraded by the in-band leakage, the cancellation needs to be performed before the LNA. The proposed technique also needs to be a wideband solution. It is designed for a transceiver using an off-the-shelf duplexer. In comparison, there are no existing techniques that can satisfy the same level of requirements at the same time, i.e. wideband, using an off-the-shelf duplexer and RF cancellation.

3.2.3.2 Delay optimization

The proposed technique satisfies the requirements of wide bandwidth, using an off-the-shelf duplexer and RF cancellation at the same time by utilizing the additional degree of optimization, i.e. the delay optimization. As mentioned earlier, the proposed cancellation system shares a similar architecture, i.e. FIR filter structure, as some of the existing techniques. However, no existing techniques have provided the delay optimization. This is mainly due to the reason that the existing RF solutions are designed either for narrow band cancellation or for transceivers using non-standard duplexing devices (e.g. a circulator or the antenna separation).

The fundamental concept of the RF cancellation is to obtain the same amplitude as the leakage but 180° out of phase at any frequency within the frequency band of interest. This represents that the transfer function of the RF cancellation block must be the same in amplitude as the isolation path of the duplexing device, but 180° out

of phase at any single frequency within the band. In theory, this requires not only the matching of the amplitude and the inverted phase between the transfer function of the duplexing device and the cancellation block, but also the delay response. In the case that the designed cancellation bandwidth is narrow like in [71], the matching of the delay response can be relaxed as the frequency deviation across the band is small. But for wideband cancellation, the matching of the delay response is critical due to the wide bandwidth. Without matching the group delay response within the band of interest, the phase will match at certain frequency range, but not for the whole frequency band.

On the other hand, if the duplexing device to be matched has simpler characteristics, the matching of the delay response over a wide bandwidth can also be achieved without a complex optimization algorithm. This can be seen in many existing publications ([68] [73] [74] [21]) that only a single group delay value is matched between the isolation path of the duplexing device and the cancellation block. This is based on the assumption that the group delay is constant across the whole frequency band of interest. As shown in Figure. 2.18, this assumption is invalid for cavity and ceramic duplexers. Therefore, for wideband RF cancellation and for transceivers with off-the-shelf duplexers, delay optimization ability at RF is required. This is the second major novelty of the proposed cancellation system.

3.2.3.3 Baseband modelling technique with the delay optimization

As a part of the delay optimization, a technique is needed to calculate the suitable delay for each cancellation path. Classic system identification techniques such as the least square algorithm will result in a large number of taps. Since the cancellation occurs at RF, the number of taps needs to be as small as possible. Not all the resulting taps using the classic identification techniques are important. For this reason, a sparse system identification technique is more suitable which only determines the most important taps. Many sparse system identification techniques are available [76][77][78][79][80]. However, with these classic techniques, the determined locations of the sparse impulses are integer samples. Therefore, the resolution of the estimated delays using the existing sparse system identification techniques heavily depends on the critical sampling frequency of the reference and leakage signals. This critical sampling frequency is also defined by the desired bandwidth of the

cancellation system. Thus, the resolution of the estimated delays τ_0 is

$$
\begin{aligned}
\tau_0 &= \tau_s \\
&= \frac{1}{f_s}
\end{aligned}
\tag{3.1}
$$

where f_s is the critical sampling frequency. Since the leakage path of the duplexer is at RF frequency, the resolution of the estimated delays τ_0 is thus not high enough. The consequence is that the delay estimation accuracy is reduced and the number of taps for modelling the leakage path is increased.

In this thesis, two novel estimation algorithms, named as modified adaptive delay filter using direct cross-correlation and modified compressive sampling matching pursuit, are proposed in order to more accurately model the isolation path of the duplexer. These two techniques are modified based on two existing solutions, i.e. adaptive delay filter and compressive sampling matching pursuit. Unlike the existing sparse system identification techniques, the two proposed techniques improved the accuracy of the estimated delays. As a result, using the same hardware resources, the cancellation performance is improved. This is the two additional novelties of this thesis. Two new modelling techniques are proposed in the next two chapters of this thesis.

3.2.3.4 Other novelties of this thesis

The additional novelty of this thesis is that a technique is proposed in order to successfully implement the proposed cancellation system using low performance RF components. The components available for implementing the cancellation system suffer from interdependences of attenuation, phase and group delay. The proposed implementation technique reduces and eliminates the interdependences of the RF components by using a number of fixed attenuators and delay lines. It enables the implementation and acceptable results have been successfully measured. The details of the technique will be shown in Chapt. 6.

3.3 Critical Aspects of the Cancellation Performance

The proposed cancellation architecture has the potential of solving the in-band TX leakage problem. However, there are factors that could seriously affect the performance. These key factors need to be addressed.

3.3.1 The Order of the System

Since the proposed cancellation system is based on the FIR filter structure, increasing the order of the system could improve the cancellation performance. This implies the need for additional cancellation paths at RF frequency. This indeed increases the overall costs of the cancellation system. Considering the form factor of each RF component, increasing the order of the system will also result in a larger RF cancellation block.

Additionally, since the cancellation system suppresses the leakage at the RF front-end of the receiver, any noise or interferences that are caused by the cancellation block will be injected into RX. The power level of such noise or interferences will directly affect the RX performance. In order to avoid significant desensitization of the receiver, passive components are preferred in the RF cancellation block. Increasing the order of the cancellation system will reduce the power of the reference signal in each cancellation path. Consequently, implementing such a system without using gain blocks could be impossible. The details of the cancellation performance with respect to the increase of the system order can be seen in Chapt. 4 and Chapt. 5.

3.3.2 Matching Requirements Between the Leakage and the Cancellation Signals

Cancellation at RF frequencies requires a high level of matching in amplitude and phase at every frequency between the cancellation and the leakage signals. Let $S_l(f)$ and $S_c(f)$ denote the frequency responses of the leakage and the cancellation signals at any frequency component f within the band of interest, respectively. These two

signals could be expressed in polar form as:

$$S_l(f) = A_{S_l}(f) \cdot e^{j\theta_{S_l}(f)} \tag{3.2}$$

$$S_c(f) = A_{S_c}(f) \cdot e^{j\theta_{S_c}(f)} \tag{3.3}$$

where $A_{S_l}(f)$ and $A_{S_c}(f)$ are the amplitudes of $S_l(f)$ and $S_c(f)$ respectively. $\theta_{S_c}(f)$ and $\theta_{S_l}(f)$ are the phases of $S_c(f)$ and $S_l(f)$. Let Z be the resulting signal after the cancellation, that is

$$
\begin{aligned}
Z(f) &= S_l(f) - S_c(f) \\
&= A_{S_l}(f) \cdot e^{j\theta_{S_l}(f)} - A_{S_c}(f) \cdot e^{j\theta_{S_c}(f)} \\
&= A_{S_l}(f) \cdot e^{j\theta_{S_l}(f)} - A_{S_l}(f) \cdot \frac{A_{S_c}(f)}{A_{S_l}(f)} \cdot e^{j\left(\theta_{S_c}(f) - \theta_{S_l}(f)\right)} \cdot e^{j\theta_{S_l}(f)} \\
&= A_{S_l}(f) \cdot e^{j\theta_{S_l}(f)} \cdot \left(1 - \frac{A_{S_c}}{A_{S_l}} \cdot e^{j(\theta_{S_c}(f) - \theta_{S_l}(f))}\right) \\
&= S_l(f) \cdot \left(1 - \frac{A_{S_c}(f)}{A_{S_l}(f)} \cdot e^{j\triangle\theta(f)}\right)
\end{aligned}
\tag{3.4}
$$

The cancellation performance is quantified by

$$
\begin{aligned}
\mathbb{C}(f) &= -20 log_{10} \left| \frac{Z(f)}{S_l(f)} \right| \\
&= -20 log_{10} \left(\left| 1 - \frac{A_{S_c}(f)}{A_{S_l}(f)} \cdot e^{j\triangle\theta(f)} \right| \right)
\end{aligned}
\tag{3.5}
$$

The phase mismatch is $\triangle\theta(f)$ and the amplitude mismatch $\triangle A(f) = 20 log_{10} A_{S_c}(f) - 20 log_{10} A_{S_l}(f)$. The cancellation performance with respect to the amplitude and phase mismatch at a single frequency is shown in Figure. 3.3. For the cancellation system to successfully suppress the leakage, the cancellation signal at each frequency component within the band of interest must match its amplitude, phase to the leakage signal. In order to achieve more than 20 dB of cancellation, the phase mismatch needs to be within approximately $\pm 6°$ at a single frequency when the amplitudes are perfectly matched. In the case of a perfect phase match, the amplitudes difference

between the cancellation signal and the leakage must be within the range between -0.92 dB and +0.83 dB, approximately.
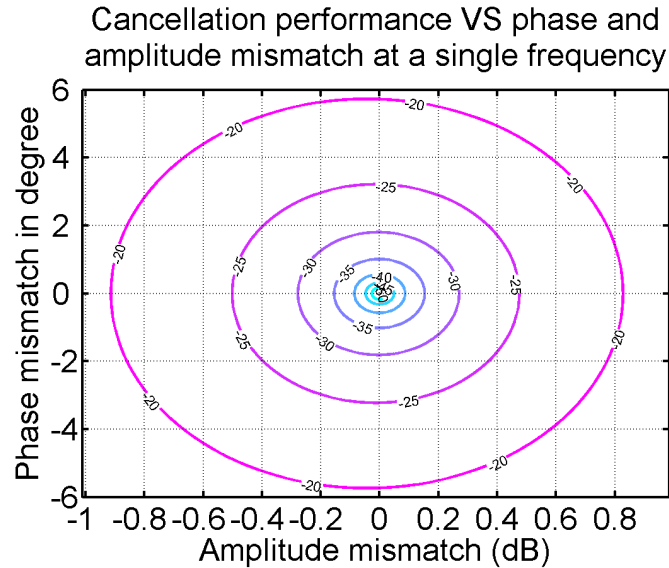
Figure 3.3: Cancellation Versus amplitude and phase mismatch

The matching requirement between the cancellation and the leakage signals can be difficult to satisfy, especially when the cancellation bandwidth is wide. This requires accurate characterization of the duplexer and careful implementation of the cancellation block.

3.3.3 Performance Requirements of RF Components

In order to achieve the strict matching requirements, high performance RF components are preferred. For fixtures, i.e., power combiners, directional couplers, cabling and connectors, the magnitude and the group delay responses ideally should be constant across the frequency band of interest and their phase responses should be linear. For the variable components in each cancellation path, the same performance requirements of the fixtures are also needed. In addition, variable components with higher tuning resolution are preferred. Poor tuning resolution could affect the achievable cancellation performance, especially when a high cancellation performance (e.g., more than 20 dB) is desired.

The three parameters, i.e., attenuation, phase and group delay of each variable component ideally need to be mutually independent when being tuned. For instance,

tuning the attenuation of a variable attenuator should not affect the phase and group delay. In the case that a variable component with interdependences of attenuation, phase and group delay is used, it can be very difficult, but it remains possible to implement the proposed cancellation system. Certainly, the achievable cancellation performance will be degraded. Further details are provided in Chapt. 6 where a technique has been proposed in order to implement the cancellation system using low performance RF components. Nevertheless, the required values of all tunable components are obtained by the baseband modelling technique. In the following section, the behavioural modelling concept will be briefly discussed.

3.4 Behavioural Modelling of the Duplexer and RF Realization

Behavioural modelling technique is used to predict the system-level performance with the reduced computational complexity of the physical level analysis of a system. In the leakage cancellation problem that we have, we basically treat the isolation path of the duplexer as a linear system. Applying behavioural modelling to the TX leakage problem can more accurately characterize the leakage path of the duplexer, which leads to better cancellation performance. It can also reduce the number of cancellation paths in the RF cancellation system. Therefore, the design complexity, as well as the cost and the form factor, of the cancellation system can be reduced. In this section, the linkage between the baseband modelling and the cancellation structure is established. Firstly, the mathematical representation of the baseband model is investigated.

3.4.1 Baseband Modelling

The characterisation of the duplexer in the proposed cancellation system is performed with the behavioural modelling technique at baseband. The duplexer is considered as a 'black-box' and modelled in terms of its input and output signals. In Figure. 3.1, the input and output signals of the duplexer at RF are $tx(t)$ and $l(t)$, and their digitized base band signals are $\hat{x}(n)$ and $\hat{y}(n)$, respectively. Full parameters of such model can be estimated and thus the cancellation system can be

implemented. Since FIR structure is chosen in modelling the duplexer, parameters including delay, amplitude and phase for each tap are essential to be determined.

Firstly, we start looking at the basic non-sparse model representation. Let the desired signal be

$$des(n) = \hat{y}(n) \tag{3.6}$$

where the size of $\hat{y}(n)$ is $1 \times N$. Let the impulse response of the duplexer at the baseband be $h(n)$ which is a $1 \times N$ vector. The output of the transversal filter is thus

$$
\begin{aligned}
out(n) &= \hat{x}(n) * h(n) \\
&= \sum_{m=0}^{N-1} h(m)\hat{x}(n-m)
\end{aligned}
\tag{3.7}
$$

where $*$ denotes the convolution operation and the input of the transversal filter $\hat{x}(n)$ is a $1 \times N$ vector. The error between the desired signal and the output of the duplexer model is

$$\hat{e}(n) = des(n) - out(n) \tag{3.8}$$

The estimation algorithm will determine the weight vector in order to minimize the error $\hat{e}(n)$.

It can be easily seen from (3.7) that the leakage signal is expressed as the combination of a number of reconditioned signals. These reconditioned signals are obtained by first delaying the input signal $\hat{x}(n)$ by m samples. Then the delayed input signal $\hat{x}(n-m)$ is amplitude scaled by the corresponding tap weight. Once $h(n)$ is estimated, the information about the duplexer will be known.

However, since the total number of values, N, in $h(n)$ is large, it is impractical to implement such a large system using (3.7). Usually, impulses are localized and not all elements in $h(n)$ have a large impact on the output. Therefore, the majority of elements in $h(n)$ can be ignored. The duplexer can then be considered as an

M-sparse system. The approximation of $out(n)$ can be obtained by $\hat{out}(n)$ which is

$$
\begin{aligned}
out(n) \approx \hat{out}(n) \\
= \hat{x}(n) * \hat{h}(n) \\
= \sum_{m=0}^{M-1} \hat{h}(m)\hat{x}\left[n - d(m)\right]
\end{aligned} \tag{3.9}
$$

where $\hat{h}(m)$ is the mth estimated weighting vector, m is the index of the M-sparse system and $d(m)$ is the sample delay. $d(m)$ can be fractional values. Increasing the value M will reduce the approximation error between $out(n)$ and $\hat{out}(n)$. This will be discussed in Chapt. 4 and Chapt. 5, along with the algorithms that are used for estimating the weights and delays of the impulse response. In this section, we focus on how to relate these parameters with practical implementation.

At the baseband of an I/Q modulated FDD transceiver, $\hat{x}(n)$ and $\hat{y}(n)$ are complex vectors, i.e.,

$$
\hat{x}(n) = \hat{x}_I(n) + j\hat{x}_Q(n) \tag{3.10}
$$

and

$$
\hat{y}(n) = \hat{y}_I(n) + j\hat{y}_Q(n) \tag{3.11}
$$

where $\hat{x}_I(n)$, $\hat{x}_Q(n)$, $\hat{y}_I(n)$ and $\hat{y}_Q(n)$ are vectors of real values. We thus write the weighting vector $\hat{h}(m)$ in complex form. That is

$$
\hat{h}(m) = \hat{h}_I(m) + j\hat{h}_Q(m) \tag{3.12}
$$

where $\hat{h}_I(n)$ and $\hat{h}_Q(n)$ are vectors of real values.

Substitute (3.12) into (3.9). We have

$$
\begin{aligned}
\hat{out}(n) = \sum_{m=0}^{M-1} \left[\hat{h}_I(m) + j\hat{h}_Q(m)\right] \hat{x}(n - d(m)) \\
= \sum_{m=0}^{M-1} \left[\hat{h}_I(m)\hat{x}\left(n - d(m)\right) + j\hat{h}_Q(m)\hat{x}\left(n - d(m)\right)\right]
\end{aligned} \tag{3.13}
$$

It can be seen that the estimated output $\hat{out}(n)$ is obtained by firstly multiplying the

real and imaginary parts of the weighting vector with the 0° and the 90° phase-shifted inputs (with corresponding delay), respectively. Then the resulting two vectors of the multiplication are combined together, before being combined to get $\hat{out}(n)$. This can thus be realised in practice by separating the in-phase and quadrature at RF and multiplying the corresponding weights. However, in each path, there are two sub-paths (I and Q paths) required in order to apply the weighting vectors. This certainly requires a large number of components in order to implement the system in practice. The complexity of the practical system is thus increased.

A better way of using the complex weighting vector is by using its polar form. We re-write weighting vector $\hat{h}(m)$ in polar form, i.e.,

$$\hat{h}(m) = B(m)e^{j\phi(m)} \tag{3.14}$$

where $B(m)$ and $\phi(m)$ are magnitude and phase of the mth weighting vector. Therefore, (3.9) becomes

$$\hat{out}(n) = \sum_{m=0}^{N-1} B(m)e^{j\phi(m)}\hat{x}\left(n - d(m)\right) \tag{3.15}$$

Each tap of the FIR filter now has a magnitude, phase and delay as variables. It is possible for this structure to be implemented at RF. The details on the RF realisation of the duplexer model are discussed in the next sub-section.

3.4.2 RF Realization

In (3.15), it shows that the modelling output can be represented by the input and estimated weighting vector. It is essential to determine how this relationship changes when such model is implemented. Let the local oscillator for the single side band IQ modulator be

$$
\begin{aligned}
lo(t) &= cos\left(2\pi f_c t\right) + jsin(2\pi f_c t) \\
&= e^{j2\pi f_c t} \tag{3.16}
\end{aligned}
$$

where f_c is the carrier frequency. We now denote the analog baseband signal of the transversal filter output $\hat{out}(n)$ as $\widetilde{out}(t)$ and the analog input signal of $\hat{x}(n)$ as $\widetilde{x}(t)$.

Let the continuous time delay of the mth tap be $\tau(m)$, so that

$$\tau(m) = d(m)\tau_0 \tag{3.17}$$

where $\tau_0 = \frac{1}{f_s}$ is the resolution of the delay estimation and f_s is the sampling frequency at the baseband. Then, from (3.15), we have

$$\widetilde{out}(t) = \sum_{m=0}^{N-1} B(m)e^{j\phi(m)}\widetilde{x}\left[t - \tau(m)\right] \tag{3.18}$$

The mathematical representation of the cancellation signal at RF is thus

$$
\begin{aligned}
out(t) &= Re\left[\widetilde{out}(t)lo(t)\right] \\
&= \sum_{m=0}^{N-1} Re\left\{B(m)e^{j\phi(m)}\widetilde{x}\left[t - \tau(m)\right]e^{j2\pi f_c t}\right\} \\
&= \sum_{m=0}^{N-1} Re\left\{B(m)\Theta(m)\widetilde{x}\left[t - \tau(m)\right]e^{j2\pi f_c[t-\tau(m)]}\right\}
\end{aligned} \tag{3.19}
$$

where $Re\{-\}$ represents the real part and $\Theta(m) = e^{j[2\pi f_c\tau(m)+\phi(m)]}$ is the phase component vector. $B(m)$ and $\Theta(m)$ can be realised by the RF attenuators and phase shifters, respectively. Furthermore, theoretically the reference signal before being down-converted by the auxiliary receiver path is

$$
\begin{aligned}
ref(t) &= Re\left\{\widetilde{x}(t)lo(t)\right\} \\
&= Re\left\{\widetilde{x}(t)e^{j2\pi f_c t}\right\}
\end{aligned} \tag{3.20}
$$

And for introducing the cancellation system, we can assume that the coupler is ideal, i.e., no phase shifts nor delay differences between ports. Then the input signal to the RF canceller is

$$in(t) = \alpha ref(t) \tag{3.21}$$

where α is the power gain between the through and coupling ports of the coupler. In the later chapter, the effect of the non-ideal components is considered. Since $B(m)$

is the magnitude vector, (3.19) then becomes

$$
\begin{aligned}
out(t) &= \sum_{m=0}^{N-1} B(m)\, Re\left\{\widetilde{x}\left[t-\tau(m)\right] e^{j2\pi f_c\left[t-\tau(m)\right]}\right\}\Big|_{\Theta(m)} \\
&= \sum_{m=0}^{N-1} A(m)\, in\left[t-\tau(m)\right]\Big|_{\Theta(m)}
\end{aligned}
\tag{3.22}
$$

where $A(m) = \frac{B(m)}{\alpha}$ is the value vector for the RF attenuator, $\big|_{\Theta(m)}$ represents that the real signal is phase shifted by $\Theta(m)$, and $\Theta(m)$ and $\tau(m)$ are values of phase shifters and time delay lines, respectively.

In summary, the relationship between the baseband modelling and the RF realization has been established. Such relationship will be used to obtain the simulated and measured results which will be shown in the following chapters.

3.5 Summary

The proposed cancellation system architecture has been presented in this chapter. It consists of a baseband modelling block and an RF cancellation block. It requires an additional down-converting link from the output of the PA for modelling purpose. The RF cancellation block consists of a number of paths. The variable components including an attenuator, a phase shifter and possibly a delay line are controlled via the modelling block. The optimization of the delay block is one of many advantages of this cancellation system in contrast to the state-of-the-art solutions. It enables the proposed system architecture for wideband cancellation. It is designed for a duplexing device with a higher order of complexity.

This chapter has also discussed the location of RF cancellation in detail. The digital baseband cancellation is unacceptable since the ADC resolution will not be utilized efficiently with the existence of the in-band leakage. In the case that the power of the in-band leakage is large, the signal to noise ratio will be reduced due to the increase of the quantization noise regardless of the digital cancellation performance. The cancellation location should be at the input of the LNA in order to avoid the use of active components in the RF cancellation block. The advantages and disadvantages of cancellation before and after the LNA have also been discussed.

The key aspects of the cancellation performance have also been discussed in this chapter, including the order of the system, the matching requirements between the leakage and the cancellation signals and the performance requirements of the RF components. Furthermore, this chapter explains that for wideband cancellation, the locations of the delays need to be optimized in order to achieve better cancellation with less hardware resources. This can be accomplished with baseband modelling.

The characterization of the duplexer can be achieved by using behavioural modelling technique. This chapter has shown that the leakage signal can be approximated using the delayed input signal and the resulting parameters of the baseband modelling. The parameters of the modelling include the delays and tap weights. The linkage between the baseband modelling and the RF realization has also been established.

This chapter has also stated that existing system identification techniques are not suitable for the proposed cancellation architecture. New modelling techniques thus are needed. In the next two chapters, two novel modelling techniques have been proposed.

3.6 Contributions of this Chapter

The main contributions of this chapter are:

1. A new cancellation system structure has been proposed in this chapter.

2. A linkage between the baseband model and the actual RF signals has been mathematically identified and established.

4 Modified Adaptive Delay Filter Modelling Technique

4.1 Introduction

In the previous chapter, the importance of behavioural modelling has been emphasized. The reason why classic sparse identification techniques are not suitable for the proposed cancellation architecture has also been discussed. In this chapter, this discussion is expanded to one of those classic techniques, i.e. the classic adaptive delay filter (C-ADF).

The classic adaptive delay filter was designed to characterize an unknown system with sparse impulse response. There are a number of variations of C-ADF: maximum deviation from regression line, delay selection from variance threshold and delay selection from cross-correlation. C-ADF with cross-correlation is proven in [81] to be a better option for its robustness and computation efficiency, providing the input is highly correlated and a large amount of data is available. However, like other classic techniques, C-ADF suffers from the low delay resolution which reduces the accuracy of the estimation. In order to apply the C-ADF for solving the FDD transceiver leakage problem, modifications are needed. For this reason, the modified adaptive delay filter using direct cross-correlation technique is proposed in this chapter. This novel modelling technique is designed to provide a higher estimation accuracy for the cancellation system that is proposed in this thesis.

This chapter starts with reviewing the C-ADF technique.

4.2 Classic Adaptive Delay Filter

The classic adaptive delay filter (C-ADF) was first introduced in [82]. It is an adaptive filter structure for modelling an unknown system by sequentially estimating the parameters of each stage of an FIR filter (shown in Figure. 4.1). The C-ADF algorithm considers the unknown system as the sum of the taps with different delays and weights. Parameters such as the delays and tap weights are determined based on the importance of those taps. Depending on the methodology, the importance of the taps can be measured in terms of the magnitude of the taps [83] or the maximum absolute value of the cross-correlation vector between the reference and error signals [81]. The parameters of the taps are determined sequentially. The delay estimation of one tap (or one stage) is performed first and is followed by the approximation of its coefficient. The same procedures are repeated for the rest of the stages on a one-by-one basis.

(a)

(b)
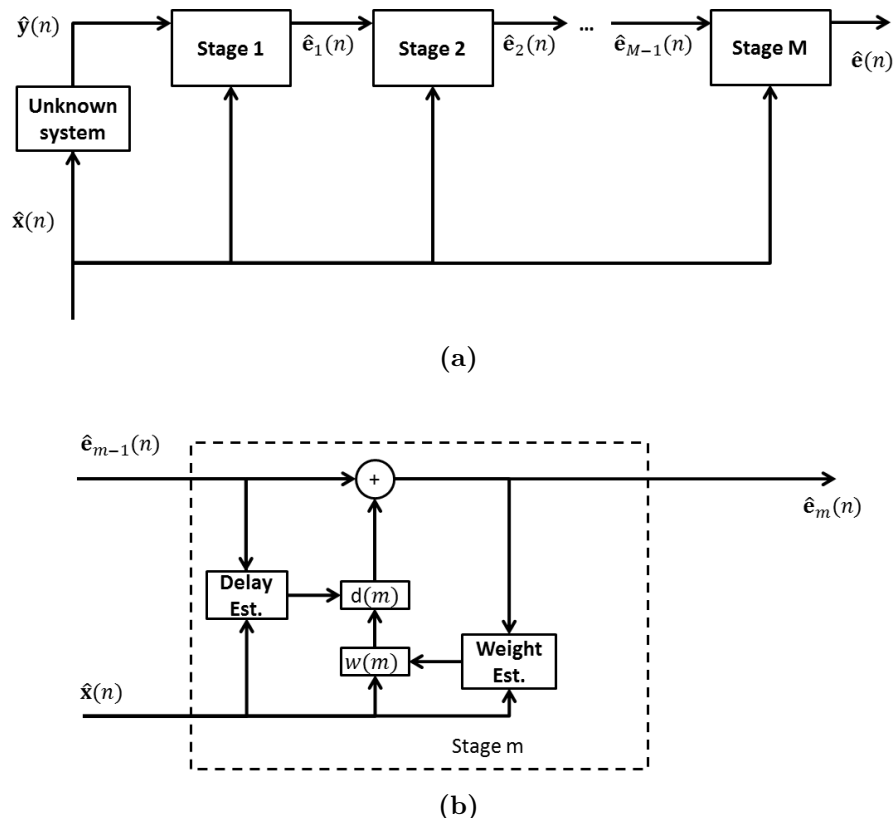
Figure 4.1: The structure of operation for the adaptive delay filter algorithm. (a) High level block diagram. (b)Block Diagram example of the mth stage

The delay of each tap is estimated using the input of the unknown system and the error signal of the previous adaptation. At the beginning of the estimation, the previous error signal is the output of the unknown system. Let the impulse response of the unknown system be $\mathbf{h}(n)$, thus the output of the unknown system $\hat{\mathbf{y}}(n)$ can be represented as

$$\hat{\mathbf{y}}(n) = \hat{\mathbf{x}}(n) * \mathbf{h}(n) \tag{4.1}$$

where $*$ is the convolution operator. If we take the cross-correlation between the input and output of the unknown system, we have

$$
\begin{aligned}
\mathbf{R}_{\hat{\mathbf{x}},\hat{\mathbf{y}}} &= \hat{\mathbf{x}}(n) \star \hat{\mathbf{y}}(n) \\
&= \hat{\mathbf{x}}(n) * \hat{\mathbf{y}}^*(-n) \\
&= \hat{\mathbf{x}}(n) * \hat{\mathbf{x}}^*(-n) * \mathbf{h}^*(-n) \\
&= \mathbf{R}_{\hat{\mathbf{x}}} * \mathbf{h}^*(-n)
\end{aligned}
\tag{4.2}
$$

where $\star$ is the operator for cross-correlation and the superscript $*$ represents the complex conjugate. If the input signal $\hat{\mathbf{x}}(n)$ is highly correlated, for instance it is white, then the auto-correlation vector is

$$\mathbf{R}_{\hat{\mathbf{x}}}(q) = \alpha\delta(n - q) \tag{4.3}$$

where $\delta(n)$ is the Dirac delta function, α is the sum of squares of elements in the vector $\hat{\mathbf{x}}(n)$ and $q = 1, 2, \ldots, 2N - 1$. Therefore, 4.2 becomes

$$
\begin{aligned}
\mathbf{R}_{\hat{\mathbf{x}},\hat{\mathbf{y}}}(q) &= \alpha\delta(n - q) * \mathbf{h}^*(-n) \\
&= \alpha\mathbf{h}^*(-n + q)
\end{aligned}
\tag{4.4}
$$

It can be seen that when the auto-correlation vector of the input signal is a scaled Dirac delta function, the cross-correlation between the input and output signals of the unknown system represents the impulse response of this system. The C-ADF algorithm developed in this thesis is based on this concept. It sequentially estimates the location of the largest weighting component using the following arguments, i.e.

$$\overline{D}(m) = \arg\max_{q} \left(|\mathbf{R}_{\hat{\mathbf{x}},\hat{\mathbf{y}}}(q - N)| \right) \tag{4.5}$$

and

$$D(m) = -(N - \overline{D}(m) - 1) \tag{4.6}$$

where $\overline{D}(m)$ is the calculated sample location in the cross-correlation function, $m = 1, 2, \ldots, M$ is the tap index and M is the total number of taps.

The weight estimation is performed after the delay of the current tap is successfully estimated. This can be seen from the operation diagram in Figure. 4.1. The input signal of the unknown system and the error of the current tap are used for the tap weight estimation. The input signal is delayed by the delay value which has been determined by the delay estimation. The weight can be determined using iterative adaptation algorithms, such as, Least Mean Squares (LMS) or Recursive Least Squares (RLS).

Upon the completion of both delay estimation and weight adaptation for the current tap, the delay and tap weights are set with the estimated values of the current stage and the parameters of the next stage can then be calculated.

4.3 Problem with the Classic Adaptive Delay Filter Technique

From (4.2) to (4.4), it can be seen that the cross-correlation based C-ADF technique requires the reference signal to have the property of *white* in order to more accurately characterize the unknown system. Therefore, the reference or the input signal needs to be critically sampled, i.e. the sampling frequency is twice of the single side bandwidth. In addition, any filtering effect on the reference signal needs to be removed using techniques such as whitening filtering[1]. Secondly, the unknown system needs to be sparse under the critical sampling frequency of the reference signal so that C-ADF can more efficiently characterize the unknown system compared to the classic technique such as least squares (LS). The first requirement is much simpler to satisfy whereas the second one can be more difficult.

In the TX leakage problem, the actual unknown system (duplexer) is at RF. The impulse response of the unknown system can be considered as an ideal impulse

---

[1]The whitening filtering technique will be discussed in more details in Chapt. 6.
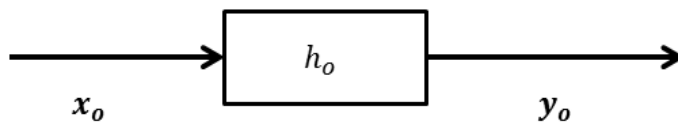
(a)
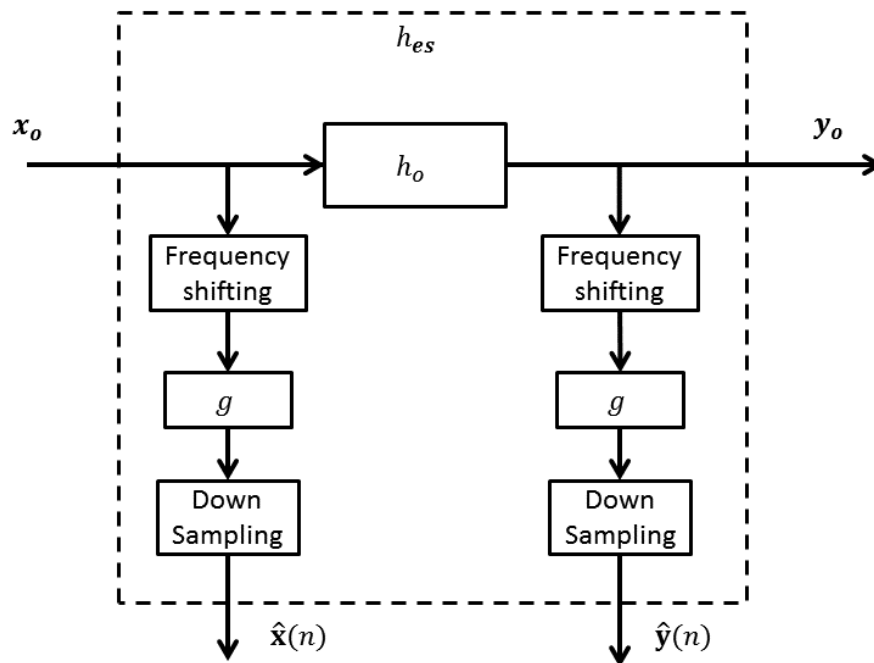
(b)

Figure 4.2: Signals for modelling. (a) Desired signals for modelling. (b) Actual signals for modelling.

response at the baseband being up-converted to RF. The ideal baseband impulse response is at an extremely high sampling frequency, f_{sH}. This is the desired impulse response. The order of the ideal approximation system depends on the sparsity of this impulse response. Theoretically, it can be obtained by using C-ADF technique, providing that the reference is *white* and both the reference and the leakage signals are sampled at f_{sH} or greater. This can be seen in Figure 4.2(a) where h_o is the ideal impulse response of the unknown system. Both x_o and y_o are the signals sampled at f_{sH} or greater, providing x_o is *white*. However, these conditions can be impossible to match in practice.

In the actual transceiver, the reference and the leakage signals of the duplexer can only be obtained at the baseband after being frequency down-converted and down-sampled at the critical sampling frequency, f_{sc} where $f_{sc} \ll f_{sH}$. This can be seen in Figure 4.2(b) where g is the impulse response of an ideal lowpass filter. The signals $\hat{\mathbf{x}}(n)$ and $\hat{\mathbf{y}}(n)$ are down-sampled to the lower sampling frequency, f_{sc} and are used for estimating the unknown system h_o. Compared to Figure 4.2(a), the estimated impulse response of the unknown system using $\hat{\mathbf{x}}(n)$ and $\hat{\mathbf{y}}(n)$ is h_{es}. It consists of not only the unknown system h_o, but also two lowpass filters and the down-sampler. Due to this reason, the estimated impulse response of the unknown system becomes less sparse at the baseband. This requires the approximation system to have a significantly higher order. The following two sections illustrate this phenomenon.

4.3.1 Delay Estimation Accuracy for a System with a Constant Group Delay Response

Firstly, we start with an example of a system with a single impulse. Please note that this example is created using a few random numbers including the initial impulse location of the unknown system and the sampling frequencies. The initial impulse location is chosen so that it is an integer value at the higher sampling frequency but non-integer at the lower one. The example is to present the problems with C-ADF when modelling an unknown system at the digital baseband of a transceiver. The impulse response of the unknown system consists of one impulse at 2801 sample location in digital domain, which is randomly chosen for illustration purposes. The sampling frequency is at $f_{sH} = 100$ MHz. The group delay of such a system is thus constant across the bandwidth of 100 MHz. The ideal input signal of this impulse

response is white Gaussian noise. As for the ideal input signal, the resulting ideal output of this unknown system is at the sampling frequency of f_{sH}. According to 4.4, the cross-correlation result between the ideal input and output represents the ideal impulse response of the unknown system. This ideal impulse response is called in this dissertation as the ideal system and is shown in Figure. 4.3.

In order to simulate the actual baseband input and output signals of the unknown system, the ideal input and output are down sampled by 500 times. As a result, the actual sampling frequency f_{sc} is 0.2 MHz. The location of the ideal impulse of the system thus changes from the integer sample location of 2801 at the sampling frequency of f_{sH} to the fractional location of $\frac{2801}{500}$ at a lower sampling frequency. At this sampling frequency, the actual input of the unknown system is still *white*. However, the cross-correlation result in Figure. 4.3 which is obtained using the actual input and output signals shows instead of a single impulse, there are now multiple impulses in the estimation of the unknown system. When using C-ADF technique, the integer location at which the peak impulse is has been chosen to be the delay of the first tap. This clearly is not the location of the ideal system. As a result, the accuracy of C-ADF in this case is questionable. In order to achieve a similar level of estimation, a larger number of taps is needed.

The estimation accuracy using C-ADF could be improved by up-sampling the signals that were sampled at f_{sc} to f_{sH}. The cross-correlation is then performed using these up and over-sampled signals and the result is also shown in Figure. 4.3. It can be seen that the peak amplitude of the cross-correlation result using the over-sampled signals lies where the ideal impulse of the system is. For the single tap system, up-sampling the input and output signals can provide a better delay estimation. However, in the case that the ideal impulse response of the unknown system consists of more than one impulse, simply using over-sampled input and output signals is not sufficient to achieve a better estimation accuracy. This can be seen from another simple example that is shown in the next section.

4.3.2 Delay Estimation Accuracy for a System with a Complex Group Delay Response

It has been shown in Figure. 4.3 that for a constant group delay system with a fractional delay component in the impulse response, the accuracy of delay estimation
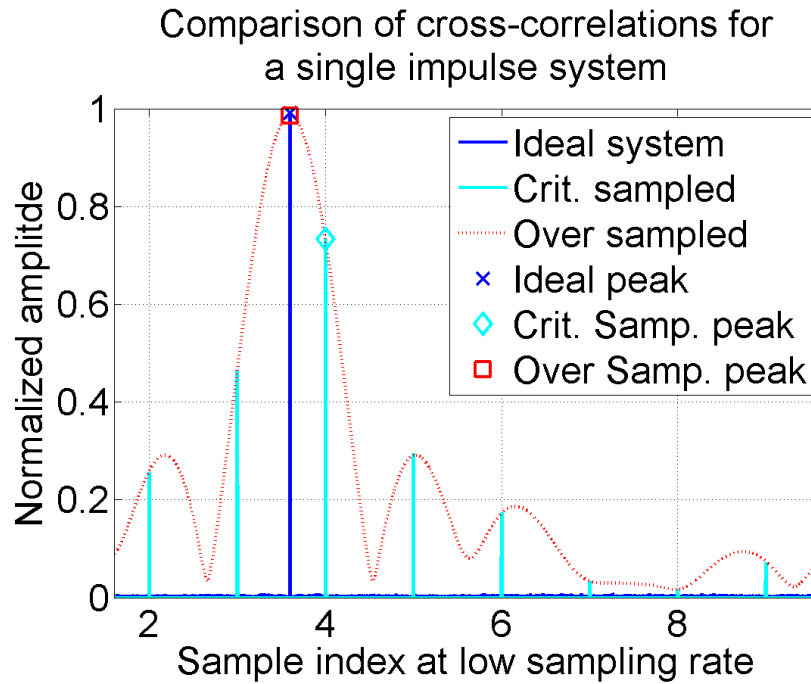
Figure 4.3: Comparison between the actual impulse response of a single tap system and the estimated one using cross-correlation technique

with cross-correlation based technique can be increased by using the up-sampled input and output signals. However, the accuracy of this method still needs to be improved when estimating the delays for a system with a complex group delay response. A system with a complex group delay response consists of more than one impulse in its impulse response. One or more of these impulses are located at the non-integer locations with respect to the low sampling frequency.

In order to simulate a system with a complex group delay response, an impulse response of the system with two impulses is created and shown in Figure. 4.4. Similar to the previous section, the impulse locations are chosen so that they are integers at the higher sampling frequency but fractional values at the lower one. The sampling frequency at which the ideal impulse response is created is assumed to be 100 MHz, i.e., $f_{sH} = 100$ MHz. There are two impulses which are assumed to be at 19.81 us and 22.31 us. In the digital domain, the two locations are equivalent to be at 1981 and 2231 sample locations. This represents that at the low sampling frequency, i.e., $f_{sc} = 0.2$ MHz, the locations of the two impulses are at 3.962 and 4.462 in the digital domain.

The cross-correlation result using the critically sampled signals at f_{sc} shows that

the location of the peak magnitude is far away from the larger impulse of the ideal impulse response. On the other hand, the cross-correlation result that is obtained by using over-sampled signals also shows the inaccuracy of the delay estimation. This is because a lowpass filter is applied when up-sampling the signals from the low sampling rate. The cross-correlation using the up-sampled signals consists of not only the ideal actual impulse response of the system, but also the impulse response of the lowpass filter. This can be analysed as follows.
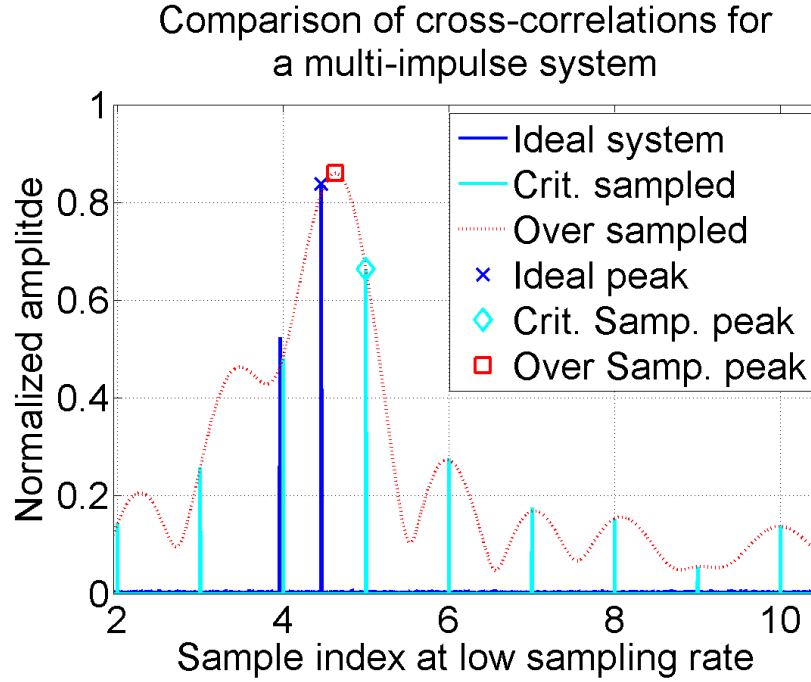
Figure 4.4: Comparison between the actual impulse response of a multi-tap system and the estimated one using cross-correlation technique

In order to investigate the cause of the estimation inaccuracy with cross-correlation based technique using up-sampled signals, we define the actual impulse response of the unknown system as

$$\mathbf{h}_{up}(n_{up}) = a\delta(n_{up} - d_1) + b\delta(n_{up} - d_2) \tag{4.7}$$

where the sample index $n_{up} = 1, 2, \ldots, N_{up}$ is at the high sampling frequency with the maximum number of samples as N_{up} and δ is the Dirac delta function. In the example, there are two components sparsely located at $d_1 = 1980$ and $d_2 = 2230$ with complex coefficients of a and b, respectively. We also know that $|a| < |b|$. We assume a white signal, $\hat{\mathbf{x}}_w(n_{up})$, which is at the same sampling rate as the actual

impulse response of the unknown system. The output of the unknown system can thus be presented as

$$\hat{\mathbf{y}}_w(n_{up}) = \hat{\mathbf{x}}_w(n_{up}) * \mathbf{h}_{up}(n_{up}) \tag{4.8}$$

The input and output signals of the unknown system at the lower sampling frequency are denoted as $\hat{\mathbf{x}}(n)$ and $\hat{\mathbf{y}}(n)$, respectively, where $n = 1, 2, \ldots, N$ is the sample index at the low sampling frequency with the maximum number of samples as N. Thus, we can present the input and the output signals $\hat{\mathbf{x}}(n)$ and $\hat{\mathbf{y}}(n)$ as

$$\hat{\mathbf{x}}(n) = DownSample \left\{ \hat{\mathbf{x}}_w(n_{up}) \right\} \tag{4.9}$$

and

$$\hat{\mathbf{y}}(n) = DownSample \left\{ \hat{\mathbf{y}}_w(n_{up}) \right\} \tag{4.10}$$

To analyse the performance of using the up-sampling technique that is shown in the previous section, the signals, $\hat{\mathbf{x}}(n)$ and $\hat{\mathbf{y}}(n)$, are up-sampled back to the high sampling frequency with an ideal brick-wall lowpass filter applied. Then each of the up-sampled input and output signals of the system can be expressed by

$$\begin{aligned} \hat{\mathbf{x}}_{up}(n_{up}) &= UpSample \left\{ \hat{\mathbf{x}}(n) \right\} \\ &= \hat{\mathbf{x}}_w(n_{up}) * \mathbf{g}_{LPF}(n_{up}) \end{aligned} \tag{4.11}$$

and

$$\begin{aligned} \hat{\mathbf{y}}_{up}(n_{up}) &= UpSample \left\{ \hat{\mathbf{y}}(n) \right\} \\ &= \hat{\mathbf{y}}_w(n_{up}) * \mathbf{g}_{LPF}(n_{up}) \\ &= \hat{\mathbf{x}}_w(n_{up}) * \mathbf{h}_{up}(n_{up}) * \mathbf{g}_{LPF}(n_{up}) * \mathbf{g}_{LPF}(n_{up}) \end{aligned} \tag{4.12}$$

with the assumption that two lowpass filters are the same.

The cross-correlation between $\hat{\mathbf{x}}_{up}(n_{up})$ and $\hat{\mathbf{y}}_{up}(n_{up})$ is

$$
\begin{aligned}
\mathbf{R}_{\hat{\mathbf{x}}_{up},\hat{\mathbf{y}}_{up}} =&\, \hat{\mathbf{x}}_{up}(n_{up}) \star \hat{\mathbf{y}}_{up}(n_{up}) \\
=&\, \hat{\mathbf{x}}_{w}(n_{up}) * \mathbf{g}_{LPF}(n_{up}) * \hat{\mathbf{x}}_{w}^{*}(-n_{up}) * \mathbf{g}_{LPF}^{*}(-n_{up}) \\
&* \mathbf{h}_{up}^{*}(-n_{up}) * \mathbf{g}_{LPF}^{*}(-n_{up}) \\
=&\, \mathbf{R}_{\hat{\mathbf{x}}_{w}} * \mathbf{R}_{\mathbf{g}_{LPF}} * \mathbf{h}_{up}^{*}(-n_{up}) * \mathbf{g}_{LPF}^{*}(-n_{up})
\end{aligned}
\tag{4.13}
$$

As $\hat{\mathbf{x}}_{w}(n_{up})$ is white, its auto-correlation vector is

$$
\mathbf{R}_{\hat{\mathbf{x}}_{w}}(q) = \beta\delta(n_{up} - q)
\tag{4.14}
$$

where β is the sum of squares of $\hat{\mathbf{x}}_{w}(n_{up})$. Thus, (4.13) becomes

$$
\mathbf{R}_{\hat{\mathbf{x}}_{up},\hat{\mathbf{y}}_{up}}(q) = \beta\delta(n_{up} - q) * \mathbf{R}_{\mathbf{g}_{LPF}} * \mathbf{g}_{LPF}^{*}(-n_{up}) * \mathbf{h}_{up}^{*}(-n_{up})
\tag{4.15}
$$

As the impulse response of an ideal brick wall lowpass filter is a sinc function, its autocorrelation is thus also a sinc function of the same shape with a scaling factor. We can rewrite (4.15) into

$$
\begin{aligned}
\mathbf{R}_{\hat{\mathbf{x}}_{up},\hat{\mathbf{y}}_{up}}(q) &= \gamma\delta(n_{up} - q) * \mathbf{g}_{LPF}^{*}(-n_{up}) * \mathbf{h}_{up}^{*}(-n_{up}) \\
&= \gamma\mathbf{g}_{LPF}^{*}(-n_{up}) * \mathbf{h}_{up}^{*}(-n_{up} + q)
\end{aligned}
\tag{4.16}
$$

where γ is the multiplication results of β and the scaling factor. Substitute (4.7) into (4.16), with some tidying, we have

$$
\begin{aligned}
\mathbf{R}_{\hat{\mathbf{x}}_{up},\hat{\mathbf{y}}_{up}}(q) &= \gamma\mathbf{g}_{LPF}^{*}(-n_{up}) * [a\delta(-n_{up} + q + d_1) + b\delta(-n_{up} + q + d_2)] \\
&= a\gamma\mathbf{g}_{LPF}^{*}(-n_{up} + q + d_1) + b\gamma\mathbf{g}_{LPF}^{*}(-n_{up} + q + d_2)
\end{aligned}
\tag{4.17}
$$

The square magnitude of the cross-correlation function is thus

$$
\begin{aligned}
\left|\mathbf{R}_{\hat{\mathbf{x}}_{up},\hat{\mathbf{y}}_{up}}(q)\right|^{2} &= |a\gamma\mathbf{g}_{LPF}^{*}(-n_{up} + q + d_1) + b\gamma\mathbf{g}_{LPF}^{*}(-n_{up} + q + d_2)|^{2} \\
&= |a\gamma\mathbf{g}_{LPF}^{*}(-n_{up} + q + d_1)|^{2} + |b\gamma\mathbf{g}_{LPF}^{*}(-n_{up} + q + d_2)|^{2} \\
&\quad + 2\left|ab\gamma^{2}\mathbf{g}_{LPF}^{*}(-n_{up} + q + d_1)\mathbf{g}_{LPF}^{*}(-n_{up} + q + d_2)\right|cos\mathbf{\Phi}
\end{aligned}
\tag{4.18}
$$

where $\mathbf{\Phi} = \angle a + \angle\mathbf{g}_{LPF}^*(-n_{up} + q + d_1) - \angle b - \angle\mathbf{g}_{LPF}^*(-n_{up} + q + d_2)$.

When the reference signal is white, i.e. $\mathbf{R}_{\hat{\mathbf{x}}_{up}}(q) = \varepsilon\delta(n_{up} - q)$, $\mathbf{g}_{LPF}$ becomes δ. Therefore, the product term in 4.18 vanishes. Therefore, the peak magnitude of the cross-correlation vector is the larger component in the original impulse response of the system. In the case that the reference is not white at the high sampling frequency, the location of the peak magnitude of the cross-correlation depends not only the magnitude of each individual impulse, but also the phase difference and the locations of the two impulses. The later terms are difficult, if not impossible, to be determined. This is the reason why the delay estimation in Figure. 4.4 using up-sampled signals was not able to correctly determine the location of the larger impulse of the two-tap system. In the case that the actual impulse response of the system consists of more taps, the difficulty increases dramatically. As a result, the estimation system requires a much higher order. This, however, can be improved by using a modified version of the adaptive delay filter, which will be discussed in the next section.

4.4 Modified Adaptive Delay Filter using Direct Cross-correlation

The classic adaptive delay filter technique is suitable for a sparse system that doesn't consist of fractional delay components. As discussed in the earlier section, the classic adaptive delay filter is not suitable for estimating the delays of the duplexer due to the existence of non-integer delay components. Applying the classic adaptive delay filter with up-sampled signals is also not adequate, which has been discussed in the previous section. In order to use as few taps as possible, but at the same time, achieve a better performance, the modified adaptive delay filter using direct cross-correlation (MADF-DC) technique is proposed.

The estimation core of the MADF-DC method is shown in Figure. 4.5. This is extended based on the already published technique [67]. As the name suggests, this technique is the modified version of the classic adaptive delay filter and uses direct cross-correlation for estimating the delays. MADF-DC utilizes the sweeping of additional three parameters named as up-sampling ratios and maximum and minimum delay limit constraints in order to improve the delay estimation accuracy.

By given each fixed set of up-sampling ration and delay limit constraints, MADF estimates one delay each time and updates the weights of all the taps which have their delay estimated. Compared to C-ADF, the latter only update one each time. Additionally, MADF-DC uses the reference and leakage signals for all tap weight estimations. Compared to C-ADF, the latter uses the approximation error from the previous stage and only updates one weight each time.

Since the accuracy of the delay estimation depends on the sampling frequency, MADF-DC uses the up-sampled signals for estimating the system. The relationship between the up-sampling ratio and the cancellation performance is explored in this thesis by estimating the duplexer with different up-sampling ratio values. The one that gives the best cancellation performance is the chosen up-sampling ratio for implementation.

On the other hand, for an unknown system of which the impulse response consists of more than one fractional delay components, the accuracy of the delay estimation cannot be guaranteed by using the up-sampled signals. This has been discussed in the previous section. For this reason, we introduce two additional parameters so that a better estimation could be achieved. These two parameters are the minimum and maximum delay limit constraints, which are used for limiting the values of the estimated delays. The optimal values of these delay limits are to be determined by first running the estimation algorithm with different delay limit constraints. The delay limits that produce the best cancellation performance are the chosen ones for implementation.

The flow chart of the MADF-DC technique is shown in Figure. 4.6. In order to determine the values mentioned above, a vector of each of these three additional parameters (up-sampling ratios, maximum and minimum delay limits) needs to be provided. The MADF-DC estimation core in Figure. 4.6 refers to the estimation procedures that are shown in Figure. 4.5. The vectors are denoted as $\mathbf{K}$, $\mathbf{d}_{min}$ and $\mathbf{d}_{max}$ for the up-sampling ratio, minimum and maximum delay limits, respectively. The elements of these vectors are denoted as $K(p)$, $d_{min}(i)$ and $d_{max}(j)$, respectively, where $p = 1, 2, \ldots, P$, $i = 1, 2, \ldots, I$ and $j = 1, 2, \ldots, J$ are corresponding vector indexes. The lengths of $\mathbf{K}$, $\mathbf{d}_{min}$ and $\mathbf{d}_{max}$ vectors, are denoted as P, I and J, respectively.

The modelling error which is measured in terms of normalised mean square error (NMSE) with respect to the leakage signal for each configuration of these three
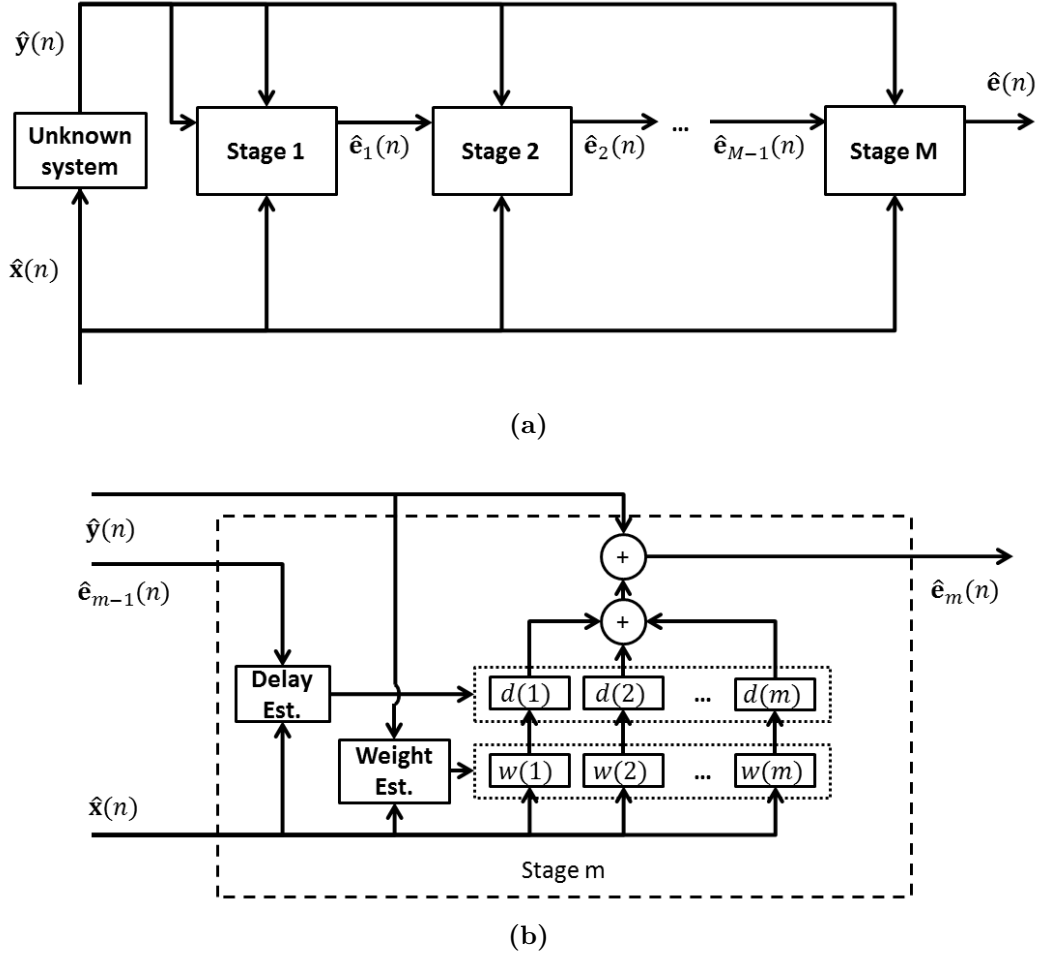
Figure 4.5: The structure of operation for MADF-DC method. (a) High level block diagram. (b)Block Diagram example of the mth stage

parameters is recorded. The set of the parameters at which the modelling error is minimized is chosen to be the one for the implementation of the leakage cancellation system. Adding delay limits is experimentally proven to be effective on the estimation of the leakage path compared to only using the up-sampled signals. The benefits of adding the delay limits can be seen from the simulated results in the later sub-sections. For each configuration of the three additional parameters, the operation of the technique is described as follows:

In each stage of MADF-DC, the delay is estimated by performing the cross-correlation between the up-sampled reference and the previous error signals. Let $\hat{\mathbf{x}}_{up}(n_{up})$ and $\hat{\mathbf{ep}}_{up}(n_{up})$ be the up-sampled reference and the previous error signals, respectively. This is shown in Figure. 4.5. In the case that the current stage is the first one, the
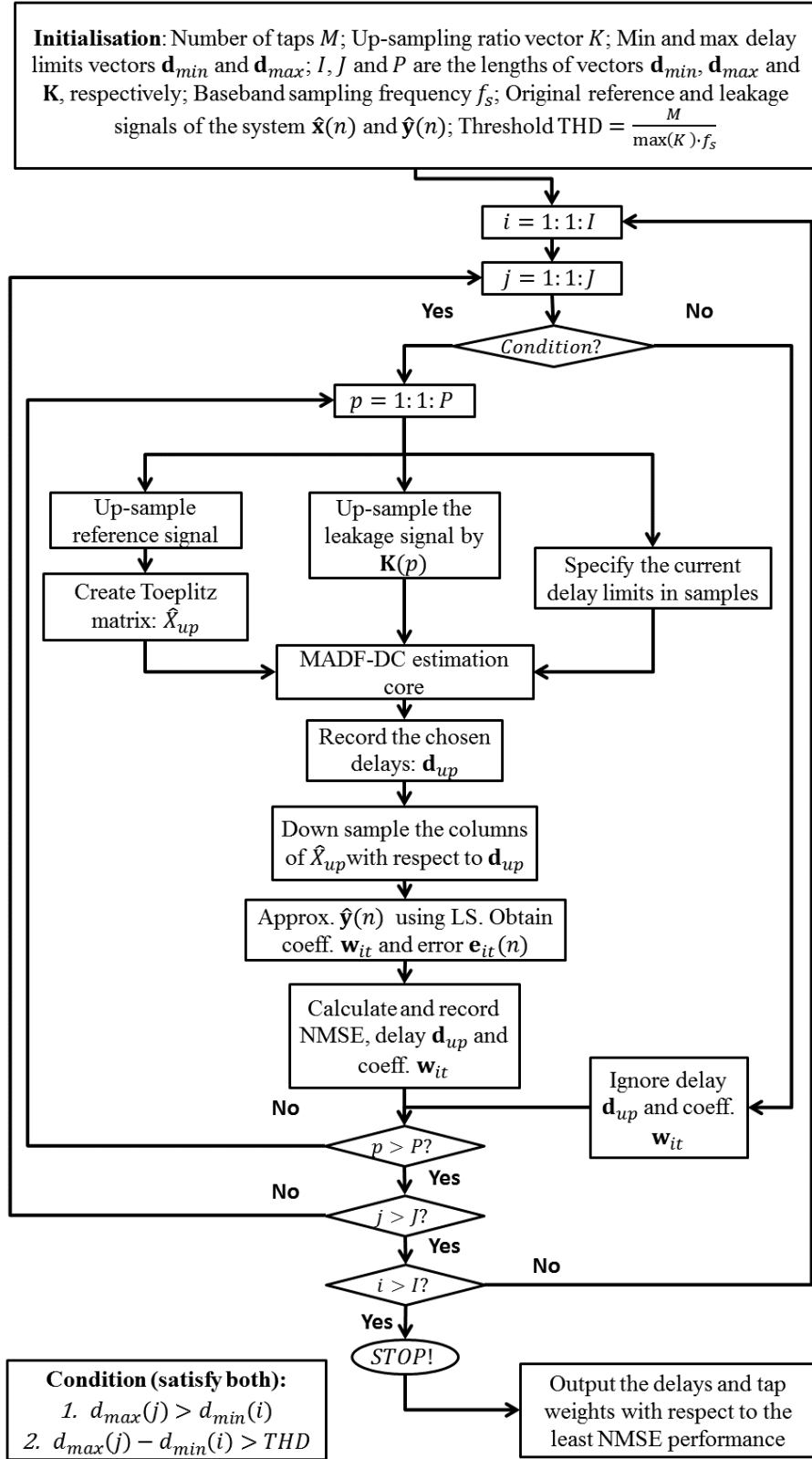
Figure 4.6: Flowchart of the MADF-DC technique

previous error signal is the original leakage signal.

Similar to (4.16), the cross-correlation function between the reference and previous error signals is

$$\mathbf{R}_{\hat{\mathbf{x}}_{up},\mathbf{e}\hat{\mathbf{p}}_{up}}(q) = \gamma \mathbf{g}^{*}_{LPF}(-n_{up}) * \mathbf{h}^{*}_{up}(-n_{up} + q) \tag{4.19}$$

where $\mathbf{h}_{up}(n_{up})$ is the ideal impulse response of the duplexer within the band of interest, at the high sampling frequency. The delay of the mth tap at the up-sampled sampling frequency can thus be estimated with

$$\hat{d}(m) = \arg\max_{q} \left(\left| \mathbf{R}_{\hat{\mathbf{x}}_{up},\mathbf{e}\hat{\mathbf{p}}_{up}}(q) \right| \right)$$

$$\text{subject to: } \hat{d}_{m} \neq d_{\bar{m}}$$

$$d_{min}(i) \leq \hat{d}(m) \leq d_{max}(j) \tag{4.20}$$

where $\hat{d}(\bar{m})$ is the estimated delay value of $\bar{m}^{th}$ tap and $\bar{m} = 1, 2, \ldots, m-1$.

The conditions in (4.20) are to ensure that the estimated delay of the current tap has not been obtained by the previous estimations and are within the range given by the minimum, $d_{min}(i)$, and the maximum, $d_{max}(j)$, values. The estimated delay of the current tap is abandoned as long as it falls outside the given delay range, regardless its magnitude. In the case that one or both of the conditions are not met, $\hat{d}(m)$ is set to the one that has the next largest absolute value of $\mathbf{R}_{\hat{\mathbf{x}}_{up},\mathbf{e}\hat{\mathbf{p}}_{up}}(q)$, until these conditions are fully satisfied.

Once the delay of one stage is estimated, the up-sampled input signal is duplicated with the number of completed estimation stages (shown in Figure. 4.5). Each duplicated and up-sampled input signal is delayed by one of the estimated delays and then down-sampled with the critical sampling frequency. An input matrix is created with these down-sampled duplicates. The coefficients of the taps of which the delays have been estimated can be updated using this input signal matrix and the leakage signal. Compared to the classic technique, MADF-DC updates all the weights of taps, of which the delays have been determined. By doing so, the estimation accuracy is improved. The coefficients of the taps are calculated using least squares (LS) algorithm. Let the input matrix for the estimated m taps be

$$\hat{X} = \left[\hat{\mathbf{x}}^{T}\left(n - d(1)\right), \hat{\mathbf{x}}^{T}\left(n - d(2)\right), \ldots, \hat{\mathbf{x}}^{T}\left(n - d(m)\right) \right] \tag{4.21}$$

where $\hat{\mathbf{x}}(n)$ is the critically sampled reference signal, $d(\tilde{m}) = \frac{\hat{d}(\tilde{m})}{K}$, is the estimated fractional delays of the previous m taps at the baseband and $\tilde{m} = 1, 2, \ldots, m$ is the index.

The weighting vector of those taps are obtained using the least square adaptive algorithm, so that

$$\mathbf{w} = \hat{X}^{-1}\hat{\mathbf{y}}^T(n) \tag{4.22}$$

where $\mathbf{w} = [w(1), w(2), \ldots, w(m)]^T$ is the weighting vector of the first m taps. The inverse of the matrix in this thesis is produced by using the Q-R decomposition technique. The error signal for estimating the delay of the next stage is updated by

$$\hat{\mathbf{e}}_{m+1}(n) = \hat{\mathbf{y}}(n) - \mathbf{w}^T\hat{X} \tag{4.23}$$

The new approximated signal is subtracted from the leakage signal in order to update the error signal for the delay estimation of the next tap. The full adaptation and estimation for one set of delay limits and up-sampling ratio are completed once all the stages have been processed. The same process is re-performed using the new set of delay limits and up-sampling ratio, until all the available additional parameters have been used. Before showing the simulated results by using MADF-DC, the general setup for the simulations is given first.

4.5 Simulation Setup

The parameters for the simulation setup are shown in Table. 4.1. The simulations are performed utilizing MATLAB. The TX signal at RF is white Gaussian noise. The leakage signal at RF is obtained by firstly transforming the time domain TX signal into frequency domain and then dot-multiplying with the S-parameters of the duplexers. The leakage signal in the frequency domain is then transformed back to the time domain.

The sampling frequency, f_s^{RF} is set to be very high in order to simulate the RF signals. In order to obtain the baseband time domain signals, TX and leakage

signals at RF are dot-multiplied with the local oscillator signal which is

$$LO = 2 \left[cos \left(2\pi f_c \frac{n}{f_s^{RF}} \right) - j sin(2\pi f_c \frac{n}{f_s^{RF}}) \right] \tag{4.24}$$

where $n = 1, 2, \ldots, N$ is the sample index and f_c is the centre frequency. An ideal lowpass filter is used in order to reject the out-of-band images. The bandwidth of the brick-wall filter is half of the bandwidth of the cancellation system. The filtered signals are then critically sampled with the baseband sampling frequency f_{sc}. At this point, the critically sampled TX signal and the leakage at the baseband are obtained.

Since MADF-DC uses cross-correlation for the delay estimation, the estimated delays could be negative values[2]. This could be due to the following reasons. Firstly, the MADF-DC technique is based on discrete signals and finite impulse response (FIR) structure, whereas the duplexer is a continuous time component and its impulse response is infinite (i.e., it is an IIR system). Therefore, when modelling the IIR system using the FIR structure, inherently negative group delay components are needed due to the feed-back path of the IIR system.

Secondly, due to the limited accuracy of the delay estimation, a larger number of taps is needed in order to approximate the unknown system. These taps are spread along both positive and negative delay axes. Negative group delay RF components have been reported in [84] [85] [86] [87]. However, since no negative group delays are available as off-the-shelf components, only positive delays are considered in this thesis. Discarding the negative delays creates a limitation of the cancellation performance. This is due to the reason that the impulses that are located in the negative delay locations can be difficult to be approximated by only using the positive delay impulses.

The vectors of the minimum and maximum delay limits are denoted as $\mathbf{d}_{min}$ and $\mathbf{d}_{max}$, respectively. The sweeping ranges of the delay limits for the circulator are given differently as the ones for the duplexers. The reason is that a more constant group delay response is expected for the circulator in comparison with the two duplexers. The largest group delay value within the band of interest for the circulator is also expected to be smaller than the duplexers. In order to show the importance

---

[2]The negative delays in this case are group delays. Pure negative delays are non-causal and cannot be realised by real components

Table 4.1: Parameters of simulation setup for MADF-DC

Symbol	Description	Circulator	Ceramic duplexer	Cavity duplexer
N	Number of samples of simulated RF signals	2097152		
$\mathbf{k}$	Vector of the system orders	2, 3, 4, 6, 8 and 14		
f_s^{RF}	Sampling frequency at RF (GHz)	40.96	17.92	
f_{sc}	Critical sampling frequency at baseband (MHz)	80	35	
f_c	The centre frequency of RF signals (MHz)	2600	897.5	
BW	Cancellation bandwidth (MHz)	80	35	
BW_{LPF}	Bandwidth of the baseband lowpass filter	40	17.5	
$\mathbf{K}$	Vector of up-sampling ratios	1 to 32 (in a step of 1), 64, 128, 256 and 512		
$\mathbf{d}_{min}$	Vector of the lower bound of the delay limit (ns)	0 to 10 (in the step of 0.5)	0 to 200 (in a step of 10)	
$\mathbf{d}_{max}$	Vector of the upper bound of the delay limit (ns)	0.4 to 10.4 (in the step of 0.5)	0.4 to 200.4 (in a step of 10)	
$\bar{d}_{min}$	Minimum delay value for unconstrained MADF-DC (ns)	0		
$\bar{d}_{max}$	Maximum delay value for unconstrained MADF-DC (ns)	500		

of the delay limit constraints for MADF-DC, simulations have also been performed when the delays that are bounded by $\bar{d}_{min}$ and $\bar{d}_{max}$. Since limiting the estimated delays by $\bar{d}_{max}$ hardly affects the achievable cancellation performance in all the simulations, the technique using these limits are named in the results as MADF-DC without constraints.

The terms: **modelling performance** and **cancellation performance**, in this dissertation, are different representations of the same thing, i.e. the performance of the modelling technique when solving the TX leakage problem. The cancellation performance (or modelling performance) is measured in terms of the normalised mean square error in log scale. That is

$$
\begin{aligned}
\mathbb{C} &= -NMSE_{dB} \\
&= -10log_{10}\left(\frac{\|\hat{\mathbf{e}}\left(n\right)\|^2}{\|\hat{\mathbf{y}}\left(n\right)\|^2}\right)
\end{aligned}
\tag{4.25}
$$

Since $\hat{\mathbf{y}}\left(n\right)$ and $\hat{\mathbf{e}}\left(n\right)$ are critically sampled leakage before the cancellation and the error signals after the cancellation, respectively, we can rewrite the leakage in terms of an ideal impulse response $\hat{\mathbf{h}}(n)$ and the critically sampled TX signal at the baseband, $\hat{\mathbf{x}}(n)$ as

$$
\hat{\mathbf{y}}\left(n\right) = \hat{\mathbf{x}}(n) * \hat{\mathbf{h}}(n)
\tag{4.26}
$$

Let the impulse response of the cancellation system be $\tilde{\mathbf{h}}(n)$, we thus have

$$
\hat{\mathbf{e}}\left(n\right) = \hat{\mathbf{x}}(n) * \left(\hat{\mathbf{h}}(n) - \tilde{\mathbf{h}}(n)\right)
\tag{4.27}
$$

Note that $\tilde{\mathbf{h}}(n)$ is different from $\mathbf{w}$, since $\mathbf{w}$ is the tap weight vector for the impulses at fractional sample locations with respect to the critical sampling frequency. In fact, $\tilde{\mathbf{h}}(n)$ is the resulting impulse response of $\mathbf{w}$ at critical sampling frequency, i.e.

$$
\tilde{\mathbf{h}}(n) = \mathbf{w} * \mathbf{g}_{LPF}
\tag{4.28}
$$

where $\mathbf{g}_{LPF}$ is the impulse response of the ideal lowpass filter.

Substitute 4.26 and 4.27 into 4.25, we have

$$
\begin{aligned}
\mathbb{C} &= 10 log_{10} \left(\frac{\left\| \hat{\mathbf{h}}(n) \right\|^2}{\left\| \triangle \hat{\mathbf{h}}(n) \right\|^2} \right) \\
&= 20 log_{10} \left(\left\| \hat{\mathbf{h}}(n) \right\| \right) - 20 log_{10} \left(\left\| \triangle \hat{\mathbf{h}}(n) \right\| \right)
\end{aligned} \tag{4.29}
$$

where $\triangle \hat{\mathbf{h}}(n) = \hat{\mathbf{h}}(n) - \tilde{\mathbf{h}}(n)$ is the resulting impulse response after the cancellation and is the difference between the impulse responses of the leakage path and the cancellation system. From (4.29), it can be seen that the cancellation performance is the logarithm difference between the Euclidean norm of the impulse responses before and after the cancellation. The MADF-DC technique can provide a much higher modelling accuracy than the classic techniques. This will be shown in the following results sections.

4.6 Simulation Results

In order to show the performance of the proposed MADF-DC method, simulations have been performed using MATLAB with three types of duplexing devices: a cavity duplexer; a ceramic duplexer and a circulator. The models of these duplexing devices in the simulations are created using measured S-parameters. The frequency responses of these components are already shown in Figure. 2.18.

Simulations have been performed using MADF-DC both with and without limiting the estimated delays, providing all delays are positive values. Cancellation performance with different system orders and up-sampling ratios has been calculated. The cancellation performance with respect to the chosen parameters is shown for each system order. For comparison reasons, system estimation using the standard LS technique has also been performed. The simulation results using the circulator are shown first and then followed by the ones using the ceramic and cavity duplexers. For each duplexing device, the following results are shown:

- Cancellation performance with respect to the delay limits

- Cancellation performance with respect to the up-sampling ratio

- Comparison of the optimal cancellation performance

- Chosen parameters for the optimal performance

- Resulting spectrum

4.6.1 Circulator

Cancellation performance with respect to the delay limits   The isolation path of the circulator within the designated bandwidth tends to be flatter in the magnitude response and more linear in the phase response in comparison with the off-the-shelf duplexers. It can be expected that the number of taps that is needed to achieve a good cancellation performance for the circulator is small, i.e., M is small. The cancellation performance with respect to the minimum and maximum delay limits for the isolation path of the circulator is shown in Figure. 4.7. The blank areas in the figures represent that the simulation was not performed at the current setting. This could be due to the reason that the maximum delay $d_{max}(j)$ during the parameter sweeping is smaller than the minimum delay $d_{min}(i)$. Or the delay difference between the maximum and minimum limits cannot allocate the required number of taps at the current up-sampling rate. It can be seen that the delay limits have large impact on the simulated cancellation performance, especially when M is small. For $M = 2$, the resulting performance varies from less than 10 dB to about 40 dB at different max and min delay limits. In comparison, for a larger order, e.g. $M = 8$, the resulting performance only changes slightly with respect to the maximum and minimum delay limits.

On the other hand, the delay limiting parameters affect the achieved cancellation performance less significantly when the number of taps increases. This is due to the reason that the circulator has relatively simpler characteristics than the off-the-shelf duplexers. The characteristics of the circulator have been shown in Figure. 2.18. With a large number of taps, the inaccuracy of the delays is compensated by the additional taps. The simulation results which will be shown later in this section.

Cancellation performance with respect to the up-sampling ratio   The cancellation performance with respect to the up-sampling ratio has been presented in Figure. 4.8. For a larger system order, there is no corresponding cancellation performance shown at the lower up-sampling ratio region. This indicates that these

Figure 4.7: Cancellation performance using MADF-DC with respect of delay limit constraints for the circulator. (a) Two taps. (b) Three taps. (c) Four taps. (d) Six taps. (e) Eight taps. (f) Fourteen taps.

up-sampling ratios are invalid since it is not possible to allocate these taps within any given delay limits at these up-sampling ratios.

The largest up-sampling ratio is chosen to be 512 for MADF-DC. This value could be further increased to provide a higher accuracy at a cost of computation time. The cancellation performance achieved using the maximum up-sampling ratio may not be the highest, e.g., in the 2-tap case. However, the difference between the performance achieved using 512 and the peak performance is insignificant. This may suggest that in order to cancel the leakage using MADF-DC for the circulator, it is sufficient to provide a single up-sampling ratio that is large enough, without degrading the cancellation performance significantly. This value might not be as large as 512. It can be seen in the figure that the cancellation performance achieved changes unnoticeably after the up-sampling ratio is greater than a value. This value depends on the order of the cancellation system as well as the characteristics of the duplexing device. From the evidence shown for the circulator, the cancellation performance is not affected significantly once the up-sampling ratio is greater than 24 for the simple structure of a circulator.

Using a large single value as the up-sampling ratio instead of sweeping could reduce the computation time significantly, which will be discussed in Sec. 4.8.2. However, in the case that the modelling accuracy is more critical than the estimation time, sweeping through the up-sampling ratio could still be a better option since a better modelling performance can be achieved. This can be seen from the simulated result of two taps.

Comparison of the optimal cancellation performance It can be difficult to observe exactly the peak cancellation performance that MADF-DC can achieve for the circulator in Figure. 4.7 and Figure. 4.8. This can be seen more clearly in the summarised peak cancellation performance with respect to the number of taps in Figure. 4.9. For comparison purposes, MADF-DC without constraints, classic LS and C-ADF techniques are also included in the results. C-ADF could achieve the same level of cancellation as the LS technique. This shows the estimated impulse response of the circulator at the critical sampling frequency is non-sparse, though ideally the impulse response is sparse. It indicates that the delay estimation accuracy of the C-ADF technique is not high enough for the TX leakage cancellation system. This has been discussed previously in this chapter.
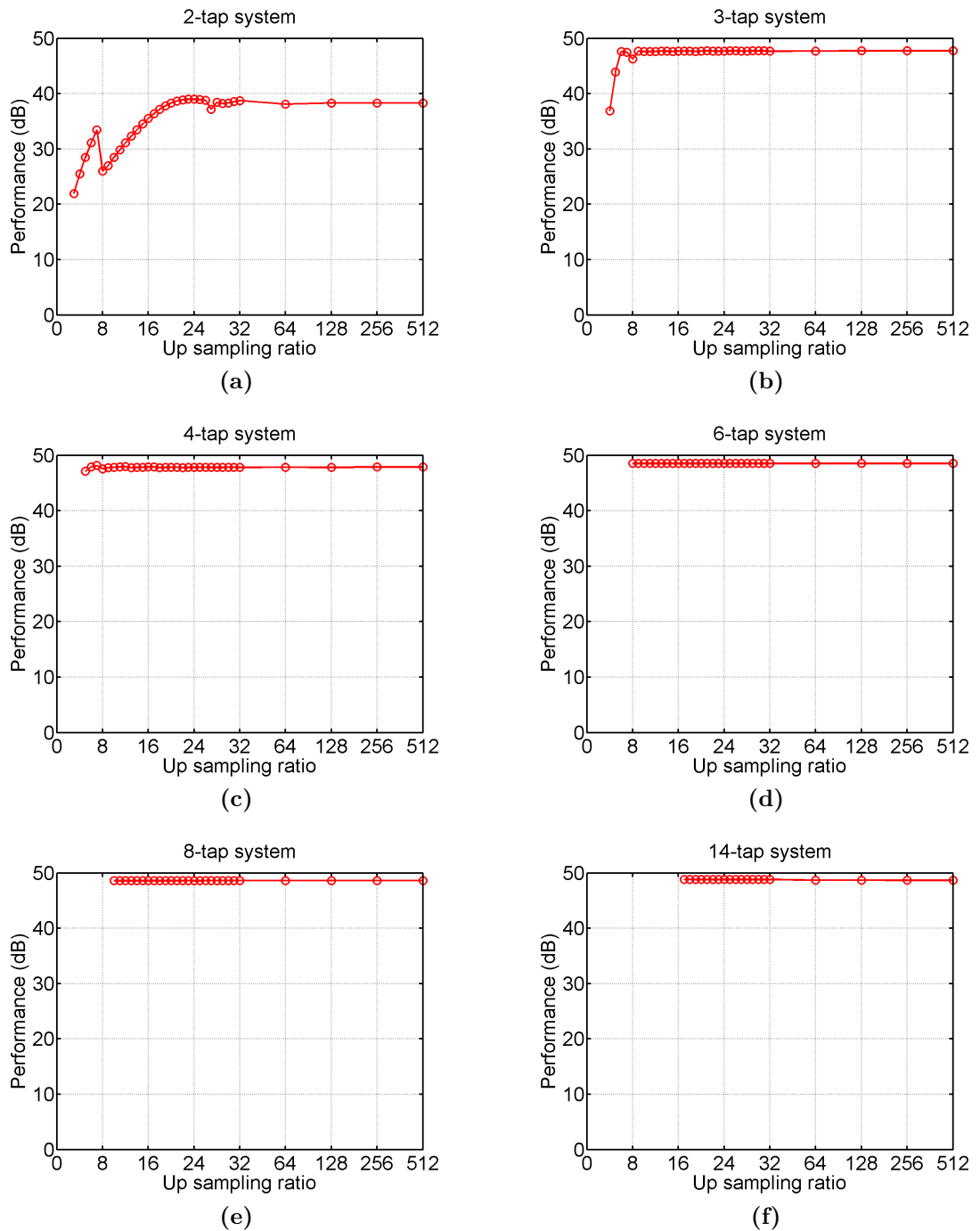
Figure 4.8: Cancellation performance using MADF-DC with respect of the up-sampling ratio for the circulator. (a) Two taps. (b) Three taps. (c) Four taps. (d) Six taps. (e) Eight taps. (f) Fourteen taps.
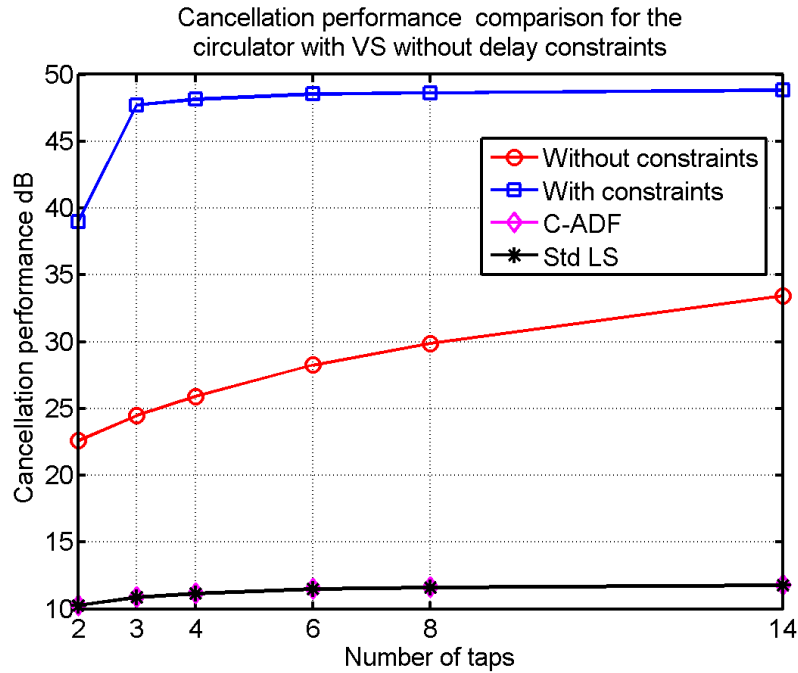
Figure 4.9: Cancellation performance comparison between with and without delay limit constraints for circulator using MADF-DC.

Compared to the unconstrained MADF-DC and LS techniques, a higher modelling accuracy for the circulator could be achieved by the constrained MADF-DC. With only three taps, MADF-DC with delay limits can reach approximately 47 dB of cancellation. The highest cancellation performance of all the simulated results is about 48 dB. In comparison, with three taps, MADF-DC without constricting the delays can only achieve approximately 24 dB of cancellation. In terms of the maximum cancellation performance, the MADF-DC without restricting the delays achieves roughly 33 dB with 14 taps. On the other hand, the LS technique only manages to cancel up to 14 dB of leakage with 14 taps. This performance inevitably reduces with a smaller number of taps.

It can be noted that there are performance bottle-necks for both MADF-DC and the LS techniques. Once the order of the system is greater than a certain value (e.g. three for constrained MADF-DC), the cancellation performance doesn't significantly increase any longer. This could indicate that the performance limitation is reached when modelling an IIR system using an FIR structure since the tap weights are only placed at positive side of the digital domain. This has been discussed in Sec. 4.5.

Additionally, as mentioned in Sec. 4.3.1 and Sec. 4.3.2, the error of the estimated

delays could degrade the modelling performance. Hence, the cancellation system could need a larger number of taps to achieve a desired performance. Though the simple characteristics of the isolation path of the circulator indicate that the actual impulse response of the system may only consist of a few taps, the locations of these taps can still be very difficult to determine. This is because of the loss of the information during the down-sampling. MADF-DC with additional delay limit constraints increases such accuracy, but is still far from optimum. More challengingly, as the cancellation performance increases, the number of the dominant components in the remaining impulse response is reduced. Therefore, a larger number of taps is required in order to achieve a small additional performance improvement.

Chosen parameters for the optimal performance The simulated cancellation performance is shown in Table. 4.2. This table shows the optimal modelling performance using MADF-DC for the circulator and the corresponding up-sampling ratio, and delay limit constraints. The corresponding up-sampling ratios and delay limits are also included. In the case of using tunable delay lines for the cancellation system with six taps, 24.4 ps of delay resolution is required. Achieving such high resolution can be difficult, but it is still possible since the required maximum tuning range of these delays is about 3.4 ns. In [88], a tunable delay line concept with 10 ps resolution has been presented though with a smaller tuning range. In the case where a larger tuning range is needed, such high delay resolution might not be feasible due to the impractical physical size.

Table 4.2: The summarised cancellation performance that is achieved using MADF-DC with corresponding delay limit constraints and up-sampling ratios for the circulator.

No. of taps	Min. delay limit (ns)	Max. delay limit (ns)	Can. perf. (dB)	Upsamp. ratio
2	0	1.4	38.98	24
3	0	4.9	47.73	26
4	0	9.4	48.15	7
6	3	3.4	48.54	512
8	8.5	10.4	48.62	64
14	0	9.9	48.84	18

Spectrum results   The resulting magnitude responses using the classic LS, C-ADF and the proposed MADF-DC techniques are shown in Figure. 4.10. As expected, the proposed MADF-DC technique with delay limit constraints outperforms the other techniques for any values of M. As expected, the resulting spectrum using C-ADF is similar to the LS technique. For any value of M, apart from $M = 2$, the leakage suppression using MADF-DC is uniformly across the whole frequency band. Poorer performance when $M = 2$ indicates that the order of the actual system is greater than two. In contrast, the classic techniques are more focused in the centre of the frequency band.

4.6.2 Ceramic Duplexer

The typical characteristics of a ceramic duplexer have been shown in Figure. 2.18.

Cancellation performance with respect to the delay limits   In terms of magnitude, group delay and phase responses, the isolation path of the ceramic duplexer is more complex than the one of the circulator. A lower cancellation performance can be expected for this duplexer with the same number of taps compared to the one for the circulator. The cancellation performance with respect to the delay limit constraints for the ceramic duplexer is shown in Figure. 4.11. The cancellation performance depends on the given delay limits and increases with the number of taps.

Cancellation performance with respect to the up-sampling ratio   The relationship between the cancellation performance and the up-sampling ratio for the ceramic duplexer is shown in Figure. 4.12. In the case that the number of taps is greater than six, only a few up-sampling ratios are invalid, i.e. no performance is recorded. This is mainly due to the reason that for a smaller up-sampling ratio value with a larger number of taps, the difference between the maximum and minimum delay limits needs to be greater to allocate all these taps. The delay limit constraints for the ceramic duplexer are swept across a wider range when being compared with the circulator case. As a result, a valid cancellation performance is recorded for the ceramic duplexer.
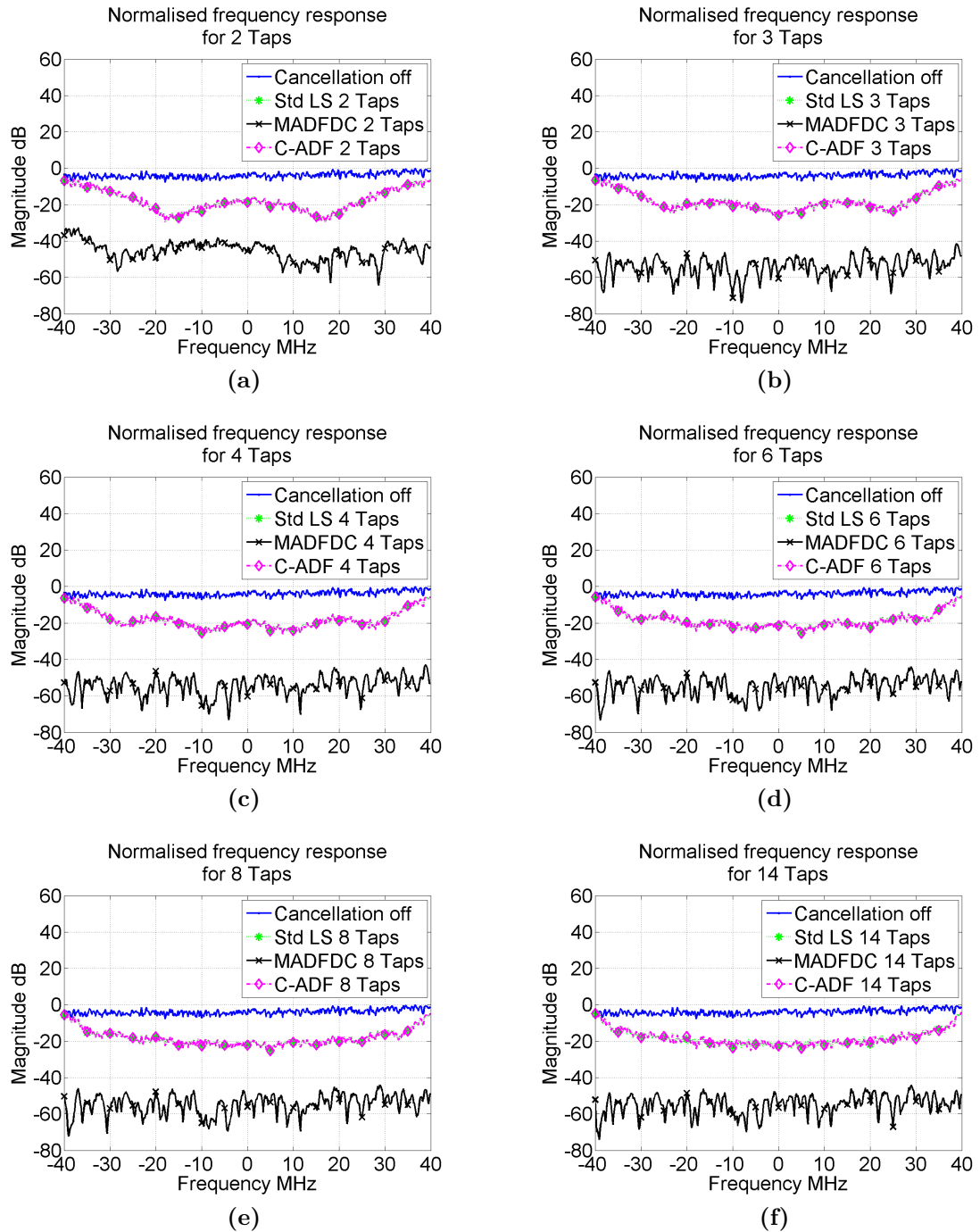
Figure 4.10: Normalised frequency response of the leakage, with and without the cancellation system using MADF-DC for the circulator . (a) Two taps. (b) Three taps. (c) Four taps. (d) Six taps. (e) Eight taps. (f) Fourteen taps.

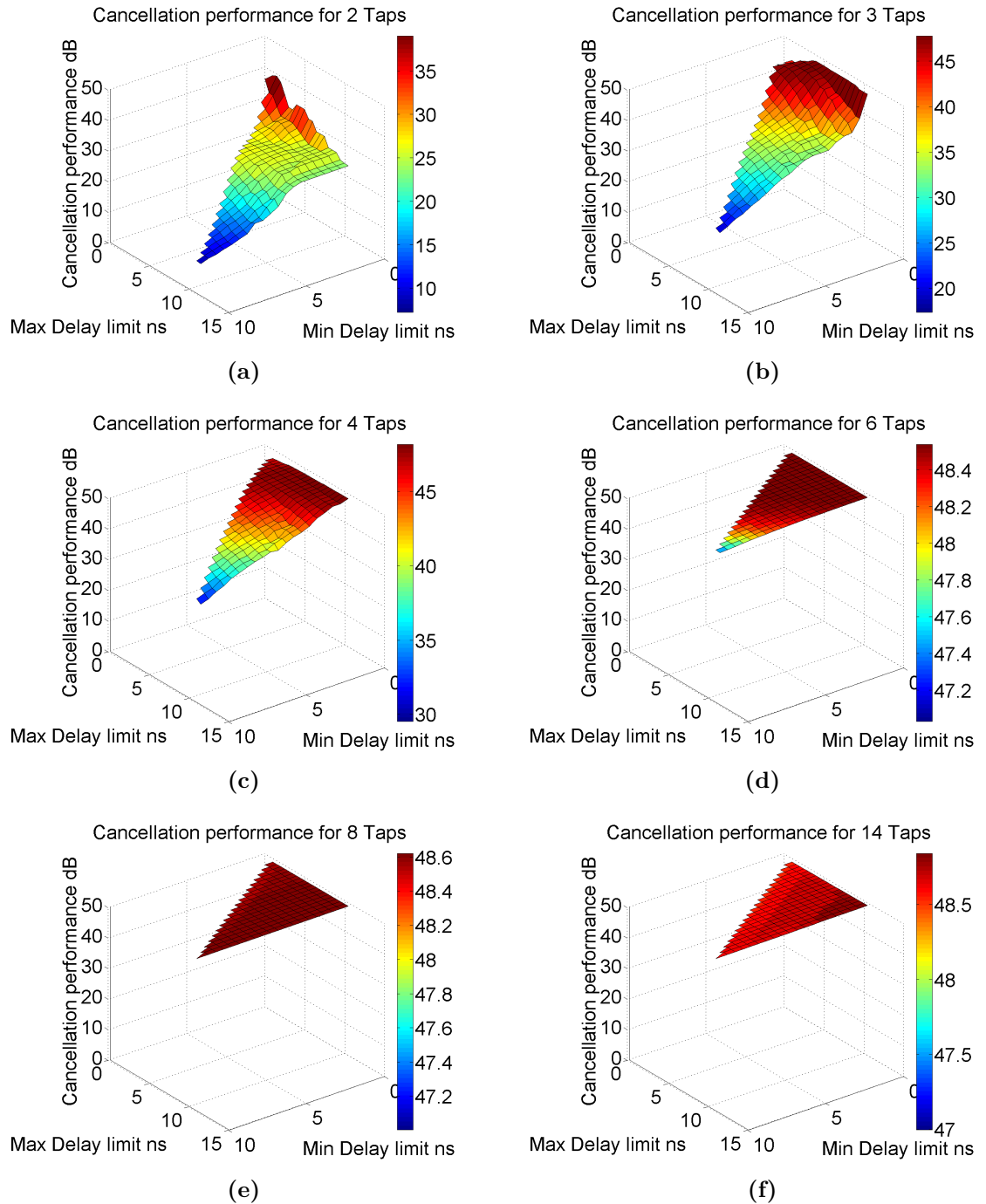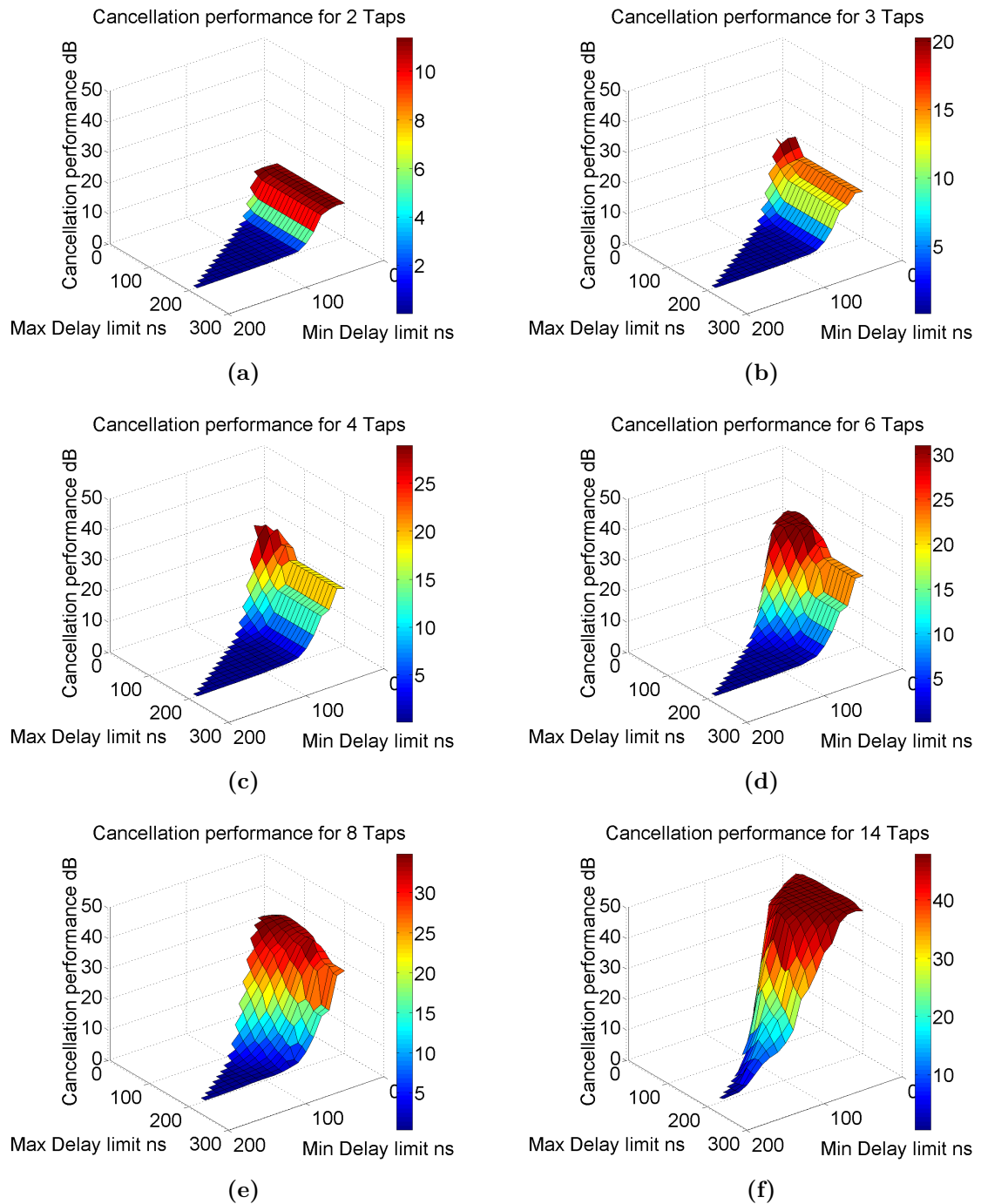**Figure 4.11:** Cancellation performance using MADF-DC with respect of delay limit constraints for the ceramic duplexer. (a) Two taps. (b) Three taps. (c) Four taps. (d) Six taps. (e) Eight taps. (f) Fourteen taps.
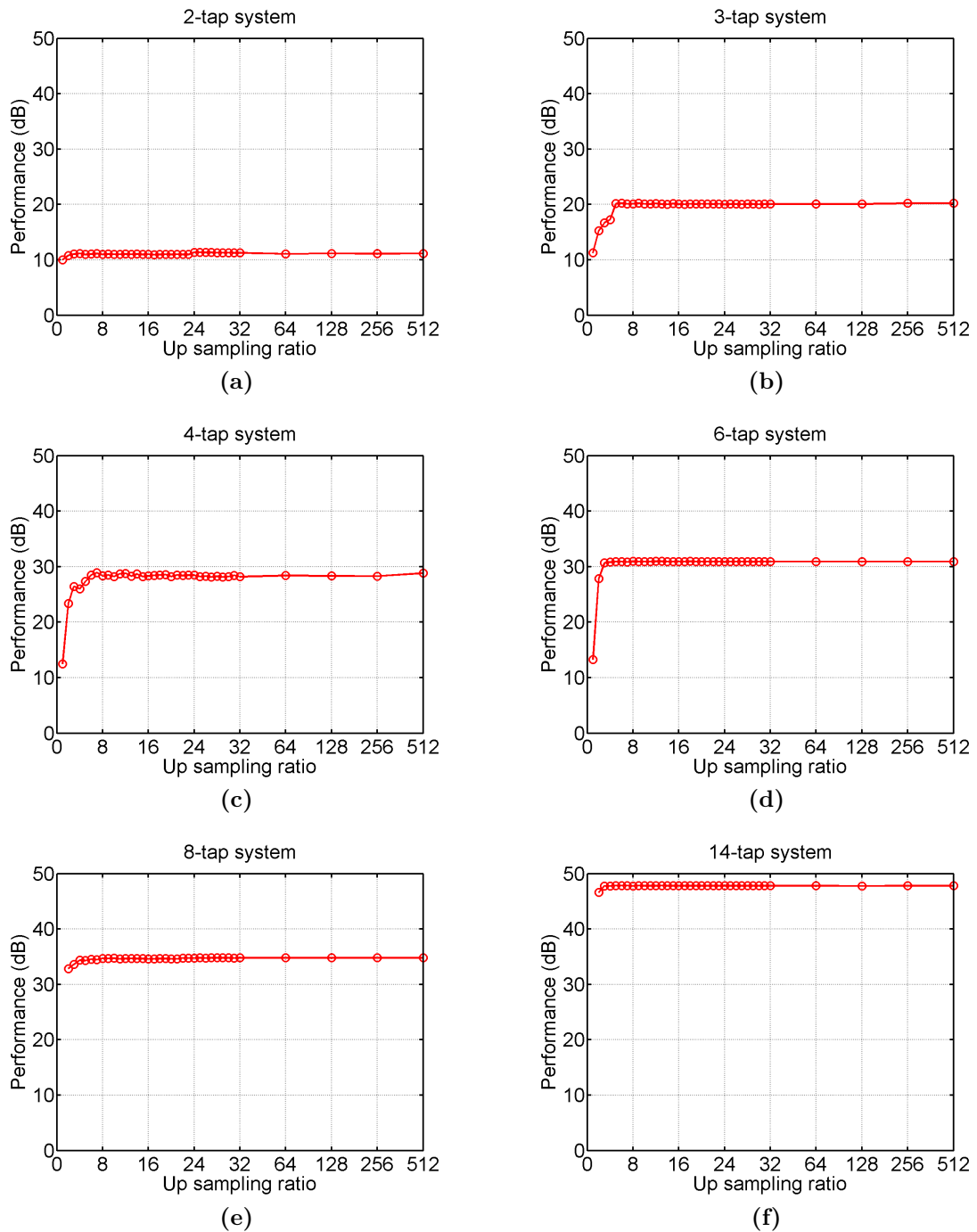
Figure 4.12: Cancellation performance using MADF-DC with respect of the up-sampling ratio for the ceramic duplexer. (a) Two taps. (b) Three taps. (c) Four taps. (d) Six taps. (e) Eight taps. (f) Fourteen taps.

For the ceramic duplexer, the advantage of sweeping the up-sampling ratio is not significant compared to using a single large up-sampling ratio. In the ceramic duplexer case, the threshold value for the up-sampling ratio being considered as large enough is about 8. This is due to the fact that for all the system order settings, the performance changes little once the up-sampling ratio is greater than this value. In the four-tap case, the peak cancellation has been recorded when the up-sampling ratio is approximately seven. However, the performance difference between the up-sampling ratio of 7 and 512 is insignificant. This is similar to what has been observed in the circulator case.

Comparison of the optimal cancellation performance   The summarised peak cancellation performance with respect to the number of taps is shown in Figure. 4.13. The MADF-DC with delay limit constraints out-performs the other three techniques. The best cancellation achieved is approximately 47 dB with 14 taps, which is more than 10 dB better than the same technique without the additional delay limiting parameters. It is also approximately 30 dB better than the standard LS technique. Once again, C-ADF performs similarly to the LS technique.

The cancellation performance of MADF-DC both with and without limiting the delays increases when the number of taps is increased. In comparison, the standard LS technique doesn't provide any better cancellation once the number of taps is greater than six. The reason of the poor cancellation performance from LS has already been discussed in the previous subsection. All three techniques manage to cancel more than 10 dB of leakage with only two taps. MADF-DC technique achieves approximately 1 dB better performance than the standard LS technique for two taps. With only four taps, approximately 30 dB of additional isolation between TX and RX has been provided by using the MADF-DC with delay limit constraints, whereas only 20 dB has been achieved using non-constrained MADF-DC. In general, MADF-DC with constraints can provide at least 5 dB more cancellation than the other two techniques. Overall, the cancellation performance that MADF-DC has achieved on the ceramic duplexer is less than the one on the circulator, which is as expected.

Chosen parameters for the optimal performance   More detailed cancellation performance with corresponding delay limits and up-sampling ratios are shown in
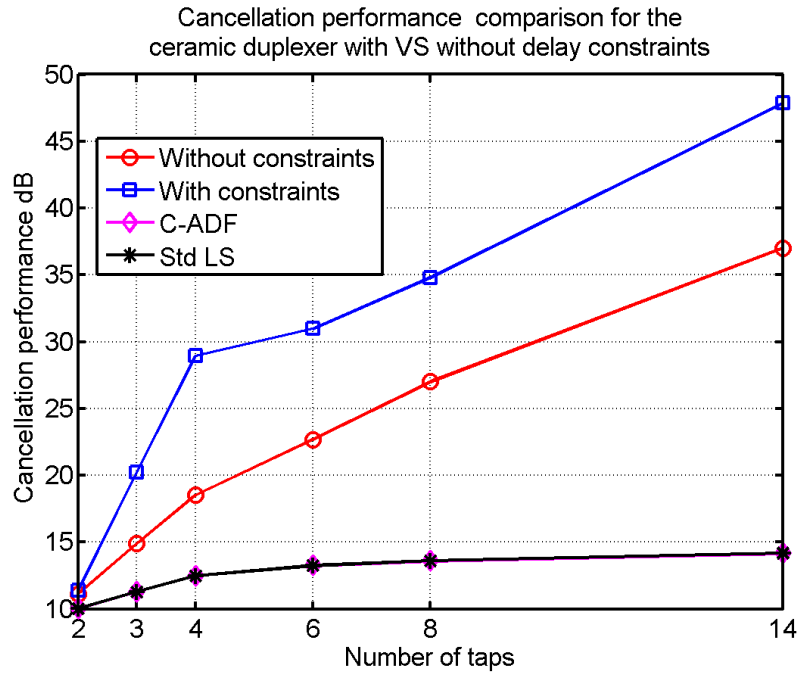
Figure 4.13: Cancellation performance comparison between with and without delay limit constraints for the ceramic duplexer using MADF-DC.

Table 4.3: The summarised cancellation performance that is achieved using MADF-DC with corresponding delay limit constraints and up-sampling ratios for the ceramic duplexer.

No. of taps	Min. delay limit (ns)	Max. delay limit (ns)	Can. perf. (dB)	Upsamp. ratio
2	20	30.4	11.38	24
3	20	20.4	20.23	512
4	20	40.4	28.92	7
6	0	40.4	30.97	8
8	30	40.4	34.8	64
14	0	160.4	47.85	5

Table. 4.3. With three taps, the estimated delays are within the range between 20 ns and 20.4 ns at the up-sampling ratio of 512. This indicates that a delay resolution of 55.8 ps[3] is required if the tunable delay lines are used. Though such delay resolution requirement is less strict than the six taps case for the circulator, the difficulty is not reduced. This is because that a larger delay sweeping range, i.e. 20.4 ns is needed in comparison with 3.4 ns in the circulator case. The rest of M settings require an up-sampling ratio that is less than 64. It is equivalent to tuning the delay components in a step of more than 446 ps, approximately. The larger the tuning step is required, the less resolution of the tunable delay lines is needed. Using fourteen taps achieves good cancellation and the required tuning resolution of the delays is only 5.7 ns. However, the cost of such high cancellation performance is that the maximum delay is over 160 ns. The value of a delay line is proportional to the length of the line. A large delay value indicates that a greater board area could be occupied. Though large group delay lines on chips are commercially available, these delay lines with larger delay values are usually made with high dielectric constant materials in order to reduce the physical size. The use of these high dielectric constant material results in the increase of the insertion loss of these delay lines. The deployment of these delay lines with large insertion losses might result in the need of active components when implementing the cancellation system. This will be discussed in more detail in Sec. 4.7.

Spectrum results The resulting magnitude responses using LS, C-ADF and MADF-DC with additional delay constraints are shown in Figure. 4.14. The proposed MADF-DC outperforms the classic techniques for most of the M settings except for two taps. For two taps, the result shows a very similar performance between the three techniques. At certain frequencies, the LS technique is better than the proposed technique, especially around the centre frequencies. On the other hand, the MADF-DC provides better leakage cancellation at the frequencies that are close to the edge of the band. There is an insignificant difference between the resulting spectrum using C-ADF and LS for all tap configurations.

---

[3]This is the time calculated using the bandwdith of the cancellation, 35 MHz multiply by 512

Figure 4.14: Normalised frequency response of the leakage, with and without the cancellation system using MADF-DC for the ceramic duplexer . (a) Two taps. (b) Three taps. (c) Four taps. (d) Six taps. (e) Eight taps. (f) Fourteen taps.

4.6.3 Cavity Duplexer

In Figure. 2.18, the measured characteristics of a typical cavity duplexer have been shown. Since the characteristics of the cavity duplexer are much more complex than that of the circulator and ceramic duplexer, it can be expected that the resulting cancellation performance would be reduced.

Cancellation performance with respect to the delay limits A set of results are shown in Figure. 4.15, from which the relationship between the resulting cancellation performance and the delay limits can be observed. Similar to the previous results, the delay limits have significant impact on the cancellation performance which experimentally proves that such additional parameters are essential for the proposed estimation technique.

Cancellation performance with respect to the up-sampling ratio The cancellation performance and the corresponding up-sampling ratio for the cavity duplexer are shown in Figure. 4.16. According to the results, a value of the up-sampling ratio that is greater than approximately eight can be considered large enough. The results also show that for MADF-DC technique, there are insignificant advantages by sweeping the up-sampling ratio compared to using only a single large value. By observing the results of all three duplexing devices, it may suggest that for MADF-DC technique, choosing a large up-sampling ratio could be more beneficial than sweeping through the vector, due to the significant reduction in estimation time.

Till now, it seems sweeping the up-sampling ratio is redundant because using a single large up-sampling ratio achieves almost the same cancellation performance. This has been seen for all three duplexing devices. However, since the author of this thesis can't provide any mathematical proof showing the above observation is always true, sweeping the up-sampling ratio is recommended in the case that modelling accuracy is more critical than the estimation time.
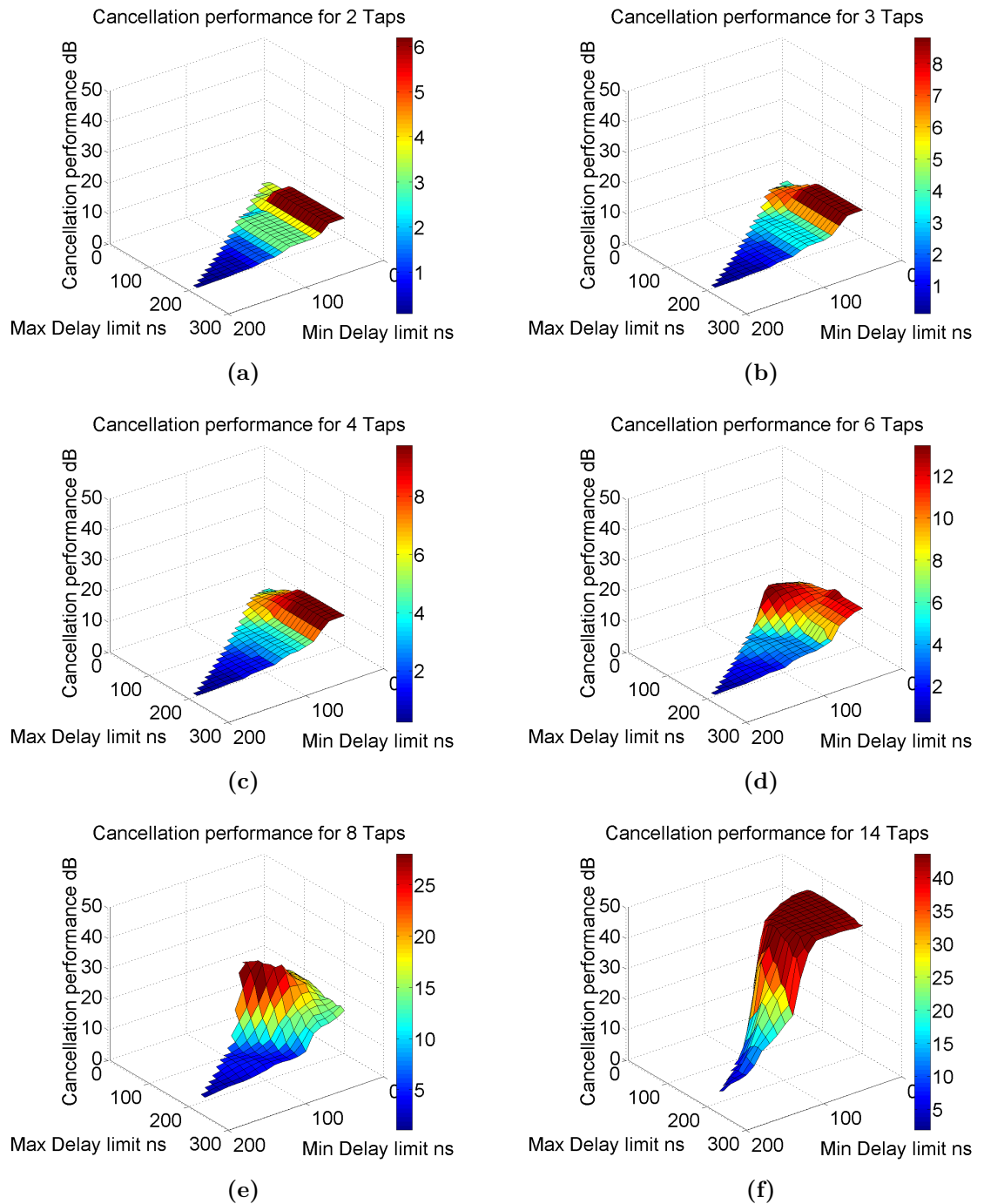
Figure 4.15: Cancellation performance using MADF-DC with respect of delay limit constraints for the cavity duplexer. (a) Two taps. (b) Three taps. (c) Four taps. (d) Six taps. (e) Eight taps. (f) Fourteen taps.
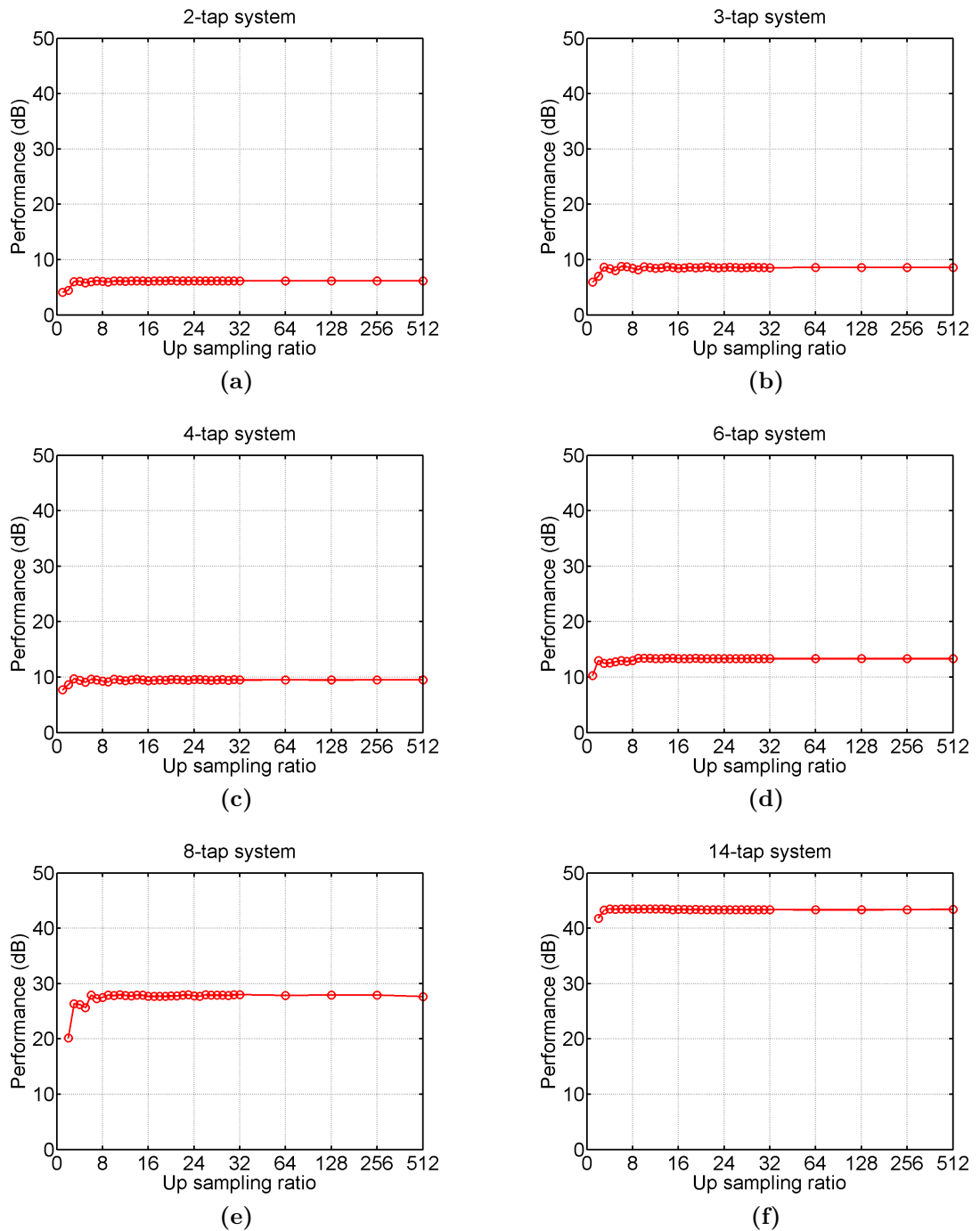
Figure 4.16: Cancellation performance using MADF-DC with respect of the up-sampling ratio for the cavity duplexer. (a) Two taps. (b) Three taps. (c) Four taps. (d) Six taps. (e) Eight taps. (f) Fourteen taps.

Comparison of the optimal cancellation performance The summarised cancellation performance of MADF-DC for the cavity duplexer with respect to the number of taps is shown in Figure. 4.17. With a smaller number of taps, i.e., less than four taps, MADF-DC with and without limiting the delays are the same in the cancellation performance. When M is greater than six, the advantages of limiting the delays can be seen more clearly. MADF-DC with delay limits achieve about 20 dB and 44 dB of cancellation with eight and fourteen taps, respectively. These performances using eight and fourteen taps are at least 10 dB and 20 dB more than the corresponding ones without limiting the delays, respectively. In contrast, the standard LS technique only achieves maximally 12 dB with fourteen taps. This result is very similar to the ones that are shown for the other two duplexing devices. When more than three taps are used, C-ADF could achieve the same performance as LS. For two and three taps, simulation results show that a better performance could be achieved by using C-ADF than LS. However, the improvement is only about 1 dB. Compared to MADF-DC, the performance achieved using C-ADF is not as effective.
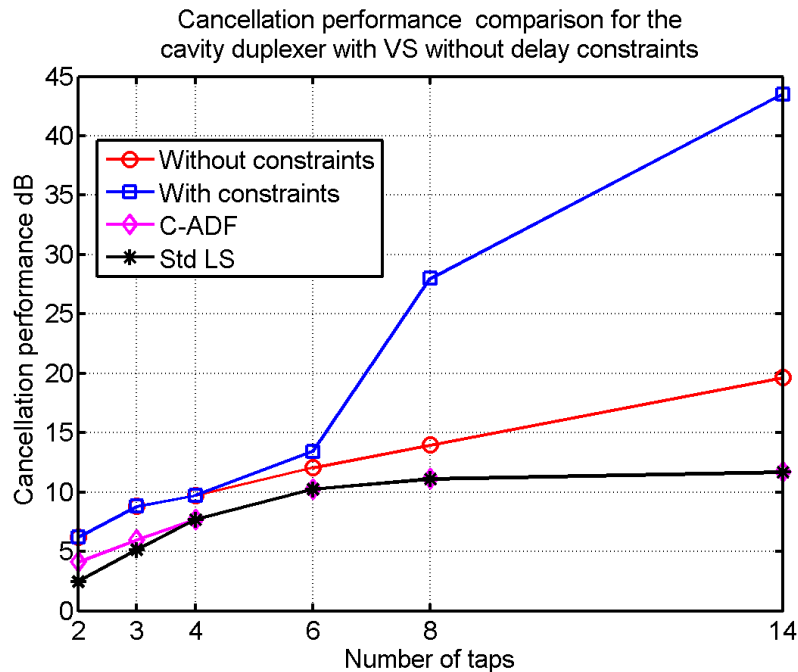
Figure 4.17: Best cancellation performance using MADF-DC for cavity duplexer with choices of taps, without limiting the estimated delays.. The bandwidth is 35 MHz and centred at 897 MHz.

Chosen parameters for the optimal performance In order to show the results in more detail, the delay limits and the up-sampling ratio at which the best cancellation performance have been obtained are shown in Table.4.4. For the cavity duplexer, the required delay resolutions are lower than the previous duplexer. The up-sampling ratio of 32 is needed for eight taps which is equivalent to the delay resolution of 0.893 ns for the bandwidth of 35 MHz. With less than 6 taps, MADF-DC with delay limits can only achieve up to approximately 13 dB of cancellation. Compared to the result achieved using the same technique for the ceramic duplexer, i.e., 30 dB for six taps, this value is significantly less. This is due to the more complex characteristics of the cavity duplexer which have been shown in Figure.2.18. However, more than 40 dB of additional isolation can be provided using MADF-DC with delay limits when fourteen taps are used for the cavity duplexer. Though it is still less than the result achieved using the same number of taps for the ceramic duplexer, the difference is only 3 dB, which is less significant. Using two taps, the proposed technique can provide approximately 6 dB of additional isolation for the cavity duplexer.

Table 4.4: The summarised cancellation performance that is achieved using MADF-DC with corresponding delay limit constraints and up-sampling ratios for the cavity duplexer.

No. of taps	Min. delay limit (ns)	Max. delay limit (ns)	Can. perf. (dB)	Upsamp. ratio
2	0	70.4	6.19	20
3	0	100.4	8.8	6
4	0	130.4	9.72	3
6	50	70.4	13.42	10
8	60	100.4	27.99	32
14	0	100.4	43.51	4

Spectrum results The magnitude responses of the leakage signals with different M settings before and after the cancellation have been shown in Figure.4.18. With less than eight taps, the resulting leakages using the MADF-DC and the other two techniques are very close. Only marginally better performance has been achieved by MADF-DC. Much more leakage signals have been suppressed using the MADF-

DC with eight and fourteen taps comparing to the classic technique, which show improved performance of the proposed MADF-DC technique with delay limit constraints.

Between C-ADF and LS, the resulting magnitude response is also the same when the order of the system is greater than three. This can also be observed in Figure. 4.17. Similar results are also observed for the circulator and ceramic duplexers which are shown in Figure. 4.10 and Figure. 4.14, respectively. The reason for such observations is that the isolation path of the duplexing device is non-sparse when using C-ADF and LS under the current sampling rate. This has been explained in Sec. 4.3.1, Sec. 4.3.2 and Sec. 4.6.1. The advantages of C-ADF over LS can be seen from the resulting magnitude response when the order of the system is less than four though the difference is not significant.

4.6.4 Summary of the Results

Simulation results of using MADF-DC have been shown for the three duplexing devices. Cancellation performance results with respect to the delay limit constraints and up-sampling ratios are presented in this section. The delay limit constraints are necessary in order to achieve a better cancellation performance. The sweeping of the two delay limit parameters is essential. The performance degradation and the estimation time regarding the sweeping of delay limit constraint vectors will be presented and discussed in Sec. 4.8.2.

The simulation results show that sweeping of the up-sampling ratio provides insignificant improvement of the cancellation performance, compared to using a single large up-sampling ratio value. However, sweeping should be chosen if the cancellation performance is more critical than the estimation time. In this thesis, the MADF-DC algorithm is performed by sweeping the up-sampling ratio if not explicitly stated otherwise. This is because in the proposed cancellation system, the modelling of the duplexer occurs when the transceiver is offline. In this case, the estimation time is less critical.

It has been shown that the constrained MADF-DC can provide a higher estimation accuracy for the devices with both simple and more complex characteristics. However, those results are ideal since few practical considerations are included in the
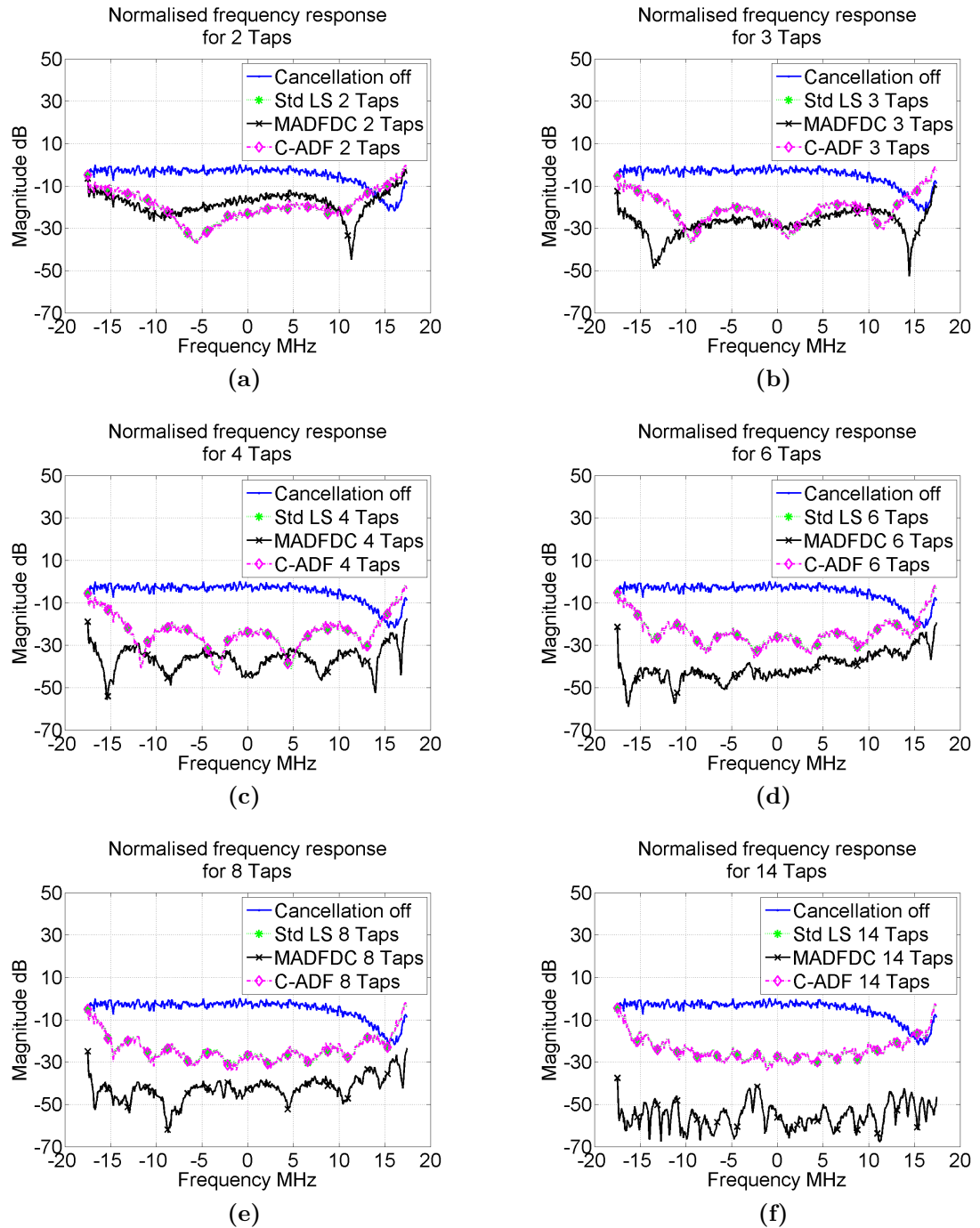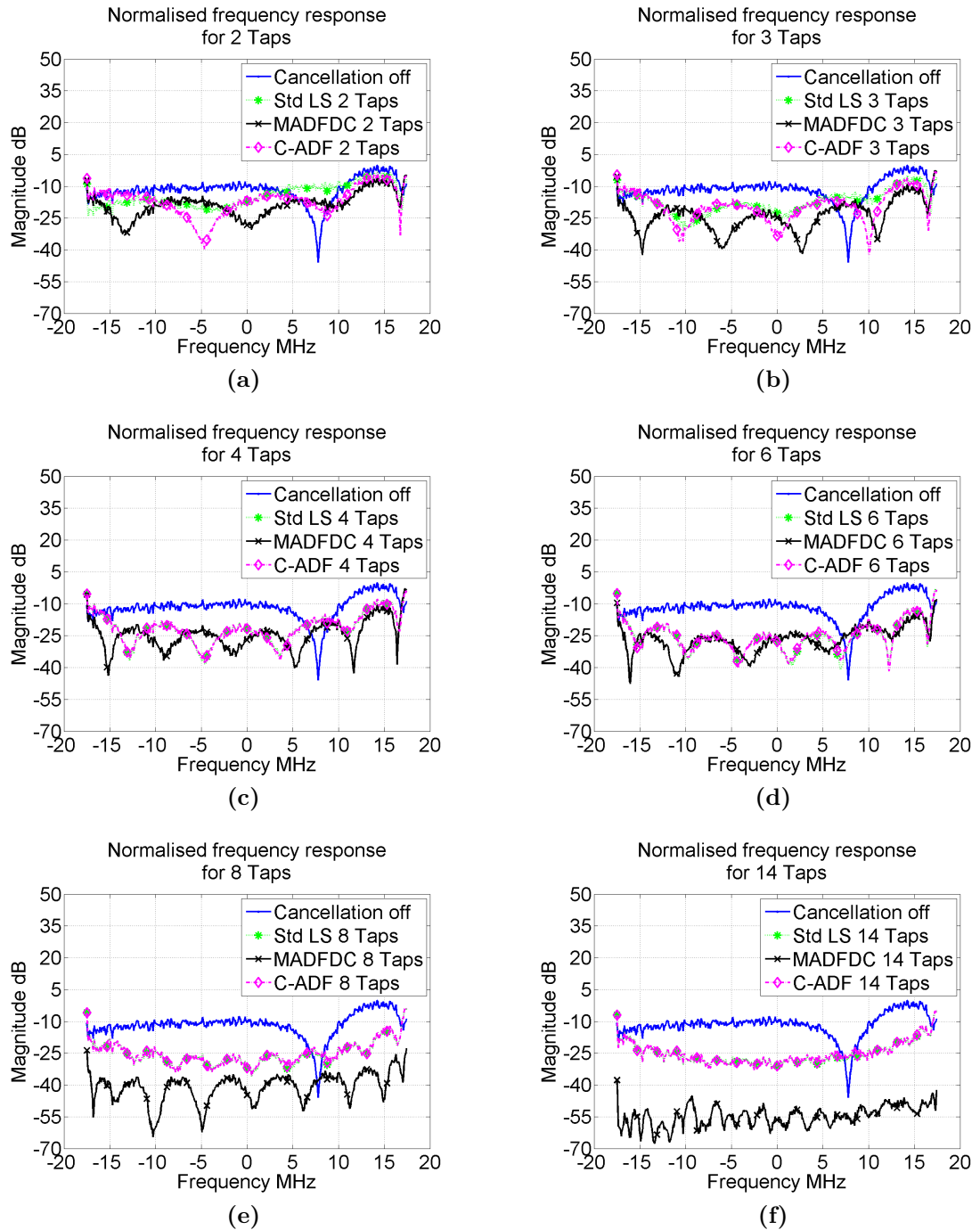
Figure 4.18: Normalised frequency response of the leakage, with and without the cancellation system using MADF-DC for the cavity duplexer . (a) Two taps. (b) Three taps. (c) Four taps. (d) Six taps. (e) Eight taps. (f) Fourteen taps.

simulations. In the following section, simulation results using only passive components will be shown.

4.7 Performance Using Only Passive Components

Since the proposed cancellation system operates at RF and is directly connected with RX front-end, any additional noise or distortions that are produced by the cancellation system will directly increase the noise floor of the receiver. This will result in the decrease of the receiver SNR. This is a potential problem not only for the proposed system architecture, but also for any RF cancellation system. Therefore, it is more desirable to use only passive components, e.g., no gain components, to avoid degrading the receiver performance. The trade-off of only using passive components is the reduction of the achievable cancellation performance. This will be explained in detail in this section.

In the previous simulation results, the insertion loss of all the components including the delays and phase shifters are not considered. This is not true in practice, especially for the delays. The insertion loss of the delay line is usually measured in the unit of dB/ns. It varies approximately from 0.1 dB/ns [89] to 1 dB/ns [90], depending on the material, design structure, operating frequency and bandwidth, etc.. Therefore, the larger the delay line is, the greater the insertion loss can be. In the ceramic duplexer simulation, the estimated delay can be as large as 160 ns. Even using delay lines with a unit loss of 0.1 dB/ns, the overall insertion loss is about 16 dB. Additionally, a voltage controlled attenuator usually has minimum attenuation value which means at least some power is lost in the attenuator. The rest of the components, e.g., power combiners, directional couplers, phase shifters all have insertion losses. Therefore, when implementing the cancellation system with the calculated attenuation level, the system may require one or more gain components which are undesirable.

To see if the cancellation system using MADF-DC can be implemented without gain blocks, simulations for each duplexing device have been performed with consideration of insertion losses of the RF components. In order to implement the cancellation system using only passive components, the calculated attenuation level of each tap must be greater than a certain value. Such minimum attenuation level can be found

from

$$IL_{min}^m = IL_{Fix}^m + IL_{del}^m \tag{4.30}$$

where the superscript $m = 1, 2, \ldots, M$ indicates the tap index, and IL_{del}^m is the insertion loss of the corresponding delay line. IL_{Fix}^m is the total insertion loss of other components of the mth tap, i.e.,

$$IL_{Fix}^m = \triangle IL_{CPL}^{TX} + \triangle IL_{CPL}^{RX} + IL_{Att}^m + IL_{PH}^m + IL_{SPL}^m + IL_{CMB}^m + IL_{misc}^m \tag{4.31}$$

where $\triangle IL_{CPL}^{TX}$ and $\triangle IL_{CPL}^{RX}$ are the insertion loss differences between the coupling and through ports of the directional couplers at the TX and RX paths respectively. IL_{Att}^m and IL_{PH}^m are the minimum insertion losses of the variable attenuator and the phase shifter in the corresponding cancellation path respectively. IL_{SPL}^m and IL_{CMB}^m are the insertion losses of each path of the splitter and combiner respectively, which depend on the total number of cancellation paths. IL_{misc}^m is the total power loss of other passive components such as cables and connectors in the mth cancellation path. There is an additional directional coupler in the proposed cancellation system shown in Figure. 3.1 which is for modelling purposes. Since the coupling factor of this coupler is high, i.e., 30 dB, the insertion loss of the through port of this coupler is negligible and, hence, is included in IL_{misc}^m.

In order to implement the cancellation system using only passive components, IL_{min}^m should be as low as possible so that the most optimal cancellation performance can be realized. Since IL_{Fix}^m is fixed as long as the components and the number of taps are chosen, the only variable is the insertion loss of the delays which indeed depends on the unit insertion loss and the time delay value of the corresponding delay lines. In order to show the significance of IL_{min}^m, further simulations have been performed for the three different duplexing devices.

4.7.1 Circulator

Simulation setup The simulations are performed based on the proposed system architecture that is shown in Figure. 3.1 with minor modifications. Since the delays of the circulator are known to be smaller than those of the other two duplexers (as

shown in Figure. 2.18), the impact of the passive implementation is mostly from the total insertion loss of the fixed components. For this reason, a coupler model with 7 dB coupling factor is used in order to redirect the TX signal to the canceller. As a result, the power of the TX signal is reduced by the insertion loss of 1 dB, approximately. Another modification from the proposed system architecture is that a two-way power combiner has been placed in the RX path in order to cancel the leakage. Within the RF canceller, a power splitter and a combiner are used in order to separate and recombine the reference signal. The power losses of each path of the power splitter and combiner are assumed to be the same as the theoretical values, i.e.,

$$
\begin{aligned}
IL^m_{SPL} &= IL^m_{CMB} \\
&= 20log_{10}M
\end{aligned}
\tag{4.32}
$$

The remaining insertion loss including the minimum power losses of the phase shifters and variable attenuators, but excluding the delays, is 7 dB.

Results   The optimal cancellation performance for the circulator is calculated under these conditions and summarised in Figure. 4.19. These results are obtained by collecting the best cancellation performance for each number of taps settings, providing that all calculated tap attenuation are greater than the corresponding required minimum attenuation level, IL^m_{min}. In order to show how the unit insertion loss affects the cancellation performance, a number of values have been chosen. They are 0.1 to 0.5 dB/ns in a step of 0.1 dB/ns. A large unit loss, i.e., 1 dB/ns, is also included in the simulations. These results are compared with the ones in which the gain blocks are allowed. Noted in Figure. 4.19, the performance using only passive components is not always available with respect to the number of taps. This indicates that it is not possible to implement the cancellation system by only using passive components. This is when the magnitude of the estimated tap weight is greater than the minimum attenuation level, IL^m_{min}.

Since the most optimal performance is obtained when active components are allowed, the performance using only passive components is expected to be equal or lower. This has been confirmed in Figure. 4.19. Also, since using delay lines with greater unit insertion loss can make the implementation (with passive components only) more difficult, it can be expected that the achievable cancellation performance will

decrease with the increase of the unit insertion loss. This can also be observed in Figure. 4.19.

It can be seen from the results that for the cancellation system with more than three taps, it is not possible to be implemented using only passive components under the current simulation setting. For cancellation systems with two and three taps, the best performance has also been degraded due to the added insertion losses of the simulation. The change of the unit insertion loss of the delay lines doesn't affect the cancellation performance significantly for the system using two taps. The system with two taps suffers with only 1 dB degradation using only passive components. In comparison, the three taps system performs worse when the unit insertion loss of the delays increases. The best leakage suppression using three taps is approximately 43 dB which is about 4 dB worse than the one without necessarily using passive components. In the case that the high unit insertion loss delay lines are used, the cancellation performance drops to about 33 dB from 48 dB.

4.7.2 Ceramic Duplexer

Setup In contrast to the circulator, the estimated delays using the proposed MADF-DC technique for the ceramic duplexer are much larger. As a result, the source of the cancellation performance degradation using only passive components is expected to be the unit insertion loss of the delays. The simulations are performed according to the proposed cancellation system architecture shown in Figure. 3.1. The coupler in the TX path of the simulation is replaced with a 10 dB one from which the insertion loss of the main TX path is reduced to about 0.5 dB, comparing to the setup for the circulator. The cancellation in the RX path is realised by using a 6 dB directional coupler. The insertion loss of the RX signal path is reduced to about 1 dB. The rest of the setup remains the same as the one in the circulator simulation.

Results According to the summarised cancellation performance figure (shown in Figure. 4.20) using only passive components, it is still not possible to implement such a system with fourteen taps. One of the reasons is that the estimated delays of one or more taps are large. This results in a large power loss just from the delay lines. This can be expected since as the way that the proposed optimization technique works is first to suppress the most significant components in the original
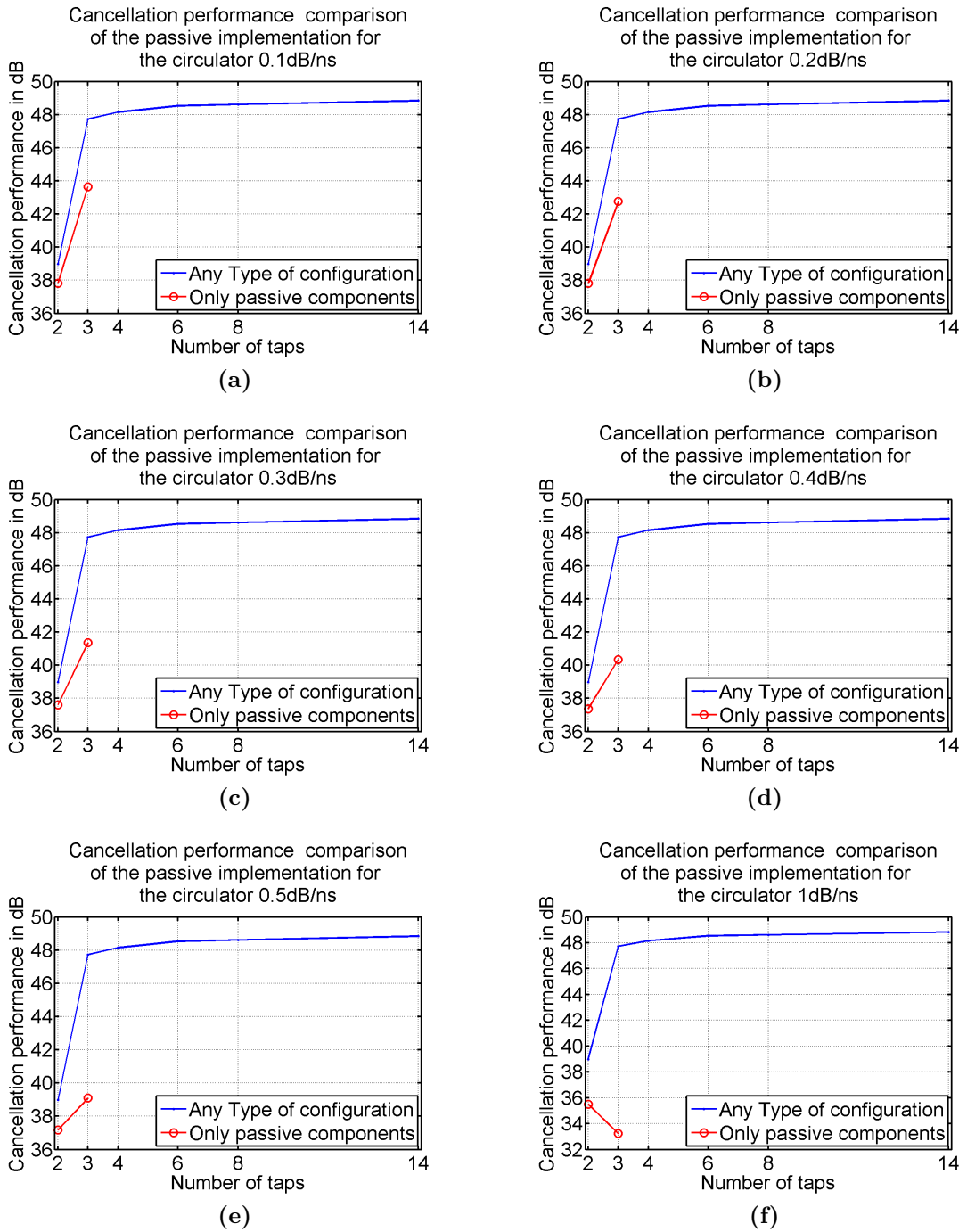
Figure 4.19: Cancellation performance comparison using MADF-DC with delay limit constraints between using passive and any type of components with respective to number of taps for the circulator. (a) Unit insertion loss of delay at 0.1 dB/ns. (b) Unit insertion loss of delay at 0.2 dB/ns. (c) Unit insertion loss of delay at 0.3 dB/ns. (d) Unit insertion loss of delay at 0.4 dB/ns. (e) Unit insertion loss of delay at 0.5 dB/ns. (f) Unit insertion loss of delay at 1 dB/ns.

impulse response. One possible reason is that as the number of taps increases, the remaining components of the impulse response become more spread and further away from where the larger components were. The maximum estimated delay without the consideration of the passive components for the fourteen taps is 160 ns which contributes 16 dB of losses.

The other possible reason is due to the inaccuracy of the estimated delays and the use of LS as weight adaptation algorithm. LS is an unconstrained adaptive filter algorithm which is designed to determine the optimal solution. Due to the inaccurately estimated delays, LS could result in some solutions with large amplitudes. This means that the LS algorithm determines the most optimal solutions. However, these solutions might not be implementable using only passive components. As it is difficult to further enhance the delay estimation accuracy, a better way of solving this is to replace LS with another technique for adapting the final tap weights. The technique should have the ability to restrict the determined solutions so that they are within a limit. Possible solutions could be global optimization technique such as the simulated annealing algorithm. However, in this thesis, these possible solutions are not explored.

For the rest of the system order settings, the cancellation performance using only passive components are not degraded significantly if the unit insertion loss of the delays is less than 0.5 dB/ns. The simulation result also shows that it is not possible to implement a larger cancellation system, i.e., more than six taps, with delay lines that are greater than 1 dB/ns.

Similarly to the results of circulator shown in Figure. 4.19, cancellation performance degradation in the case of the ceramic duplexer is expected when only passive components are used. This can be seen in Figure. 4.20. However, the degradation is not as large as the circulator case. For instance, when the order of the cancellation system is four, such performance degradation is less than 3 dB for the unit insertion loss less than 1 dB/ns. For eight taps, performance achieved using only passive components is at most 3 dB less than using gain blocks for the unit insertion loss less than 0.4 dB/ns. The performance degradation on the three taps is approximately 10 dB when the unit insertion of the delay line is 1 dB/ns. When using a less lossier delay line, the achievable performance using three taps is almost the same as the active components case. There is no significant degradation on the performance when the cancellation system only consists of two taps.
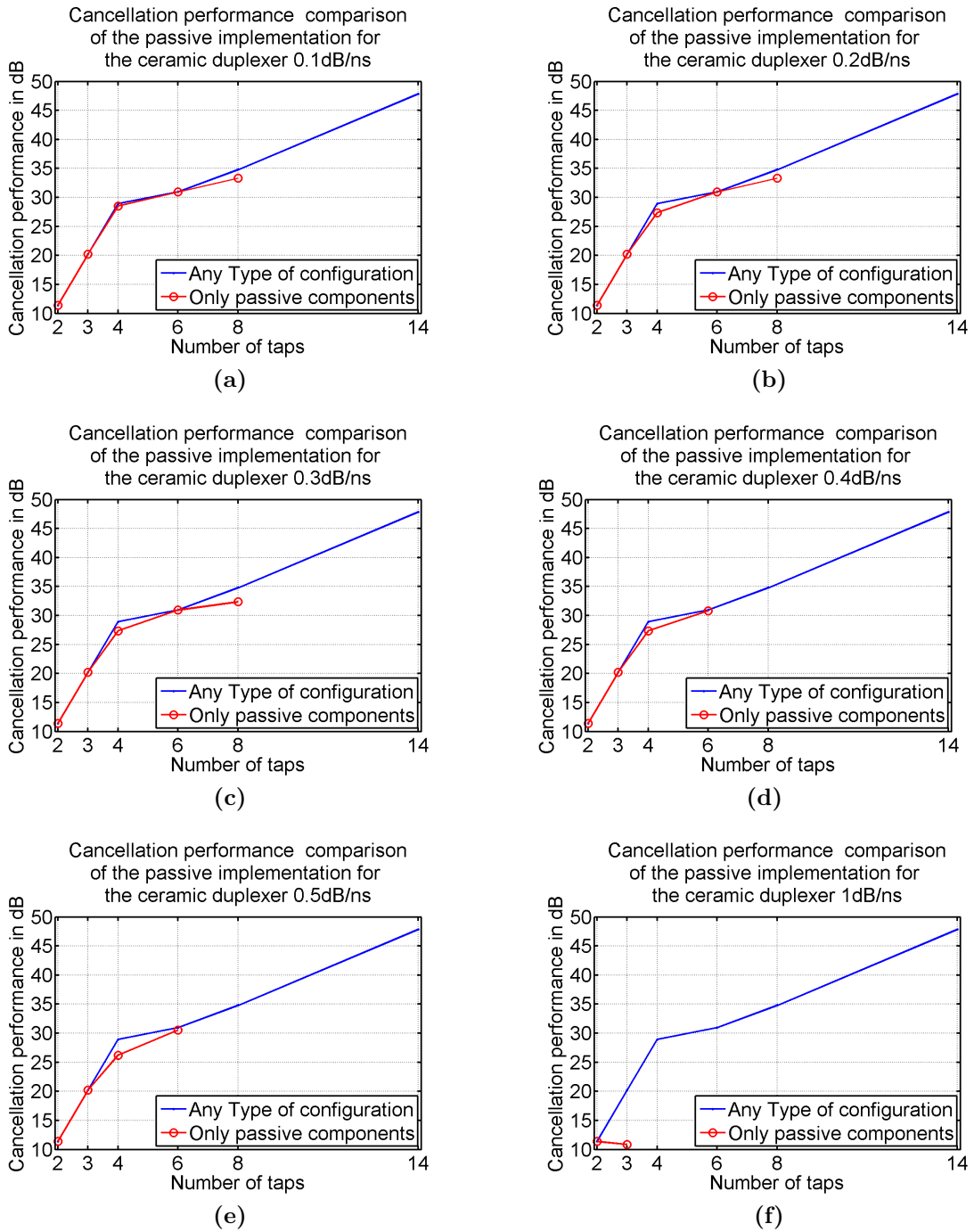
Figure 4.20: Cancellation performance comparison using MADF-DC with delay limit constraints between using passive and any type of components with respective to number of taps for the ceramic duplexer. (a) Unit insertion loss of delay at 0.1 dB/ns. (b) Unit insertion loss of delay at 0.2 dB/ns. (c) Unit insertion loss of delay at 0.3 dB/ns. (d) Unit insertion loss of delay at 0.4 dB/ns. (e) Unit insertion loss of delay at 0.5 dB/ns. (f) Unit insertion loss of delay at 1 dB/ns.

4.7.3 Cavity Duplexer

Setup   The simulations for the cavity duplexer are also performed based on the architecture shown in Figure. 3.1. The simulation settings for the cavity duplexer are the same as the ones for the ceramic duplexer.

Results   For the cavity duplexer, implementing the cancellation system using MADF-DC with a larger number of taps and passive components is as difficult as the case for the ceramic one. According to the simulation results shown in Figure. 4.21, it is not possible to implement such a system with fourteen taps, though the unit insertion loss is as small as 0.1 dB/ns. In the case of the eight taps, though it is possible to implement the system when the unit insertion loss of the delay lines is less than 0.3 dB/ns, the achievable cancellation performance is reduced to about 20 dB. With six taps or less, the suppression rate using only passive components doesn't change significantly as long as the unit insertion loss is less than 0.5 dB/ns. The highest cancellation of the six taps system using only passive components is around 13 dB. The best cancellation performance for the system using either three or four taps is around 10 dB. Using delays with higher insertion loss reduces the possibility of implementing such system with six taps.

4.8 Estimation Speed

In the previous sections, the improved performance of the proposed MADF-DC has been shown. However, like any techniques, there are disadvantages with the proposed technique. In order to increase the delay estimation accuracy, there are three parameter vectors introduced in this technique, i.e., up-sampling ratio, maximum and minimum delay limits for constraining the estimated delays. Since the algorithm performs the estimation using each unique configuration of the elements of these vectors, the computation load is much heavier than for the C-ADF technique.

4.8.1 Speed in General

In order to compare the estimation speed of C-ADF and MADF-DC, the computation time has been shown in Table. 4.5. The estimation time in the table has been
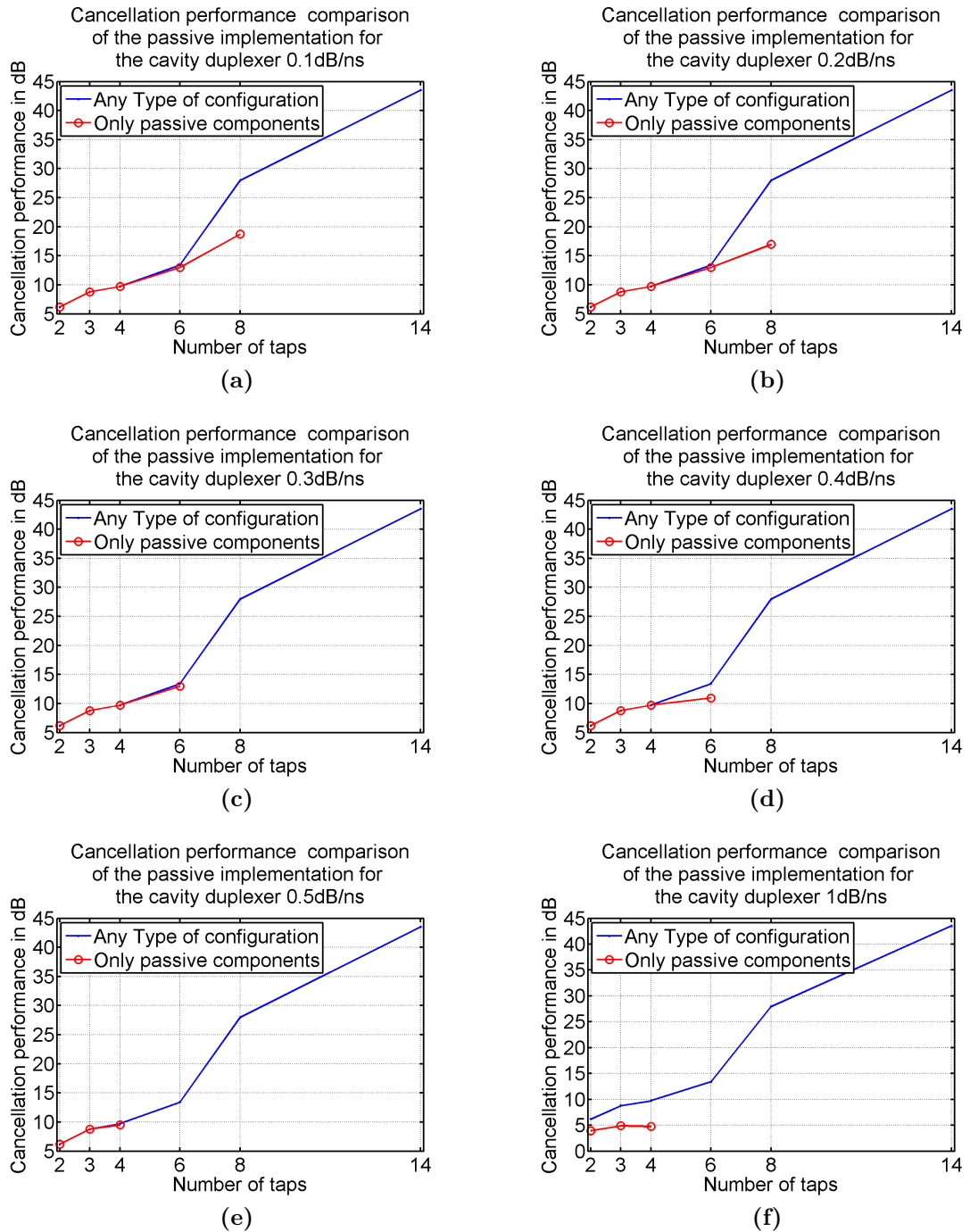
Figure 4.21: Cancellation performance comparison using MADF-DC with delay limit constraints between using passive and any type of components with respective to number of taps for the cavity duplexer. (a) Unit insertion loss of delay at 0.1 dB/ns. (b) Unit insertion loss of delay at 0.2 dB/ns. (c) Unit insertion loss of delay at 0.3 dB/ns. (d) Unit insertion loss of delay at 0.4 dB/ns. (e) Unit insertion loss of delay at 0.5 dB/ns. (f) Unit insertion loss of delay at 1 dB/ns.

recorded using the *tic* and *toc* functions in MATLAB.

Comparing the estimation time of the ceramic and cavity duplexers for the same system order, the computation time using MADF-DC is similar. It suggests that the computation speed using MADF-DC is irrespective to the duplexer types. It is strongly related to the order of the system. The computation time increases when a larger order system is used, which can be expected. On the other hand, the computation time for C-ADF technique increases with the order of the system as well. Overall, the estimation time using MADF-DC is dramatically higher than the one using C-ADF. The latter only takes a few seconds whereas the MADF-DC technique takes hours to complete the estimation.

Table 4.5: Comparison of the estimation speed between C-ADF and MADF-DC

Type of Duplexer	System Order	Estimation Time	
		C-ADF (s)	MADF-DC (hours)
Cavity	2	0.58	3.36
	3	0.79	4.99
	4	1.07	5.56
	6	1.67	11.29
	8	2.34	11.77
	14	4.42	32.75
Ceramic	4	1.27	5.55

4.8.2 Reducing the Estimation Time

Though MADF-DC suffers from long estimation time, it could still be acceptable. This is because in the proposed cancellation architecture of this thesis, the modelling block is only operating when the transceiver is off-line. However, it would still be beneficial if the computation time could be reduced.

Firstly, in the original simulation, for the ceramic duplexer, the cancellation performance achieved by using four taps is approximately 28.92 dB. The delay limit increment is 10 ns. The minimum delay limit is incremented from 0 ns to 200 ns whereas the maximum delay limit is swept from 0.4 ns to 200.4 ns. The up-sampling

ratio vector consists of elements from 1 to 32 in a step of 1 and some discrete elements of 64, 128, 256 and 512.

Using a single up-sampling ratio   As discussed earlier in this chapter, the sweeping of the up-sampling ratio could provide a better cancellation performance than using a single large value. However, such improvement can be insignificant. Therefore, in the case that estimation time is more desirable than the cancellation performance, a single up-sampling ratio (as large as possible) should be used instead of sweeping. By doing so, the estimation time could be vastly reduced. This can be seen from the results shown in Table. 4.6.

In Table. 4.6, it shows the simulated cancellation performance and the resulting estimation time when the up-sampling ratio is set to be 32 and 512, respectively. The order of the system is set to be four and the duplexing device is the ceramic duplexer.   The settings of the delay limit constraints are not changed, i.e., the maximum delay limit is swept between 0.4 ns to 200.4 ns in a step of 10 ns and the minimum delay limit is swept between 0 ns to 200 ns.

The results show that using 512 as the up-sampling ratio, the estimation time is reduced from 5.55 hours which is obtained by sweeping, to 1.18 hours. Compared to the cancellation performance that is shown in Table. 4.3, there is only marginal degradation. When using 32 as the up-sampling ratio, the estimation time is further reduced to 0.15 hours. Therefore, by replacing the sweeping procedure of the up-sampling ratio with a single value, the estimation time could be significantly reduced. The estimation time obtained using 32 is less than the one obtained using 512 as the up-sampling ratio. This is due to the reason that there is a heavier computation load using the larger up-sampling ratio than the lower one. The performance achieved is 28.17 dB which is about 0.6 dB less than using 512 as the up-sampling ratio.

In summary, from the results shown in Table. 4.6, it seems replacing the sweeping procedure of the up-sampling ratio with a large single value would not affect the achievable cancellation performance. However, whether or not this is true needs to be proved. Since this thesis focuses on obtaining the optimal cancellation performance, no actions have been taken on how to prove such observation. Therefore, if estimation time is not critical, sweeping is still recommended.

Table 4.6: The reduced estimation time and cancellation performance using MADF-DC with single up-sampling ratio

	Up-sampling Ratio	Estimation Time (hours)	Cancellation Performance (dB)
MADF-DC	32	0.15	28.17
	512	1.18	28.83

Increasing the increment of the delay limit constraints In order to explore if the estimation time could be reduced by changing the delay limit settings, the simulations have been re-performed by replacing the increment of the delay limit constraints from 10 ns to a number of values. During these experiments, the up-sampling ratio is swept according to the setting described at the beginning of Sec. 4.8.2. The order of the cancellation system is set to be four and the duplexing device is the ceramic duplexer. The resulting estimation time and cancellation performance have been shown in Table. 4.7.

From the results, it can be seen that the estimation time decreases with the increase of the delay limit increment. The reduction rate of the estimation time is approximately in a power of two of the increasing rate of the delay increment. This is due to the reason that the delay limit step affects both the minimum and maximum delay limit constraints. Regarding the cancellation performance, it is only significantly degraded when the delay increment is greater than 20 ns.

Overall, the estimation time could be reduced by increasing the increment of the delay limit constraints, without significantly affect the modelling performance. However, the optimal value of the increment could be difficult to determine. This value is dependent of the characteristics of the duplexer. For this reason, the increment of the delay limit constraints should be chosen as small as possible to avoid degrading the modelling accuracy.

The impact of the estimation time and the performance due to either the up-sampling ratio or the delay limit constraints has been discussed in this section. By using a single up-sampling ratio as well as a large delay limit increment, the estimation time could be vastly reduced. For a certain duplexing device, it is possible to achieve a much smaller estimation time without significantly affecting the cancellation performance. However, these haven't been tested.

Table 4.7: Table cancellation performance and computation time VS the delay increments using MADF-DC

	Delay Limit Increment (ns)	Estimation Time (hours)	Cancellation Performance (dB)
	3	58.23	29.00
	5	23.62	28.99
MADF-DC	10	5.55	28.92
	20	1.34	28.92
	50	0.28	23.09
	100	0.10	18.52

Additional methods for reducing the estimation time   Apart from the methods that are shown above, the estimation time could also be reduced by increasing the step size for sweeping the up-sampling ratio. By doing so, the total number of elements in the up-sampling ratio vector is reduced. In theory, the reduction rate of the estimation time is proportional to the reduction rate of the number of elements in the vector. Performance-wise, when sweeping the up-sampling ratio, the optimal performance is achieved at the largest up-sampling ratio. Since increasing the step size of the sweeping doesn't remove the largest up-sampling ratio from the vector, no performance degradation is expected. Compared to the performance using a smaller step size for sweeping the up-sampling ratio, the one obtained using a larger step might be significantly decreased. However, as discussed in Sec. 4.8.2, it could be dependent on the characteristics of the duplexer.

Additionally, reducing the largest values for sweeping the maximum and minimum delay limit constraints could also decrease the estimation time. As seen in Figure. 4.7, Figure. 4.11 and Figure. 4.15, the performance degradation depends on the characteristics of the duplexer.

4.8.3 Summary of the Estimation Time using MADF-DC

In summary, the estimation time using MADF-DC can be reduced significantly if the modelling is set up carefully. It seems that using a large single value instead of sweeping the up-sampling ratio may suffice without seriously affecting the cancellation performance. However, this is only a pattern that is concluded by observing

the results for the three duplexing devices. Whether or not this pattern applies to another duplexer is not yet known.

Additionally, it can be summarised that increasing the step size for sweeping the delay limit vectors could reduce the estimation time dramatically without degrading the cancellation performance. However, the optimal step size depends on the order of the system and the characteristics of the duplexer. For this reason, it is difficult to determine this optimal value. The step size should always be chosen as small as possible to avoid degrading the modelling accuracy.

4.9 Summary

In this chapter, a novel modified adaptive delay filter using direct cross-correlation technique has been proposed in order to estimate the delays and determine the tap weights for the proposed cancellation system. The classic adaptive delay filter algorithm has been reviewed. Due to the limited resolution of the delay estimation when using the classic adaptive delay filter, several modifications have been proposed so that this estimation technique can be utilized in solving the leakage problem. Using a higher sampling rate for estimating the delays is one of the modifications. Up-sampled signals are used to estimate the most significant components of the impulse response of the duplexing device. Delay limit parameters are introduced to MADF-DC so that the accuracy of the delay estimation can be increased. The MADF-DC is a sequential estimation technique which is the same as C-ADF. Therefore, a new error signal must be obtained after estimating the delay and tap weight of each stage. The new error signal will be used for the delay estimation process of the next stage. Instead of only adapting the current tap, MADF-DC updates all the taps of which the delays have been determined. Critically sampled reference and leakage signals are used for the tap weight adaptations.

Simulations have been firstly carried out in order to show the outstanding performance of the proposed MADF-DC technique. Three duplexing devices have been used in the simulation in order to show that the proposed cancellation system using MADF-DC is not only suitable for the circulator with simpler characteristics, but also capable for duplexers with more complex characteristics.

As the cancellation occurs in the receiver at RF frequencies, in order to avoid the injection of unwanted noise into the receiver, only passive components are preferred for the implementation. Simulations have been performed with adding in insertion losses of major components of the RF canceller. The unit insertion loss, i.e., dB/ns, is introduced in the simulations in order to describe the power losses of the delays. They are 0.1 dB/ns to 0.5 dB/ns in a step of 0.1 dB, in addition to 1 dB/ns.

Simulation results show that with consideration of implementation using passive components, the achievable cancellation performance decreases. For certain numbers of taps, the system cannot be implemented using only passive components. One of the reasons is that the order of the cancellation system is too large so that the power of the reference signal in each cancellation path is too small. The other possible reason is that LS is used as the adaptation algorithm for calculating the tap weights. It is accurate but not constrained. Changing to a constrained algorithm such as simulated annealing could improve the possibility of implementing the cancellation system using passive components. However, this is not included in the discussion in this thesis.

One of the disadvantages of the proposed MADF-DC is that the estimation time is much greater than the classic techniques. The long estimation time might not be a large problem for the modelling of the TX leakage path since the modelling of the duplexer is operated off-line. However, it would be more desirable if such long estimation time could be reduced. In the last section of this chapter, the results are shown in order to discuss the possibility of reducing the estimation time. It can be done by replacing the sweeping process of the up-sampling ratio with a single large value. According to the simulation results, this method could reduce the time without significantly affecting the cancellation performance. However, since there is no definite proof to support such observation, the author of this thesis suggests that sweeping of the up-sampling ratio should be used if the cancellation performance is more critical than the estimation time.

In addition, by increasing the step size of the delay limit constraints, the estimation time could be vastly reduced without affecting the cancellation performance significantly. However, the optimal value of the step size depends on the order of the system and the characteristics of the duplexer. Hence, such optimal value could be difficult to determine. The delay step size should be chosen as small as the estimation time budget allows. A smaller delay step size increases the number of sweeps.

Hence, the estimation time increases.

In summary, this chapter has shown that the MADF-DC (with delay constraints) can provide much better modelling accuracy than the classic techniques. However, the long estimation time is its main disadvantage. Since the modelling technique will be used offline in the proposed cancellation system, the disadvantage of the long estimation time is still acceptable.

4.10 Contributions of this Chapter

The main contributions of this chapter are:

1. Explaining that the classic adaptive delay filter technique is not suitable for the TX leakage problem of this thesis

2. Proposing the MADF-DC technique in order to estimate the delays of the proposed adaptive delay cancellation system of this thesis.

3. Discussing the implementability of the cancellation system using MADF-DC with passive components.

4. Discussing the possibility of reducing the estimation time of MADF-DC.

5 Modified Compressive Sampling Matching Pursuit Modelling Technique

5.1 Introduction

The previous chapter has presented the MADF-DC modelling technique which is designed to improve the modelling accuracy, especially the delay estimation accuracy for the proposed RF cancellation system. In order to obtain a higher modelling performance, the maximum and minimum delay limits need to be swept across a large range of values in a relatively fine step. The consequence is that the estimation time is extremely large. Reducing the number of sweeps for the delay limit constraints (maximum and minimum delay limits) could reduce the required estimation time significantly. However, since the MADF-DC technique is a sequential-based technique and the high delay estimation accuracy is obtained by artificially up-sampling the reference and the leakage signals, the modelling performance heavily depends on the delay limit constraints. For this reason, altering the sweeps of the delay limit constraints significantly degrades the performance.

Therefore, an alternative modelling technique has been investigated so that the estimation time could be reduced while the high modelling performance could be maintained. For this purpose, we start with the introduction of the well-known compressive sampling matching pursuit technique. In order to differentiate this technique from the proposed method in this chapter, we call this already published technique as the *classic* compressive sampling matching pursuit (C-CoSaMP). The proposed technique in this chapter is named as the modified compressive sampling matching pursuit (MCoSaMP). As the name suggested, MCoSaMP is developed

from C-CoSaMP with improved delay estimation accuracy. The C-CoSaMP technique is chosen as the foundation of the proposed algorithm because it can provide fast, reliable and iterative modelling.

5.2 Theory of the Classic Compressive Sampling Matching Pursuit

The C-CoSaMP technique is a compressive sampling technique that was originally developed in order to more efficiently solve under-determined systems, providing that those systems have sparse nature. Therefore, before explaining the C-CoSaMP technique, the theory of the compressive sampling is introduced.

Let $\hat{\mathbf{y}}$ be the vector of the measured output, the size of which is $Q \times 1$. Mathematically, it can be represented as

$$\hat{\mathbf{y}}(n) = \hat{X}\mathbf{h} \tag{5.1}$$

where the size of the model matrix $\hat{X}$ is $Q \times N$, providing that $Q \ll N$, and the coefficients vector $\mathbf{h}$ ($N \times 1$) is sparse. The input model matrix $\hat{X}$ here is the Toeplitz matrix of the input reference signal $\hat{\mathbf{x}}(n)$, i.e.:

$$\hat{X} = [\hat{\mathbf{x}}(n), \hat{\mathbf{x}}(n-1), \dots, \hat{\mathbf{x}}(n-Q)]^T \tag{5.2}$$

where $\hat{\mathbf{x}}(n)$ is a $N \times 1$ vector and the superscript ^{T} of a matrix represents the transpose of a matrix. Traditional compressive sampling algorithms tend to approximate the sparse systems by obtaining the coefficients vector $\hat{\mathbf{h}}$, which satisfies the following condition:

$$min \left\| \hat{\mathbf{h}} \right\|_{l_1} \ subject \ to \ \left\| \hat{X}\hat{\mathbf{h}} - \hat{\mathbf{y}}(n) \right\|_{l_2} < \varepsilon \tag{5.3}$$

where ε is the desired tolerance of the error.

Rather than reducing the number of measurement samples, compressive sampling can also be utilised for reducing the number of coefficients of a sparse system. This requires that the sizes of the input matrix $\hat{X}$, the output signal of the system $\hat{\mathbf{y}}(n)$ and the coefficients vector $\mathbf{h}$ are $N \times Q$, $N \times 1$ and $Q \times 1$, respectively, providing

that **h** is sparse. Typical applications of compressive sampling in terms of reducing the number of coefficients are behavioural modelling and digital pre-distortion of high power amplifiers in wireless communications [50] [91]. Compared to the traditional compressive sampling algorithms, C-CoSaMP is more efficient and less complex.

C-CoSaMP was developed in [80] and is based on the orthogonal matching pursuit (OMP) algorithm. It approximates the coefficients vector **h** iteratively by obtaining the sparse representation **w** and calculating the residual error. C-CoSaMP algorithm has the advantage of low-complexity and provides faster speed and stronger guarantees than the original OMP [80] . The C-CoSaMP algorithm requires some information including: the input model matrix; the desired signal vector $\hat{\mathbf{y}}(n)$; the desired sparsity of the approximation M; and the stopping conditions. The stopping conditions include the maximum number of iterations and the desired tolerance ε. The desired tolerance is the threshold value that defines the minimum Euclidean norm of the residue at the current iteration. It is also used to terminate the iterations when the difference of the Euclidean norm between the previous and the current iterations is small. The algorithm estimates the locations of the most significant taps iteratively. The algorithm is ended when the stopping criteria is reached. Upon the completion of C-CoSaMP algorithm, the coefficients and the locations of the most significant taps are determined.

The details of the procedures after the initialization are summarised as follows and these procedures repeat until the stopping criteria is reached:

1. **Identification** : Approximating the residue signal using the input matrix and determining the locations of the largest $2M$ coefficients.

2. **Merging** : Merging the locations of the determined largest $2M$ coefficients with the ones that are obtained by the previous iteration.

3. **Estimation** : Re-calculating the coefficients at the merged locations.

4. **Pruning** : Choosing the locations of the largest M coefficients for the next iteration.

5. **Sample Updating** : Approximating the desired signal $\hat{\mathbf{y}}$ utilizing the input matrix and determined locations of the coefficients. The error between the

> desired and the approximated signals is updated as the residue for the next iteration.

In this work, the LS adaptive algorithm is used to determine the tap weights, due to its low implementation complexity and high modelling performance. Similar to C-ADF technique, C-CoSaMP has an issue with the accuracy of the delay estimation. Since the signals that are obtained at the baseband are sampled at the critical sampling frequency, i.e., the sampling frequency is the same as the cancellation bandwidth, the accuracy of the delay estimation is thus limited. As explained in Sec. 3.2.3.3, when characterizing the duplexer using critically sampled signals, the order of the cancellation system could be significantly increased. This also applies to C-CoSaMP. For this reason, we propose the new modelling technique, the modified compressive sampling matching pursuit technique.

5.3 Modified Compressive Sampling Matching Pursuit

The modified compressive sampling matching pursuit (MCoSaMP) technique uses the up-sampled reference and leakage signals, rather than the critically sampled signals. However, the optimal up-sampling ratio is not known at the beginning of the approximation. This value can be determined by running the C-CoSaMP kernel with different up-sampling ratio. The one that achieves the best modelling performance is chosen for the implementation. At this stage, it is not yet known whether it could achieve a significant performance improvement by sweeping the up-sampling ratio compared to using a single large value. The simulation results will be shown and discussed in Sec. 5.5.

Additionally, through experiments, we found out that limiting the estimated delays with maximum and minimum delay values could further improve the modelling performance. For this reason, in order to obtain the optimal modelling performance, the maximum and minimum delay vectors are needed. The delay limits that result the best modelling performance are the optimal ones. By using the optimized up-sampling ratio and delay limits, more accurate delays could be estimated. Then based on the estimated delays, the tap weights can then be obtained. The concept is similar to the MADF-DC technique which has been discussed in the previous

chapter. The detailed procedures of the proposed modelling technique are shown in Figure. 5.1 and Figure. 5.2.

Let the vector of the up-sampling ratios be $\mathbf{K}$. Before sweeping through $\mathbf{K}$ and estimating the system with the C-CoSaMP kernel, the validity of the current values of the delay limit vectors, i.e., $d_{min}(i)$ and $d_{max}(j)$ must be checked first, where $i = 1, 2, \ldots, I$ and $j = 1, 2, \ldots, J$ are loop indexes for the vector of minimum and maximum delays, respectively. The values I and J are the number of elements in $\mathbf{d}_{min}$ and $\mathbf{d}_{max}$, respectively. The values $d_{min}(i)$ and $d_{max}(j)$ are elements of the vectors $\mathbf{d}_{min}$ and $\mathbf{d}_{max}$, respectively. This is to ensure that $d_{min}(i) < d_{max}(j)$ and $d_{max}(j) - d_{min}(i) > THD$. The value THD is the threshold value that defines the minimum range in which the locations of all M taps are valid. It is defined as

$$THD = \frac{M}{max(\mathbf{K})f_s} \tag{5.4}$$

Let $K(p)$ be the element of the up-sampling vector $\mathbf{K}$, where $p = 1, 2, \ldots, P$ is the sweeping index and P is the length of the vector $\mathbf{K}$. For any $K(p)$, the original input reference vector $\hat{\mathbf{x}}(n)$ and leakage signals $\hat{\mathbf{y}}(n)$ are up-sampled accordingly. Thus the input matrix $\hat{X}_{up}$ can be created with the up-sampled reference vector $\hat{\mathbf{x}}_{up}(n)$. With $\hat{X}_{up}$ and the up-sampled leakage signal $\hat{\mathbf{y}}_{up}(n)$, the system can be modelled utilizing C-CoSaMP algorithm.

The kernel of C-CoSaMP needs to be modified so that the delay limits can take effect. The flowchart of C-CoSaMP is shown in Figure. 5.2. The delay constraints in samples, i.e., D_{min} and D_{max} are included as two additional input parameters to C-CoSaMP technique. During the identification and pruning procedures of C-CoSaMP algorithm, the locations of the most significant coefficients must be chosen within the range that is bounded by D_{min} and D_{max}.

The locations of the most significant coefficients are determined by the C-CoSaMP kernel. Let these locations be $\mathbf{l}_m$. The vectors in $\hat{X}_{up}$ that correspond to $\mathbf{l}_m$ are down-sampled to f_s. A new matrix $\hat{X}_{CS}$ is formed using those vectors. The leakage signal $\hat{\mathbf{y}}(n)$ is approximated with $\hat{X}_{CS}$ using LS algorithm. Along with the delays $\mathbf{l}_m$, the resulting tap weights and normalised mean square error (NMSE) of the remaining error signal are recorded, separately. The above procedures are repeated until all elements of $\mathbf{K}$, $\mathbf{d}_{min}$ and $\mathbf{d}_{max}$ vectors have been applied. The up-sampling ratio,
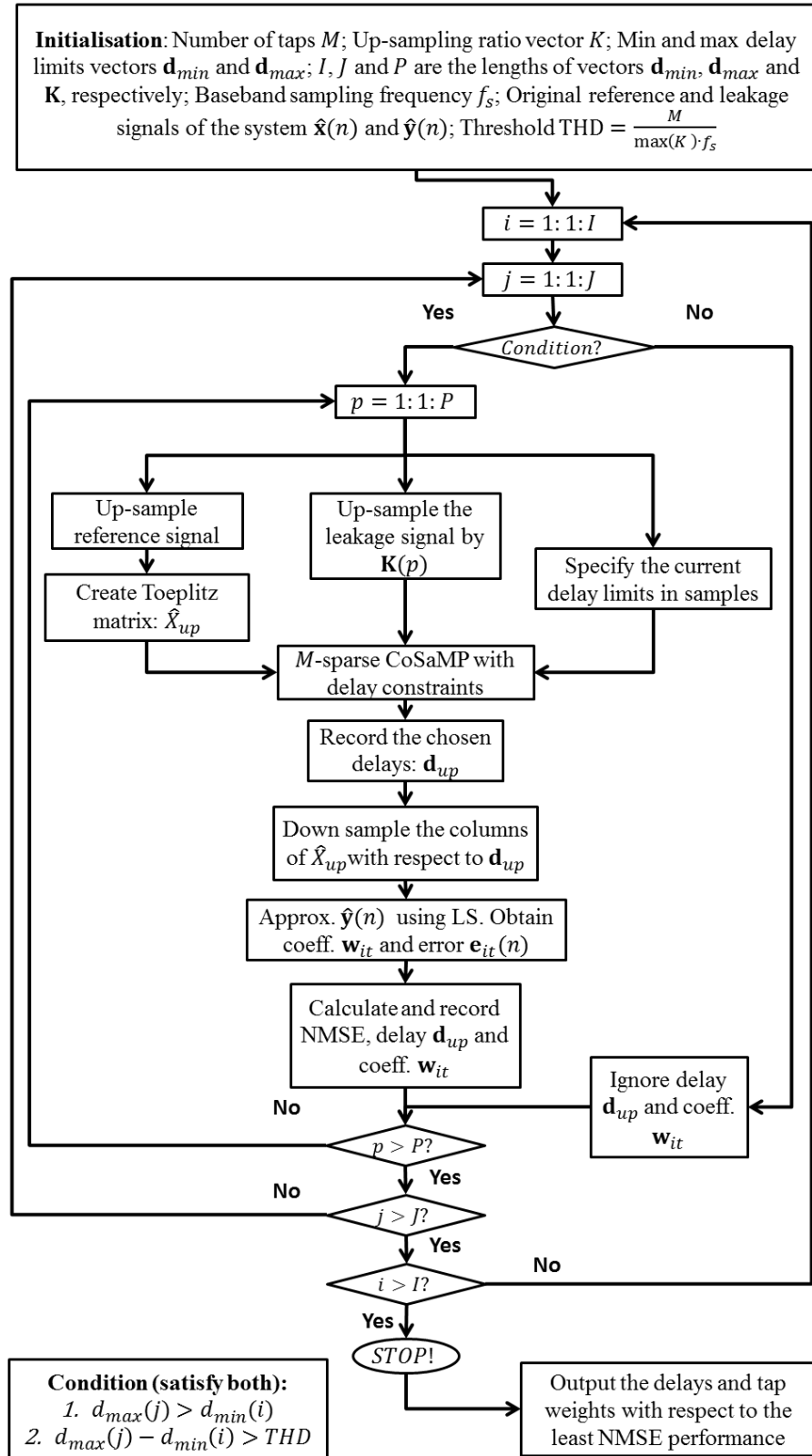
Figure 5.1: Flowchart of the MCoSaMP technique
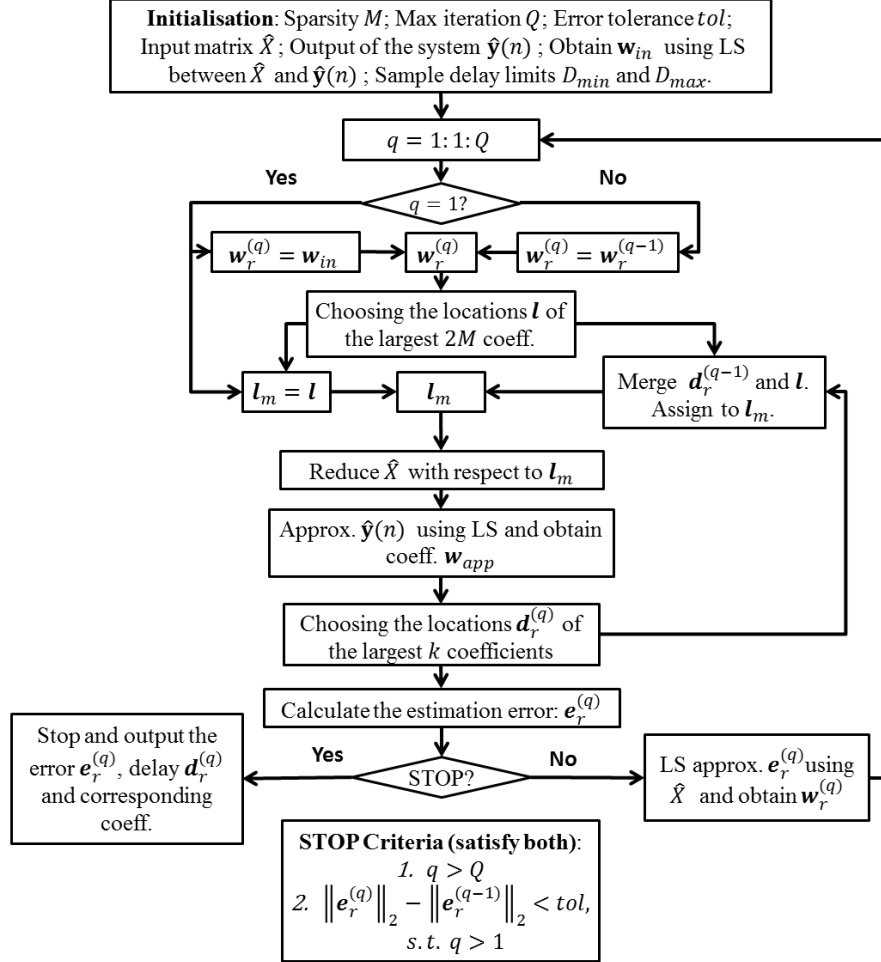
Figure 5.2: Flowchart of C-CoSaMP with delay constraints

minimum and maximum delay limits that produce the lowest NMSE are chosen and the corresponding tap weights and delays are the ones for implementing the cancellation system.

In summary, in the proposed cancellation system, the MCoSaMP algorithm is operated as follows:

1. **Looping** : Setting up the algorithm, particularly with delay limits, up-sampling rate. For each different combination of the three parameters, the estimation technique using MCoSaMP will proceed the following **THREE** steps:

2. **Initialisation** : Re-sampling the baseband reference and desired signals so that the sampling frequency is as requested. Create the input matrix with the re-sampled reference signal. Providing the desired sparsity and stopping criterion. Initiating the error of the previous iteration with the desired signal.

3. **Estimation** :Estimating the locations of the largest components of all the taps using the C-CoSaMP algorithm. Discarding any locations that are outside the given delay limits and replace with the locations of the smaller components.

4. **Re − calculation** : Creating a new matrix in which each vector is produced by delaying the up-sampled reference signal correspondingly with the estimated delay. Down-sampling the new matrix to the critical sampling frequency and approximating the coefficients of those taps using the new input matrix and the original desired signal. Updating the cancellation residue with the error between the reference and approximated signals.

5. **Selecting** : Selecting the delay limits and up-sampling rate that produce the lowest NMSE and returning the corresponding taps weights and delays as the final results of estimation.

Compared to C-CoSaMP, the MCoSaMP technique has increased the search space by adding the three parameters, i.e., the up-sampling ratio, maximum and minimum delay limits. For this reason, the C-CoSaMP is in fact a special case of the MCoSaMP. Therefore, it can be expected that the modelling performance of MCoSaMP is better than C-CoSaMP. The two techniques could achieve the same level of modelling performance only when the impulse response of the unknown system consists of a finite number of impulses at the critical sampling frequency. The

modelling performance of MCoSaMP can be seen from the simulation results that will be shown in more detail in Sec. 5.5.

5.4 Simulation Setup

The block diagram of the simulation using MCoSaMP is shown in Figure. 5.3. The simulation setup using MCoSaMP is very similar to the one that is shown in Table. 4.1. The symbol $\bar{n} = 1, 2, \ldots, \bar{N}$ in the block diagram represents the sample index for the simulated RF signal and $\bar{N} = 2097152$ is the total number of samples. The bandwidth of the lowpass filter is half of the desired bandwidth of the cancellation system. The down-sampling factor $\mathbf{U} = \frac{f_s^{RF}}{f_s}$ can be a fractional number. In that case, the down-sampling block in the block diagram consists of up-sampling, filtering and down-sampling procedures.

The desired tolerance in the simulations is set to be 0.1×10^{-9} and the maximum number of iterations is set as 100. Parameters such as the total number of samples for simulated RF signals, the RF sampling frequency, the bandwidth of the cancellation system and delay limits are the same as the ones in the previous chapter. The main difference between MCoSaMP and MADF-DC is that the first one estimates the delays of all taps at the same time comparing to the sequential operation of the latter. As a result, estimation using the MCoSaMP technique requires a very large matrix in order to cover all the possible delay components. The size of the matrix is extremely large if the product between the up-sampling ratio and the number of taps is large. When this happens, a large size of memory is needed for the PC to complete the simulation. In order to avoid such problem, the up-sampling ratio vector for the simulations using the MCoSaMP is set between 1 and 32 using increments of 1.

5.5 Simulation Results

In this section, the performance of the cancellation system using MCoSaMP is shown. Similar to the ones in the previous chapter, the simulation results for the circulator are shown first and followed by the ones for the ceramic and cavity duplexers. For each duplexing device, the results are also presented as follows:
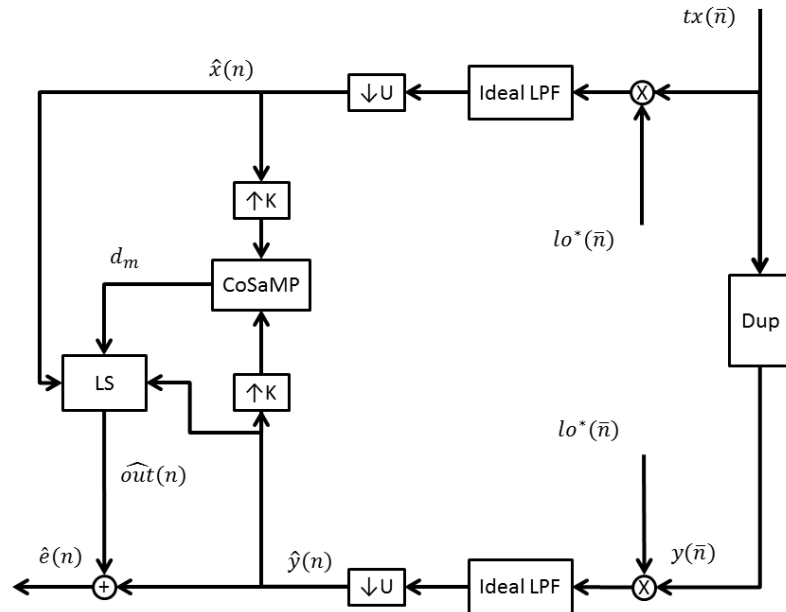
Figure 5.3: The block diagram simulation using MCoSaMP

- Cancellation performance with respect to the delay limits

- Cancellation performance with respect to the up-sampling ratio

- Comparison of the optimal cancellation performance

- Chosen parameters for the optimal performance

- Resulting spectrum

5.5.1 Circulator

Cancellation performance with respect to the delay limits The achieved cancellation performance with respect to the delay limit constraints for the isolation path of the circulator have been shown in Figure. 5.4. It can be seen that the variation of the cancellation performance using MCoSaMP is smaller than the one using MADF-DC technique when the minimum delay limit is fixed. This suggests that the peak cancellation of using MCoSaMP technique is less dependent on the delay limit constraints compared to MADF-DC. Additionally, in comparison with the MADF-DC technique, there are more blank areas in the figure. This is more noticeable

when the order of the system is large. This indicates that more sets of delay limit constraints are invalid when using MCoSaMP technique. This is due to the reason that the maximum up-sampling ratio for MCoSaMP is only 32, whereas it is 512 for MADF-DC. According to (5.4), with the same number of taps, a larger up-sampling ratio will result in a smaller threshold value. As a result, less sets of delay limits are valid using MCoSaMP compared to using MADF-DC.

Cancellation performance with respect to the up-sampling ratio The cancellation performance with respect to the up-sampling ratio is shown in Figure. 5.5. For the circulator, the peak cancellation performance for the two-tap and four-tap cases occurs at the up-sampling ratios of 10 and 18, respectively. This suggests that by sweeping the up-sampling ratio when the order of the system is two or four, there is performance improvement compared to using a single up-sampling ratio, i.e., 32. However, improvement is insignificant. For other system orders, the performance achieved by using the largest up-sampling ratio is about the same as the peak one. This indicates that estimating the circulator using MCoSaMP with up-sampling ratio sweeping is less beneficial since it could result in a large estimation time. This will be explored with the other two duplexing devices.

Comparison of the optimal cancellation performance The summarised peak cancellation performance has been shown in Figure. 5.6. The summarised results from the previous technique and C-CoSaMP have also been added into the comparison figure. It can be seen that C-CoSaMP has achieved the same level of cancellation as the LS technique. This represents that for the circulator, the resulting impulse response at the critical sampling frequency is less sparse. This his similar to the performance seen in the previous chapter.

As expected, the classic LS technique achieved the poorest performance. The C-CoSaMP achieves the same level of performance as the LS technique for the circulator. As discussed in Sec. 3.2.3.3 and Sec. 4.6.1, due to the limited sampling frequency, the sparse system becomes non-sparse when using these two classic techniques. The MCoSaMP technique with and without the delay limit constraints has achieved improved modelling performance than the classic techniques. It is interesting to see that the MCoSaMP technique with and without the additional delay limit constraints has a very similar performance to each other. It can be interpreted

Figure 5.4: Cancellation performance using MCoSaMP with respect of delay limit constraints for the circulator. (a) Two taps. (b) Three taps. (c) Four taps. (d) Six taps. (e) Eight taps. (f) Fourteen taps.

Figure 5.5: Cancellation performance using MCoSaMP with respect of the up-sampling ratio for the circulator. (a) Two taps. (b) Three taps. (c) Four taps. (d) Six taps. (e) Eight taps. (f) Fourteen taps.

that for the circulator, the advantages of limiting the delays using MCoSaMP are less significant than the technique in the previous chapter. On the other hand, when limiting the delays, MADF-DC achieved a better performance than the MCoSaMP technique, using any number of taps except six. At six taps, MCoSaMP is actually 0.03 dB better than the MADF-DC, which can be seen in Table. 5.1, though the performance differences between the two are not significant.
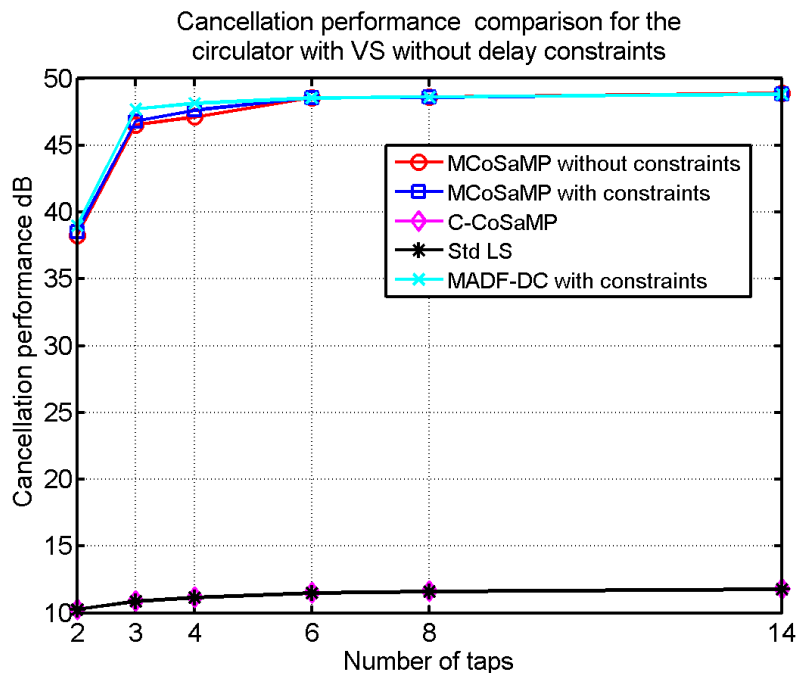
Figure 5.6: Cancellation performance comparison between with and without delay limit constraints for circulator using MCoSaMP.

Chosen parameters for the optimal performance The resulting cancellation performance is shown in Table. 5.1. The corresponding delay limits and up-sampling ratios with respect to the number of taps are also presented. Since the upper bound of the up-sampling ratio has been limited to 32 for MCoSaMP technique, the required delay resolution for the circulator is 390.6 ps. Such requirement is relaxed compared to the 24.4 ps given in Sec. 4.6.1.

Spectrum results The resulting magnitude responses of the cancellation system for the circulator have been shown in Figure. 5.7. As expected, the resulting leakage signals after the cancellation using the constrained MCoSaMP technique are very

Table 5.1: The summarized cancellation performance that is achieved using MCoSaMP with corresponding delay limit constraints and up-sampling ratios for the circulator.

No. of taps	Min. delay limit (ns)	Max. delay limit (ns)	Can. perf. (dB)	Upsamp. ratio
2	0	1.4	38.53	32
3	0	3.9	46.82	26
4	0	5.9	47.63	18
6	0	2.4	48.57	32
8	0	10.4	48.59	10
14	0	10.4	48.85	21

similar to the ones that are achieved using the constrained MADF-DC technique. The resulting spectrum using LS and C-CoSaMP is the same as expected since using these classic techniques, the sparse system becomes less sparse due to the limited sampling rate. This has been explained in Sec. 4.3.1, Sec. 4.3.2 and Sec. 4.6.1. In comparison to the classic technique, the proposed MCoSaMP technique provides significantly more isolation for the circulator compared to the duplexing devices.

5.5.2 Ceramic Duplexer

As shown in Figure. 2.18, the ceramic duplexer has more complex characteristics than the circulator. Its magnitude and group delay responses change rapidly and phase response is non-linear. It can be expected that the modelling performance achieved using the proposed technique will be decreased. For the LS and C-CoSaMP techniques, such performance degradation will be more severe. This can be seen from the results shown in this section.

Cancellation performance with respect to the delay limits In order to present how the different combinations of the maximum and minimum delay limits affect the achievable peak cancellation performance, Figure. 5.8 has been presented. For the ceramic duplexer, the resulting cancellation performance using MCoSaMP is also less sensitive to the delay limit constraints than the one using MADF-DC.

Figure 5.7: Normalised frequency response of the leakage, with and without the cancellation system using MCoSaMP for the circulator . (a) Two taps. (b) Three taps. (c) Four taps. (d) Six taps. (e) Eight taps. (f) Fourteen taps.

Additionally, for two taps, the maximum cancellation using MCoSaMP is around 14 dB whereas it is about 10 dB using MADF-DC. This has been confirmed by the summarised peak cancellation figure that is shown in Figure. 5.10.

Cancellation performance with respect to the up-sampling ratio In order to determine if sweeping value of the up-sampling ratio can significantly improve the cancellation performance, the cancellation performance with respect to the up-sampling ratio is shown in Figure. 5.9. Unlike the circulator case, the results show that sweeping the up-sampling ratio vector could cause a significant performance improvement compared to using a single large value. For two taps, the peak cancellation which is approximately 15 dB, occurs at the up-sampling ratio of three. In comparison, when using the up-sampling ratio of 32, the performance is only about 10 dB. Similar results can be seen for the three-tap and four-tap cases. In both cases, the difference between the peak performance and the one achieved by using a single up-sampling ratio is about 3 dB. In comparison, it can be seen from the results shown in Figure. 4.12 that sweeping the up-sampling ratio doesn't provide a significant performance increase than using a single large up-sampling ratio. This will be explored in more detail for the cavity duplexer later in this chapter.

Comparison of the optimal cancellation performance The peak cancellation performance can also be observed in the summarised results which are shown in Figure. 5.10. As before, the proposed MCoSaMP technique with or without the delay limit constraints has outperformed the classic LS and C-CoSaMP methods. Once again, LS and C-CoSaMP have achieved the same performance indicating that for the ceramic duplexer, the impulse response is less sparse at the critical sampling frequency, within the band of interest.

For two taps, the MCoSaMP technique with additional delay limits provides approximately 5 dB better performance compared to the classic one. The non-constrained MCoSaMP has approximately 3 dB worse performance, compared to the constrained one for the two and eight taps system. In the cases where the tap number of the system is three, four or six, MCoSaMP, with and without delay limit constraints, could achieve very similar leakage suppression performance. Such performance difference increases by about 2 dB as the number of taps increases to fourteen. Such results show that the cancellation performance using MCoSaMP technique is less

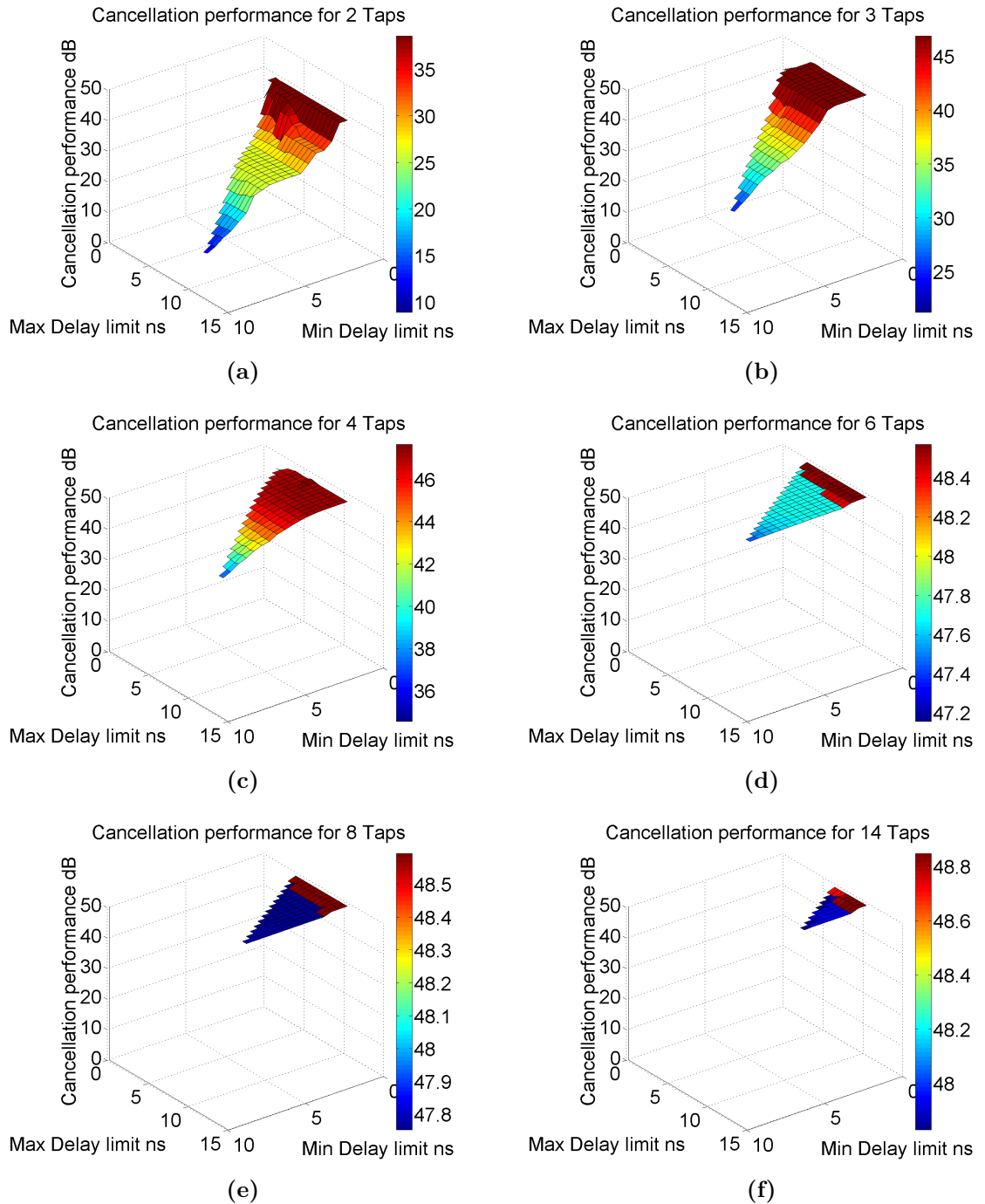**Figure 5.8:** Cancellation performance using MCoSaMP with respect of delay limit constraints for the ceramic duplexer. (a) Two taps. (b) Three taps. (c) Four taps. (d) Six taps. (e) Eight taps. (f) Fourteen taps.
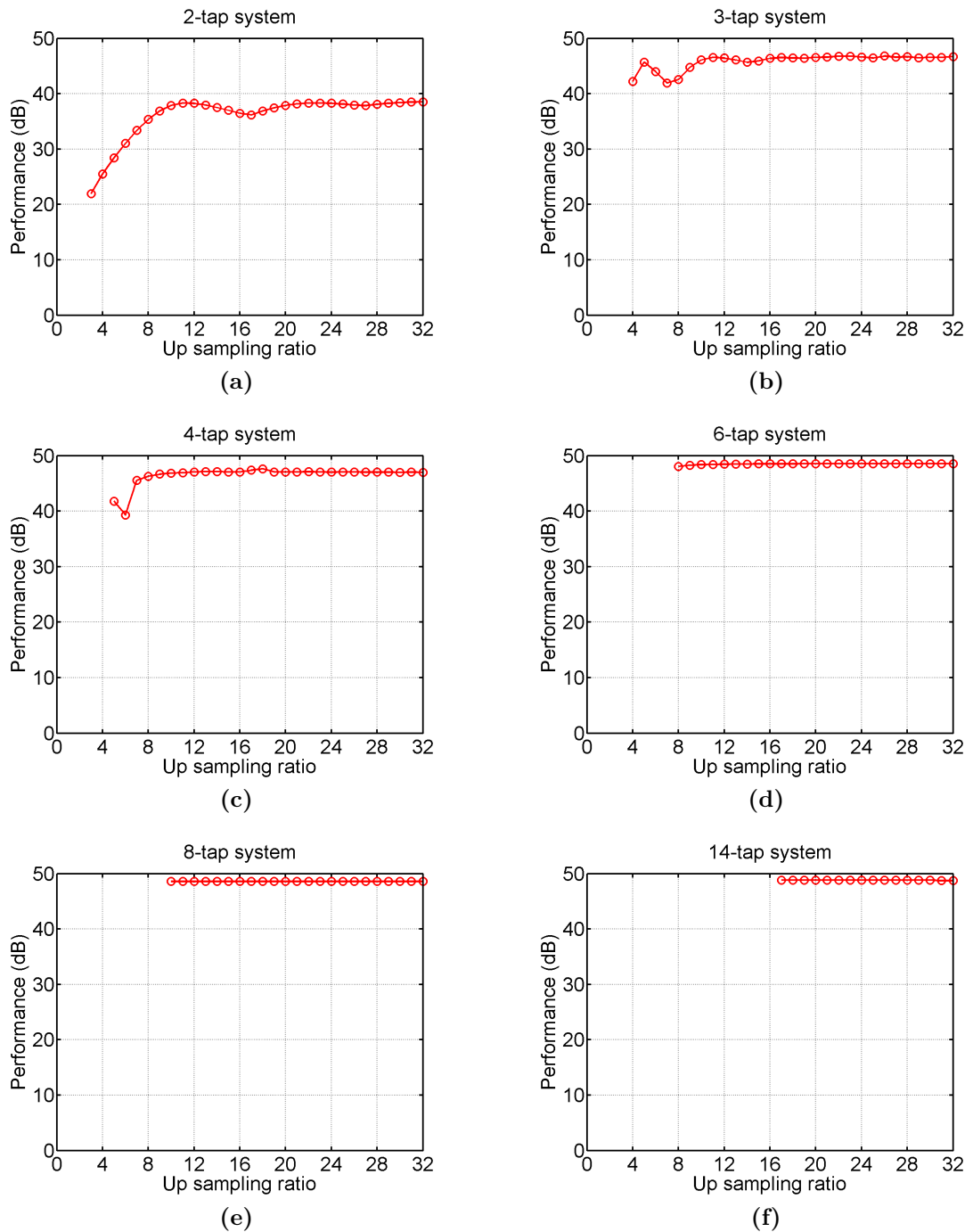
Figure 5.9: Cancellation performance using MCoSaMP with respect of the up-sampling ratio for the ceramic duplexer. (a) Two taps. (b) Three taps. (c) Four taps. (d) Six taps. (e) Eight taps. (f) Fourteen taps.

dependent to the delay limit constraints compared to MADF-DC. With additional delay limit parameters, MCoSaMP and MADF-DC are similar in the peak cancellation performance. Estimation of the duplexer using MADF-DC is slightly more accurate than MCoSaMP, providing that the number of taps is more than two.
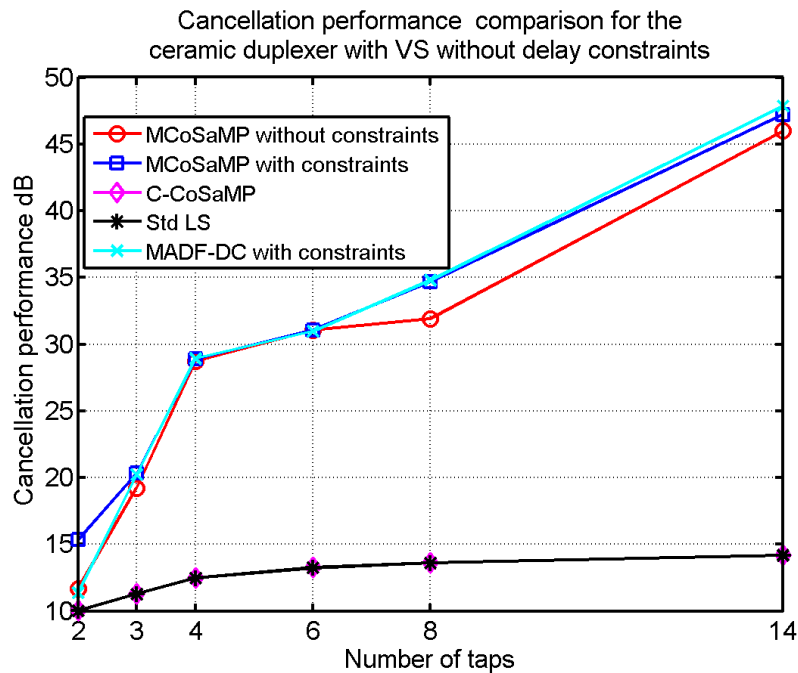
Figure 5.10: Cancellation performance comparison between with and without delay limit constraints for ceramic duplexer using MCoSaMP.

Chosen parameters for the optimal performance   The summarised cancellation performance and the corresponding up-sampling ratios and the delay limits are shown in Table. 5.2. Unlike MADF-DC, there are no large delays, nor high delay resolution requirements for achieving the peak cancellation performance. The maximum delay of all the number of taps configurations is about 85.7 ns. It is when the cancellation system uses fourteen taps. The corresponding delay resolution that is required is 3.57 ns if tunable delay lines are used. The greatest delay resolution of all the taps is approximately 1.24 ns, which is significantly less, compared to 55.8 ps in the MADF-DC simulations for the same duplexer.

Spectrum results   The magnitude responses of the leakage before and after the cancellation using the proposed MCoSaMP technique have been shown in Figure. 5.11.

Table 5.2: The summarized cancellation performance that are achieved using MCoSaMP with corresponding delay limit constraints and up-sampling ratios for the ceramic duplexer.

No. of taps	Min. delay limit (ns)	Max. delay limit (ns)	Can. perf. (dB)	Upsamp. ratio
2	20	50.4	15.33	3
3	20	30.4	20.31	11
4	10	50.4	28.87	23
6	0	60.4	31.08	10
8	30	50.4	34.69	22
14	40	90.4	47.22	8

As the summarised cancellation performance in Table. 5.2 suggests, for the two taps system, MCoSaMP suppresses the leakage more than the MADF-DC technique. In comparison to the classic LS technique and C-CoSaMP for the two taps system, MCoSaMP is better, particularly at the edge of the frequency band. But at the frequencies around -5 MHz from the centre, the leakage after the cancellation using MCoSaMP is significantly larger than the one using the LS method. For more than two taps, MCoSaMP performs similarly to the previous MADF-DC technique and is significantly better than the classic technique across the whole frequency band.

5.5.3 Cavity Duplexer

As shown in Figure. 2.18, the characteristics of the cavity duplexer are the most complex of all the duplexing devices discussed in this thesis. For this reason, it can be expected that further performance degradation will occur for this type of duplexer in comparison with others.

Cancellation performance with respect to the delay limits For the cavity duplexer, simulations of the proposed cancellation system using the MCoSaMP technique have been performed with and without limiting the estimated delays. The resulting cancellation performance with respect to the delay limits have been shown in Figure. 5.12. Comparing to MADF-DC, MCoSaMP is less sensitive to the delay
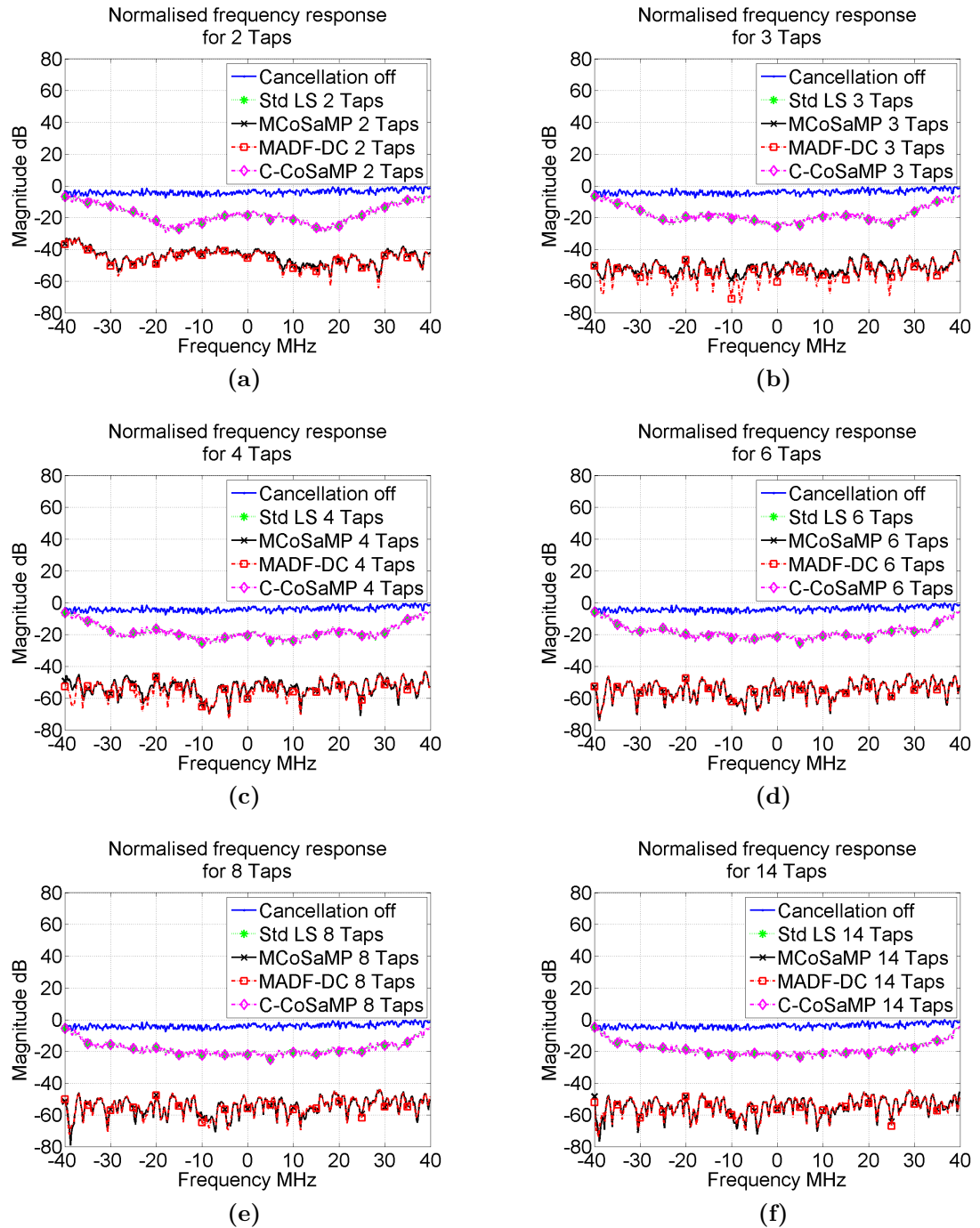
Figure 5.11: Normalised frequency response of the leakage, with and without the cancellation system using MCoSaMP for the ceramic duplexer . (a) Two taps. (b) Three taps. (c) Four taps. (d) Six taps. (e) Eight taps. (f) Fourteen taps.

limits, which has already been discussed previously. The results also suggest that the achievable performance for the cavity duplexer is noticeably reduced compared to the duplexer with ceramic material. This is mainly because this type of duplexing device is more complex in characteristics and more difficult to be modelled.

Cancellation performance with respect to the up-sampling ratio The relationship between the cancellation performance and the up-sampling ratio is presented in Figure. 5.13. In the cases that the order of the cancellation system is four or eight, the peak cancellation occurs when the up-sampling ratio is not the maximum value. This suggests that for these two cases, sweeping can provide noticeable performance improvement, i.e., approximately 2 dB for both four-tap and eight-tap systems. For the fourteen-tap case, the peak cancellation occurs when the up-sampling ratio is about 8. However, the performance improvement is not significant, compared to the one achieved using the up-sampling ratio of 32.

Comparison of the optimal cancellation performance The summarised cancellation performance results are shown in Figure. 5.14. At eight taps, the performance difference between the constrained and unconstrained MCoSaMP is significant, i.e., greater than 10 dB. At fourteen taps, the difference reduces to about 5 dB. For other system orders, the performance difference between the constrained and unconstrained MCoSaMP is less than 3 dB, approximately. At four and six taps, the unconstrained MCoSaMP achieves nearly identical performance compared to the classic LS technique. Otherwise, MCoSaMP is more accurate in estimating the duplexer than LS.

For the cavity duplexer, C-CoSaMP performs better than the classic LS technique when the order of the cancellation system is less than four. This indicates that the isolation path of the cavity duplexer is more sparse than the other duplexing devices since C-CoSaMP is designed for sparse system. However, the improvement is only less than 2 dB.

Comparing between the constrained MCoSaMP and MADF-DC techniques, the latter is better for all tap numbers. However, the difference is negligible when the number of taps is greater than three. MADF-DC achieves about 2 dB better performance than MCoSaMP when the system is implemented using two or three taps.

148
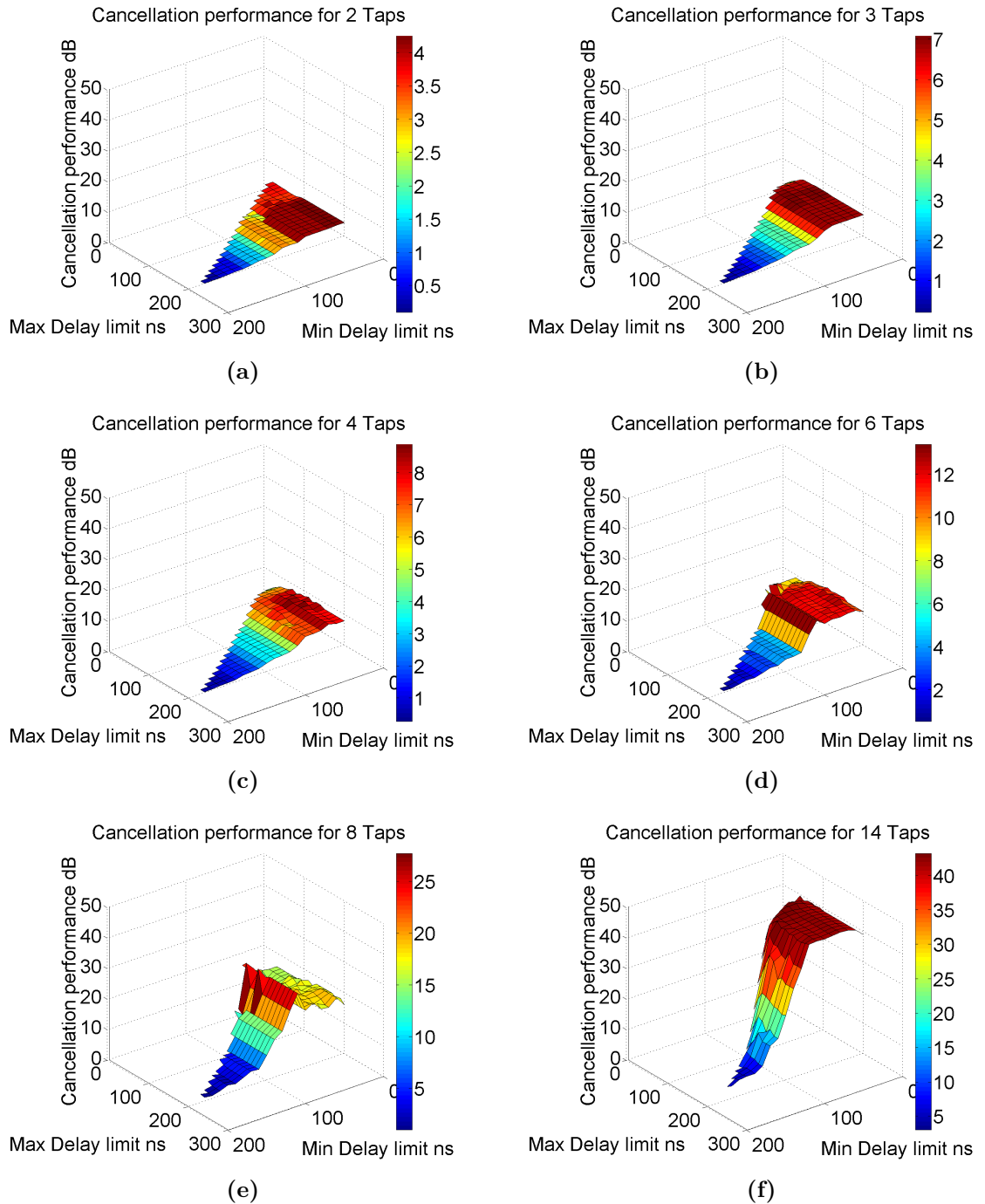
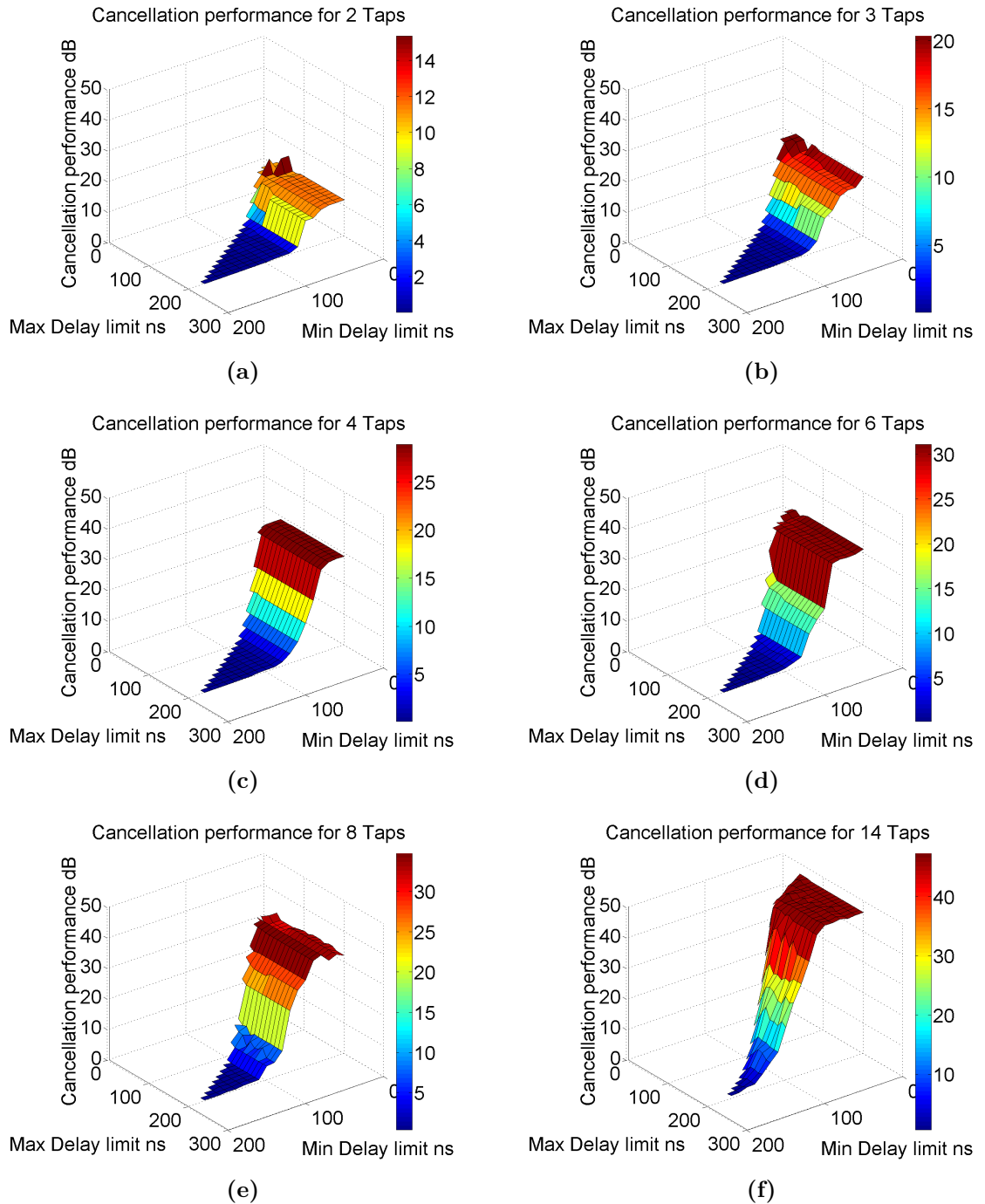**Figure 5.12:** Cancellation performance using MCoSaMP with respect of delay limit constraints for the cavity duplexer. (a) Two taps. (b) Three taps. (c) Four taps. (d) Six taps. (e) Eight taps. (f) Fourteen taps.
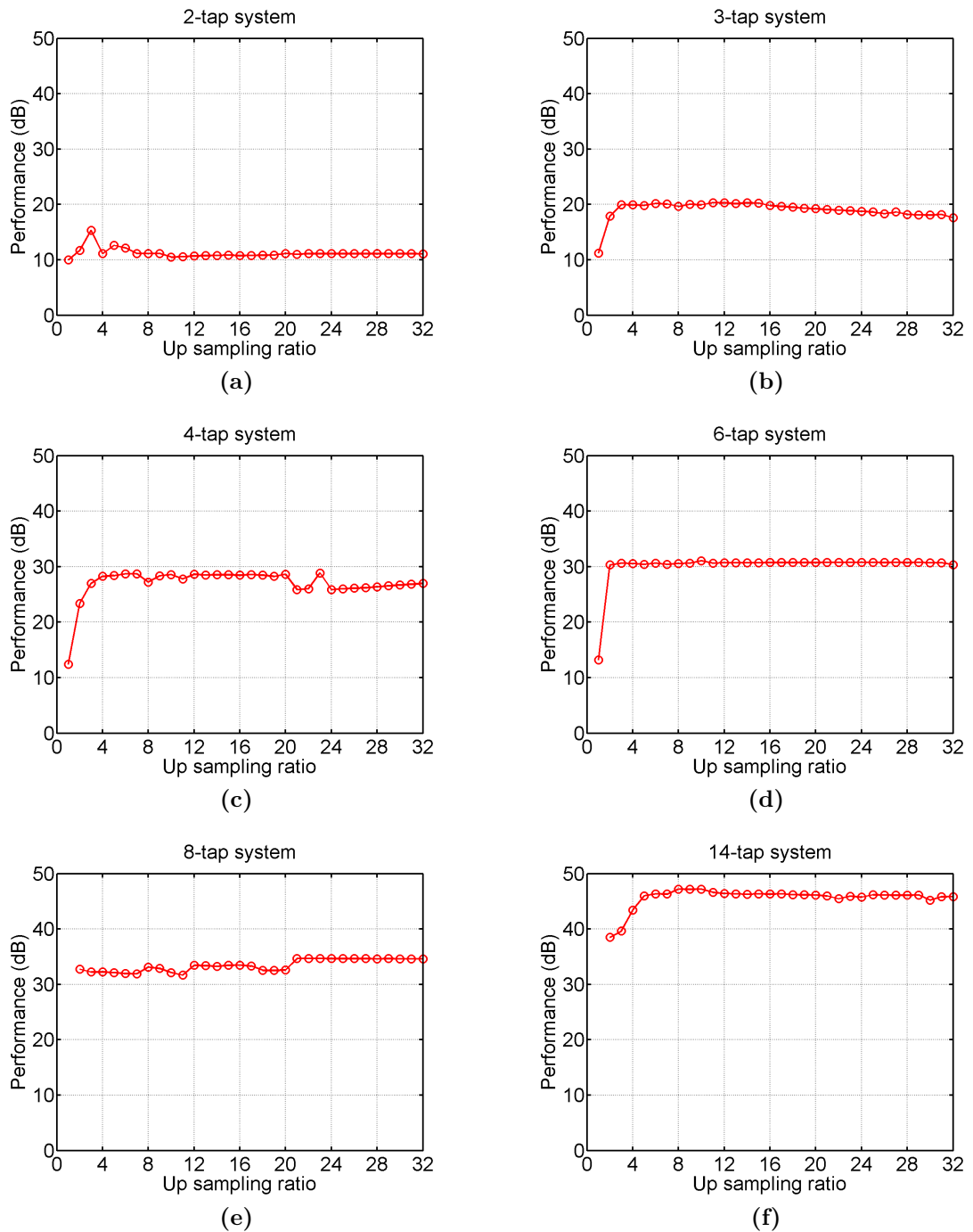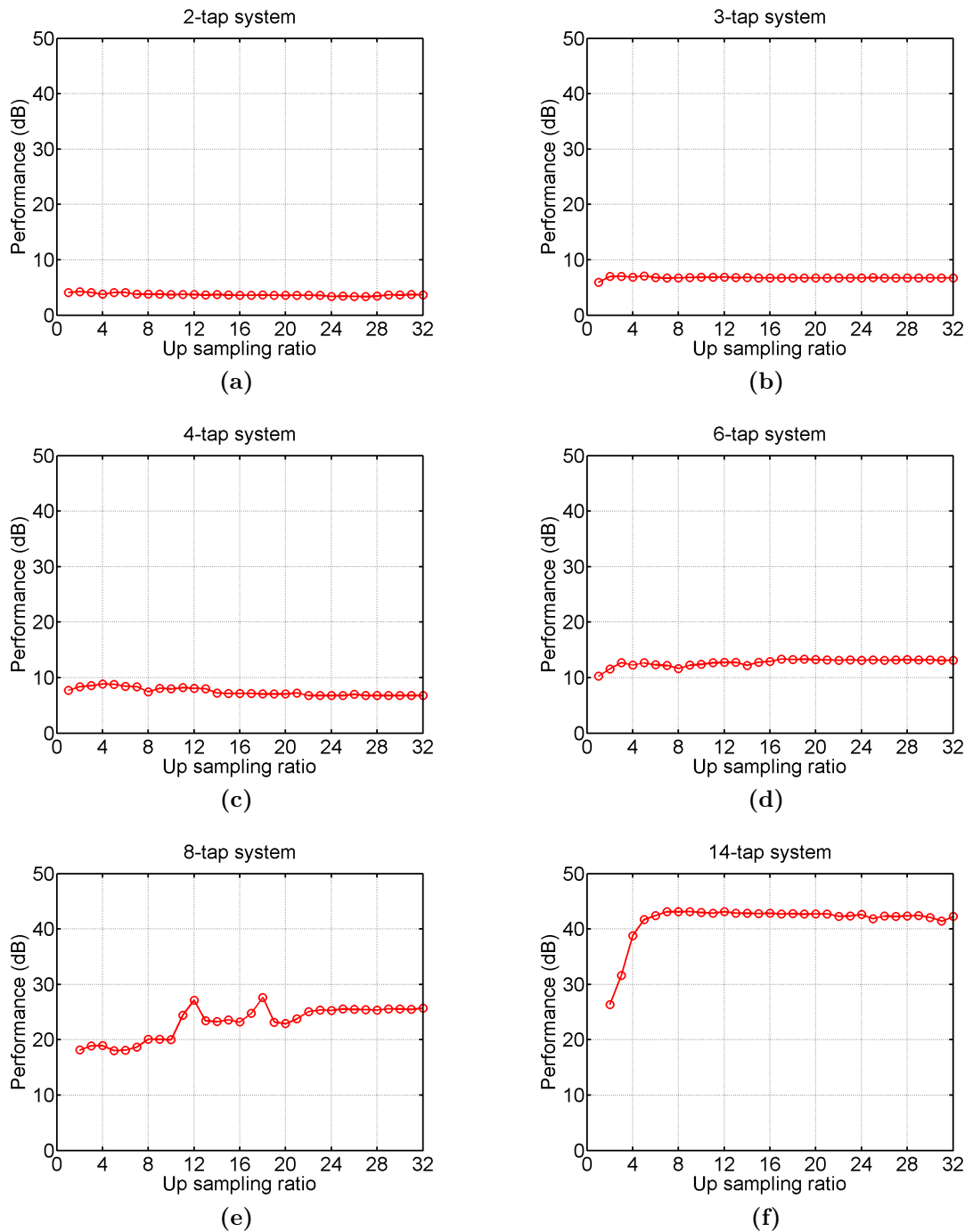
Figure 5.13: Cancellation performance using MCoSaMP with respect of the up-sampling ratio for the cavity duplexer. (a) Two taps. (b) Three taps. (c) Four taps. (d) Six taps. (e) Eight taps. (f) Fourteen taps.
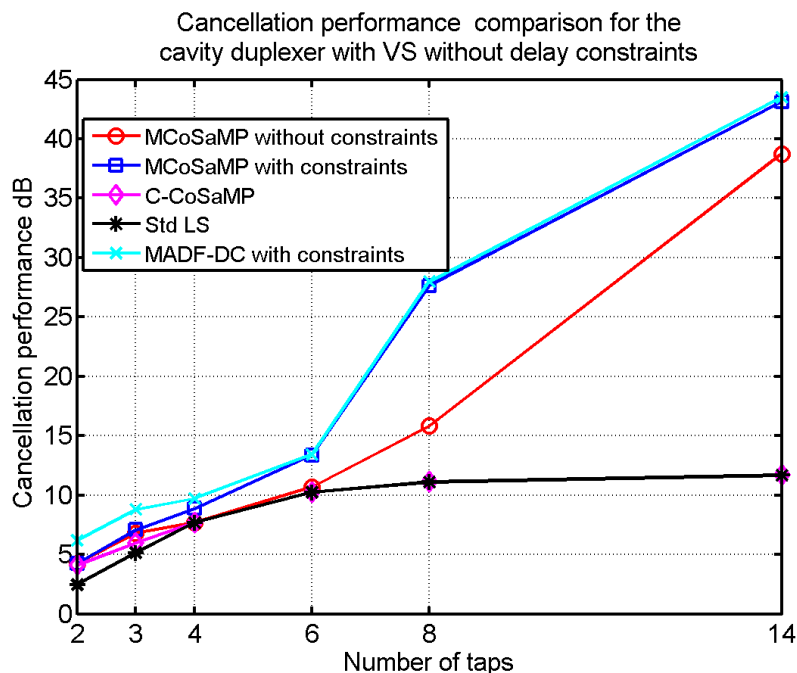
Figure 5.14: Cancellation performance comparison between with and without delay limit constraints for cavity duplexer using MCoSaMP.

Chosen parameters for the optimal performance   The details of the peak cancellation performance, as well as the corresponding up-sampling ratios and delay limits are summarised in Table. 5.3. For all the number of taps settings, the maximum up-sampling ratio is 18. This represents the maximum delay resolution of 1.59 ns. Compared to the results that are shown in Table. 4.4, this value is more implementable when tunable delay lines are used. The required maximum delay values for MCoSaMP using two, three, eight and fourteen taps are more than the ones for MADF-DC. However, for the differences between the maximum and minimum values of the estimated delays, they are smaller for MCoSaMP than for the MADF-DC technique, with an exception of the system using two taps. One of the possible reasons is that MCoSaMP adapts both the delays and tap weights at the same time, versus MADF-DC only estimates one delay each time. Therefore, for MADF-DC, the previous tap delay could have more errors and require later taps to compensate. For this reason, the later taps could become more spread.

Spectrum results   The magnitude responses of the remaining leakage after the cancellation are shown in Figure. 5.15. With two taps, MCoSaMP produces more suppression at most of the frequencies than the LS algorithm within the band of

Table 5.3: The summarized cancellation performance that is achieved using MCoSaMP with corresponding delay limit constraints and up-sampling ratios for the cavity duplexer.

No. of taps	Min. delay limit (ns)	Max. delay limit (ns)	Can. perf. (dB)	Upsamp. ratio
2	0	100.4	4.24	2
3	20	80.4	7.07	5
4	10	120.4	8.86	4
6	60	70.4	13.36	17
8	70	120.4	27.64	18
14	70	120.4	43.15	9

interest. However, at the lower side of the frequency band, the resulting leakage after cancellation using MCoSaMP rises up and reaches to a point that is approximately 5 dB greater in magnitude than the one before the cancellation. At the frequencies between 5 MHz and 9 MHz to the right side of the centre frequency, i.e., where the null is without the cancellation, the resulting leakage is much greater than the original one. The poor performances at these frequencies are mainly due to the insufficient number of taps that are used in the cancellation system. The resulting spectrum using C-CoSaMP shows that there is about 10 dB of suppression at -5 MHz location from the centre frequency. As the frequency moves away from -5 MHz, the cancellation reduces.

For the cancellation system using three taps, the proposed MCoSaMP technique is better in cancellation performance than the LS algorithm at most of the frequencies across the band of interest. The exceptions are at the frequencies between -11 MHz and -6 MHz on the left side of the centre frequency where the classic technique is better than the proposed one. Comparing C-CoSaMP with LS, the first one has two more nulls in the resulting spectrum. They are located at the centre frequency and 10 MHz locations. At other frequencies, the results using the two techniques are similar.

For four taps, at any frequency that is less than 4 MHz from the centre, MCoSaMP is in general better than the other techniques. At the frequency that is greater than 4 MHz, MADF-DC overall performs better. Using more than four taps, LS and
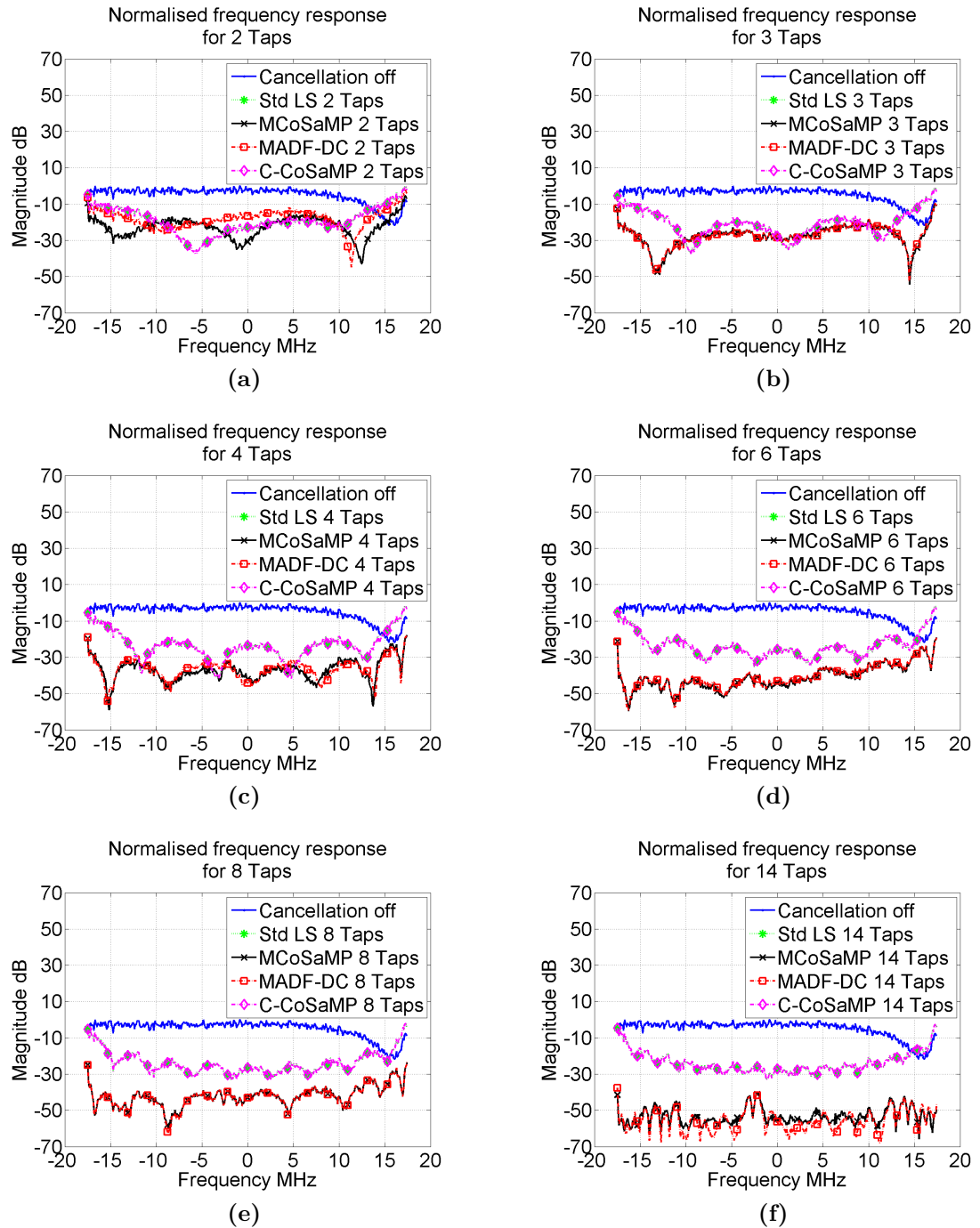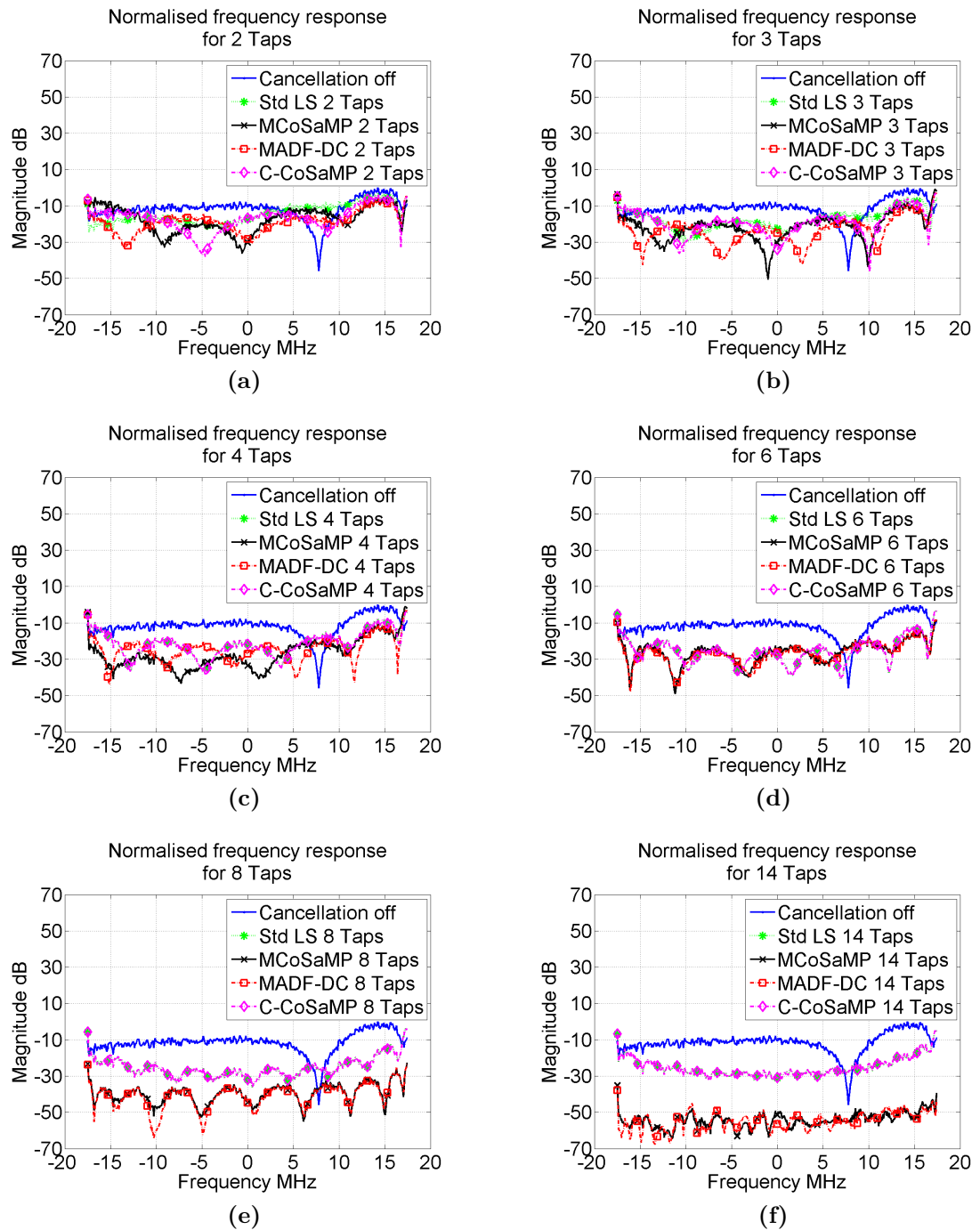
Figure 5.15: Normalised frequency response of the leakage, with and without the cancellation system using MCoSaMP for the cavity duplexer . (a) Two taps. (b) Three taps. (c) Four taps. (d) Six taps. (e) Eight taps. (f) Fourteen taps.

C-CoSaMP are the same in the resulting spectrum.

In the case that the cancellation system is implemented using six taps, the resulting leakages between using the proposed MCoSaMP and the classic LS techniques are similar. Overall, the performance of MCoSaMP is slightly better than the classic technique. Increasing the number of taps beyond six advances the performance difference between the proposed technique and the LS algorithm, significantly. In comparison with the MADF-DC, the resulting magnitude responses of the leakage after the cancellation using the MCoSaMP technique are very similar, which agree with the results that are shown in Figure. 5.14.

5.5.4 Summary of the Results

Simulation results using MCoSaMP have been presented and discussed in this section. These simulations have been performed for the three duplexing devices, i.e., the circulator, the ceramic and the cavity duplexers. The results have shown that constraining the estimated delays within a certain range can potentially provide better modelling performance. However, unlike the MADF-DC technique, the performance improvement by using the delay limit constraints is limited. In most of the simulations, the performance improvement is only marginal. As discussed at the beginning of this chapter, it is desirable to have a second modelling technique which can achieve the same level of modelling performance as the MADF-DC technique, but is less dependent on the delay limit constraints so that the estimation time could be further reduced without affecting the modelling performance significantly. Therefore, it seems MCoSaMP is well suited to do this. However, for the cavity duplexer with eight taps, the performance advantage of using the delay limit constraints can improve the performance by approximately 12 dB when using MCoSaMP. This could indicate that the effectiveness of constraining the estimated delays for MCoSaMP is dependent on the characteristics of the duplexing device. By observing the results, it seems that constraining the estimated delays is more useful when the characteristics of the duplexer are more complex. The estimation time reduction will be discussed in more detail later in this chapter.

The relationship between the cancellation performance and the up-sampling ratio has been established for the proposed MCoSaMP technique. Simulation results show that for MCoSaMP, sweeping the up-sampling ratio achieved up to 5 dB of the

performance improvement, compared to using a single large up-sampling ratio value. In comparison, for MADF-DC, the performance improvement is only marginal. We could receive a similar conclusion that sweeping the up-sampling ratio is a better option if the cancellation performance is more critical over the estimation time. The details of the estimation time of the proposed technique will be discussed further later in this chapter.

Overall, the results have shown that the proposed MCoSaMP can provide much better modelling performance than the classic techniques. Between MCoSaMP and MADF-DC, there is no solid evidence showing one is better than the other. As discussed earlier, estimation time reduction with less modelling performance penalty is the aim. In the next section, comparisons between MCoSaMP and MADF-DC will be further explored when the cancellation system is implemented using only passive components.

5.6 Performance Using Only Passive Components

As discussed in the previous chapter, it is important to know the performance of the proposed modelling technique when only passive components are used. This is done by performing simulations with insertion loss of the passive components added. The performance for the circulator is shown first and followed by ones for the ceramic and cavity duplexers.

5.6.1 Circulator

The cancellation performance that is obtained by using only the passive components has been shown in Figure. 5.16. This figure is obtained with a circulator as the duplexing device. For comparison purposes, the leakage suppression rates that are obtained without the consideration of only using passive components are also shown. In addition, the passive implementation results for the same duplexing device from the previous chapter are also shown in this figure. As discussed in Sec. 4.7, it is expected to see that the performance using passive components reduces from the performance obtained using active components (shown in Figure. 5.16 as $AnyType.MCoSaMP$). A higher order system suffers from more degradation in

performance compared to a lower order system. The result also shows that in general, using only passive components has a bigger performance impact on MCoSaMP than MADF-DC when the circulator is used as the duplexing device.

For four taps or more, there are no cancellation performance shown in Figure. 5.16 for all unit insertion loss settings. This indicates that the cancellation system using the proposed MCoSaMP requires active components in order to be implemented using more than three taps. This is similar to results that are achieved in the previous chapter. With three taps, it is possible to implement the system without the need for gain components, providing that the unit insertion loss of the delays is less than 0.4 dB/ns. However, the resulting cancellation performance decreases by approximately 13 dB from 47 dB which is obtained without the additional considerations of the implementation. Compared to MADF-DC, MCoSaMP with three taps achieves about 10 dB worse cancellation performance. The leakage suppression rates using two taps are similar for both of the proposed techniques with passive components. They are less than 1 dB worse than those without passive components considerations. However, MADF-DC is less than 1 dB better than MCoSaMP. The performance of both techniques decreases with the increase of the unit insertion loss of the delays. However, the degradation of the performance is negligible.

5.6.2 Ceramic Duplexer

In Figure. 5.17, the performance comparison results are shown for the ceramic duplexer. In general, the simulation results show the performance degradation of using the passive components when the ceramic duplexer is used is not as severe as the circulator case. When the unit insertion loss is 0.1 dB/ns, there is no degradation in performance at three and four taps for both MCoSaMP and MADF-DC techniques. The performance remains the same for three taps when the unit insertion loss increases to 0.5 dB/ns. Although other taps suffer from performance degradation, the performance drop is not as significant as the circulator case. This can be expected as the optimal tap weights of the circulator case are in general greater than the ceramic. This is due to the reason that the ceramic duplexer has higher attenuation (approximately 55 dB, see Figure. 2.18) within the band of interest than the circulator.

Unlike MADF-DC, a cancellation system using MCoSaMP with fourteen taps can
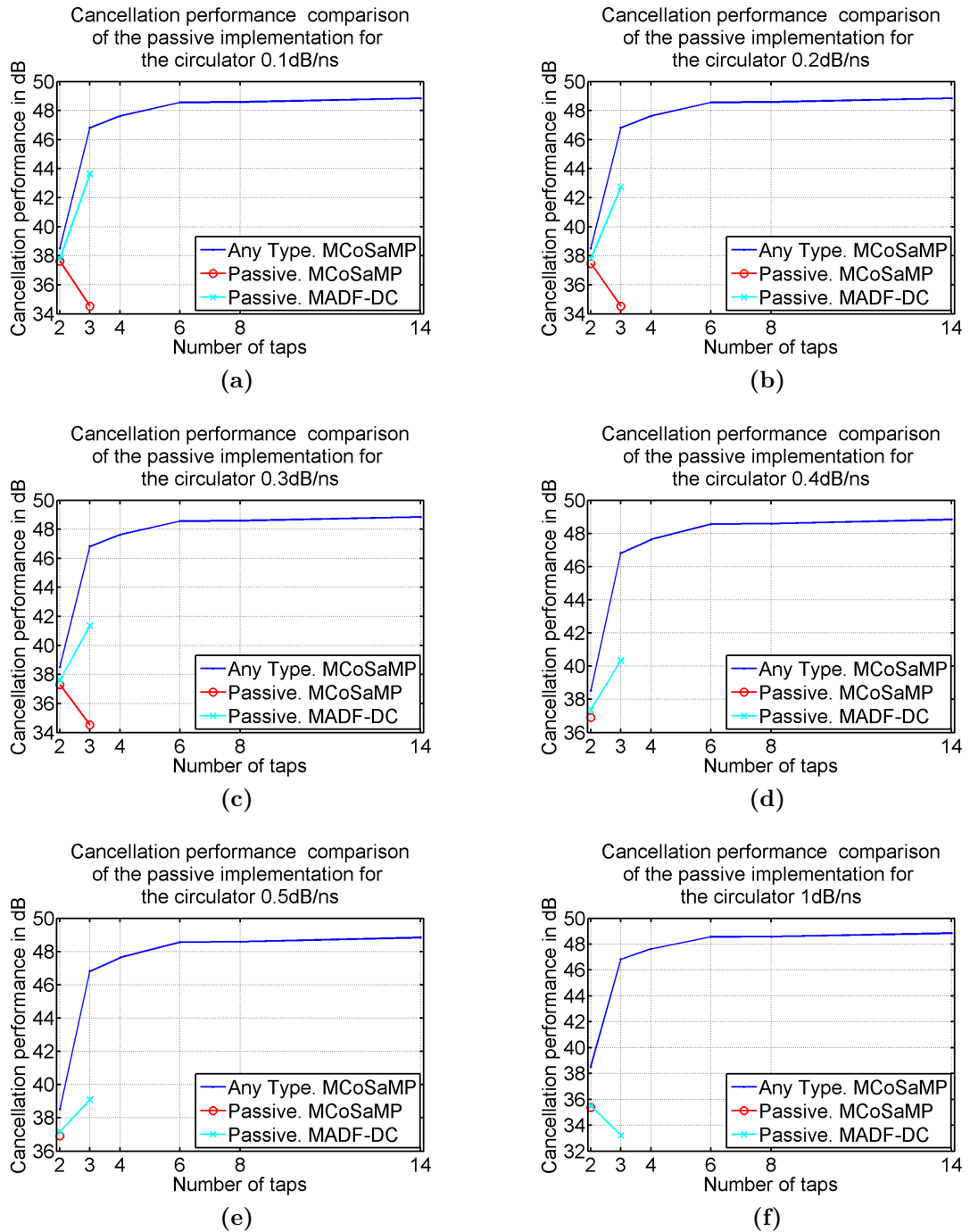
Figure 5.16: Cancellation performance comparison using MCoSaMP with delay limit constraints between using passive and any type of components with respective to number of taps for the circulator. (a) Unit insertion loss of delay at 0.1 dB/ns. (b) Unit insertion loss of delay at 0.2 dB/ns. (c) Unit insertion loss of delay at 0.3 dB/ns. (d) Unit insertion loss of delay at 0.4 dB/ns. (e) Unit insertion loss of delay at 0.5 dB/ns. (f) Unit insertion loss of delay at 1 dB/ns.

be implemented using only passive components at no more than 0.1 dB/ns unit insertion loss of the delays, though the performance is decreased from 47 dB to 39 dB. For eight taps, the system with MCoSaMP is implementable using only passive components. The reduction of the cancellation performance is less than 3 dB, providing that the unit insertion loss of the delays is no more than 0.3 dB/ns. In the four and six taps cases, the unit insertion loss requirement of the delays is changed to less than 1 dB/ns in order to implement the system with passive components using the MCoSaMP technique. The degradation of the cancellation performance is approximated as 1 dB at most. In comparison with the MADF-DC technique, MCoSaMP is slightly worse. Compared to the MADF-DC technique, better cancellation performance for the two taps case using passive components are given by MCoSaMP. The maximum difference is only about 5 dB when the delays with less than 1 dB/ns unit insertion loss are used. In the case of three taps, the performance with MCoSaMP decreases with the increasing of the unit insertion loss. The reduction of such performance reaches its maximum when the unit insertion loss is at about 1 dB/ns. Such degradation is about 10 dB for both MADF-DC and MCoSaMP techniques. As discussed in Sec. 4.7 and the previous section, such large performance degradation is expected as the estimated tap weights are further constrained by the unit insertion loss of the delay lines.

5.6.3 Cavity Duplexer

Setup   The simulations for the cavity duplexer are also performed based on the architecture shown in Figure. 3.1. The simulation settings for the cavity duplexer are the same as the ones for the ceramic duplexer.

Results   For the cavity duplexer, the cancellation system using MCoSaMP with fourteen taps is only implementable without gain components when the unit insertion loss of the delays is 0.1 dB/ns. This can be seen from Figure. 5.18. The modelling performance using MCoSaMP with only passive components reduces to about 25 dB from 42 dB which was obtained without limiting the types of components. However, this result can be seen as an improvement compared to MADF-DC. This is because the same passive system using MADF-DC is not implementable according to Figure. 4.21. For eight taps, the unit insertion loss needs to be less than or equal
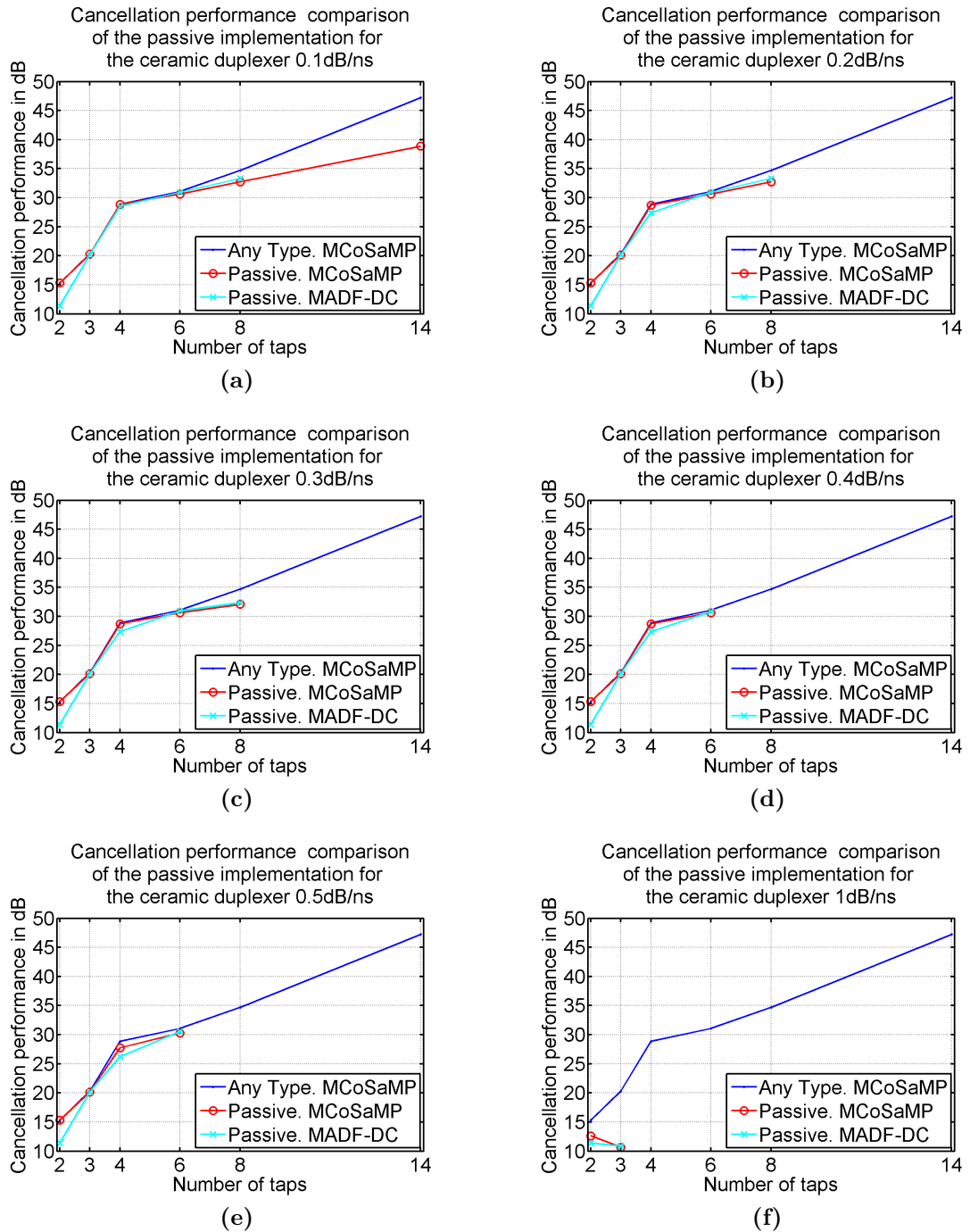
Figure 5.17: Cancellation performance comparison using MCoSaMP with delay limit constraints between using passive and any type of components with respective to number of taps for the ceramic duplexer. (a) Unit insertion loss of delay at 0.1 dB/ns. (b) Unit insertion loss of delay at 0.2 dB/ns. (c) Unit insertion loss of delay at 0.3 dB/ns. (d) Unit insertion loss of delay at 0.4 dB/ns. (e) Unit insertion loss of delay at 0.5 dB/ns. (f) Unit insertion loss of delay at 1 dB/ns.

to 0.2 dB/ns in order to implement the delays and taps weights that are obtained by MCoSaMP using only passive components. The performance is degraded by about 13 dB compared with the one obtained without passive components considerations. For fourteen taps, this requirement becomes 0.1 dB/ns and the performance is degraded by approximately 17 dB (from 43 dB to 26 dB).

For a six taps passive system using MCoSaMP, the unit insertion loss of the delays must be smaller than 0.4 dB/ns. Even with the passive components consideration, the performance of such a system is no more than 2 dB lower than the system using any types of components. For two, three and four taps, the performance of the passive system is nearly identical to the one without passive considerations, as long as the unit insertion loss is no more than 0.5 dB/ns. Those systems are still implementable with lossier delay lines at the cost of performance degradation.

Generally, MADF-DC still achieves better performance than MCoSaMP for passive components implementation, apart from the fourteen taps case. At 0.4 dB/ns, MCoSaMP failed to provide parameters that are implementable using only passive components for six taps case. In comparison, MADF-DC achieves about 10 dB of cancellation performance under the same conditions.

5.7 Estimation Speed

Previous sections have shown that the proposed MCoSaMP technique has a similar modelling performance to the MADF-DC technique. This has achieved a part of the goal set at the beginning of this chapter, i.e. an alternative technique with little performance degradation from the MADF-DC technique. In this section, the estimation speed will be explored. This section will start with the estimation speed comparison of the two proposed techniques as well as the classic techniques. Since MCoSaMP can achieve a better modelling performance by sweeping through the elements of up-sampling and delay limit constraints vectors, a low estimation speed can be expected. The speed reduction techniques will be then discussed. The reduced estimation time as well as the modelling performance will be compared between MCoSaMP and MADF-DC. At the end of this section, it will be clearer on if the objective of this chapter has been achieved.
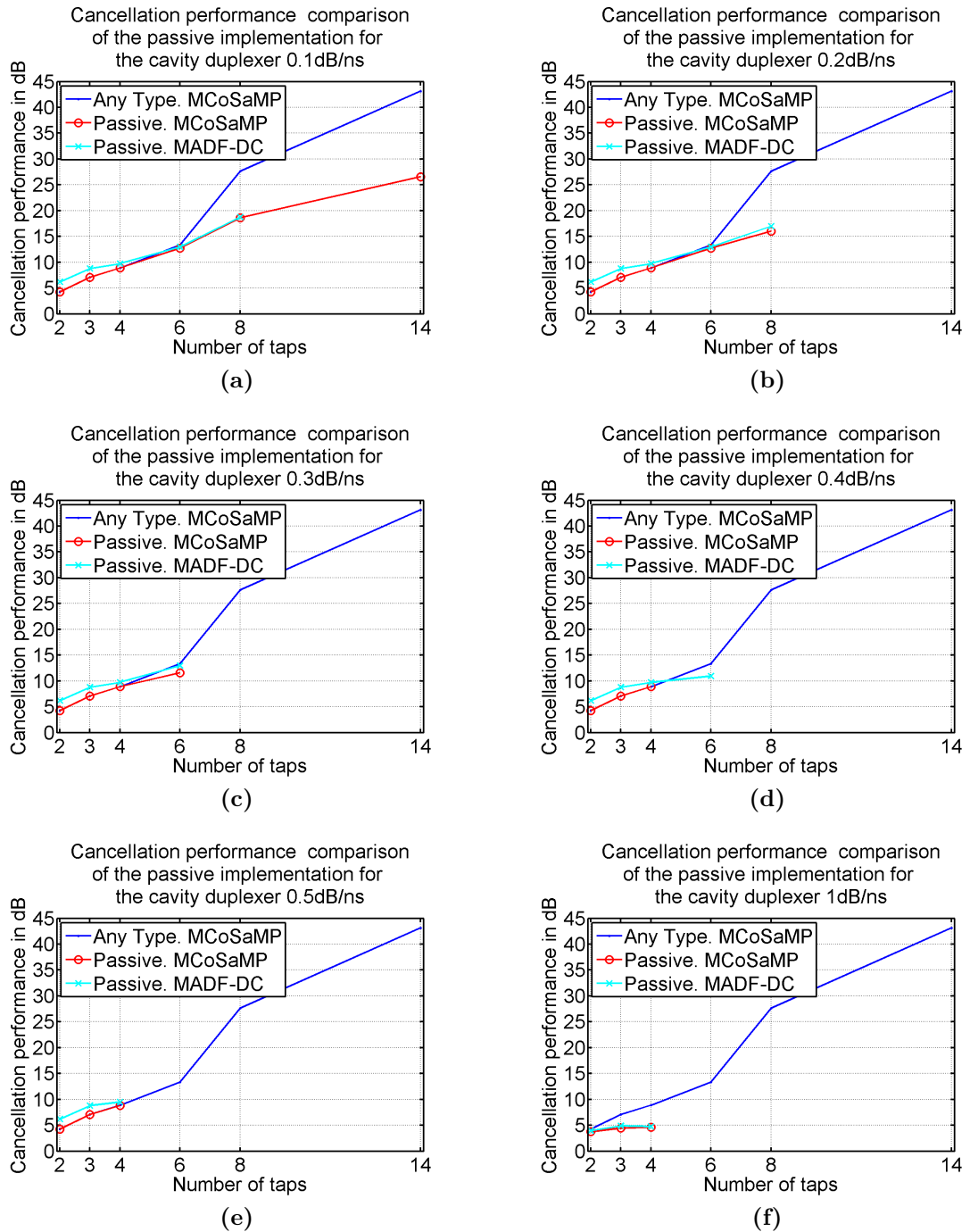
Figure 5.18: Cancellation performance comparison using MCoSaMP with delay limit constraints between using passive and any type of components with respective to number of taps for the cavity duplexer. (a) Unit insertion loss of delay at 0.1 dB/ns. (b) Unit insertion loss of delay at 0.2 dB/ns. (c) Unit insertion loss of delay at 0.3 dB/ns. (d) Unit insertion loss of delay at 0.4 dB/ns. (e) Unit insertion loss of delay at 0.5 dB/ns. (f) Unit insertion loss of delay at 1 dB/ns.

5.7.1 Speed in General

The estimation time using MCoSaMP is shown in Table. 5.4. In the comparison table, the estimation speed using classic techniques and MADF-DC has also been included.

Table 5.4: Comparison of the estimation speed between the classic techniques and MCoSaMP

Type of Duplexer	System Order	Estimation Time			
		C-ADF (s)	MADF-DC (hours)	C-CoSaMP (s)	MCoSaMP (hours)
Cavity	2	0.58	3.36	1.39	9.68
	3	0.79	4.99	1.52	13.25
	4	1.07	5.56	0.06	10.97
	6	1.67	11.29	0.08	18.63
	8	2.34	11.77	0.05	20.12
	14	4.42	32.75	0.06	52.19
Ceramic	4	1.27	5.55	0.29	6.5

MCoSaMP   Firstly, the estimation time using MCoSaMP increases with the order of the system in general. However, in the case that the cancellation system has three taps, the estimation time is longer than the four taps case. Additionally, unlike MADF-DC, the increase of the estimation time using MCoSaMP follows neither a linear, nor an exponential pattern. Furthermore, for the fourth order cancellation system using MCoSaMP, the estimation time for the cavity duplexer is 10.97 hours, whereas for the ceramic duplexer, it is only 6.5 hours.

The reason for these observations is that for each unique configuration of the up-sampling ratio and delay limit constraints, MCoSaMP would iteratively process the estimation, i.e., up to the maximum iteration value that is specified during the initialization. In the simulation setup of this chapter, the maximum iteration is 100 which is already given in Sec. 5.4. The estimation is terminated once the number of iterations has reached the maximum value. Additionally, a desired tolerance is also supplied in the initialization step. As explained in Sec. 5.2, this value defines the desired Euclidean norm of the current residue, as well as the difference of the residues

between the current and the previous iterations. Once either of these two values has been reached, an early termination of the estimation process occurs. The number of iterations that is required for each unique configuration of the up-sampling ratio and delay constraints is different. This value also depends on the characteristics of the duplexing devices. As a result, the estimation time for different types of duplexing devices is different. Also the estimation time doesn't follow a simple pattern.

MCoSaMP VS C-CoSaMP Comparing MCoSaMP with C-CoSaMP, the prior one takes much longer to complete the estimation. For the C-CoSaMP technique, it can be noted that the computation speed for the system using more than three taps is faster than the one for the second or third order system. This is simply due to the reason that a larger number of iterations are needed for the system using less than four taps. This has been discussed in the previous sub-section. For the ceramic duplexer, the estimation time of four taps is also different from the one for the cavity duplexer when C-CoSaMP is used. This phenomenon is similar to MCoSaMP and has been discussed in the previous sub-section.

MCoSaMP VS MADF-DC It can be seen from Table. 5.4 that the estimation time using MCoSaMP is generally much longer than the one using MADF-DC. For the ceramic duplexer, the computation time using the two techniques is similar. However, MADF-DC still takes about 1 hour less time than the MCoSaMP technique. This seems that MCoSaMP has failed the objective of this chapter. It is still too early to justify this since the estimation time shown in Table. 5.4 is based on a large number of sweeps of the up-sampling ratio and delay limit constraints parameters. Reducing the number of sweeps can significantly reduce the modelling estimation time. This will be shown in Sec. 5.7.2 in more detail.

C-ADF VS C-CoSaMP Both of the classic techniques complete the estimations in seconds, which is dramatically less than the two proposed modelling techniques. Between the two classic techniques, in the case that the order of the cancellation system is less than four, C-ADF takes less time than the C-CoSaMP technique. However, once the order of the system is greater than four, the required estimation time using C-CoSaMP is dramatically reduced and is much less than the C-ADF technique.

5.7.2 Reducing the Estimation Time

In the previous chapter, the estimation time using MADF-DC could be reduced by replacing the sweeping of the up-sampling ratio with a single value and increasing the step size of the delay limit constraints. In this section, similar methods will be explored.

The duplexing device used for these explorations is the ceramic duplexer. The order of the system is set to be four. The original settings are already provided in Sec. 5.4. The maximum and minimum delay limit constraints are swept from 0.4 ns to 200.4 ns and from 0 ns to 200 ns, respectively. The step size for both of the delay vectors is 10 ns. The original up-sampling ratio vector is swept from 1 to 32 in step of 1. Firstly, reducing the estimation time by using a single up-sampling ratio is discussed.

Using a single up-sampling ratio As previously discussed in this chapter, MCoSaMP is more dependent on the sweeping of the up-sampling ratio than MADF-DC. It can be expected that for the MCoSaMP, replacing the sweeping procedures of the up-sampling ratio with a single value could degrade the cancellation performance more than the MADF-DC technique. On the other hand, the estimation time should be greatly reduced compared to the original time that is shown in Table. 5.4 using MCoSaMP. From the results that are shown in Table. 5.5, the expectation has been met. The estimation time of MCoSaMP using a single up-sampling ratio is reduced from 6.5 hours to 0.4 hours. However, the performance is degraded by about 1.89 dB. The original performance that is given in Table. 5.2 is 28.87 dB.

Compared to MADF-DC, the estimation time using MCoSaMP is greater. This is because of the iteration property of this technique. The performance obtained by using MCoSaMP is not as good as MADF-DC. This is as expected since MADF-DC is less dependent on the sweeping of the up-sampling ratio. For MCoSaMP, sweeping the up-sampling ratio could improve the performance.

Once again, the estimation time obtained using MCoSaMP is longer than the one obtained using MADF-DC. The performance degradation of the MCoSaMP by using a large single up-sampling ratio is also a lot greater than MADF-DC. The estimation time comparison between MCoSaMP and MADF-DC will continue by reducing the number of sweeps of the delay limit constraints parameters.

Table 5.5: The reduced estimation time and cancellation performance using MCoSaMP with single up-sampling ratio

	Up-sampling Ratio	Estimation Time (hours)	Cancellation Performance (dB)	Performance Degradation (dB)
MADF-DC	32	0.15	28.17	0.75
MCoSaMP	32	0.40	26.98	1.89

Increasing the increment of the delay limit constraints   The estimation speed can also be improved by increasing the step size of the delay limit constraints. Simulations have been performed with different step sizes. The resulting performance and the estimation time are shown in Table. 5.6.

Firstly, as expected, the estimation time is vastly reduced when the delay step is increased. In general, MCoSaMP requires more time to estimate the system than MADF-DC. As discussed earlier, this is mainly due to the reason that MCoSaMP is an iterative algorithm and the number of iteration for each set of up-sampling ratio and delay limits can be as large as 100. This value has been set in the simulation setup. Secondly, the cancellation performance for the ceramic duplexer using MCoSaMP is not degraded significantly, which is different from what has been seen in the MADF-DC chapter. This can be seen in Table 5.6(c) where for cancellation performance greater than 28 dB, MCoSaMP only uses about 0.11 hours. In comparison, MADF-DC needs 1.34 hours to achieve a similar level of cancellation performance. This is a major improvement over MADF-DC if the estimation time requirement is critical. The results shown in Table. 5.6 indicate that the goal of investigating the MCoSaMP technique, i.e. reducing the estimation time without significant performance degradation over MADF-DC, has been fully achieved. On the other hand, by setting the delay limit increment to a large value or even without sweeping the delay limit parameters, the MCoSaMP could achieve a much better performance than MADF-DC (under the same condition) when the same estimation time is given.

Although sweeping the delay limit constraints may seem unnecessary from the modelling performance of the ceramic duplexer, it can provide a much better modelling performance for the cavity duplexer as shown in Figure. 5.14. The advantages of sweeping the delay limit constraints depend on the characteristics of the duplexing

device. For this reason, the sweeping of the delay limit constraints is recommended and a smaller delay limit increment should be chosen unless the estimation time is critical.

Certainly, if estimation time is critical, it can be reduced by using a single up-sampling ratio in combination with a large delay limit increment. However, the discussion on the resulting performance and the estimation time will not be included in this thesis.

Additional methods for reducing the estimation time   Two additional methods for reducing the estimation time are the same as discussed in Sec. 4.8.2. Since MCoSaMP is an iterative algorithm, it can be expected that the time reduction ratio of the estimation time using MCoSaMP would be lower than the one using MADF-DC. Since the cancellation performance achieved both by increasing the step size for sweeping the up-sampling ratio and reducing the sweeping range of the delay limit constraints depends on the characteristics of the duplexer, performance degradation is possible. For this reason, these two methods are not suggested while estimation time is not a critical aspect.

5.7.3 Summary of the Estimation Time using MCoSaMP

In order to compare MADF-DC and MCoSaMP techniques more directly, the comparison between MADF-DC and MCoSaMP has been summarised in Table. 5.7, although these results have already been shown in this chapter. The default setups include sweeping the up-sampling ratio from 1 to 32 in step of 1, sweeping the minimum and maximum delay limit constraints from 0 ns to 200 ns and 0.4 ns to 200.4 ns, respectively in step of 10 ns. The ceramic duplexer is used as the duplexing device. The order of the cancellation system is four. The performance and estimation time shown in Table. 5.7 are obtained by using the default setups except the corresponding row in the table.

It was shown in Table. 5.7 that MCoSaMP suffers from slow estimation compared with MADF-DC and classic techniques when the up-sampling ratio and delay limit constraints parameters are swept according to the setup shown in Sec. 5.4. By keeping the sweeping of the delay limit constraints unchanged, the estimation time could

Table 5.6: Table cancellation performance and computation time VS the delay increments using MCoSaMP. (a) Estimation time. (b) Cancellation performance. (c) Minimum estimation time comparison for more than 28 dB of cancellation.

(a)

Delay Limit Increment (ns)	Estimation Time (hours)	
	MADF-DC	MCoSaMP
3	58.23	78.0133
5	23.62	35.0147
10	5.55	6.5067
20	1.34	2.3776
50	0.28	0.3738
100	0.10	0.1108

(b)

Delay Limit Increment (ns)	Cancellation Performance (dB)	
	MADF-DC	MCoSaMP
3	29.00	29.14
5	28.99	28.95
10	28.92	28.87
20	28.92	28.73
50	23.09	28.73
100	18.52	28.73

(c)

	Estimation Time (hours)	Achieved Performance (dB)	Delay Limit Increment (ns)
MADF-DC	1.34	28.92	20
MCoSaMP	0.1108	28.73	100

be significantly reduced by using a large single up-sampling ratio instead of sweeping. However, the resulting estimation time for MCoSaMP is still much longer than MADF-DC and the modelling performance is also degraded. When keeping the sweeping of the up-sampling ratio according to the setup shown in Sec. 5.4 and reducing the number of sweeps of the delay limit constraints, the estimation time is significantly reduced for the MCoSaMP. The performance achieved is only marginally degraded. In comparison, the performance achieved using MADF-DC is degraded significantly when the sweep step of the delay limit constraints is changed to 100 ns. This shows that it is possible to achieve a better performance using MCoSaMP at less cost of the estimation time compared with MADF-DC. Nevertheless, in the case that the estimation time is not critical such as the proposed cancellation system, sweeping of the up-sampling ratio and delay limit constraints should be carried out and the sweep step size should be chosen as small as possible to achieve a better performance.

Table 5.7: Summarised comparison between MCoSaMP and MADF-DC techniques.

Simulation Setup	Values of Setup	Cancellation Performance (dB)		Estimation Time (Hours)	
		MADF-DC	MCoSaMP	MADF-DC	MCoSaMP
Up-sampling ratio sweeping step	1	28.92	28.73	5.55	6.5
Single up-sampling ratio	32	28.17	26.98	0.15	0.4
Delay limit constraints sweeping step (ns)	3	29.00	29.14	58.23	78.0133
	5	28.99	28.95	23.62	35.0147
	10	28.92	28.87	5.55	6.5067
	20	28.92	28.73	1.34	2.3776
	50	23.09	28.73	0.28	0.3738
	100	18.52	28.73	0.10	0.1108

5.8 Summary

Since the MADF-DC technique suffers from slow estimation speed, an alternative modelling technique has been investigated in this chapter. This technique is named as MCoSaMP and is designed to achieve a similar level of modelling performance as MADF-DC, but at a faster estimation speed. This has been shown in Table 5.6(c). The MCoSaMP is developed based on the C-CoSaMP technique. The simulation results in this chapter have shown that a better modelling accuracy can be achieved by using the proposed MCoSaMP technique in comparison with the C-CoSaMP and LS techniques. This is achieved by sweeping the up-sampling ratio and delay limit constraint parameters. Using each combination of these three parameters, the C-CoSaMP is performed. The parameters (up-sampling ratio, maximum and minimum delay limit constraints) that produce the highest modelling performance are chosen to be the optimal ones. The corresponding estimated delays and tap weights will be used for RF implementation.

Simulations using MCoSaMP have been performed with three types of duplexing devices, including the circulator, the ceramic and the cavity duplexers. Simulated results have been shown in this chapter and comparisons between MCoSaMP (delay constrained and unconstrained) and the classic LS techniques have been presented. Considerations of using only passive components have been added and simulations have been performed with respect to different values of unit insertions of the delays. Generally, significantly better performance has been achieved using either the constrained or the unconstrained MCoSaMP, compared to the classic LS algorithm.

Between MCoSaMP and MADF-DC techniques, it is difficult to choose a better one. The unconstrained MCoSaMP is significantly more accurate than the unconstrained MADF-DC. Its performance is in general not significantly degraded from the constrained one, with a few exceptions for the cavity duplexer. This is due to the reason that MCoSaMP estimates all the taps, including the delays and tap weights, at the same time. The error of the estimated group delay response could be compensated during iteration. In comparison, the MADF-DC only determines the delays in a sequential manner. It is more prone to delay estimation error. Therefore, MADF-DC is more dependent on the sweeping of the delay limit constraints.

On the other hand, MADF-DC generally produces a better performance. In certain cases, the passive system using MADF-DC is more implementable than MCoSaMP,

i.e., the system using six taps when the unit insertion loss of the delay is 0.4 dB/ns for the cavity duplexer. Due to the sequential operation property of MADF-DC, estimating the unknown system with a larger number of taps and up-sampling ratios are possible without the critical performance requirement of the PC. In comparison, when using MCoSaMP, a large memory is needed and it is not always feasible. Overall, the performance between MADF-DC and MCoSaMP is similar. The performance difference is only marginal in most of the cases. This satisfies the aim of this chapter, i.e. develop an alternative technique that can achieve a similar level of modelling performance.

Regarding the estimation time, MCoSaMP is compared with MADF-DC technique. The estimation speed of MCoSaMP is slower when the up-sampling ratio and delay limit constrains are swept across a large range in a smaller step. This is mainly due to the reason that MCoSaMP is an iterative algorithm. The maximum iteration is set to be 100 at the simulation setup. This value could be reduced to increase the speed. However, it could result the performance degradation.

When replacing the sweeping of the up-sampling ratio with a single large value and keeping the sweeping of the delay limit constraints unchanged, the estimation time of MCoSaMP is significantly reduced. However, it is still a lot longer than MADF-DC and performance penalty is larger compared with MADF-DC. This is still as expected since the modelling performance results in this chapter have shown that MCoSaMP is more dependent on the sweeping of the up-sampling ratio whereas MADF-DC more depends on the sweeping of the delay limit constraints.

In the case that the number of sweeps of the delay limit constraints is reduced by increasing the sweep size, the estimation time of MCoSaMP reduces significantly. Though the reduced estimation time is still more than for the MADF-DC technique, the difference is small, especially when the delay limit sweeping step is set as 100 ns (shown in Table. 5.6). More importantly, the performance degradation of MADF-DC by increasing the sweeping step of the delay limit constraints is significant. In comparison, MCoSaMP is almost not affected by changing the sweeping step of the delay limit constraints. This can be expected since in the modelling performance results shown in the earlier sections of this chapter, it can be seen that the performance of the MCoSaMP technique is less dependent on the sweeping of the delay limit constraints. Therefore, MCoSaMP is useful if the estimation speed is more important than the modelling performance whereas MADF-DC sacrifices the esti-

mation speed for performance. Since performance cannot be guaranteed by either using a single up-sampling ratio or by increasing the delay limit step, sweeping of these parameters are still suggested with a cost of estimation time.

Upon the completion of this chapter, two proposed estimation techniques in this thesis have all been discussed. All the results that have been presented are from the simulations. In the next chapter, these proposed techniques are applied in an experimental measurement test bench.

5.9 Contributions of this Chapter

The main contributions of this chapter are:

1. Proposing MCoSaMP technique in order to achieve a similar modelling performance, but at a faster estimation speed than the MADF-DC approach.

2. Comparisons have been performed between MCoSaMP and MADF-DC techniques in terms of the resulting cancellation performance, ability of implementing the system using only passive components and the feasibility of expanding the cancellation system regarding the number of taps and up-sampling ratios.

3. Discussing the possibility of reducing the estimation time of MCoSaMP.

6 Implementation and Verification of the Proposed Cancellation System

6.1 Introduction

The previous two chapters have described two methods for determining the delay as well as the attenuation and phase values of each cancellation path in the proposed cancellation architecture. Successful implementation of such cancellation system could theoretically improve the isolation performance of a duplexing device. This has been proven by simulations in the previous two chapters. In this chapter, a test bench will be presented and the effectiveness of the proposed cancellation architecture will be measured. This chapter starts with explaining the transceiver of the test bench.

6.2 The Transceiver of the Test Bench

In order to verify the proposed cancellation system, a test bench is designed. The architecture of the test bench is shown in Figure. 6.1. The test bench consists of the transceiver and the cancellation block. The transceiver includes a transmitter for simulating the source of the in-band TX leakage. In an actual transceiver, this source is the noise floor of the TX signal within RX band. In this section, the transceiver of the test bench is briefly described. The block diagram of the transceiver is shown in Figure. 6.2. This diagram shows the major components and instruments for capturing the reference and the leakage signals. The RF cancellation block is only shown as a sub-system in this diagram. The details of the implementation of the cancellation block will be explained in later sections.
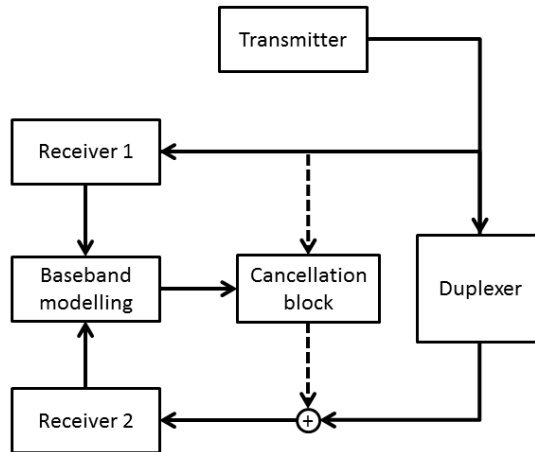
Figure 6.1: The architecture of the test bench

6.2.1 Transmitter

The transmitter consists of a signal source, an amplifier and a filter. The signal source is the Vector Signal Generator (SMU200A, manufactured by Rohde & Schwarz). A 35 MHz bandwidth white noise signal is transmitted by SMU200A. Since the full up-link of WCDMA band VIII is between 880 MHz and 915 MHz, the centre frequency of the TX signal is set as 897.5 MHz so that the cancellation bandwidth covers the full RX band.

A high power amplifier (PA) is used to boost the signal that is generated by SMU200A. The part number of the PA is $1184 - BBM3O6QCK$ which is manufactured by Empower RF systems, INC. The maximum output power is 15 Watt with a gain of approximately 43 dB at 900 MHz. The usable bandwidth is from 700 MHz to 3800 MHz.

Spurious components are generated at 1.9 GHz due to the harmonic distortion of the PA. The ceramic duplexer under-test does not have a good rejection at that frequency comparing to 900 MHz. Thus, the actual leakage signal is much lower in power comparing to the signal at the first harmonic frequencies. The existence of the harmonic component would degrade the receiver performance. For this reason, a bandpass filter[1] is placed in the TX path. Although the maximum peak power

---

[1] The cavity duplexer which has been discussed in the previous chapters is used for this purpose. The antenna to RX path of this duplexer is the desired bandpass filter, with $50\,\Omega$ terminated at the third port .
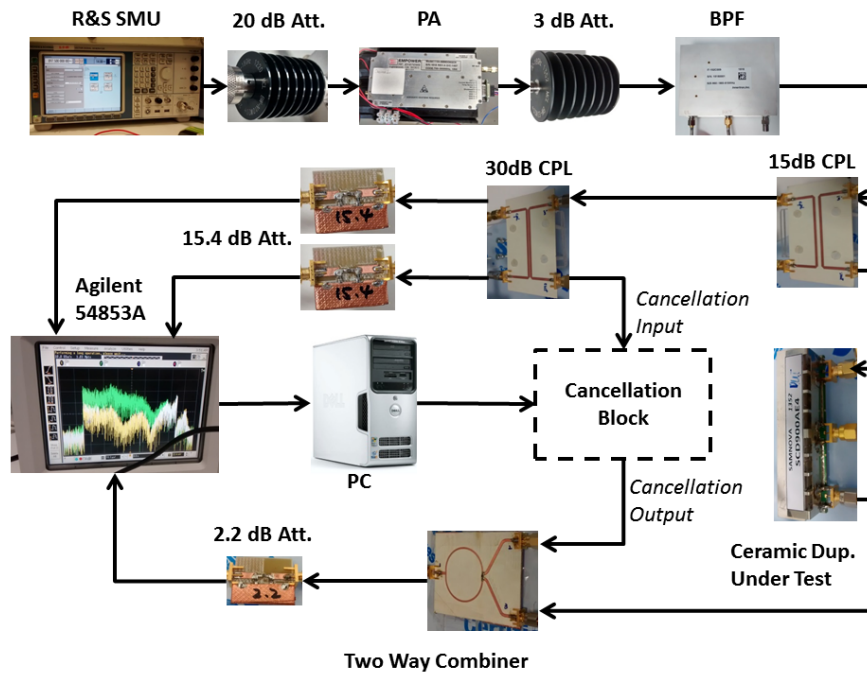
Figure 6.2: Block diagram of the transceiver

rating of SMU200A is about 20 dBm, the PA is still needed in the test bench. This is to ensure that the noise floor of the receiving instrument doesn't affect the cancellation performance. Since the purpose of the PA relates to the performance of the receiving instrument, it will be explained in detail in the receiver part.

Apart from the major components including the SMU200A, the PA and the band-pass filter, there are also a number of components in the transmitter path that is implemented. The 20 dB attenuation that is placed at the input of the PA is only for power limiting purpose. In order to improve the return loss, a 3 dB attenuator is placed at the output of the PA.

6.2.2 Receiver

The duplexer under test is the ceramic one which is used in the previous chapters. In order to capture the reference which is the input signal of the cancellation system and the leakage simultaneously, a high speed digital oscilloscope (54853A) by Agilent has been used. The oscilloscope is controlled by the PC with MATLAB. The scope is equipped with an 8-bits ADC for each channel. The sampling frequency of each

ADC can get as high as 20 GHz. The total noise power of the oscilloscope is approximately -75.2 dBm for the 35 MHz bandwidth[2].

Now, the purpose of the PA in our test bench can be explained in detail. The leakage signal after the cancellation needs to be above the noise floor of the oscilloscope. This is to ensure that the noise level doesn't limit the cancellation performance. From the simulation results that are shown in the previous chapter, the cancellation system could achieve approximately 25 dB of suppression using four taps. For the purpose of observing and capturing, let the leakage after the cancellation be 15 dB above the noise floor. It is already known that the ceramic duplexer can provide at least 55 dB of TX to RX isolation. The power of the TX signal at the input of the duplexer thus needs to be $55 + 25 + 15 = 95\,dB$ above the noise floor of the scope. This requires the average power of TX signal needs to be about $95 - 75.2 = 20\,dBm$ (recall -75.2 dBm is the total noise power of the oscilloscope). The maximum peak power that is available from SMU200A is only 20 dBm. The peak to average power ratio of our TX training signal is about 10 dB. Therefore, the average power that can be delivered by SMU200A is only 10 dBm. As a result, a high power amplifier is placed in the transmitter path.

The 15 dB and 30 dB couplers are for capturing the TX signal. The reference signal should be as close to the input port of the cancellation block as possible. In our test bench, the signal is measured at the through port of the 30 dB coupler. This is used as the reference signal, with the assumption that it is the same as the input signal of the cancellation block when connected. The assumption is valid since the change of signals with different load devices of the same characteristic impedance is very limited. The design technique of the directional couplers will be explained in detail in Sec. 6.2.3.1. Two 15 dB attenuators are placed at the coupling and through ports of the 30 dB coupler in order to improve the return loss. The attenuators are also designed and fabricated in the lab, using resistors and an FR-4 substrate. The reference signal at the coupling port of the 30 dB coupler is used as the trigger source for all the measurements.

A two-way power splitter is used in the RX path to perform the actual cancellation.

---

[2]At minimum scale setting which is 1 mV/div and without any input signals, the centre two divisions of the scope are filled with signals. This is assumed to be the noise floor and the RMS voltage V_{RMS} is measured as 0.33 mV. The bandwidth of the scope, BW_{scope}, is 2.5 GHz. Therefore, the total power across the bandwidth is calculated by: $10log_{10}(\frac{V_{RMS}^2}{50}) + 30 - 10log_{10}(BW_{scope}) + 10log_{10}(BW_{sig}) = -75.2\,dBm$, where $BW_{sig} = 35\,MHz$ is the bandwidth of the TX signal.

One of the two splitting ports is connected to the duplexer. During the modelling mode, the other splitting port is connected to a 3 dB attenuator which has one end terminated with a 50 Ω load. This is to increase the return loss of the power splitter. A 2 dB attenuator is placed at the combining port in order to increase the return loss at this port so that the accuracy of the measured leakage is improved. The details of the power splitter design will be shown in Sec. 6.2.3.2. The attenuators are also implemented using the lab facilities and the details will be shown in Sec. 6.2.3.3.

Note that the additional attenuators mentioned above are only for this particular test bench due to the limited return loss of the RF components used, e.g. the lab fabricated components and the PA. Since the deployment of those attenuators doesn't change the architecture of the proposed cancellation system, it does not affect the generality of the proposed cancellation system.

6.2.3 The design of RF Components

Since the test bench is only for the proof-of-concept purpose, many RF components are specified and designed by the author of this thesis. Then these components are fabricated in the lab using off-the-shelf materials. The RF components that are used for the implementation of the transceiver, including the directional couplers, power splitter and fixed attenuators are briefly described as follows.

6.2.3.1 Directional couplers

There are two directional couplers implemented in the transceiver of the test bench. Both of the couplers are designed using ADS design tool. The microstrip coupled line architecture is used for the design of these couplers. Each completed design is firstly simulated using Electrical simulator of the ADS software to ensure the performance meets the desired specification of the test bench. Then the 3D Momentum simulator is used in order to further verify the design before being fabricated in the lab using the RO4350B substrate by Rogers Corporation. The thickness of the substrate is 0.03 inches. The picture of the 30 dB coupler is shown in Figure. 6.3. The 15 dB coupler is similar to the 30 dB one, but with a wider gap between the two coupled microstrip lines.

The widths of the transmission lines for the 15 dB and 30 dB couplers are 1.632 mm and 1.716 mm, respectively. The gaps between the coupled lines are 0.44 mm and 2.539 mm for the 15 dB and 30 dB couplers, respectively. In order to add the SMA connectors to the couplers, there are right angles and 50 Ω matching transmission lines (at 900 MHz) connected at both sides of the couplers. The width of the matching transmission lines is 1.724 mm.

Since the substrate used for the directional coupler is very thin, the completed components are not strong enough and can be bent easily. Slight bending of the coupler can cause the microwave properties of the component to change and thus affect the implementability and repeatability of the test bench. The couplers are thus first connected using two SMA through connectors. Then they are mounted on a small piece of Perspex sheet using four nylon screws. The use of nylon screws doesn't affect the electrical properties of the couplers.
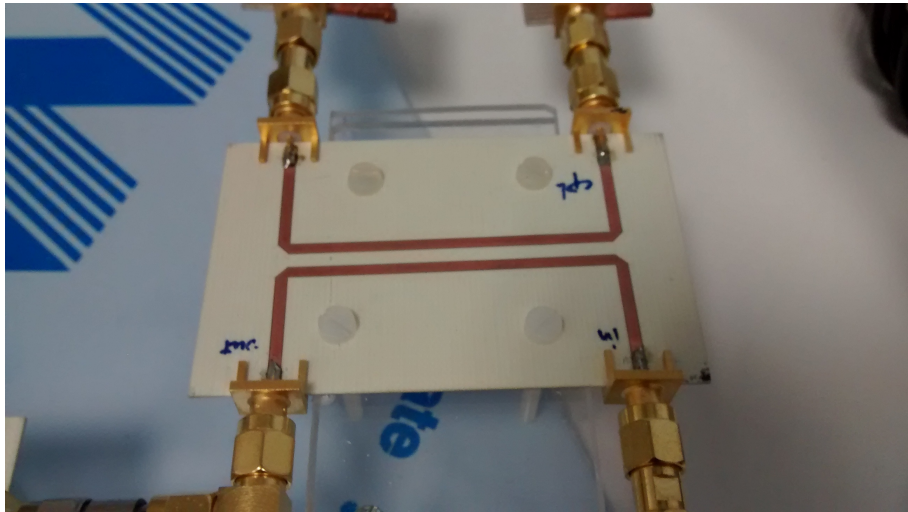
Figure 6.3: The 30 dB directional coupler implemented for the test bench

6.2.3.2 Two-way power splitter

The two-way power splitter is shown in Figure. 6.4. It is designed using Wilkinson structure. The input port (the one on the top of the picture) of the Wilkinson power splitter is split into two quarter-wave long transmission lines. Each of the two transmission lines has characteristic impedance of 70.7 Ω which is $\sqrt{2}$ times of the input impedance. The two lines are designed to be circular so that the insertion loss is minimized. The width of the circular transmission lines is 0.94 mm. It also

requires a 100 Ω resistor placed between the two splitting ports. It is a surface mount 0805 resistor. In order to minimize the effect of the parasitic capacitance when splitting the signals, the transmission line tracks are designed to have smooth bending curve. The transmission lines for connecting the splitting circuit with SMA connectors are designed to match 50 Ω at 900 MHz. The line width is 1.724 mm.

The design of the power splitter has been carried out using ADS. Both electrical and electromagnetic (EM) simulations have been performed in order to verify the design of the component. The power divider is implemented using the same RO4350B material as the directional couplers.
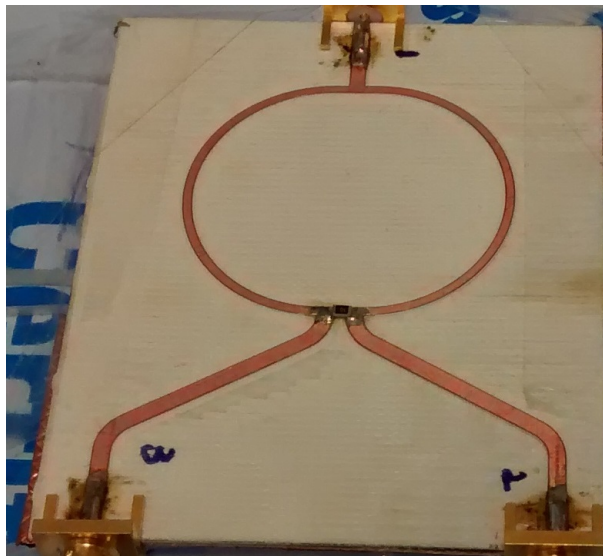
Figure 6.4: The two-way power splitter implemented for the test bench

6.2.3.3 Fixed attenuators

The 15 dB (shown in Figure. 6.5) and 2 dB fixed attenuators implemented in the transceiver are also designed and fabricated in the laboratory. They are designed using the π-network. The block diagram of the π-network has been shown in Figure 6.5(a). In the figure, Z_{in} and Z_{out} represents the input and output impedance of the network. In this case, both of the impedance are equal to the characteristic impedance of the transmission line $Z_0 = 50\,\Omega$. There are three resistors (R_1, R_2 and R_3) in this network. The attenuation depends on the values of the resistors. The theory of the π-network can be found in [92].

(a)

(b)
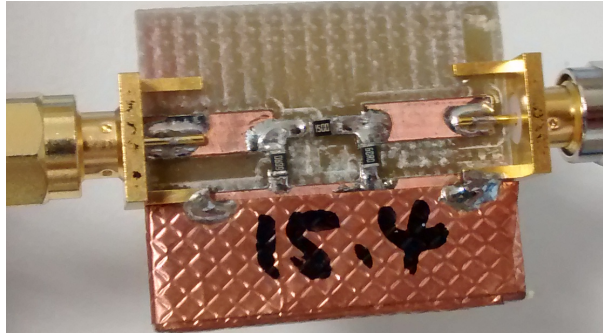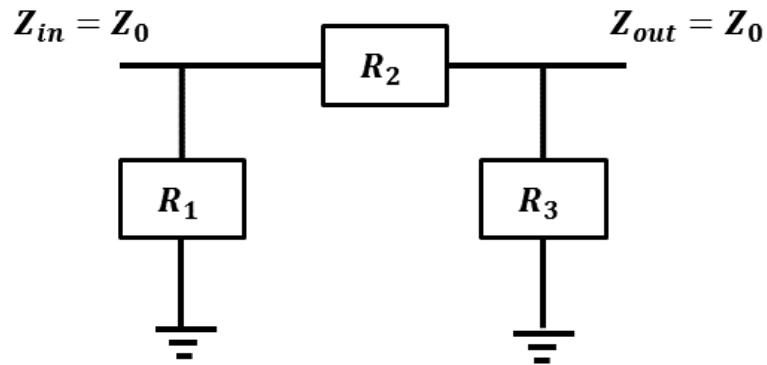
Figure 6.5: The fixed attenuators implemented for the test bench. (a) Block diagram of the Pi-network for designing the fixed attenuators. (b) The picture of the 15 dB attenuator

When fabricating microwave components, there is a type of connections called a via which is commonly used to connect two circuits from two sizes of the PCB board. The designed attenuator requires vias to connect the surface mounted resistors to the ground plane on the opposite side of the substrate. Placing the vias requires a piece of special equipment which is not available in the lab. For this reason, when designing the layout of the attenuators, a piece of copper has been left on the top of the substrate. This is used as the extension of the ground plane. It is done by wrapping some copper tape around the two sides of the substrate (This can be seen in Figure. 6.5). The two vertical resistors are then grounded by being soldered on this piece of copper.

The substrate for the attenuators is FR-4. This design is used for all fixed atten-

uators implemented in the RF cancellation block. The values of the resistors are obtained by using ADS. The layout is also created using ADS. An electrical and EM co-simulation (ADS) has been performed for the verification purpose before fabricating the layout.

Upon the completion of implementing the transceiver, the reference and the leakage signals can thus be captured for modelling purposes. This will be discussed in more detail later in Sec. 6.3.

6.3 Baseband Modelling of the Duplexer

As mentioned in the previous section, the reference signal is measured at the through port of the 30 dB coupler. Between the through port of the coupler and the input port of the oscilloscope, a cable and a 15 dB attenuator are connected. In order to model the isolation path of the duplexer, the measured reference signal needs to be calibrated from the input port of the oscilloscope to the through port of the 30 dB coupler as illustrated in Figure. 6.6. The calibration is done by first measuring the S-parameters of the 15 dB attenuator, as well as the cable that is used for connecting the attenuator to the oscilloscope by using the vector network analyser (VNA) which is manufactured by Rohde & Schwarz (model number is ZVB-20). The group delay, insertion loss and phase parameters of the attenuator and the cable have been recorded at the frequency of 897.5 MHz. Since the desired calibrated signal is the one before being delayed by the attenuator and the cable, it can be obtained by first leading the measured reference signal by the delay value of the component combination (the attenuator and the cable). The resulting signal is needed to scale up by using the total insertion loss of the attenuator and the cable in linear scale. Finally, the calibrated reference signal at the through port of the 30 dB coupler can be obtained by phase shifting the measured total phase of the attenuator and the cable counter-clock-wise.

Similar procedures are also applied to the captured leakage signal which is also shown in Figure. 6.6. The measured leakage needs to be calibrated from another input port of the oscilloscope to one of the splitting ports of the two-way power splitter. In this case, the component combination to be calibrated out in the leakage path include the 2 dB attenuator, the combining path from one splitting port to the summing
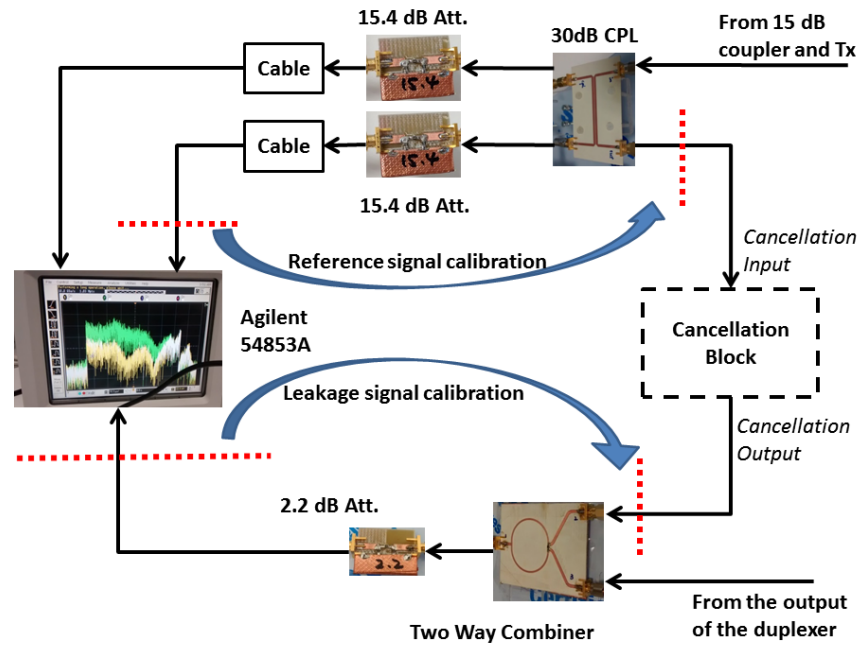
Figure 6.6: The reference and the leakage signals calibration.

port and necessary cables and connectors. After all the calibrations, the input signal of the cancellation system at the through port of the 30 dB coupler is obtained, as well as the original leakage signal at the one splitting port of the two-way power splitter.

Before the calibrated reference and the leakage signal can be used for modelling the isolation path of the duplexer, normalization and reconditioning of the signals is needed. These will be shown in Sec. 6.3.1.

6.3.1 Reconditioning Signals

The calibrated reference and the leakage signals are not yet suitable for modelling. They are digitized by the oscilloscope at RF frequency and consist of all the distortions from the PA and the oscilloscope. Therefore, filtering and frequency down-converting are necessary before being used for modelling. This is managed by using a PC with MATLAB. The digitized RF signals are filtered with an ideal brick-wall lowpass filter which has the bandwidth of 915 MHz. The purpose of this filter is to clean the harmonics and odd-order distortions from the PA and the oscilloscope. The

resulting signals are frequency down-converted directly to baseband using IQ demodulation technique and filtered with another lowpass filter which has the bandwidth of 17.5 MHz. The sampling frequency of those signals is still at 10 GHz. Therefore, down-sampling has been performed to the critical sampling rate of 35 MHz. At this stage, the baseband reference and leakage signals are obtained.

6.3.1.1 Whitening Filter

The resulting baseband reference signal has non-white characteristics due to the non-ideal frequency response of the PA and the low return loss of the duplexer at TX port. Since the modelling techniques require the reference signal being white, a whitening filter is needed. The general structure of whitening the reference signal has been shown in Figure. 6.7. Let $\mathbf{g}$ and $\mathbf{h}$ be the impulse responses of the filtering effect of the PA and the duplexer, respectively. The signals $\mathbf{ref}(n)$ and $\mathbf{leak}(n)$ are the baseband reference and leakage signals, respectively. Thus, we have

$$\mathbf{ref}(n) = \overline{\mathbf{ref}}(n) * \mathbf{g} \tag{6.1}$$

and

$$\begin{aligned} \mathbf{leak}(n) &= \mathbf{ref}(n) * \mathbf{h} \\ &= \overline{\mathbf{ref}}(n) * \mathbf{g} * \mathbf{h} \end{aligned} \tag{6.2}$$

where $\overline{\mathbf{ref}}(n)$ is the ideal reference signal with white property, from which $\mathbf{ref}(n)$ is obtained.

The whitening filter is a set of FIR coefficients which are obtained by applying the forward linear prediction techniques on $\mathbf{ref}(n)$ [93]. Therefore, apply such filter on both side (6.2), we have

$$\mathbf{leak}(n) * \mathbf{w}_w = \overline{\mathbf{ref}}(n) * \mathbf{g} * \mathbf{h} * \mathbf{w}_w \tag{6.3}$$

Let

$$\hat{\mathbf{ref}}(n) = \overline{\mathbf{ref}}(n) * \mathbf{g} * \mathbf{w}_w \tag{6.4}$$

and

$$\hat{\textbf{leak}}(n) = \textbf{leak}(n) * \textbf{w}_w \tag{6.5}$$

we then have

$$\hat{\textbf{leak}}(n) = \hat{\textbf{ref}}(n) * \textbf{h} \tag{6.6}$$

The equation (6.6) shows that, applying the whitening filter on both reference and the leakage signals does not change the impulse response of the duplexer which is included between the two signals. After whitening, these signals can then be used for modelling the isolation path. The modelling is performed using both MCoSaMP and MADF-DC techniques and the order of the system is set to be four since a fourth order RF cancellation system will be implemented.
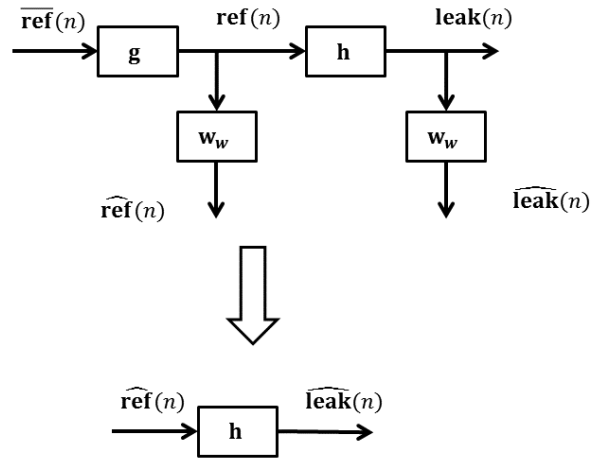
Figure 6.7: The structure of whitening the reference signal

6.3.2 Baseband Modelling Setup

In this sub-section, the modelling performance using both MADF-DC and MCoSaMP techniques is presented. The reference and the leakage signals that are used for

modelling are the whitened results from the previous sub-section. At the end of this sub-section, we will get the modelling performance for both modelling techniques and the optimized values for delays, attenuators and phase shifters. These optimized values will then be used in the next section for the implementation of the cancellation system.

Minimum attenuation threshold Since the two modelling techniques have already been discussed in the previous two chapters, they will be used to obtain the theoretical modelling performance and the corresponding parameters for each cancellation path. However, practical considerations must be considered first. As discussed in Sec. 4.7 and Sec. 5.6, the two modelling techniques could potentially produce some tap weights that are unrealisable using only passive components. In order to ensure that all the parameters (including the delays, attenuation and phase) are implementable, a minimum attenuation value for each cancellation path needs to be specified. This value is shown in Table. 6.1 and is calculated using the formula of (4.31). Since the reference signal is measured at the through port of the 30 dB coupler, the term $\triangle IL_{CPL}^{TX}$ in (4.31) can be considered as zero. On the other hand, a two-way power combiner is used at the receiver path for cancelling the leakage. Since there is no significant difference in insertion loss between the two combining ports of the combiner, the term $\triangle IL_{CPL}^{RX}$ is also considered as zero.

Table 6.1: Specified minimum attenuation level for each cancellation path.

	Description	Insertion Loss (dB)
IL_{Att}^m	Specified minimum value of the variable attenuator	5.2
IL_{PH}^m	Specified minimum value of the phase shifter	3.5
IL_{SPL}^m	Insertion loss of the power splitter	6
IL_{CMB}^m	Insertion loss of the power combiner	6
IL_{misc}^m	Insertion loss of other components	7
IL_{Fix}^m	Specified minimum attenuation level: the sum of all above	27.7

Unit insertion loss of the delays   The delay lines for implementing the cancellation block will be constructed with microstrip technology. Through experiments, the unit insertion loss of the delay lines is found to be less than 0.2 dB/ns. Therefore, this value is set as the unit insertion loss of the delay lines for modelling. The details of the delay line implementation will be described later in Sec. 6.4.1.2.

Delay limit constraints and up-sampling ratio   Regarding the delay limit constraints for both MADF-DC and MCoSaMP techniques, the minimum delay limit is not swept from 0 ns. The reason is that there is a delay for each RF component within the cancellation block. These delays must be excluded from the ones that are estimated using the proposed modelling techniques. The minimum value for the lower boundary of the delay limit constraints is shown in Table. 6.2. The term *Others* in Table. 6.2 refers to the sum of delays that could be caused by miscellaneous components such as connectors and cables.

From the simulation results that are shown in Sec. 4.6.2 and Sec. 5.5.2, the optimized minimum delay limit value is within the range between 0 ns and 40 ns. The maximum delay limit is between 30 ns to 80 ns. Taking advantage of this information, the minimum delay limit constraint is thus swept from 15.5 ns which is shown in Table. 6.2 to 45.5 ns in a step of 10 ns. The maximum delay limit is swept from 30.4 ns to 80.4 ns in a step of 10 ns.

The up-sampling ratio is swept between 2 and 32 in a step of 1 for both modelling techniques.

Table 6.2: The minimum value for the lower boundary of the delay limit constraints.

	Delay (ns)
Four way Splitter	4
Four way Combiner	4
Variable Attenuator	1
Phase Shifter	2.5
Others	4
Total	15.5

Other settings The other key settings for MCoSaMP are the maximum number of iterations and the desired tolerance which are set to 100 and 0.1×10^{-9}, respectively. These are the same as the ones in Sec. 5.4.

Under the settings that are shown in this section, the modelling of the duplexer can thus be performed using MADF-DC and MCoSaMP techniques. The parameters including the delay, attenuation and phase for each cancellation path can then be estimated.

6.3.3 Baseband Modelling Results

The estimated parameters using MADF-DC and MCoSaMP techniques are shown in Table. 6.3, as well as the resulting normalised mean square errors (NMSE) with respect to the original leakage. The cost functions of both techniques require subtraction between the original leakage and the approximated signal. In the actual cancellation system, the two signals are added using the combiner. For this reason, the phase values in Table. 6.3 obtained by summing the estimated phase using the estimation techniques and 180°. The resulting NMSE by using MCoSaMP technique is slightly lower than the one by using the MADF-DC, which indicates better performance is achieved by using MCoSaMP. However, the difference is only approximately 0.5 dB which is insignificant.

Table 6.3: Estimated parameters and modelling error

Modelling technique	Tap index	Insertion loss (dB)	Phase (degree)	Delay (ns)	NMSE (dB)
MADF-DC	1	47.52	79.29	40.34	-21.89
	2	32.8	215.58	21.85	
	3	37.64	186.29	16.81	
	4	37.22	55.79	28.57	
CoSaMP	1	44.71	243.06	40.82	-22.37
	2	42.05	254.83	16.33	
	3	43.8	166.89	12.24	
	4	44.83	188.85	36.73	

The estimated parameters using both MADF-DC and MCoSaMP techniques are re-applied to the measured reference and leakage signals. These two signals are the ones before being filtered by the whitening filter. The cancellation signal is thus obtained and the magnitude response of the leakage after the cancellation is shown in Figure. 6.8. The leakage signal before the cancellation is also included in this figure. All the signals have been normalised by the peak magnitude of the measured leakage. As expected, the resulting leakage signals after cancellation using both techniques are very similar. The maximum cancellation occurs between 890 MHz and 895 MHz, which is approximately 35 dB. Between 882.5 MHz and 902.5 MHz, i.e. 20 MHz bandwidth, the minimum cancellation performance is 20 dB. Since the leakage power level at 902.5 MHz and above is much smaller than the one at lower frequencies, the cancellation is degraded. The minimum cancellation within the above frequency range is about 7 dB. This occurs where the notch of the measured leakage is. Apart from the small frequency region around this area, the leakage reduction at most of the higher frequencies is above 10 dB.
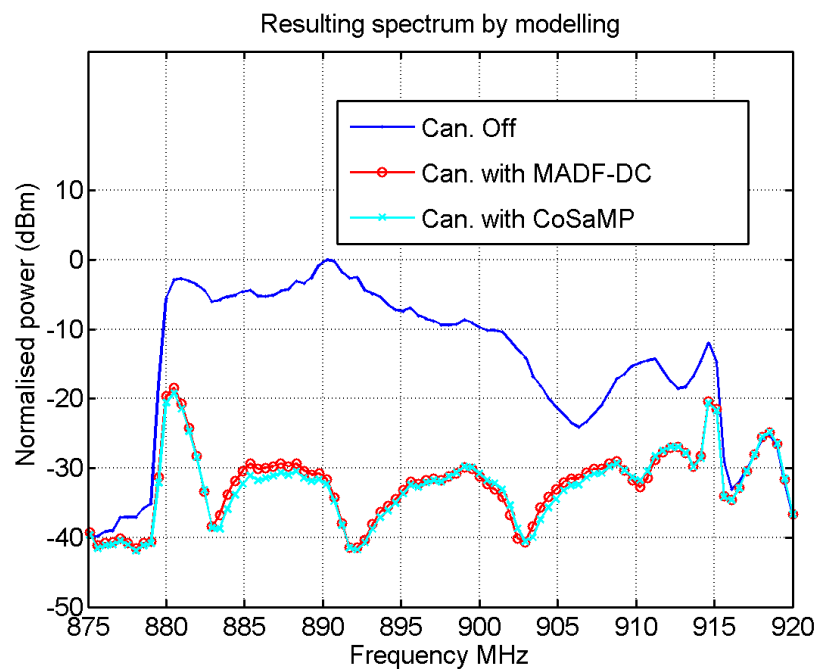
Figure 6.8: The expected spectrum of the leakage before and after the cancellation

Problem with the edge of the frequency band At the edges of the cancellation bandwidth, the suppression performance is significantly reduced to 15 dB and 8 dB at lower and upper frequencies, respectively. This is because the TX signal is recon-

ditioned by the bandpass filter at the output of the PA. Due to the sharp roll-off at the edge of the filter, it starts to have significant changes on frequency response of the original TX signal. The whitening filter that is used in the modelling is not sufficient to restore the *white* property of the original TX signal. Therefore, more modelling errors occur at these edges of the frequency band. Increase the order of the whitening filter will reduce the error. However, it is not possible to reduce the error to the same level as the one by using the pure white TX signal.

Since the bandpass filter is applied in this test bench due to the distortion problems of the PA (as mentioned earlier), in general, this is not needed if the harmonic distortion of the PA is insignificant. In that case, a TX signal with wider bandwidth can be transmitted. The isolation path of the duplexer can thus be modelled using the reference and the leakage with wider bandwidth. The problem of the poor cancellation performance at the edges of the band could then be minimized.

In this chapter, the reference and leakage signals are obtained by measuring the input and output of the ceramic duplexer. By using these two signals, the frequency response of the isolation path of the ceramic duplexer can be obtained. In theory, this frequency response should be the same as or very similar to the measured S-parameter model which has been used for simulations in Chapt. 4 and Chapt. 5. However, significant differences have been found which will be shown in the following section.

6.3.4 Comparison of System Modelling Results - Measured Signals VS S-parameters

The magnitude response of the leakage path can be obtained by dot-dividing the measured leakage by the reference signal in the frequency domain. We also have another magnitude response that is directly measured by using VNA. Both responses are for the same ceramic duplexer. In this section, the differences between the two responses are discussed.

The most accurate way of obtaining the leakage path characteristics is certainly by measuring the duplexer with the VNA, which has been used for simulations in the previous chapters. Thus, the simulations in the earlier chapters represent the true response of the cancellation system, if the rest of the components in the cancellation

system are ideal. This means that the characteristic impedance of the rest of the components is perfectly 50 Ω and there are no distortions in frequency response. This is not feasible in practice. As a result, errors occur when modelling the leakage path by capturing the reference and leakage signals. This is especially true for this test bench. In order to distinguish the two models, we call the model that is obtained by using the VNA as the ideal model and the one using the frequency domain signals as the actual model.

Magnitude responses of the two models In order to obtain the frequency response of the actual model, a whitening filter has been created using the captured reference signal, as discussed at the beginning of this section. This whitening filter is applied to both the reference and leakage signals.

On the other hand, the RF reference signal is filtered using the ideal model of the duplexer by using Fast Fourier Transform (FFT). The resulting RF leakage is down-converted and filtered with the same whitening filter. This is to ensure that two models are using the same reference signal. The resulting leakage signals of the two models are normalised with their own peak magnitude and shown in Figure. 6.9. It should be seen that the resulting leakage signals of the two models are very different. At the centre frequency, the two magnitude responses approximately match each other. However, when the frequency is less than the centre frequency, the ideal magnitude response (shown in Figure. 6.9 as *Leakage using S − parameters*) is lower than the actual model (named as *Leakage using live signals* in the figure). The two magnitude responses cross over at the frequency of approximately -15 MHz from the centre. When the frequency offset is greater than zero, the ideal magnitude response is greater than the actual one. The latter reaches its minimum at the frequency offset of approximately 8 MHz. The two magnitude responses cross over once again at about 12 MHz to the right of the centre frequency. The ideal response reaches its minimum at around 13 MHz.

The reason for the differences of magnitude responses Apart from the non-ideal impedance of the components in the test bench, the return loss of the duplexer within the RX band at the TX port plays an important role in the modelling error between the ideal and actual models. Such return loss is about 1 dB. The duplexer reflects, instead of absorbs, most of the power back towards to the direction of the
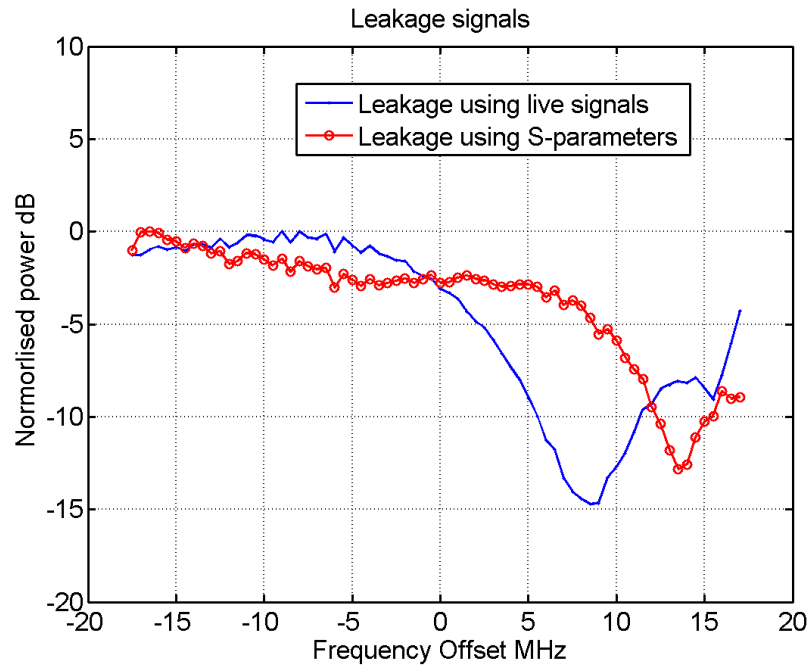
Figure 6.9: Comparing the leakages between modelled using live signals and S-parameters

transmitter. Only a small fraction of the TX signal passes through the duplexer and arrives at the receiver side. In order to more accurately model the duplexer, only the TX signal needs to be captured. However, due to the poor return loss, a significant portion of TX signal reflects back towards to the output port of the directional coupler. The isolation between the output port and the coupling port of the directional coupler is about 20 dB. Therefore, at the coupling port of the coupler, the signal consists of not only the attenuated TX signal, but also its attenuated reflected portion. These two portions of signals are comparable since the reflected TX signal is only attenuated by the directional coupler (20 dB) plus the return loss of the duplexer (1 dB) whereas the desired TX reference signal is attenuated by 15 dB. The actual reference signal consisting of the TX and reflected portions is then used to model the duplexer instead of only the TX portion. Hence, modelling error is introduced.

Potential method of reducing the differences The reflection of the TX signal from duplexer could be reduced by placing some isolators between the through port of the coupler and the TX port of the duplexer. Each isolator can provide about 20 dB of isolation with the cost of less than 1 dB of power loss in the main transmitter

path.

By using the estimated parameters that are shown in Table. 6.3, the RF cancellation block can finally be implemented which will be shown in Sec. 6.4.

6.4 Implementation of the Cancellation Block

Having estimated the delay, attenuation and phase parameters for each cancellation path, the implementation of the cancellation block can proceed. The block diagram of the RF cancellation block is shown in Figure. 6.10. The part number of the variable attenuators is ZX73-2500+. They are manufactured by Mini-Circuits. The attenuation tuning range is from 3 dB to 43 dB. Each of them can be continuously varied by a control voltage from 0 V to 17 V.
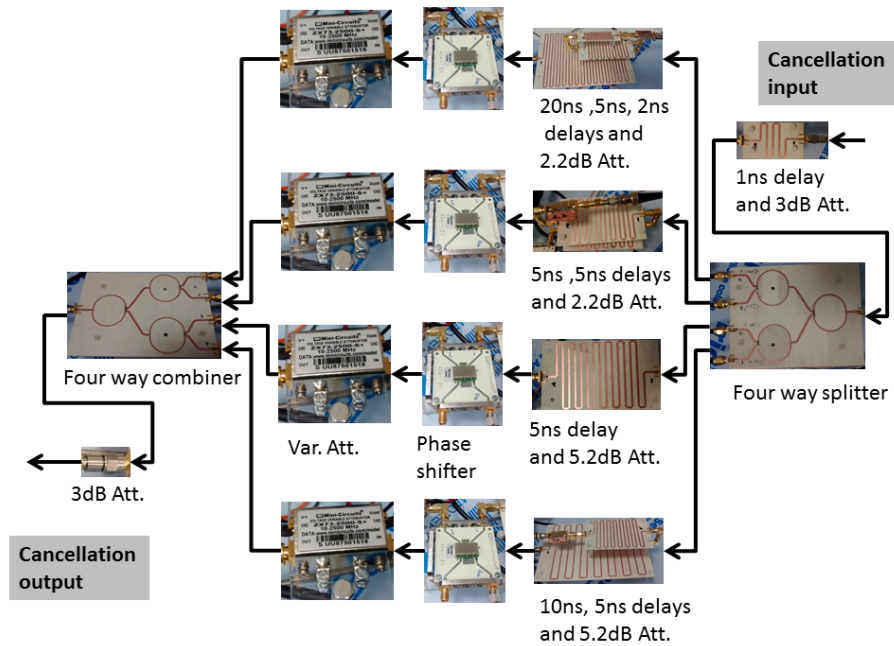
Figure 6.10: Block diagram of the cancellation block

The phase shifters (SPHSA-152+) are also from Mini-Circuits. They can be controlled continuously to cover 360° using the bias voltage. The range of the control voltage is between 0 V and 15 V.

In our test bench, the DC supply voltage is set as 3 V. All the DC voltages in our test bench are given by the NI-6723 DAQ card with a BNC-2115 connector

block. The DAQ card is equipped with a 13-bit digital-to-analog converter (DAC) for ± 10 V output range. As a result, the resolution of the DC voltages is approximately 2.44 mV.

Apart from the components purchased, some RF parts have been designed and fabricated in the lab by the author of this thesis.

6.4.1 The Design of RF Components in the Cancellation Block

The customized RF components include fixed delay lines, fixed attenuators and four-way power splitters/combiners. There is also one microstrip transmission line built in each cancellation path which is used for physically separating these paths. The reason of designing the RF parts instead of purchasing these is mainly for reducing the implementation cost. The design of these RF components will be described in this sub-section. Since the technique used for designing the fixed attenuators for the cancellation block is the same as the one for the transceiver which has been described in Sec. 6.2.3.3, this will not be discussed again in this sub-section.

6.4.1.1 Four-way power combiners/splitters

Since the cancellation block consists of four paths, two four-way RF power combiners are implemented. One is used for splitting the reference signal into four paths and the other one is used to re-combine the signals to form the cancellation signal. The picture of one of the four-way combiner is shown in Figure. 6.11. This component consists of three two-way combiners which has been described in Sec. 6.2.3.2. The design is also fabricated using the RO4350B material.

6.4.1.2 Fixed delay lines

Each delay block in the test bench is a configuration of a number of smaller delays. In later sections, detailed process will be provided on how to obtain the value of the delay block in each cancellation path. Here, only the design of the delay units is described. Small delay lines are designed by the author and fabricated in the lab with RO4350B substrate. These smaller delay lines include 1 ns, 2 ns, 5 ns, 10 ns and 20 ns
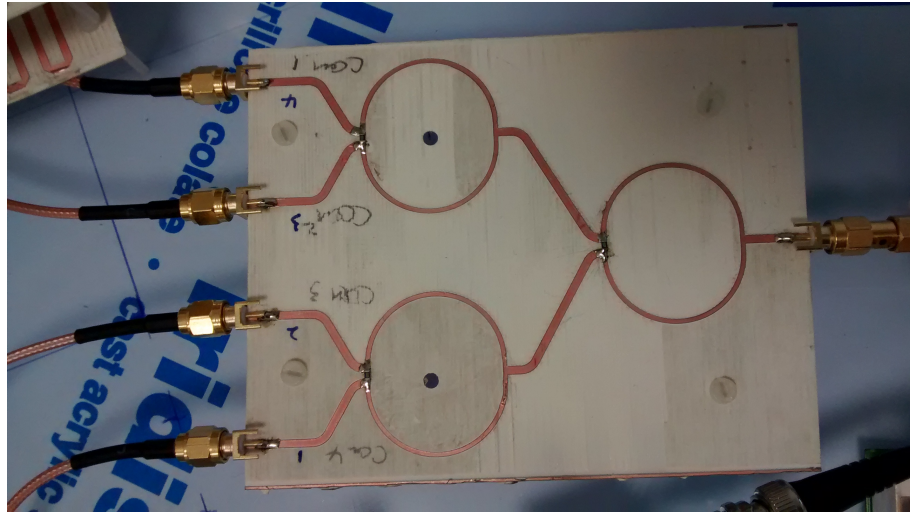
Figure 6.11: The four-way power combiner implemented for the test bench

in order to implement the possible delay values that are obtained using modelling techniques. The example of a single 1 ns delay line is shown in Figure 6.12(a). Please note that due to the non-ideal fabrication, the actual measured delay values are up to 20% different from the values mentioned. For instance, the actual delay value of a 1 ns delay line is about 1.2 ns. By using these smaller delay lines, the implementation accuracy of 0.5 ns has been achieved for the total delay in each cancellation path.

The fixed delay lines are designed using meander-line technique with the assistance of ADS. The advantage of using meander line structure is to reduce the overall length of the delay line, especially for a large delay value. The meander line delay consists of a number of long and short segments. Each segment is a transmission line matched at 50 Ω. The space between two adjacent long segments depends on the length of these segments. Since longer segments experiences more coupling, a wider gap is needed. Otherwise, the actual delay value and insertion loss of the delay line will significantly differ from the designed one.

Through experiments, it has been found that when the length of the long segments is close to even number of multiples of the quarter-wave length at the operating frequency (900 MHz, in this case), the implemented delay line differs the most from the designed one. It seems that the two long segments at these lengths enter the resonance and thus cause the overall delay line to be different from the design. When designing the delays for the test bench, this has been avoided by carefully

choosing the length of the long segments and the space between two adjacent ones. The unit insertion loss of less than 0.2 dB/ns has been achieved for each delay line implemented for this test bench.
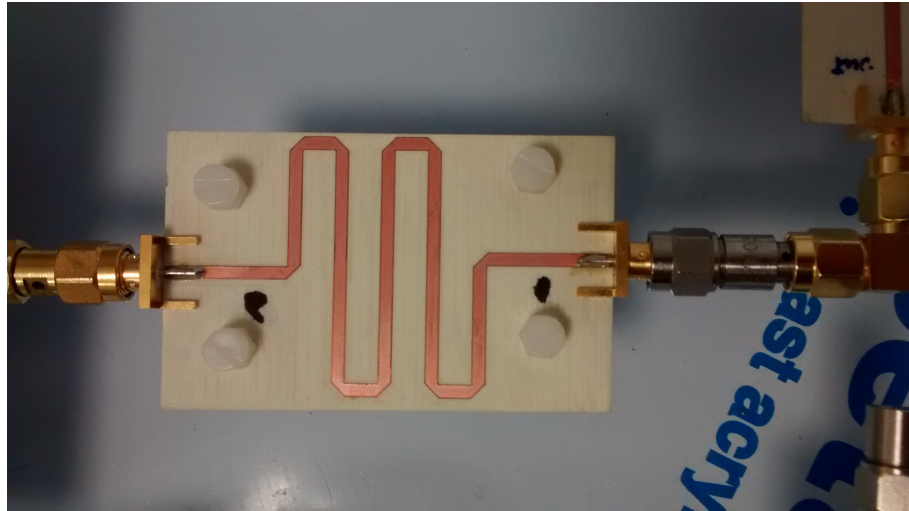
(a)
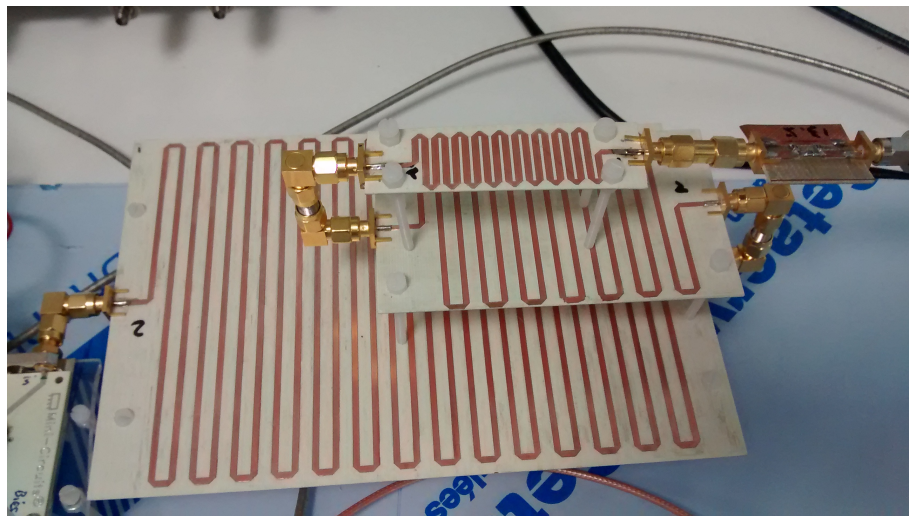
(b)

Figure 6.12: The fixed delay line implemented for the test bench

The delay block in each cancellation path has been constructed by connecting a number of smaller delay units using SMA through connectors. This can be seen from the example picture shown in Figure 6.12(b). As mentioned at the beginning of this sub-section, the process on how to obtain the value of the delay block will be discussed in Sec. 6.4.3.

6.4.1.3 RF microstrip fixtures

Four RF fixtures have been designed and implemented in order to physically separate the four cancellation paths. These RF fixtures are shown in Figure. 6.13. These fixtures are transmission lines designed for 50 Ω matching at 900 MHz using microstrip technology. The material used is FR-4 and thus the widths of the transmission lines are designed to be 3.071 mm. There are multiple of 90° bends and mitred by 45° in order to minimize the discontinuity when bending the transmission lines [94]. The RF microstrip fixtures are designed using ADS software and fabricated in the lab.
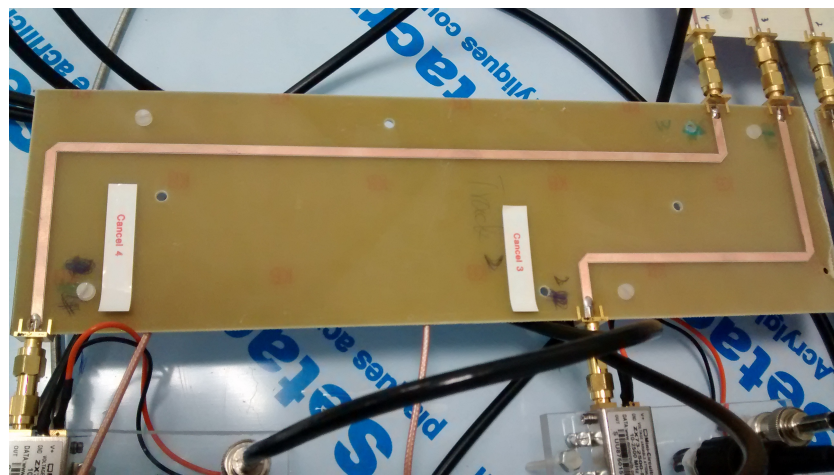
(a)
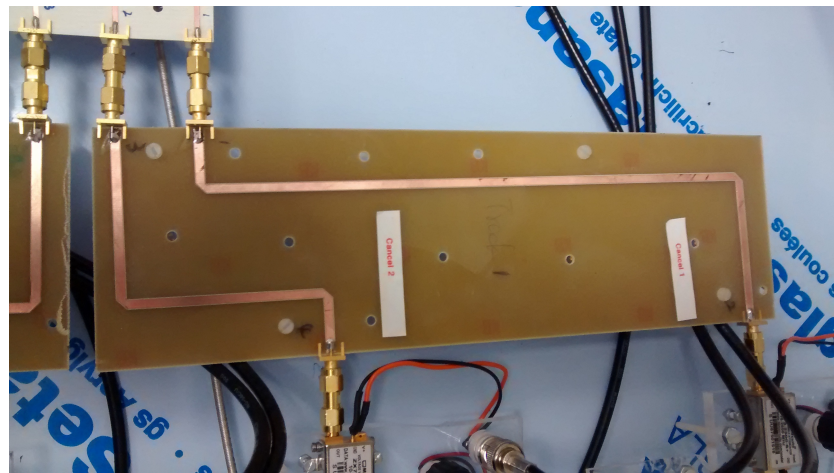
(b)

Figure 6.13: The RF microstrip fixture implemented for the test bench

6.4.2 Challenges of Using Low Performance RF Components and the solutions

Prior to the implementation of the cancellation block, there are some critical problems that need to be solved first. The RF components for the cancellation block in our test bench are low performance. For the cancellation system, there are three critical parameters, i.e., attenuation, phase and delay. The low performance RF tunable components suffer from interdependences of these three critical parameters. Altering one parameter will result in changing the other two. With these low performance RF components, it can be very difficult to successfully implement the cancellation block.

6.4.2.1 Problem with the Tunable Attenuators and the Solution

Problem The variable attenuators in this test bench similarly suffer from the problem that changing the attenuation value of each variable attenuator also changes the phase significantly, as well as the group delay slightly. For instance, this can be seen from the measured characteristics of one of the variable attenuators as shown in Figure. 6.14. These characteristics are the ones at the centre frequency at different control voltages. Other variable attenuators have similar characteristics as the one shown in the figure. Ideally when the cancellation system is adapting, we want to vary the attenuation without affecting the phase and the group delay.

Overview of the solution to the attenuator problem To solve this problem, a fixed attenuator is deployed in each tap in order to limit the voltage range of the variable attenuator from 4 V onward, so that the group delay and phase of the attenuator stay approximately constant. The resulting tuning range of the variable attenuators is thus limited by a range between 3 dB and 8 dB, approximately. The attenuation resolution is approximately 0.002 dB which is good enough for the desired cancellation level. Effectively, the total attenuation in each tap is divided into coarse and fine parts which are realized by the fixed and variable attenuators, respectively. The fixed attenuators are designed using *pi* network technique with the assistance of the Advance Design System (ADS) software. The details of the implementation of the cancellation system as well as the calculation will be given in Sec. 6.4.3.
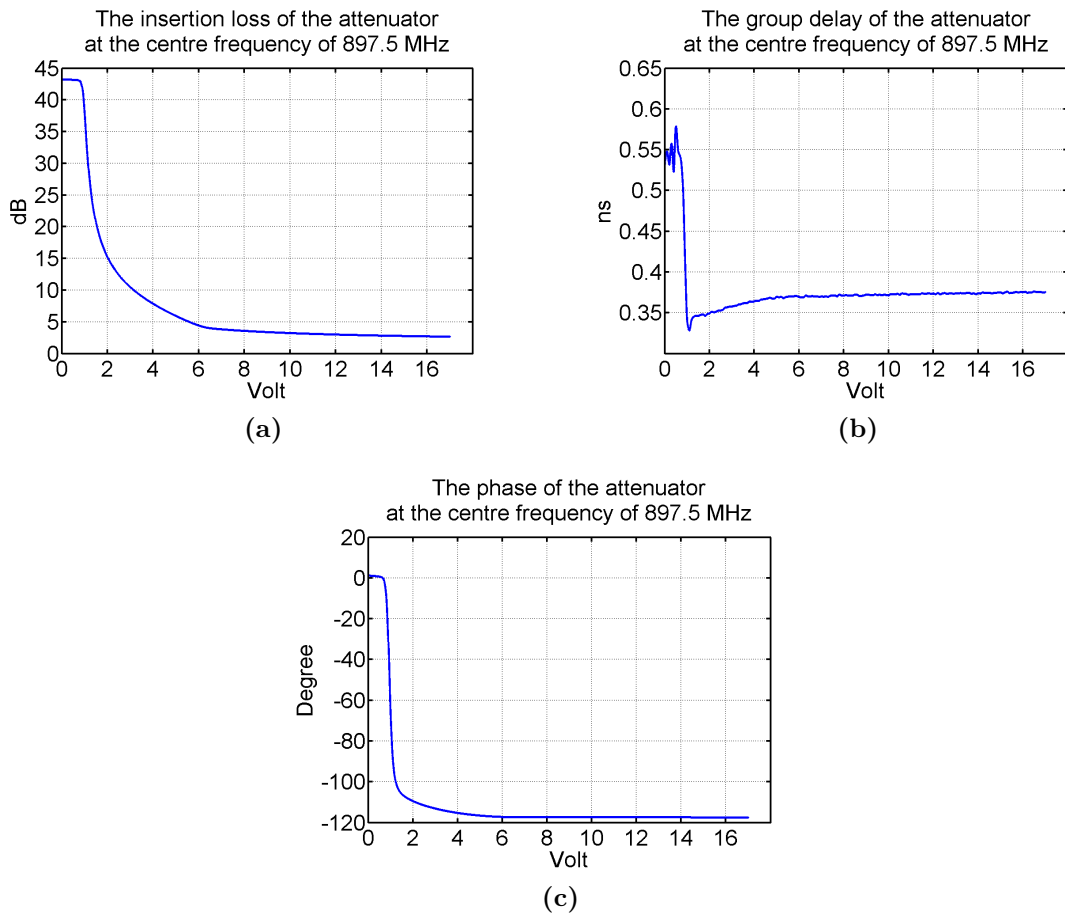
Figure 6.14: Measured characteristics of one of the variable attenuators with re-spect to control voltages at 897.5 MHz. (a) Attenuation. (b) Group delay. (c) Phase shift.

6.4.2.2 Problem with the Phase Shifters and the Solution

Problem   The measured characteristics of a phase shifter used in the test bench are shown in Figure. 6.15. Other phase shifters have similar characteristics as the example one. The lowest phase resolution occurs where the slope of the phase is the largest. This resolution is approximately 0.12° and may degrade the cancellation by approximately 1 dB. Similar to the variable attenuators, changing the phase of these phase shifters also changes the insertion loss and group delay significantly. The insertion loss can vary between just over 3.6 dB and approximately 1.9 dB. The group delay with respect to the control voltage can change between 1.9 ns and 2.9 ns.

The insertion loss of the phase shifter
at the centre frequency of 897.5 MHz

(a)

The group delay of the phase shifter
at the centre frequency of 897.5 MHz

(b)

The phase of the phase shifter
at the centre frequency of 897.5 MHz

(c)
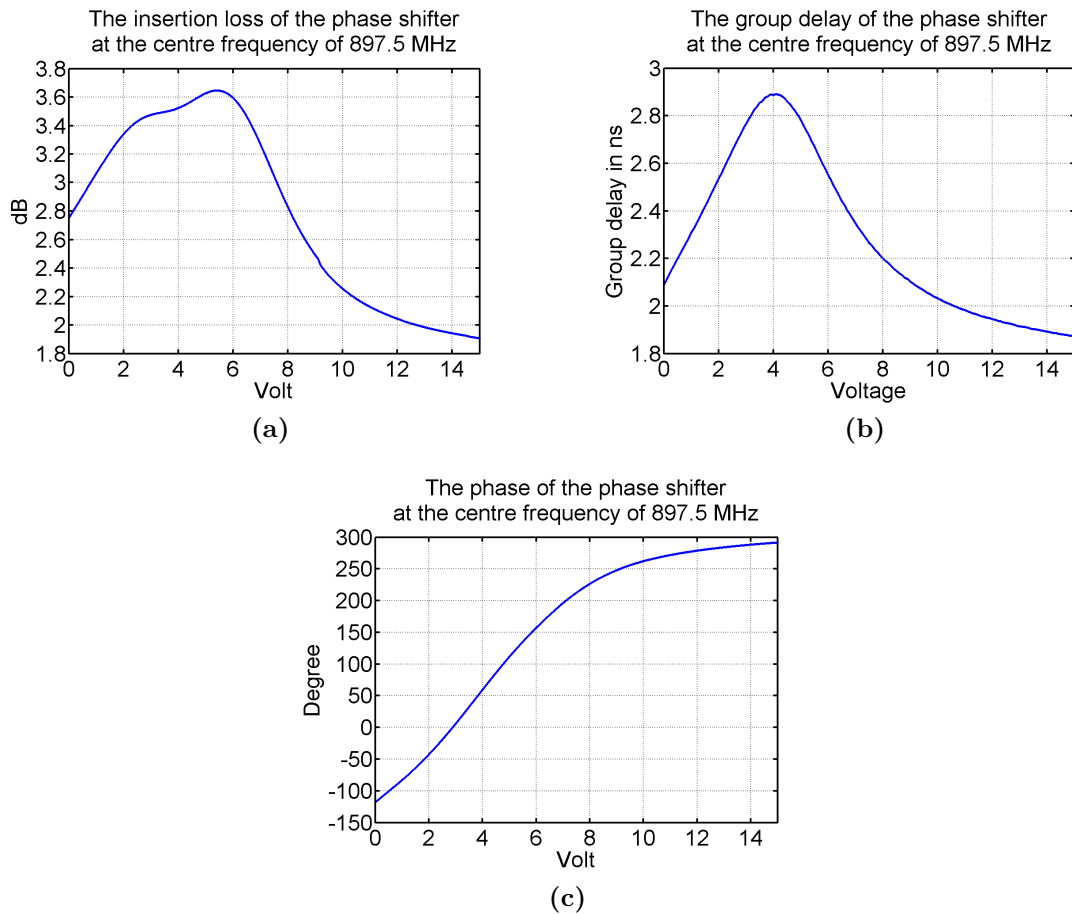
Figure 6.15: Measured characteristics of one of the phase shifters with respect to control voltages at 897.5 MHz. (a) Insertion loss. (b) Group delay. (c) Phase shift.

Overview of the solution to the phase shifter problem   Since the tuning of the variable attenuator is limited to a range where the phase and group delay are not affected by the change of the attenuation, the large variation of the insertion loss of the phase shifter can be compensated by the adaptation of the variable attenuator.

In order to compensate the variance of the group delay while varying the phase shifter, manual and precise tuning of the delays is required. This is not feasible, nor practical. In this test bench, fixed delay lines are used and the values are pre-calculated.

One of the disadvantages of using the pre-calculated delay lines is that the implementation process is complex. It requires the characterization of each RF component including all the delay lines. The process will be discussed in more detail in the next

section.

Another disadvantage is that the implementation accuracy for the delay value in each cancellation is low. This accuracy depends on the delay values of the fabricated delay lines. In this test bench, the accuracy is about 0.5 ns from the desired value. Therefore, the inaccuracy of the group delay becomes the performance limitation of this test bench.

In the case that RF tunable components with less interdependences are available for implementing the test bench, the problems with components would diminish with less impact on the performance of the cancellation block. A possible solution would be using vector modulators instead of the variable attenuators and phase shifters. A vector modulator in theory can obtain any combination of phase and attenuation within its operating range. An example of such a device is HMC630 by Analog Devices, Inc.

6.4.3 Implementation of the Cancellation Block Using Low Performance RF Components

In order to implement the cancellation block with the low performance RF components, an implementation technique is proposed. The proposed technique is overviewed as follows:

1. Characterization of all RF components.

2. Calculation of the desired value of the delay block in each cancellation path.

3. Calculation of the value of the fixed attenuator in each cancellation path.

4. Final implementation of the cancellation block.

Characterization of all RF components   The characteristics of all the components in the cancellation block have been measured in order to calculate the desired parameters of the delay blocks. As mentioned earlier, the variation of the group delay of the phase shifters is large. Therefore, in order to calculate the value of the delay block in each path, the average between the maximum and minimum group

delay values within the voltage control range (0 to 10 V) has been used. The corresponding voltage at which the group delay of the phase shifter is equal to the calculated average can thus be obtained. This is the reference voltage of the phase shifter for further tuning. Consequently, the reference attenuation and phase at the reference voltage are also obtained.

Since the group delay and phase are relatively constant for the variable attenuator, the mean attenuation between the maximum and minimum values within the control range is used as the reference attenuation level. The corresponding voltage is thus the reference voltage of the variable attenuator for calculating the parameters of the fixed attenuator and delay block in each tap. Based on the reference voltage, we thus have the reference phase and group delay for the attenuator.

Table 6.4: The measured insertion loss (attenuation) and group delay of the components in the cancellation block, excluding the delay blocks.

| Components | Insertion loss (dB) | | | | Delay (ns) | | | |
| | Tap index | | | | Tap index | | | |
	1	2	3	4	1	2	3	4
Power splitter configuration	9.96	10.29	10.19	10.23	5.39	5.47	5.46	5.47
Fixed Attenuation	To be calculated				0.25			
Phase shifter (at the reference voltage)	3.4	3.45	3.38	3.49	2.52	2.37	2.37	2.36
Variable. Attenuation. (at the reference voltage)	5.59	5.55	5.58	5.61	0.36	0.37	0.37	0.36
Power combiner configuration	9.9	9.63	9.74	10.12	4.1	3.19	3.3	4.24
Total	20.85	28.92	28.89	29.45	12.37	11.28	11.75	12.68

The measured insertion losses (attenuation) and group delays of all the major RF components at the centre frequency in the cancellation block are shown in Table. 6.4. The phase values are not measured at this point because they are not relevant in calculating the values of the delay blocks and the fixed attenuators. Furthermore,

the attenuation values of the fixed attenuators at this stage are not known yet. As a result, the values are not shown in the table. On the other hand, the delays of those attenuators are shown in the table since they can be estimated from the measurement of the 15 dB attenuator which was introduced in the earlier section. These values will not be significantly different from the actual values. This is due to the path length of the designed attenuators are the same, which contribute the most to the group delay of the attenuators.

The term *power splitter configuration* in the table represents the bundle of components that are close to the input port in the cancellation block. It consists of a 3 dB attenuator, a 1 ns delay line, a four-way power splitter, cables, and some connectors. The 1 ns delay line is for tuning the delay of the cancellation block, globally.

The term *power combiner configuration* represents a group of components that are close to the output port in the cancellation block. These components are connected to the four-way power combiner. One of these components is the connector fixture which is formed with a number of connectors to provide the desired angle for joining the cancellation block with the two-way power combiner. The rest of the components are the 3 dB attenuator, four-way power combiner, and RF microstrip fixtures (which have been described in Sec. 6.4.1.3). The RF microstrip fixtures are for physically separating the cancellation paths and reducing the construction difficulty of these paths.

Table 6.5: The calculated values for the delay blocks

Estimation technique	Delay (ns)			
	Tap index			
	1	2	3	4
MADF-DC	27.72	10.2	5.06	15.89
CoSaMP	28.45	5.05	0.49	24.05

Calculation of the desired value of the delay block in each cancellation path
By subtracting the estimated delays that are obtained using the proposed techniques with the total delays in Table. 6.4, the remaining values are the ones for the delay blocks. Since the structures of the cancellation system using MADF-DC and CoSaMP estimation techniques are the same, the test bench has only been

implemented using MADF-DC. The delay blocks have been constructed using the calculated delays from the MADF-DC technique and then measured using the VNA. The measured delays and insertion losses, as well as the calculated desired values of the delay blocks are shown in Table. 6.6. The term *Configuration* describes the configuration of each delay block. The differences between the desired and measured delay values are also shown.

It can be seen that the error of implementation in terms of the delays is limited to maximum of 0.55 ns. The delay error could be reduced if smaller delay lines are available. However, the improvement could be limited. This is because these values are calculated and implemented based on the group delay of the phase shifters at the reference voltages. Upon the completion of constructing the cancellation block, variable attenuators and phase shifters need to be fine-tuned, in order to obtain the optimal cancellation performance. According to Figure. 6.15, when tuning the phase shifter, the variance of the group delay is about 0.4 ns. Therefore, the error of the delay could be dominated by the phase shifter, even when smaller delay lines are available.

Table 6.6: Calculated and measured delay and insertion loss of the delay blocks for MADF-DC

Tap index	Desired delay (ns)	Configuration	Measured delay (ns)	Measured insertion loss (dB)	Delay difference from desired (ns)
1	27.72	20 ns, 5 ns, 2 ns and connectors	28.27	6.05	-0.55
2	10.2	5 ns, 5 ns and connectors	9.99	2.1	0.21
3	5.06	5 ns	5.32	1.18	-0.26
4	15.89	10 ns,5 ns and connectors	15.68	3.14	0.21

Calculation of the value of the fixed attenuator in each cancellation path
The value of the fixed attenuator in each cancellation path can thus be calculated by subtracting the measured total insertion loss of the components shown in Table. 6.4 and the measured insertion loss of the corresponding delay block that is shown in Table. 6.6. The subtraction results are shown in Table. 6.7. Since the variable

attenuators can be tuned by approximately ± 2.5 dB from the reference value without affecting the phase and group delays, the attenuation difference between the desired and measured values can be compensated by these variable components.

Table 6.7: The calculated and measured values of the fixed attenuators

Tap index	Desired attenuation (dB)	Measured attenuation (dB)	Attenuation difference from desired value (dB)
1	12.77	13.5	-0.73
2	1.78	2.2	-0.42
3	7.57	8.5	-0.97
4	4.64	5.2	-0.56

Final implementation of the cancellation block   Once the desired delay and attenuation values for the delay blocks and fixed attenuators have been calculated, the cancellation block can thus be implemented. The photograph of the test bench is shown in Figure. 6.16.

Table 6.8: The control voltages after the optimization for the variable attenuators and phase shifters

	Variable Attenuators				Variable Phase Shifters			
	Tap Index				Tap Index			
	1	2	3	4	1	2	3	4
Optimal Voltage (V)	6.355	4.6364	4.6019	4.1069	3.708	2.0152	5.1445	7.988

After completing the construction of the cancellation block, fine tuning of the variable components is needed in order to achieve the cancellation. Fine tuning can be performed using the simulated annealing algorithm. Simulated annealing is one of the well-known global optimization algorithms. In this test bench, the goal we use for the optimization is to minimize the total power of the resulting leakage after the cancellation within the frequency band of interest. There are eight parameters, in total, to be adapted including four voltages for controlling the attenuators and four

for varying the phase shifters. Since simulated annealing adapting the parameters in infinite resolution comparing to the 13-bit resolution from the DAC, it is possible that the algorithm is stuck in one annealing cycle for too long time. To avoid this, the re-annealing interval is set to be 70 which is obtained experimentally. It is big enough for the algorithm to settle, but small enough to avoid the algorithm from sticking in a single cycle before reaching the optimal point. The control voltages for the variable attenuators and phase shifters that are returned by the optimization algorithm are shown in Table. 6.8.

Discussions on the two-way combiner   Due to the use of the two-way combiner, there is a 3 dB insertion loss in the RX path. As a result, the leakages are 3 dB smaller than what they should be. Such insertion loss can be reduced by replacing the two-way combiner with a direction coupler. The coupler with a large coupling factor could reduce the implementability of the cancellation system that uses only passive components. Therefore, the coupling factor should be chosen to be as large as possible, as long as no gain is needed in any of the cancellation paths. The implementability of the cancellation system using only passive components has been discussed in the previous two chapters.

When a directional coupler is used as the combining component, the output of the cancellation block and the RX port of the duplexer need to be connected with the *through* and *output* ports of the coupler, respectively. The rest of the receiver can thus be connected at the *input* port. The remaining attenuation of the cancellation block can be calculated by firstly subtracting the coupling factor and the insertion loss of the coupler. Then the subtraction result can then be taken away from the desired attenuation of the cancellation block to give the remaining values. These remaining attenuations should be positive values as negative values represent the need for extra gain.

The completion of the cancellation block implementation allows the cancellation performance to be measured. The results are shown in the following section.
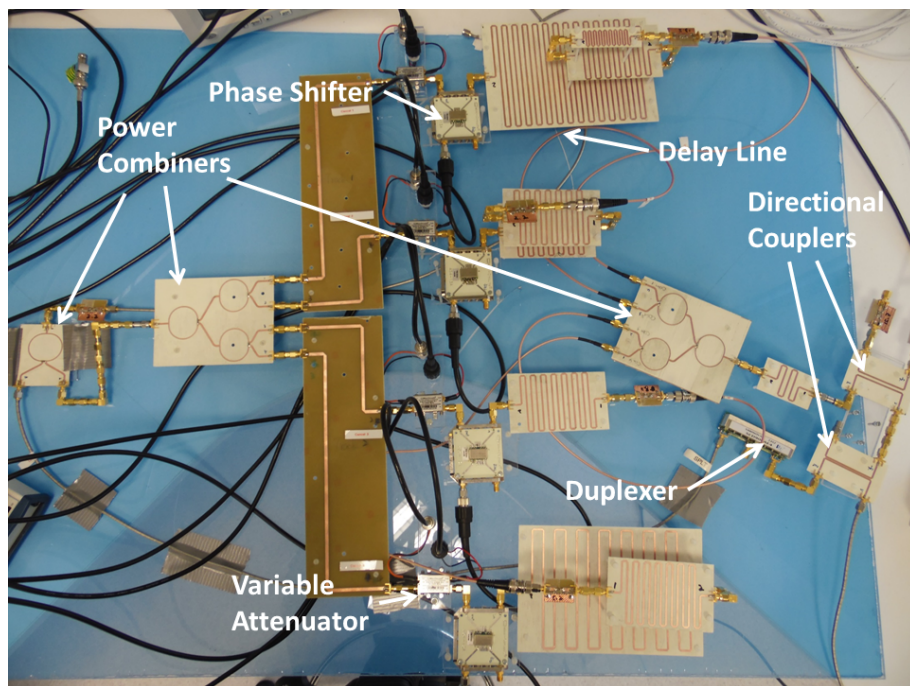
(a)
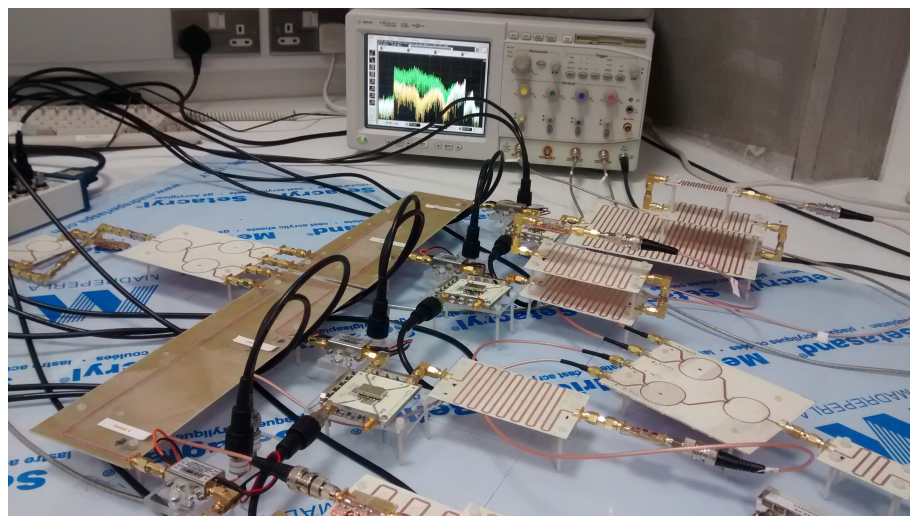
(b)

Figure 6.16: Test photograph of the leakage cancellation using MADF-DC. (a) Top view. (b) Side view

6.5 Measured Results using MADF-DC

The leakages before and after cancellation are measured and shown in Figure. 6.17. The resulting leakage using the ideal components are also shown in the figure. This

result is obtained using MADF-DC. Since it has been shown in Figure. 6.8 that the expected performance (using ideal components) between MADF-DC and MCoSaMP is very similar, the expected leakage using MCoSaMP is not shown in Figure. 6.17. It can be seen that the measured cancellation performance is degraded from the ideal one. This can be expected since the tunable RF components suffer from high interdependences of the attenuation, phase and delays. In general, the cancellation performance is implemented successfully.

The best cancellation of the measured result is approximately 30 dB at about 893 MHz. Between 888 MHz and 898 MHz, i.e. 10 MHz bandwidth, the cancellation is greater than 20 dB. From the lower frequency edge up to around 907 MHz, there is at least 10 dB cancellation. At the frequencies that are greater than 907 MHz, the cancellation performance decreases dramatically. At about 912 MHz the resulting leakage is about 2 dB greater than the one before cancellation. Compared to the simulated result, the measured one achieves approximately 5 dB less cancellation, on average. At 906 MHz where the notch of the original leakage is, the measured signal achieved better performance than the simulated one.
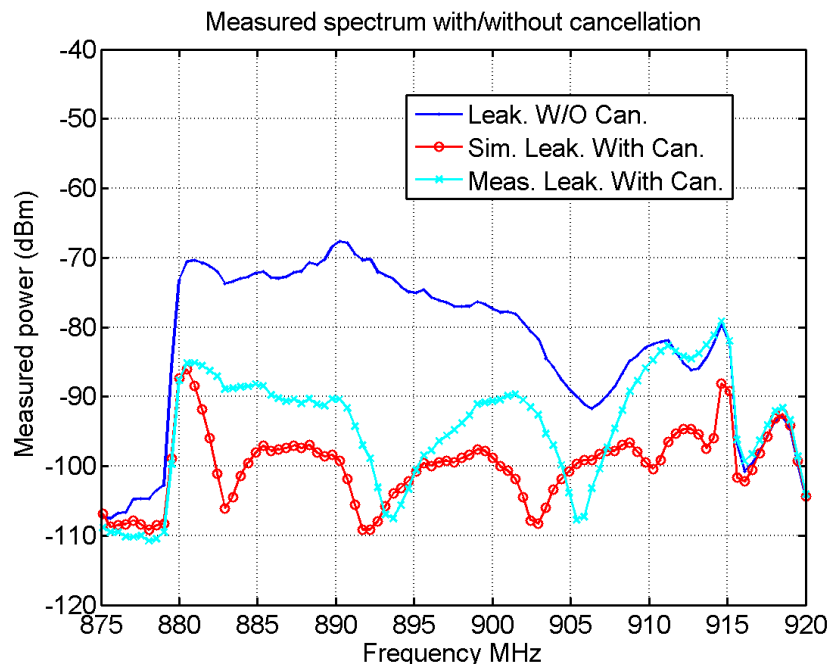
Figure 6.17: Measured cancellation results

The performance difference between the measured and simulated results are mainly due to the attenuation, phase and delay mismatches of each individual path com-

pared to the desired ones. Particularly, the delay mismatch dominates the source of errors since each delay block is manually and coarsely constructed. Furthermore, as explained in earlier sections in this chapter, the phase shifter changes the phase as well as group delay. This has hardly been compensated. Therefore, the final optimized result is a compromise of the attenuation, phase and group delay.

The group delay mismatch between the desired and the implemented values of each individual path can be resolved by placing a tunable delay line. Such tunable delay line doesn't necessarily need an ultra-wide tuning range. The one that can cover the range of group delay variation that is caused by the phase shifter is sufficient, i.e., 1 ns in this test case.

Or else, the phase shifters that are used in the test bench should be replaced with the ones which can provide independent phase tuning. A vector modulator can be a good candidate for this purpose since it can provide any combination of phase and attenuation. Once tuning the attenuation and phase doesn't affect the group delay, the delay blocks can be more accurately implemented.

6.6 Performance Comparison with Other Published Techniques

In this section, a direct comparison is performed between the proposed system and the state-of-the-art techniques. The existing solutions in the comparison were designed for solving the leakage problem in FDD systems. The comparison results are shown in Table. 6.9. Only techniques which use duplexers are compared. Since the measured results of the proposed cancellation system suffer from performance degradation due to the use of low performance RF components, the modelling results are also included in the table for comparison. The cancellation performance that is obtained both by simulation and modelling is presented for the bandwidths of 30 MHz and 35 MHz.

Table 6.9: Performance comparison

Publications	Techniques	Duplexer type	Duplexer Part Number	Duplexer Isolation (dB)	Centre Frequency (MHz)	BW (MHz)	Fractional BW	Ave. Can. (dB)	P-P. Can. (dB)
Aparin et al. [65]	Analog LMS	SAW	N/A	56	835	1.23	0.002	16	15
Kim et al. [74]	Tap based	SAW	N/A	25	1950	60	0.031	25	22
Zhang et al. [72]	Four port canceller	FBAR	Avago ACMD-7612	55	1950	5	0.003	23	23
O'Sullivan et al. [71]	Tap based	SAW	EPCOS B4224	40	836.5	4.5	0.005	20	20
O'Sullivan et al. [71]	Tap based	SAW	EPCOS B4224	40	836.5	16	0.019	9	9
This work (modelling)	**Tap based**	**Ceramic**	**Samnova SCD900AE4**	**55**	**897.5**	**35**	**0.039**	**21**	**20**
This work (modelling)	**Tap based**	**Ceramic**	**Samnova SCD900AE4**	**55**	**897.5**	**30**	**0.033**	**27**	**30**
This work (measuring)	**Tap based**	**Ceramic**	**Samnova SCD900AE4**	**55**	**897.5**	**35**	**0.039**	**16**	**11**
This work (measuring)	**Tap based**	**Ceramic**	**Samnova SCD900AE4**	**55**	**897.5**	**30**	**0.033**	**16**	**15**

In addition to the average cancellation performance, the peak-to-peak cancellation performance ($P - P.Can.$) has also been shown in the table. The peak-to-peak figure of merit describes the difference between the peak magnitudes (in dB) that are obtained before and after the cancellation. This figure of merit is more useful than the average ($Ave.Can.$) or minimum cancellation performance. This is because the magnitude response of a duplexer will inherently consist of peaks and nulls. At the frequencies where the nulls are, the cancellation tends to be small since the leakage at those frequencies is already insignificant. Due to the existence of these nulls, the performance that is given by the average or the minimum metric is degraded. The main purpose of the leakage cancellation is to decrease the noise floor of RX which is caused by the existence of TX leakage. Therefore, comparing the peak magnitude before and after the cancellation within the frequency band is more useful. Since this merit is not given in any of the published techniques, we can only approximate it from the available information within these publications.

Existing techniques The technique that has been proposed by Kim et al. [74] achieves a wide cancellation bandwidth. More than 20 dB of cancellation for 60 MHz bandwidth has been reported at the centre frequency of 1.95 GHz. This gives that the bandwidth with respect to the carrier frequency is about 0.031. However, the SAW duplexer that is used in this paper can only provide 25 dB of isolation. From the evidence that is shown in the publication, the magnitude response of this SAW duplexer is relatively flat across the cancellation bandwidth. This is the main reason why using the similar tap-based structure, a wide bandwidth cancellation can be achieved by [74] with only two taps, especially no delay matching is considered. It will struggle with more complex filter structure.

A better cancellation performance has been achieved in Zhang et al. [72] compared to Aparin et al. [65]. Both of the techniques use off-the-shelf duplexers with over 55 dB of isolation. However, only 5 MHz cancellation bandwidth at the centre frequency of 1.95 GHz has been achieved in [72]. There is no evidence showing that this technique can perform well for a much wider bandwidth. In the technique by Aparin et al. [65], the cancellation bandwidth is only 1.23 MHz at the centre frequency of 835 MHz, yielding 16 dB of cancellation.

The technique that has been proposed by O'Sullivan et al. [71] uses an off-the-shelf duplexer and achieves over 9 dB across the 16 MHz bandwidth. The centre frequency

is given as 836.5 MHz. It failed to cover the full RX band and the cancellation performance is not as promising as the proposed system in this thesis. There is little evidence showing that the bandwidth of this technique can be extended to the full RX band.

Summary of Comparison   Compared to the already published techniques, the proposed cancellation system using four taps achieves the best cancellation performance for the widest bandwidth with respect to the centre frequency. As explained earlier in this section, only active cancellation techniques that are designed for duplexers are added in the comparison. The techniques for simple filter structure are included in the comparison. For covering the full band, the modelling results show over 20 dB of cancellation could be achieved by the proposed cancellation technique of this dissertation. As discussed in the earlier chapter, the performance limitation of the modelling result is only at the edge of the frequency band. As a result, if the bandwidth is reduced to 30 MHz at the same centre frequency, the peak-to-peak cancellation performance could be increased to 30 dB. This could improve the isolation of this ceramic duplexer from minimum of 55 dB to 85 dB. On the other hand, the measured results are not as good as the simulated one. However, still over 10 dB of peak-to-peak cancellation has been achieved across the full WCDMA-VIII band and over 15 dB for 30 MHz bandwidth. The above results are obtained using an off-the-shelf duplexer. This duplexer has much more complex characteristics, than the customised ones that some of published techniques use. Therefore, the techniques shown in this thesis are the general solution to the leakage problem in rather than a specific solution for a particular duplexer.

Overall, the proposed cancellation system outperforms the existing solutions by means of wider bandwidth, better cancellation performance and less dependence on the characteristics of the duplexer, particularly where better performance RF components could be used. It has the potential of solving the TX leakage problem when a high performance duplexer is replaced with a lower one. Hence, the overall cost and the size of an FDD base station could potentially be reduced. This could be more useful for the future wireless communication systems since the required bandwidth will be dramatically increased compared to the current 4G LTE systems.

6.7 Summary

This chapter has presented a test bench which is used to prove the concept of the proposed TX leakage cancellation system. Measured cancellation performance has been shown and discussed in this chapter.

The deployment of the test bench consists of modelling and actual implementation. The modelling involves capturing the reference and the original leakage signals by the synchronized receivers. Then desired delays, attenuation and phase are calculated with the two captured signals, using MADF-DC and MCoSaMP algorithms. The difference between the ideal model which is obtained by measured S-parameters of the duplexer and the actual model has been discussed. The reason of such significant difference is mainly due to the reflected TX signals at the TX port of the duplexer. A potential solution could be that an isolator is placed between the 15 dB coupler at the TX path and the duplexer.

The impact of non-ideal phase shifters and variable attenuators have been discussed in this chapter. The solutions to these non-ideal components are given which require the deployment of fixed attenuators. The desired parameters that are calculated by modelling are used to obtain the requested delay and attenuation values so that delay blocks and fixed attenuators can be deployed.

The measured results have shown in this chapter. The comparisons between the measured and the modelled results have been performed. The reasons for the difference have been discussed which is mainly due to the inaccuracy of the delays. The inaccuracy includes the mismatch between the fixed delay block and the desired delay before adapting the variable components. Also, the group delay variance of the phase shifters is also a source of mismatch. Potential solutions can be that a small tunable delay line is placed in order to fine tune the total delay in each cancellation path.

At the end of the chapter, comparisons have been performed between the proposed architecture in this thesis and the published ones. One of the strengths of the proposed system in this thesis is that it is designed to have wideband cancellation capability. The fractional bandwidth of the system is the largest of all the techniques in the comparison. More than 20 dB and 10 dB of the peak-to-peak cancellation performance have been achieved for the modelled and measured results, respectively.

Due to the configuration of the test bench, the performance limitation is at the edge of the band. This can be eliminated by removing the band pass filter at the output of the PA and using a wider bandwidth TX signal for training, providing that the harmonic distortions of the PA is not as significant as the one we are using. If the bandwidth of cancellation is reduced to 30 MHz, the peak-to-peak cancellation performance of the proposed system increases to 30 dB and 15 dB for the modelled and measured results, respectively.

6.8 Contributions of the Chapter

The main contributions of this chapter are:

1. Specifying and designing RF components for the test bench implementation.

2. Optimizing the modelling performance by utilizing a whitening filter.

3. Analysing the impact of RF components imperfection.

4. Proposing an implementation technique for reducing the impact of RF components imperfection.

5. Carrying out a comparative review on the state-of-the-art cancellation techniques.

6. Experimentally prove that the proposed cancellation system can successfully suppress the leakage over the full bandwidth of the designated frequency band of an off-the-shelf duplexer. No existing solutions can achieve both good cancellation and wide bandwidth as the proposed techniques when using an off-the-shelf duplexer.

7 Conclusions and Future Work

7.1 Conclusions

In order to relax the isolation performance of the duplexer in an FDD base station, a novel TX leakage cancellation system is proposed in this thesis. The proposed cancellation system has the potential of achieving wideband suppressing on the in-band TX leakage at RF frequency. It provides the best cancellation for the duplexing devices with complex characteristics. The proposed cancellation system is designed to model the duplexer by using the noise of the PA and the leakage signal. The use of the whitening filter at the baseband removes the dependences of the types of the TX signals. For this reason, the proposed cancellation system could be widely deployed in FDD systems, whether it is an LTE or WCDMA system etc.

The main contributions of this thesis are as follows:

- **A review on the state-of-the-art active cancellation techniques has been carried out.** In this review, the state-of-the-art techniques have been discussed. It has shown that digital cancellation techniques can provide a high performance with little hardware resources. However, due to the existence of the high power in-band leakage, the noise floor of the receiver increases and causes the desensitization of the receiver. The desensitization occurs irrespective of the digital cancellation performance. Therefore, digital solutions are not sufficient for solving the in-band TX leakage problem. The leakage needs to be suppressed at the RF before the LNA. The state-of-the-art RF cancellation techniques can't satisfy all the requirements of: wideband; high cancellation and are designed for more complex filter structures. Therefore, the in-band TX leakage is an unsolved challenge. The new cancellation system is proposed based on this review.

- **A novel cancellation architecture has been presented**. The proposed cancellation system consists of an RF cancellation block and baseband modelling block. The cancellation block is an RF implementation of an FIR filter. It consists of a number of cancellation paths in which there is a variable attenuator, a phase shifter and a delay block. The baseband modelling block characterizes the duplexer at the baseband of the transceiver and generates a set of parameters including the attenuation, phase and delay for each path in the cancellation block. The existing techniques don't have the ability to optimize the delays. Hence, a wide band cancellation for duplexing devices with complex characteristics hasn't been reported except the proposed system in this thesis.

- **A novel modelling algorithm, MADF-DC has been proposed**. This is one of the two modelling algorithms that have been presented in this dissertation. This algorithm is designed to improve the delay estimation accuracy using digital baseband signals. This estimation technique is developed from the classic adaptive delay filter (C-ADF) technique. In order to achieve a better delay estimation accuracy, three parameters have been introduced. They are the up-sampling ratio, maximum and minimum delay limit constraints. Sweeping of these three parameters is needed and the optimal ones are chosen so that the corresponding modelling performance is the best. Simulation results have shown that the modelling accuracy of MADF-DC is significantly higher than the C-ADF and LS algorithms.

- **A novel modelling algorithm, MCoSaMP has been proposed**. This is the second modelling algorithm that has been proposed in this thesis. MCoSaMP is based on the compressive sampling matching pursuit (CoSaMP) technique. The motivation of developing this technique is to achieve the same outstanding modelling performance as the MADF-DC technique, but for a shorter estimation time. This algorithm uses the up-sampled reference and leakage signals and optimizes the delays and tap weights utilizing the classic CoSaMP kernel, iteratively. The three parameters that are introduced for MADF-DC are also required for this technique. Simulation results show that the modelling performance of MCoSaMP is also significantly better than the classic techniques. Between MCoSaMP and MADF-DC, the modelling performance achieved using both techniques is similar. This satisfies the performance requirement when developing MCoSaMP. The simulation results have

also shown that MCoSaMP is less dependent on the sweeping of the delay limit constraints than MADF-DC. The estimation time of MCoSaMP could be reduced by eliminating the sweeping of the delay limit constraints, at a small cost of modelling performance. In comparison, the estimation time of MADF-DC could also be reduced by eliminating the sweeping of the delay constraining parameters. However, the performance degradation is significant. Therefore, the aim of developing the MCoSaMP has been achieved. This thesis also suggests that for performance critical applications, the sweeping of the up-sampling ratio and delay limit constraints is essential, especially when the characteristics of the duplexer is more complex (such as a cavity duplexer).

- **The impact of the low performance RF components has been analysed.** It has shown in this thesis that changing the phase of the phase shifter used in this test bench causes altering of its insertion loss and group delay, significantly. For a variable attenuator, it also suffers from interdependences of attenuation, phase and group delay. It is impossible to implement the proposed cancellation system using these low performance RF components, without a complex implementation process and technique.

- **A novel implementation technique for the FIR filter structure using low performance RF components has been proposed**. This technique enables the implementation of the proposed cancellation architecture using low performance RF components. Fixed attenuators have been used to reduce the interdependences caused by the variable attenuators. The performance impact from the altered insertion loss of the phase shifter has also been eliminated. This thesis also proposes that the impact of the low performance RF components could be reduced to minimum when using variable delay lines for the implementation of the test bench.

- **A test bench has been successfully constructed and measured for the proof of concept purpose**. The measured results show that the proposed system has achieved over 16 dB cancellation for 35 MHz of bandwidth. Though this performance is degraded from the expected performance (21 dB), it is mainly due to the configuration of this test bench. The measured performance can be improved significantly if better performance components are used. The performance comparison has shown that the proposed cancellation system achieves a better cancellation performance and wider bandwidth than

the state-of-the-art techniques.

7.2 Future Work

The operation of the presented cancellation system requires the transceiver being turned off during the modelling and at the early stage of the cancellation. The presented system could be further improved if the characterization of the duplexer could be achieved without turning off the transceiver.

The presented cancellation system is designed to suppress the in-band leakage whereas the cancellation of the out-of-band leakage relies on the conventional filter. The main reason is that suppressing both the in-band and out-of-band leakage requires a much higher order cancellation system. It would be desirable to develop the presented system so that it has the ability of cancelling both portions of the TX leakage without significantly increasing the hardware resources.

Additionally, the test bench that has been constructed is for verifying the concept of the proposed cancellation system. It was constructed using prototype level components. For this reason, the form factor of the proposed system is not as compact. Therefore, silicon level integration could be another avenue for the future development of the proposed cancellation architecture.

Bibliography

[1] J. Penttinen, *The telecommunications handbook: Engineering Guidelines for Fixed, Mobile and Satellite Systems.* N.J.: Wiley, 2015, ISBN: 978-1-119-94488-1.

[2] Alcatel-Lucent, "Alcatel-Lucent 9364 Metro Cell Outdoor V2 1900/850 MHZ | RELEASE BCR 3.0," Accessed: Dec. 02, 2015. [Online]. Available: http://www3.alcatel-lucent.com/wps/DocumentStreamerServlet? LMSG_CABINET=Docs_and_Resource_Ctr&LMSG_CONTENT_FILE= Data_Sheets/9364_Metro_Cell_Outdoor_V2_EN_Datasheet.pdf

[3] K&L Microwave, "K&L Microwave Product Catalog," 2014, Accessed: Oct. 23, 2015. [Online]. Available: http://www.klmicrowave.com/catalog/ KLCat2014highres.pdf

[4] William F., Lieske Sr., "Understanding, Maintaining and Re-Tuning Antenna Duplexers," Accessed: Oct. 22, 2015. [Online]. Available: http: //www.repeater-builder.com/antenna/pdf/emr-corp-antenna-duplexers.pdf

[5] Tektelic Communications, "New engineering approach to Metrocell design," 2013, Accessed: Nov. 15, 2015. [Online]. Available: http://www.tektelic.com/ new-engineering-approach-to-metrocell-design/

[6] I. C. Hunter, L. Billonet, B. Jarry, and P. Guillon, "Microwave filters-applications and technology," *IEEE Transactions on Microwave Theory and Techniques*, vol. 50, no. 3, pp. 794–805, Mar 2002.

[7] High Frequency Electronics, "Basic Data on High-Q Ceramic Coaxial Resonators," 2002, Accessed: Nov. 10, 2015. [Online]. Available: http: //www.highfrequencyelectronics.com/Nov02/HFE1102_Resonators.pdf

[8] Vectron, "SAW Products," Accessed: Oct. 25, 2015. [Online]. Available: http://www.vectron.com/products/brochures/saw_brochure.pdf

[9] Taiyo Yuden Co., Ltd., "Working principles and Applications of SAW/FBAR Devices," Accessed: Oct. 25, 2015. [Online]. Available: https://www.yuden.co.jp/productdata/navigator/en/004/E-SP2_101013.pdf

[10] R. Aigner, "SAW and BAW technologies for RF filter applications: A review of the relative strengths and weaknesses," in *IEEE Ultrasonics Symposium*, Nov 2008, pp. 582–589.

[11] R. Aigner, "Saw, baw and the future of wireless," 2013, Accessed: Dec. 02, 2015. [Online]. Available: http://www.edn.com/design/wireless-networking/4413442/SAW--BAW-and-the-future-of-wireless

[12] C.-H. Lin, H.-R. Chen, and W. Fang, "Design and fabrication of a miniaturized bulk acoustic filter by high aspect ratio etching," *Journal of Micro/Nanolithography, MEMS, and MOEMS*, vol. 4, no. 3, p. 033010, 2005.

[13] Benzacar, S., "Understanding Filter Types and Their Characteristics," 2010, Accessed: Nov. 15, 2015. [Online]. Available: http://www.mpdigest.com/issue/Articles/2010/may/anatech/Default.asp

[14] MECA Elecronics, "Isolator and Circulator Basics," 2008, Accessed: Nov. 10, 2015. [Online]. Available: http://www.mpdigest.com/issue/articles/2008/may/meca/default.asp

[15] E. Dahlman, S. Parkvall, and J. Skold, *4G: LTE/LTE-Advanced for Mobile Broadband*, 1st ed. Academic Press, 2011, ISBN: 978-0123854896.

[16] J. Zhang, "Tutorial on Small Cell/HetNet Deployment, Part 1: Evolutions towards small cell and HetNet," 2012, Accessed: Oct. 25, 2015. [Online]. Available: http://globecom2012.ieee-globecom.org/downloads/t1/1SmallCellTutorialGlobecom12Jie_v1b.pdf

[17] NEC, "Empowering the next generation of mobile network: LTE Small Cell Solutions - Micro Cell System Package," Accessed: Oct. 23, 2015. [Online]. Available: http://au.nec.com/en_AU/media/docs/brochures-solutions/NEC-LTE-Small-Cell-Solutions-Micro-Cell-System-Package.pdf

[18] Parker, T., "Global femtocell market to top 3B in 2020, report says," 2014, Accessed: Oct. 23, 2015. [Online]. Available: http://www.fiercewireless.com/tech/story/global-femtocell-market-top-3b-2020-report-says/2014-04-27

[19] Global Mobile Suppliers Association, "GSA confirms 521 LTE networks launched, LTE-Advanced now mainstream," 2016, Accessed: Apr. 16, 2017. [Online]. Available: https://gsacom.com/press-release/gsa-confirms-521-lte-networks-launched-lte-advanced-now-mainstream/

[20] H. T. Y. Urabe and H. Yamasaki, "Time division duplex transceiver," U. S. Patent 5 446 770, 1995.

[21] D. Bharadia, E. McMilin, and S. Katti, "Full Duplex Radios," in *Proceedings of the ACM SIGCOMM 2013 Conference on SIGCOMM*, ser. SIGCOMM '13. New York, NY, USA: ACM, 2013, pp. 375–386.

[22] D. Korpi, T. Riihonen, V. Syrjälä, L. Anttila, M. Valkama, and R. Wichman, "Full-Duplex Transceiver System Calculations: Analysis of ADC and Linearity Challenges," *IEEE Transactions on Wireless Communications*, vol. 13, no. 7, pp. 3821–3836, July 2014.

[23] J. Zhou, T. H. Chuang, T. Dinc, and H. Krishnaswamy, "19.1 Receiver with >20MHz bandwidth self-interference cancellation suitable for FDD, coexistence and full-duplex applications," in *IEEE International Solid-State Circuits Conference - (ISSCC)*, Feb 2015, pp. 1–3.

[24] Z. Abate, *WiMax RF Systems Engineering.* Artech House, 2009, ISBN: 978-1-59693-975-2.

[25] Abdelhalem, S.H. and Gudem, P.S. and Larson, L.E., "Hybrid Transformer-Based Tunable Differential Duplexer in a 90-nm CMOS Process," *IEEE Transactions on Microwave Theory and Techniques*, vol. 61, no. 3, pp. 1316–1326, March 2013.

[26] J. Audet, "Theory and testing of duplexers," 2002, Accessed: Dec. 02, 2015. [Online]. Available: http://www.repeater-builder.com/antenna/pdf/ve2azx-duplexerinfo.pdf

[27] P. Wang, L. Li, and S. Wei, "Design of a tunable S-band narrow-band coaxial cavity filter," in *International Conference on Microwave and Millimeter Wave Technology (ICMMT)*, vol. 1, May 2012, pp. 1–4.

[28] T. Shen, K. A. Zaki, and C. Wang, "Tunable dielectric resonators with dielectric tuning disks," *IEEE Transactions on Microwave Theory and Techniques*, vol. 48, no. 12, pp. 2439–2445, Dec 2000.

[29] S. W. Chen, K. A. Zaki, and R. G. West, "Tunable, temperature-compensated dielectric resonators and filters," *IEEE Transactions on Microwave Theory and Techniques*, vol. 38, no. 8, pp. 1046–1052, Aug 1990.

[30] J. Krupka, A. Abramowicz, and K. Derzakowski, "Magnetically tunable filters for cellular communication terminals," *IEEE Transactions on Microwave Theory and Techniques*, vol. 54, no. 6, pp. 2329–2335, June 2006.

[31] A. R. Brown and G. M. Rebeiz, "A varactor-tuned RF filter," *IEEE Transactions on Microwave Theory and Techniques*, vol. 48, no. 7, pp. 1157–1160, Jul 2000.

[32] B.-W. Kim and S.-W. Yun, "Varactor-tuned combline bandpass filter using step-impedance microstrip lines," *IEEE Transactions on Microwave Theory and Techniques*, vol. 52, no. 4, pp. 1279–1283, April 2004.

[33] S. Fouladi, F. Huang, W. D. Yan, and R. R. Mansour, "High- Q Narrowband Tunable Combline Bandpass Filters Using MEMS Capacitor Banks and Piezo-motors," *IEEE Transactions on Microwave Theory and Techniques*, vol. 61, no. 1, pp. 393–402, Jan 2013.

[34] K&L Microwave, "WSD-00136 AMPS Fullband Duplexer," Accessed: Oct. 23, 2015. [Online]. Available: http://www.klmicrowave.com/product_attach/2/_plk309_1_WSD00136.pdf

[35] T. Cooper and R. Farrell, "Value-Chain Engineering of a Tower-Top Cellular Base Station System," in *IEEE 65th Vehicular Technology Conference*, April 2007, pp. 3184–3188.

[36] CTS Corporation, "UPD: Universal-footprint Pico Cell Duplexers," Accessed: Nov. 17, 2015. [Online]. Available: http://www.ctscorp.com/components/UPD/UPD_Universal_Footprint_Pico_Cell_Duplexer.pdf

[37] Analog Devices, Inc., "Analog Front End for 3G Femto Base Stations Bring Wireless Connectivity Home," 2008, Accessed: Dec. 02, 2015. [Online]. Available: http://www.analog.com/library/analogdialogue/archives/42-12/femtocell.html

[38] CTS Corporation, "UMD: Universal-footprint Metro Cell Duplexers," Accessed: Nov. 15, 2015. [Online]. Available: http://www.ctscorp.com/components/UMD/UMD_Universal_Footprint_Metro_Cell_Duplexers.pdf

[39] Token Electronics Industry Co. Ltd., "What is SAW filters-Advantage of Token Piezoelectric SAW Devices," 2010, Accessed: Nov. 15, 2015. [Online]. Available: http://www.token.com.tw/pdf/saw/saw-devices.pdf

[40] Ebata, Yasuo, et al., "Power Durability of SAW Devices," Accessed: Nov. 10, 2015. [Online]. Available: http://www.te.chiba-u.jp/~ken/Symp/Symp2001/PAPER/EBATA.PDF

[41] K. M. Lakin, "hin film resonator technology," *IEEE Transactions on Ultrasonics, Ferroelectrics, and Frequency Control*, vol. 52, no. 5, pp. 707–716, May 2005.

[42] Y. S. Choi and H. Shirani-Mehr, "Simultaneous Transmission and Reception: Algorithm, Design and System Level Performance," *IEEE Transactions on Wireless Communications*, vol. 12, no. 12, pp. 5992–6010, December 2013.

[43] B. Debaillie, D. J. van den Broek, C. Lavín, B. van Liempd, E. A. M. Klumperink, C. Palacios, J. Craninckx, B. Nauta, and A. Pärssinen, "Analog/RF Solutions Enabling Compact Full-Duplex Radios," *IEEE Journal on Selected Areas in Communications*, vol. 32, no. 9, pp. 1662–1673, Sept 2014.

[44] Trans-Tech, Inc., "Use of Ferrimagnetic Material in Circulators," 2013, Accessed: Oct. 26, 2015. [Online]. Available: http://www.trans-techinc.com/documents/Ferrimagnetic_Material_in_Circulators_202840A.pdf

[45] ETSI, "Digital cellular telecommunications system (Phase 2+); Radio transmission and reception (3GPP TS 45.005 version 12.5.0 Release 12)," Tech. Rep. TS 1 V12.5.0.

[46] 3GPP, "LTE; Evolved Universal Terrestrial Radio Access (E-UTRA); Base Station (BS) radio transmission and reception (3GPP TS 36.104 version 12.7.0 Release 12)," Tech. Rep. TS 36.104 v12.7.0, April 2015.

[47] M. V. D. Nair, R. Giofrè, L. Piazzon, and P. Colantonio, "A comparative study on digital predistortion techniques for Doherty amplifier for LTE applications," in *International Workshop on Integrated Nonlinear Microwave and Millimetre-wave Circuits (INMMiC)*, April 2014, pp. 1–3.

[48] Y. Liu, J. J. Yan, H. T. Dabag, and P. M. Asbeck, "Novel Technique for Wideband Digital Predistortion of Power Amplifiers With an Under-Sampling ADC," *IEEE Transactions on Microwave Theory and Techniques*, vol. 62, no. 11, pp. 2604–2617, Nov 2014.

[49] P. M. Suryasarman and A. Springer, "A Comparative Analysis of Adaptive Digital Predistortion Algorithms for Multiple Antenna Transmitters," *IEEE Transactions on Circuits and Systems I: Regular Papers*, vol. 62, no. 5, pp. 1412–1420, May 2015.

[50] A. Abdelhafiz, A. Kwan, O. Hammi, and F. M. Ghannouchi, "Digital Predistortion of LTE-A Power Amplifiers Using Compressed-Sampling-Based Unstructured Pruning of Volterra Series," *IEEE Transactions on Microwave Theory and Techniques*, vol. 62, no. 11, pp. 2583–2593, Nov 2014.

[51] H. Darabi, "A Blocker Filtering Technique for SAW-Less Wireless Receivers," *IEEE Journal of Solid-State Circuits*, vol. 42, no. 12, pp. 2766–2773, Dec 2007.

[52] T. D. Werth, C. Schmits, R. Wunderlich, and S. Heinen, "An Active Feedback Interference Cancellation Technique for Blocker Filtering in RF Receiver Front-Ends," *IEEE Journal of Solid-State Circuits*, vol. 45, no. 5, pp. 989–997, May 2010.

[53] D. Lee and B.-W. Min, "1-TX and 2-RX in-band full-duplex radio front-end with 60 dB self-interference cancellation," in *IEEE MTT-S International Microwave Symposium*, May 2015, pp. 1–4.

[54] I. Choi, M. Cha, S. Lee, and I. Kwon, "A TX leakage canceller based on an autotransformer with loss compensating amplifier," in *Asia-Pacific Microwave Conference*, Dec 2011, pp. 271–274.

[55] M. Mikhemar, H. Darabi, and A. A. Abidi, "A Multiband RF Antenna Duplexer on CMOS: Design and Performance," *IEEE Journal of Solid-State Circuits*, vol. 48, no. 9, pp. 2067–2077, Sept 2013.

[56] N. Li, W. Zhu, and H. Han, "Digital Interference Cancellation in Single Channel, Full Duplex Wireless Communication," in *8th International Conference on Wireless Communications, Networking and Mobile Computing (WiCOM)*, Sept 2012, pp. 1–4.

[57] A. Frotzscher and G. Fettweis, "Least Squares Estimation for the Digital Compensation of Tx Leakage in zero-IF Receivers," in *IEEE Global Telecommunications Conference, GLOBECOM 2009.*, 2009, pp. 1–6.

[58] D. Korpi, L. Anttila, V. Syrjälä, and M. Valkama, "Widely Linear Digital Self-Interference Cancellation in Direct-Conversion Full-Duplex Transceiver," *IEEE Journal on Selected Areas in Communications*, vol. 32, no. 9, pp. 1674–1687, Sept 2014.

[59] H. Kamizuma, T. Masuda, and M. Onishi, "Third-order intermodulation product canceller for LTE base station receiver," in *41st European Microwave Conference (EuMC)*, Oct 2011, pp. 230–233.

[60] A. Kiayani, L. Anttila, and M. Valkama, "Modeling and dynamic cancellation of TX-RX leakage in FDD transceivers," in *IEEE 56th International Midwest Symposium on Circuits and Systems (MWSCAS)*, Aug 2013, pp. 1089–1094.

[61] L. Anttila, D. Korpi, V. Syrjala, and M. Valkama, "Cancellation of power amplifier induced nonlinear self-interference in full-duplex transceivers," in *Asilomar Conference on Signals, Systems and Computers*, Nov 2013, pp. 1193–1198.

[62] P. Pratt, P. Forbes, and J. McCormack, "Digitally assisted RF filter Self Interference cancellation system," in *44th European Microwave Conference (EuMC)*, Oct 2014, pp. 929–932.

[63] M. Duarte, C. Dick, and A. Sabharwal, "Experiment-Driven Characterization of Full-Duplex Wireless Systems," *IEEE Transactions on Wireless Communications*, vol. 11, no. 12, pp. 4296–4307, December 2012.

[64] ETSI, "Universal Mobile Telecommunications System (UMTS); Base Station (BS) radio transmission and reception (FDD)," Tech. Rep. TS 125 104-v12.5.0.

[65] V. Aparin and G. J. Ballantyne and C. J. Persico and A. Cicalini, "An integrated LMS adaptive filter of TX leakage for CDMA receiver front ends," *IEEE Journal of Solid-State Circuits*, vol. 41, no. 5, pp. 1171–1182, May 2006.

[66] J. Glover, "Adaptive noise canceling applied to sinusoidal interferences," *IEEE Transactions on Acoustics, Speech, and Signal Processing*, vol. 25, no. 6, pp. 484–491, Dec 1977.

[67] H. Su, G. Szczepkowski, and R. Farrell, "Wideband Tx leakage cancellation using adaptive delay filter at RF frequencies," in *Irish Signals Systems Conference 2014 and 2014 China-Ireland International Conference on Information and Communications Technologies (ISSC 2014/CIICT 2014). 25th IET*, June 2014, pp. 396–401.

[68] S. Kannangara and M. Faulkner, "Analysis of an Adaptive Wideband Duplexer With Double-Loop Cancellation," *IEEE Transactions on Vehicular Technology*, vol. 56, no. 4, pp. 1971–1982, July 2007.

[69] K. Kolodziej, J. McMichael, and B. Perry, "Adaptive RF canceller for transmit-receive isolation improvement," in *IEEE Radio and Wireless Symposium (RWS)*, Jan 2014, pp. 172–174.

[70] J. McMichael and K. Kolodziej, "Optimal tuning of analog self-interference cancellers for full-duplex wireless communication," in *50th Annual Allerton Conference on Communication, Control, and Computing (Allerton)*, Oct 2012, pp. 246–251.

[71] T. O'Sullivan, R. A. York, B. Noren, and P. M. Asbeck, "Adaptive duplexer implemented using single-path and multipath feedforward techniques with BST phase shifters," *IEEE Transactions on Microwave Theory and Techniques*, vol. 53, no. 1, pp. 106–114, Jan 2005.

[72] T. Zhang, A. R. Suvarna, V. Bhagavatula, and J. C. Rudell, "An Integrated CMOS Passive Self-Interference Mitigation Technique for FDD Radios," *IEEE Journal of Solid-State Circuits*, vol. 50, no. 5, pp. 1176–1188, May 2015.

[73] S. S. Hong, J. Mehlman, and S. Katti, "Picasso: Flexible RF and Spectrum Slicing," in *Proceedings of the ACM SIGCOMM 2012 Conference on Applications, Technologies, Architectures, and Protocols for Computer Communication*, ser. SIGCOMM '12. New York, NY, USA: ACM, 2012, pp. 37–48.

[74] H. Kim, S. Woo, S. Jung, and K. H. Lee, "A CMOS Transmitter Leakage Canceller for WCDMA Applications," *IEEE Transactions on Microwave Theory and Techniques*, vol. 61, no. 9, pp. 3373–3380, Sept 2013.

[75] Q. Gu, *RF system design of transceivers for wireless communications*. Springer Science & Business Media, 2005, ISBN: 978-0-387-24162-3.

[76] G. Gui and F. Adachi, "Adaptive sparse system identification using normalized least mean fourth algorithm," *International Journal of Communication Systems*, vol. 28, no. 1, pp. 38–48, 2015.

[77] D. Etter and Y.-F. Cheng, "System modeling using an adaptive delay filter," *IEEE Transactions on Circuits and Systems*, vol. 34, no. 7, pp. 770–774, Jul 1987.

[78] K. Kusaba, A. Okamura, and T. Sekiguchi, "A complex adaptive delay filter," in *Processing IEEE International Conference on Acoustics, Speech, and Signal, (ICASSP '01)*, vol. 6, 2001, pp. 3761–3764 vol.6.

[79] Y. Chen, Y. Gu, and A. O. Hero, "Sparse LMS for system identification," in *Processing IEEE International Conference on Acoustics, Speech and Signal*, April 2009, pp. 3125–3128.

[80] D. Needell and J. Tropp, "CoSaMP: Iterative signal recovery from incomplete and inaccurate samples," *Applied and Computational Harmonic Analysis*, vol. 26, no. 3, pp. 301 – 321, 2009.

[81] J. H. Gross and D. Etter, "Comparison of echo cancellation algorithms for the adaptive delay filter," in *IEEE 42nd Vehicular Technology Conference*, 1992, pp. 574–576 vol.1.

[82] D. Etter, "Identification of sparse impulse response systems using an adaptive delay filter," in *Processing IEEE International Conference on Acoustics, Speech, and Signal, ICASSP*, vol. 10, Apr 1985, pp. 1169–1172.

[83] Y.-F. Cheng and D. M. Etter, "Analysis of an adaptive technique for modeling sparse systems," *IEEE Transactions on Acoustics, Speech, and Signal Processing*, vol. 37, no. 2, pp. 254–264, Feb 1989.

[84] G. Chaudhary and Y. Jeong, "Distributed Transmission Line Negative Group Delay Circuit With Improved Signal Attenuation," *IEEE Microwave and Wireless Components Letters*, vol. 24, no. 1, pp. 20–22, Jan 2014.

[85] G. Chaudhary, Y. Jeong, and J. Im, "A Design of Reconfigurable Negative Group Delay Circuit Without External Resonators," *IEEE Antennas and Wireless Propagation Letters*, vol. 14, pp. 883–886, 2015.

[86] A. Sanchez-Merono, J. Arias, and M. Sanchez-Lopez, "Negative Group Delay of Reflected Pulses on Microstrip Slabs and Bragg Reflectors," *IEEE Journal of Quantum Electronics*, vol. 46, no. 4, pp. 546–553, April 2010.

[87] B. Ravelo, A. PÉrennec, M. L. Roy, and Y. G. Boucher, "Active Microwave Circuit With Negative Group Delay," *IEEE Microwave and Wireless Components Letters*, vol. 17, no. 12, pp. 861–863, Dec 2007.

[88] S. Ibrahim, G. Szczepkowski, and R. Farrell, "Wideband MEMS switched delay lines with high phase linearity," in *Electronics, Circuits and Systems (ICECS), 2014 21st IEEE International Conference on*, Dec 2014, pp. 187–190.

[89] TriQuint Semiconductor, "2140 MHz SAW Delay Line," Accessed: Oct. 25, 2015. [Online]. Available: http://www.triquint.com/products/d/DOC-A-00000609

[90] Anaren, Inc., "Model XDL15-2-020S (Rev. F) Delay line," Accessed: Dec. 02, 2015. [Online]. Available: https://www.anaren.com/sites/default/files/Part-Datasheets/XDL15-2-020S%20Data%20Sheet%20RevF.pdf

[91] D. Wisell, J. Jalden, and P. Handel, "Behavioral Power Amplifier Modeling Using the LASSO," in *IEEE Instrumentation and Measurement Technology Conference Proceedings, IMTC 2008.*, May 2008, pp. 1864–1867.

[92] D. M. Pozar, *Microwave Engineering*, 4th ed. Wiley, 2011, ISBN: 978-0-470-63155-3.

[93] S. Haykin, *Adaptive Filter Theory*, ser. ISBN: 9788131708699. Pearson Education, 2008. [Online]. Available: http://books.google.ie/books?id=MdDi_PF7gMsC

[94] R. J. P. Douville and D. S. James, "Experimental Study of Symmetric Microstrip Bends and Their Compensation," *IEEE Transactions on Microwave Theory and Techniques*, vol. 26, no. 3, pp. 175–182, Mar 1978.